

Washington University in St. Louis

Washington University Open Scholarship

Arts & Sciences Electronic Theses and
Dissertations

Arts & Sciences


Spring 5-15-2019

Isotopically-Resolved Neutron Cross Sections as Probe of the Nuclear Optical Potential

Cole Davis Pruitt

Washington University in St. Louis

Follow this and additional works at: https://openscholarship.wustl.edu/art_sci_etds

 Part of the [Nuclear Commons](#), [Nuclear Engineering Commons](#), [Other Chemistry Commons](#), and the [Radiochemistry Commons](#)

Recommended Citation

Pruitt, Cole Davis, "Isotopically-Resolved Neutron Cross Sections as Probe of the Nuclear Optical Potential" (2019). *Arts & Sciences Electronic Theses and Dissertations*. 1813.
https://openscholarship.wustl.edu/art_sci_etds/1813

This Dissertation is brought to you for free and open access by the Arts & Sciences at Washington University Open Scholarship. It has been accepted for inclusion in Arts & Sciences Electronic Theses and Dissertations by an authorized administrator of Washington University Open Scholarship. For more information, please contact digital@wumail.wustl.edu.

WASHINGTON UNIVERSITY IN ST. LOUIS

Department of Chemistry

Dissertation Examination Committee:

Lee Sobotka, Chair

Robert Charity

Willem Dickhoff

Ronald Lovett

Richard Mabbs

Demetrios Sarantites

Isotopically-Resolved Neutron Cross Sections
as Probe of the Nuclear Optical Potential

by

Cole Davis Pruitt

A dissertation presented to
The Graduate School
of Washington University in
partial fulfillment of the
requirements for the degree
of Doctor of Philosophy

May 2019

Saint Louis, Missouri

© 2019, Cole D. Pruitt

TABLE OF CONTENTS

List of Figures	vii
List of Tables	xii
Acknowledgements	xvi
Abstract	xviii
1 Introduction	1
1.1 Models of the Atomic Nucleus: Overview	1
1.1.1 Liquid Drop Model	2
1.1.2 Mean-field and Beyond-mean-field Models	5
1.1.3 Optical Models	8
1.2 Relevant Experimental Nuclear Data	15
1.2.1 Nucleon Scattering Data	15
1.2.2 Nuclear Masses, Matter Radii, and Charge Radii	21
1.3 Motivation, Scope, and Dissertation Outline	24
2 Neutron Total Cross Sections: Experimental Setup	25
2.1 Overview of Neutron σ_{tot} Experiments	25

2.2	Detector Construction	28
2.3	Sample Preparation	30
2.4	Experimental Facility at LANSCE	36
2.5	Data Acquisition	45
3	Neutron Total Cross Sections: Analysis and Results	49
3.1	Timing Considerations	49
3.2	Deadtime Correction	59
3.3	Cross Section Calculation	66
3.4	Results	69
3.4.1	Benchmarking σ_{tot} Results with Natural Samples	69
3.4.2	$^{16,18}\text{O}$ σ_{tot} Results	74
3.4.3	$^{58,64}\text{Ni}$ σ_{tot} Results	77
3.4.4	^{103}Rh σ_{tot} Results	80
3.4.5	$^{112,124}\text{Sn}$ σ_{tot} Results	82
4	Neutron Elastic Differential Cross Sections: Experimental Setup	85
4.1	Overview of Neutron $\frac{d\sigma}{d\Omega}$ Experiments	85
4.1.1	Pulse-Shape Discrimination (PSD)	86
4.2	Sample Preparation	90
4.3	Experimental Facility at TUNL	90
4.4	Data Acquisition	95
5	Neutron Elastic Differential Cross Sections: Analysis and Results	97

TABLE OF CONTENTS

5.1	Event Identification	97
5.2	Normalization	100
5.3	Finite-Size Corrections	103
5.4	Results	109
5.4.1	$^{112,124}\text{Sn}$ $\frac{d\sigma}{d\Omega}$ at 11 MeV	109
5.4.2	$^{112,124}\text{Sn}$ $\frac{d\sigma}{d\Omega}$ at 17 MeV	110
6	Dispersive Optical Model: Overview	113
6.1	The Single-Particle Propagator	113
6.1.1	Perturbation Expansion and The Dyson Equation	117
6.1.2	The Dispersion Relation	122
6.2	Connection to Experimental Observables	124
6.2.1	Elastic and Inelastic Nucleon Scattering	124
6.2.2	Bound-state Properties	126
6.3	Parameterization of the Potential	129
6.3.1	Functional Forms	130
6.3.2	Real Part	132
6.3.3	Imaginary Part	134
6.3.4	Parameterization of Asymmetry Dependence	137
6.4	Computational Considerations	138
6.4.1	Fitting Procedure	140
7	Dispersive Optical Model:	
	Results on $^{16,18}\text{O}$, $^{40,48}\text{Ca}$, $^{58,64}\text{Ni}$, $^{112,124}\text{Sn}$, ^{208}Pb	141
7.1	Results for $^{40,48}\text{Ca}$	142

TABLE OF CONTENTS

7.1.1	Results for ^{40}Ca	142
7.1.2	Results for ^{48}Ca	155
7.2	Results for $^{16,18}\text{O}$	157
7.2.1	Results for ^{16}O	158
7.2.2	Results for ^{18}O	160
7.3	Results for $^{58,64}\text{Ni}$	162
7.3.1	Results for ^{58}Ni	162
7.3.2	Results for ^{64}Ni	163
7.4	Results for $^{112,124}\text{Sn}$	164
7.4.1	Results for ^{112}Sn	165
7.4.2	Results for ^{124}Sn	167
7.5	Results for ^{208}Pb	168
7.6	General Trends	172
7.6.1	Neutron Skins Sensitive to Shell Structure	172
7.6.2	Depletion, Momentum Content, and Deep Imaginary Strength	172
7.6.3	Overestimation of RMS Charge Radius	176
8	Conclusions	179
8.1	Advancements in Digitizer-enabled Neutron σ_{tot} Measurements of Rare Isotopes	179
8.2	Implications of DOM Results	180
8.3	Additional Directions for Future Study	186
	Bibliography	189
	Appendix A Isotopic Composition of Enriched Samples	211

TABLE OF CONTENTS

Appendix B Experimental Data Used to Constrain DOM Potentials	213
B.1 ^{16}O Scattering Data	214
B.2 ^{18}O Scattering Data	216
B.3 ^{40}Ca Scattering Data	218
B.4 ^{48}Ca Scattering Data	220
B.5 ^{58}Ni Scattering Data	222
B.6 ^{64}Ni Scattering Data	224
B.7 ^{112}Sn Scattering Data	226
B.8 ^{124}Sn Scattering Data	227
B.9 ^{208}Pb Scattering Data	228
Appendix C Parameter Values of DOM Potentials	231
Appendix D Visualization of DOM Fit Results	235
D.1 DOM fit of ^{16}O	237
D.2 DOM fit of ^{18}O	241
D.3 DOM fit of ^{40}Ca	245
D.4 DOM fit of ^{48}Ca	249
D.5 DOM fit of ^{58}Ni	253
D.6 DOM fit of ^{64}Ni	257
D.7 DOM fit of ^{112}Sn	261
D.8 DOM fit of ^{124}Sn	265
D.9 DOM fit of ^{208}Pb	269
Glossary	275

LIST OF FIGURES

1.1	Experimental neutron σ_{tot} data and strongly-absorbing-sphere predictions .	10
1.2	An illustration of the nuclear Ramsauer effect	14
1.3	Landscape of existing neutron σ_{tot} data in 2019	17
1.4	Landscape of existing proton σ_{rxn} data in 2019	18
1.5	^{186}W - ^{182}W neutron σ_{tot} relative difference and Ramsauer model predictions	19
1.6	^{186}W - ^{182}W neutron σ_{tot} relative difference and Ohio global optical model predictions	20
1.7	Root-mean-squared charge radii of Sn isotopes	22
2.1	TOF detector partially assembled	29
2.2	Cutaway CAD figure of TOF detector.	29
2.3	$^{112,\text{nat},124}\text{Sn}$, $^{\text{nat},18}\text{O}$, and $^{58,\text{nat},64}\text{Ni}$ samples used for neutron σ_{tot} measurements	34
2.4	^{103}Rh sample used for the neutron σ_{tot} measurements	35
2.5	Layout of the 15R beamline at the WNR facility at LANSCE	39
2.6	Sample changer, monitor detector, and collimation stack	40
2.7	Veto and TOF detectors installed in the 15R beamline	41
2.8	Monitor detector, sample changer, and TOF detector	42
2.9	Overview of σ_{tot} experimental setup in the 15R beamline	43

LIST OF FIGURES

2.10	Pulse structure of the neutron beam at the WNR facility	44
2.11	Radiographic film showing precision alignment of the sample changer . . .	44
2.12	Logic diagram for neutron σ_{tot} data acquisition	47
3.1	Event times for left and right PMTs of time-of-flight detector	52
3.2	Effect of energy gating on left/right PMT time difference	53
3.3	Intrinsic time resolution of time-of-flight detector as a function of signal amplitude	54
3.4	Deviation of the average γ -ray arrival time by macropulse	55
3.5	Stability of the beam pick-off (T_0) frequency during the experiment	56
3.6	Improving timing precision with a software CFD and γ -ray averaging . . .	57
3.7	Determining the time-of-flight detector distance using $^{\text{nat}}\text{C}$ resonances . . .	58
3.8	“Looking period” logic from previous neutron σ_{tot} measurements at LANSCE	60
3.9	Time difference between consecutive events in the time-of-flight detector . .	63
3.10	Digitizer-busy probability as a function of time within micropulse	64
3.11	The effect of deadtime correction on a typical time-of-flight spectrum . . .	65
3.12	Typical time-of-flight spectrum after timing and deadtime corrections . . .	66
3.13	σ_{tot} relative difference between deuterium and hydrogen from our measure- ment	68
3.14	Comparison of our natural-sample σ_{tot} measurement against literature data	72
3.15	Neutron σ_{tot} relative difference between short and long $^{\text{nat}}\text{C}$ samples	73
3.16	Neutron σ_{tot} for $^{16,18}\text{O}$: our results and literature data	75
3.17	$^{16,18}\text{O}$ neutron σ_{tot} relative difference	76
3.18	Neutron σ_{tot} for $^{58,64}\text{Ni}$: our results and literature data	78

3.19	$^{58,64}\text{Ni}$ neutron σ_{tot} relative difference	79
3.20	Neutron σ_{tot} for ^{103}Rh : our results and literature data	81
3.21	Neutron σ_{tot} for $^{112,124}\text{Sn}$: our results and literature data	83
3.22	$^{112,124}\text{Sn}$ neutron σ_{tot} relative difference	84
4.1	Example Jablonski diagram for organic scintillator	89
4.2	Diagram of the neutron TOF room at TUNL	93
4.3	Image of the neutron TOF room at TUNL	94
4.4	Logic diagram for neutron $\frac{d\sigma}{d\Omega}$ data acquisition	96
5.1	Event pulse height (PH) vs. pulse-shape-discrimination (PSD) for a typical run	98
5.2	Scaled event histograms showing neutron elastic scattering peak	99
5.3	Reference runs of neutron scattering on C and $(\text{CH}_2)_n$	102
5.4	Illustration of finite-size effects relevant for $\frac{d\sigma}{d\Omega}$ cross section measurements .	105
5.5	Effect of finite-size corrections on previous TUNL neutron $\frac{d\sigma}{d\Omega}$ measurement	106
5.6	Effect of finite-size corrections on our neutron $\frac{d\sigma}{d\Omega}$ measurement	107
5.7	Relative counts due to multiple scattering in the sample volume	108
5.8	Neutron $\frac{d\sigma}{d\Omega}$ on $^{112,124}\text{Sn}$ at 11 MeV: our results and literature data	110
5.9	Neutron $\frac{d\sigma}{d\Omega}$ on $^{112,124}\text{Sn}$ at 17 MeV: our results and literature data	112
6.1	Example diagrams of the single-particle propagator perturbation expansion	120
6.2	The Dyson equation in diagrammatic form.	121
6.3	Radial dependence of the real part of the potential	133
6.4	Radial dependence of the imaginary part of the potential	135
6.5	Energy dependence of the imaginary and real-dispersive parts of the potential	136

LIST OF FIGURES

6.6	Volume integral of the imaginary part of the potential	137
7.1	Proton $\frac{d\sigma}{d\Omega}$ on ^{40}Ca : DOM predictions and experimental data	145
7.2	Neutron $\frac{d\sigma}{d\Omega}$ on ^{40}Ca : DOM predictions and experimental data	146
7.3	Proton σ_{rxn} of ^{40}Ca : DOM predictions and experimental data	147
7.4	Neutron σ_{rxn} and σ_{tot} of ^{40}Ca : DOM predictions and experimental data . .	147
7.5	Single-particle levels in ^{40}Ca	148
7.6	Proton spectral functions in ^{40}Ca	149
7.7	Proton single-particle density distributions in ^{40}Ca	150
7.8	Proton single-particle density distributions in ^{40}Ca	150
7.9	Proton momentum distribution in ^{40}Ca	151
7.10	Neutron momentum distribution in ^{40}Ca	151
7.11	Volume integral of proton imaginary potential in ^{40}Ca	152
7.12	Proton and neutron matter density distributions in ^{40}Ca	153
7.13	Energy density distribution for protons in ^{40}Ca	154
7.14	Total energy density integral in ^{40}Ca	154
7.15	Volume integral of proton imaginary potential in ^{48}Ca	156
7.16	Proton and neutron matter density distributions in ^{48}Ca	157
7.17	Charge density distribution of ^{16}O	159
7.18	Proton single-particle density distributions in ^{16}O	159
7.19	Proton and neutron matter density distributions in ^{18}O	161
7.20	Proton and neutron matter density distributions in ^{58}Ni	163
7.21	Proton momentum distribution in ^{112}Sn	166
7.22	Neutron momentum distribution in ^{112}Sn	166

7.23	Proton and neutron matter density distributions in ^{124}Sn	168
7.24	Proton momentum distribution in ^{208}Pb	170
7.25	Neutron momentum distribution in ^{208}Pb	170
7.26	Proton and neutron matter density distributions in ^{208}Pb	171
7.27	Proton single-particle momentum distributions in $^{40,48}\text{Ca}$	175
8.1	Correlation between the neutron skin of ^{208}Pb and several nuclear structure observables	184
8.2	Proton and neutron RMS radii in the Sn isotopes computed with FSUGold and NL3 interactions	184

LIST OF TABLES

2.1	Selected results from a literature study of isotopically-resolved σ_{tot} data using the EXFOR database [35]	27
2.2	Physical characteristics of samples used for neutron σ_{tot} measurements . . .	33
4.1	Physical characteristics of samples used for neutron $\frac{d\sigma}{d\Omega}$ measurements . . .	90
7.1	^{40}Ca proton and neutron occupancies from our DOM analysis	143
7.2	Neutron skins extracted from DOM analysis	172
7.3	Valence spectroscopic factors extracted from DOM analysis	173
7.4	High-momentum content extracted from DOM analysis	174
8.1	Sensitivity of optical potential terms to the experimental nucleon scattering data types	181
8.2	Sensitivity of optical potential terms to bound-state experimental data types	182
A.1	D_2O sample isotopic distribution	212
A.2	H_2^{18}O sample isotopic distribution	212
A.3	^{58}Ni sample isotopic distribution	212
A.4	^{64}Ni sample isotopic distribution	212

A.5	^{112}Sn sample isotopic distribution	212
A.6	^{124}Sn sample isotopic distribution	212
B.1	Sources for bound-state data on all nuclei	213
B.2	^{16}O proton $\frac{d\sigma}{d\Omega}$ data	214
B.3	^{16}O neutron $\frac{d\sigma}{d\Omega}$ data	214
B.4	^{16}O proton AP data	215
B.5	^{16}O neutron AP data	215
B.6	^{16}O proton σ_{rxn} data	215
B.7	^{16}O neutron σ_{rxn} data	215
B.8	^{16}O neutron σ_{tot} data	215
B.9	^{18}O proton $\frac{d\sigma}{d\Omega}$ data	216
B.10	^{18}O neutron $\frac{d\sigma}{d\Omega}$ data	216
B.11	^{18}O proton AP data	217
B.12	^{18}O neutron σ_{rxn} data	217
B.13	^{18}O neutron σ_{tot} data	217
B.14	^{40}Ca proton $\frac{d\sigma}{d\Omega}$ data	218
B.15	^{40}Ca neutron $\frac{d\sigma}{d\Omega}$ data	218
B.16	^{40}Ca proton AP data	219
B.17	^{40}Ca neutron AP data	219
B.18	^{40}Ca proton σ_{rxn} data	219
B.19	^{40}Ca neutron σ_{rxn} data	219
B.20	^{40}Ca neutron σ_{tot} data	219
B.21	^{48}Ca proton $\frac{d\sigma}{d\Omega}$ data	220

LIST OF TABLES

B.22	^{48}Ca neutron $\frac{d\sigma}{d\Omega}$ data	220
B.23	^{48}Ca proton AP data	221
B.24	^{48}Ca proton σ_{rxn} data	221
B.25	^{48}Ca neutron σ_{tot} data	221
B.26	^{58}Ni proton $\frac{d\sigma}{d\Omega}$ data	222
B.27	^{58}Ni neutron $\frac{d\sigma}{d\Omega}$ data	222
B.28	^{58}Ni proton AP data	223
B.29	^{58}Ni neutron AP data	223
B.30	^{58}Ni proton σ_{rxn} data	223
B.31	^{58}Ni neutron σ_{tot} data	223
B.32	^{64}Ni proton $\frac{d\sigma}{d\Omega}$ data	224
B.33	^{64}Ni neutron $\frac{d\sigma}{d\Omega}$ data	224
B.34	^{64}Ni proton AP data	225
B.35	^{64}Ni proton σ_{rxn} data	225
B.36	^{64}Ni neutron σ_{tot} data	225
B.37	^{112}Sn proton $\frac{d\sigma}{d\Omega}$ data	226
B.38	^{112}Sn neutron $\frac{d\sigma}{d\Omega}$ data	226
B.39	^{112}Sn proton σ_{rxn} data	226
B.40	^{112}Sn neutron σ_{tot} data	226
B.41	^{124}Sn proton $\frac{d\sigma}{d\Omega}$ data	227
B.42	^{124}Sn neutron $\frac{d\sigma}{d\Omega}$ data	227
B.43	^{124}Sn proton AP data	227
B.44	^{124}Sn proton σ_{rxn} data	227
B.45	^{124}Sn neutron σ_{tot} data	227

B.46	^{208}Pb proton $\frac{d\sigma}{d\Omega}$ data	228
B.47	^{208}Pb neutron $\frac{d\sigma}{d\Omega}$ data	228
B.48	^{208}Pb proton AP data	229
B.49	^{208}Pb neutron AP data	229
B.50	^{208}Pb proton σ_{rxn} data	229
B.51	^{208}Pb neutron σ_{rxn} data	229
B.52	^{208}Pb neutron σ_{tot} data	229
C.1	Real parameters (volume-like, symmetric)	231
C.2	Real parameters (volume-like, asymmetric)	231
C.3	Imaginary parameters (volume-like, symmetric)	232
C.4	Imaginary parameters (volume-like, asymmetric)	232
C.5	Imaginary parameters (surface-like, symmetric)	232
C.6	Imaginary parameters (surface-like, asymmetric)	233
C.7	Spin-orbit parameters	233

ACKNOWLEDGEMENTS

Being a member of the Radiochemistry group at Washington University has defined my experience in graduate school. Demetrios Sarantites, Jon Elson, Walter Reviol, Bob Charity, and – especially – my advisor Lee Sobotka have spent countless hours mentoring me over the last five years, encouraging my successes and spurring my development as a scientist. My mental model of the nucleus derives from their (far deeper) knowledge. I can only hope to repay their kindness by sharing their insights with future students and colleagues.

Fellow Radiochemistry graduate students Kyle Brown, Tyler Webb, Dan Hoff, and Dan Mulrow, have been both great friends and capable colleagues at the lab. Their emotional and social support have been an important part of my growth throughout graduate school.

My collaboration with the Washington University Theoretical Nuclear Physics group has been an enriching one. The DOM results presented in this work are a testament to the patience and intellect of Wim Dickhoff and the assistance of Physics graduate students Natalia Calleya, Hossein Mahzoon, and especially Mack Atkinson.

Many faculty and staff at LANSCE and TUNL were critical for the experimental measurements detailed in this work. In particular, I want to thank Matt Devlin, Hye Young Lee, Shea Mosby, and Nik Fotiadis at LANSCE and Calvin Howell and Ron Malone at TUNL. Without their abundant know-how and generous assistance, our experiments could

ACKNOWLEDGEMENTS

not have succeeded.

Lastly, I am forever grateful to my family, especially my parents, for kindling my curiosity as a child and for supporting my pursuits wherever they lead.

Cole D. Pruitt

Washington University in St. Louis

May 2019

ABSTRACT OF THE DISSERTATION

Isotopically-Resolved Neutron Cross Sections as Probe of the Nuclear Optical Potential

by

Cole Davis Pruitt

Doctor of Philosophy in Chemistry

Washington University in St. Louis, 2019

Professor Lee Sobotka, Chair

Neutron scattering experiments provide direct access to the forces experienced by nucleons in the nuclear environment. Due to the experimental difficulty of cross section measurements with neutrons, isotopically-resolved neutron scattering cross sections are sorely needed as inputs for many nuclear models. This dissertation presents the results from a campaign of isotope-specific neutron total cross section measurements on $^{16,18}\text{O}$, $^{58,64}\text{Ni}$, $^{112,124}\text{Sn}$, and ^{103}Rh from 3-450 MeV and elastic scattering differential cross section measurements on $^{112,\text{nat},124}\text{Sn}$ at 11 and 17 MeV. Equipped with these new data and with computational improvements to the Dispersive Optical Model (DOM), we present DOM treatments of $^{16,18}\text{O}$, $^{40,48}\text{Ca}$, $^{58,64}\text{Ni}$, $^{112,124}\text{Sn}$, and ^{208}Pb . From these analyses across the nuclear chart, we place additional constraints on the neutron-proton asymmetry-dependence of nuclear properties, extract essential bound-state quantities including spectroscopic factors and neutron skins, and identify experimental data sets most needed for further enhancing our understanding of nuclear structure.

INTRODUCTION

“The grandest discoveries of science have been but the rewards of accurate measurement and patient long-continued labour in the minute sifting of numerical results.”

William Thompson, 1st Baron Kelvin

1.1 Models of the Atomic Nucleus: Overview

The nuclear many-body problem remains one of the most challenging problems in physical science despite a century of experimental and theoretical advances. Basic questions, including how nucleons are distributed throughout the nuclear volume and how they share the energy of binding, are still only qualitatively answered. At the core of the issue is the short-range and extremely strong nature of nuclear forces, which confine quarks to nucleons and cannot be treated perturbatively in the MeV-energy regime. Rather than take a truly *ab initio* approach where quarks and gluons are the relevant degrees of freedom, a series of approximations must be made for calculations to be tractable. As long as the energy domain is less than that of the lowest-lying nucleon excitation, it is well-justified to reduce the nuclear problem to choosing protons and neutrons as the nuclear building blocks. The proton and neutron

masses are so close, and their behaviors in the nucleus so similar, that the problem can be further simplified by introducing a new (approximate) quantum number t , the isospin, and treating protons and neutrons as generic “nucleons” with differing isospin projections t_z .

Starting with these simplifications, many nuclear models have been developed to describe existing data on nucleon-nucleon, nucleon-nucleus, lepton-nucleus scattering as well as nuclear binding. Successful models should not only reproduce existing experimental data accurately but also possess predictive power for as-yet unmeasured quantities. For parametric models with many tunable parameters, these two criteria pull in opposite directions: increasing the number and acceptable range of model parameters often helps to reproduce experimental data but may jeopardize predictive power if new parameters are not connected to the underlying physics. We begin by presenting a few workhorse model families most relevant to the new work presented in this dissertation. Each model’s successes, failures, and regimes of validity are briefly discussed, with extra attention paid to each model’s confrontation with certain challenging data. A central motivation for this work is to provide experimental data most useful for a particular type of optical model of the nucleus that attempts to connect nuclear structure information (i.e., bound state information) with nuclear reactions, a longtime goal in nuclear physics.

1.1.1 Liquid Drop Model

The Liquid Drop Model (LDM) describes nuclei as drops of ideal nuclear fluid and has been successfully employed since the earliest days of nuclear science to describe nuclear masses, gross fission energetics, and some ground-state properties. The binding of each nucleus is approximated by five physically-intuitive terms appropriate for a droplet of nuclear

matter:

$$BE(A, Z) = a_{vol}A - a_{surf}A^{\frac{2}{3}} - a_{coul}\frac{Z(Z-1)}{A^{\frac{1}{3}}} - a_{asym}\frac{(A-2Z)^2}{A} + a_{pair}(A, Z) \quad (1.1)$$

In order, these terms are:

- A volume term that describes “bulk” binding that would be experienced in an infinite sea of nuclear matter,
- A surface term that incorporates the finite size of a nucleus (i.e., it is a drop, not an ocean), equivalent to considering surface tension,
- A coulomb term that incorporates the electric repulsion experienced by protons kept in close proximity inside the drop,
- An asymmetry term representing the relative chemical potential of neutrons and protons as a function of their relative population (which can be re-balanced by beta decay), and
- a pairing term to account for the experimental observation that nuclei with an even number of both protons and neutrons are slightly more bound, implying a favorable pairing interaction.

A and Z are the total number of nucleons and number of protons, respectively and the nuclear radius is assumed to scale as $r = r_0A^{\frac{1}{3}}$. The free parameters in each term can be fitted to the hundreds of well-measured nuclear masses across the chart of nuclides. These five simple terms are quite successful in describing masses and radii of spherical nuclei, leading

early nuclear scientists to expect that shell structure was less important in the nuclear many-body problem than in the atomic one. In this ansatz, the quantum nature of constituent nucleons is not explicitly considered, so the LDM is unsuitable for extracting excited-state wavefunction information or predicting scattering cross sections.

The Droplet Model [1] considers a systematic two-dimensional expansion of Eq. 1.1 about two fundamental independent quantities, the nucleon density and neutron-proton asymmetry:

$$\bar{\epsilon} = -\frac{1}{3} \frac{(\rho - \rho_0)}{\rho_0} \quad (1.2)$$

$$\bar{\delta} = \frac{\rho_n - \rho_z}{\rho} \quad (1.3)$$

Here, ρ_0 is the saturation density of $0.16 \text{ nucleons fm}^{-3}$. Relevant quantum effects, such as changes in level densities near shell closures that affect the observed masses, can be incorporated through a series of corrections that approximate shell effects and geometric deformation. The Droplet Model of Atomic Nuclei deploys nine independent coefficients to describe spherical droplets and six additional coefficients to accommodate non-spherical effects. This expanded scope can successfully recover the degree of ground-state deformation in non-spherical nuclei and fission barriers.

Because the LDM is not based upon shell structure, its utility is diminished compared to other models that reproduce experimental data associated with the quantum behavior of the nucleus. However, the model still is a useful reference for providing information about bulk properties of nuclear matter. Per the approach pioneered by Strutinsky [2, 3], modern macroscopic-microscopic models [4, 5] explicitly equip Droplet-type models with shell model physics (described in the next section). At present, these are the state-of-the-art

for calculating nuclear masses and fission properties.

1.1.2 Mean-field and Beyond-mean-field Models

Mean-field models begin with a simple motivation: that nucleons traverse the nuclear environment independently, in an average potential generated by all other nucleons, smeared out over the nuclear volume. The assumption of independent nucleon motion may seem dubious, given the crowded environment of the nucleus and immense strength of nucleon-nucleon forces, but the Pauli exclusion principle provides some justification. From such a mean field, a shell model can be developed wherein protons and neutrons each obey a nuclear aufbau, filling orthogonal states with quantum numbers N , L , and J , just as electrons do in the atomic case. From a mean field consisting of a central potential and a spin-orbit potential, as in the seminal shell-model work of Goeppert-Mayer and Jensen [6], the basic ground-state quantum properties of most nuclei (spins, parities, magnetic moments) are recovered for nuclei near major shell closures. For non-spherical nuclei (in open shells), deformation effects must be included as well, as deformations break degeneracies found in models that assume spherical symmetry.

Confined in the mean-field potential, nucleons can be excited into higher (but still bound) states and the low-lying excitation spectra can be predicted. The consequences of shell structure are obvious in the experimental record and include increased particle separation energies and decreased nuclear radii at shell closures, directly analogous to the atomic ionization energies and radii in the noble gases. The independent treatment of nucleons is most valid near shell closures, where the level density is reduced, and near beta-stability, where coupling to the asymptotically-free states of the continuum is least important. In very light nuclear systems ($A < 12$), the underpinning mean-field assumption begins to break down as nucleons

become too granular to treat on average. Despite these restrictions, mean-field models have been extremely successful at explaining the fundamentals of nuclear structure near the Fermi surface.

In a modern treatment, the mean field (usually a Hartree-Fock potential) is typically considered only as a starting point for a perturbative expansion that collects residual nucleon-nucleon interactions associated with correlated behavior, many of which can be categorized as collective rotations and vibrations. Coupled excitations of two or more nucleons to higher orbitals within or across shells and relativistic effects may be included to accommodate the experimental phenomena under investigation. Models built on this premise are termed “beyond-mean-field”, for obvious reasons.

In light systems, where the number of nucleons is not too large, every nucleon may be allowed to participate in excitations into the valence space of the model (a “no-core shell model”). As the system size increases, the configuration space grows combinatorially until calculations become prohibitively expensive. To ease calculations for these larger nuclei, a variety of approaches are employed, including simply restricting the valence space and prohibiting deeply-bound nucleons from participating in excitations, hopefully while still capturing the essence of the physical properties under investigation.

Other beyond-mean-field approaches dispense with the assumption of an average potential and build up the nuclear Hamiltonian from nucleon-nucleon potentials folded over the nucleon density profile. An advantage of this approach is the connection between fundamental nucleon data (for example, neutron-proton scattering phase shifts) and the many-body properties of light nuclear systems [7]. Many studies have confirmed the importance of spin-orbit, isospin, tensor, and three-body terms in the nucleon-nucleon potential for accurately reproducing structure even in very light nuclei. Present computational resources have made

systems as large as $A=12$ accessible for this type of modeling.

In contrast to the LDM, both mean-field and beyond-mean-field models have something to say about nuclear reactions and decays. Incident nucleons or nuclei can transfer nucleons to/from the nucleus being modeled and standard techniques of scattering theory can be applied, though at high excitation energies and where the continuum becomes important, accuracy declines.

When the properties of deeply-bound nucleons are investigated, cracks appear in the mean-field picture. First, it has been known for decades that shell models give nuclear binding energies that are too small, an indication that deeply-bound nucleons are not being well-described. Evidence from $(e,e'p)$ and $(p,2p)$ knockout reactions consistently shows that the occupancy of single-particle levels deep in the nucleus is lower than the mean-field expectation of full occupancy [8, 9, 10]. For levels near the Fermi surface, the depletion is on the order of 30% and can partially be explained as a consequence of coupling between single-particle states and low-lying collective states, physics addressed by many beyond-mean-field models. However, even for very deeply bound nucleons, like the $0s_{\frac{1}{2}}$ and $0p_{\frac{3}{2}}$ protons in ^{208}Pb , there is still significant depletion, around 10% from unity. Further, the “hole” states left behind in the target nuclei after knockout are spread over a broad energy range, at odds with the mean-field assertion that bound nucleons reside in a single subshell with a discrete energy. Clearly, while mean-field models succeed in describing much of the relevant physics near the Fermi surface, they miss something fundamental about the behavior of deeply-bound nucleons. Additional evidence is available from elastic electron scattering measurements from which nuclear charge density distributions can be generated (compiled in [11]). Compared to these distributions, mean-field potentials generate charge-density distributions with too high a density in the nuclear core (see [12] for an example of this in the Ca

isotopes). Related effects have been seen in GeV-scale deep-inelastic scattering to probe the momentum distribution of quarks in deeply-bound nucleons. In these experiments, excess high-momentum content indicates that a few percent of the time, nucleons are traveling far faster than expected. Including short-range correlations, or interactions between quarks of different nucleons that are in close proximity, is important for bridging these discrepancies and continues to be an outstanding issue in nuclear theory. From a more fundamental point of view, these results also raise questions about when nucleons can be assumed to be good degrees of freedom and quark degrees of freedom can be ignored.

1.1.3 Optical Models

For the LDM and mean-field models presented thus far, the primary motivation has been recovery of structural observables like nuclear masses, radii, low-lying excitations, and magnetic moments. A comprehensive understanding of the nucleus must also say something about what nuclei *do*, as in higher-energy nucleon-nucleus scattering experiments and in astrophysical reactions. The nuclear optical model (OM) was developed to this end and continues to be a widely-used tool for generating nucleon, α , and heavy-ion scattering cross sections, though it has had less to say about nuclear structure. Partially to lay a groundwork for the Dispersive Optical Model (DOM) summary of Chapter 6, more space is devoted here to optical models than to the LDM or mean-field models above. Motivations for OMs, stemming from a simple Ramsauer-effect picture, are summarized, and references to several successful OM potential parameterizations are provided in this section.

Due to the magnitude of the strong nuclear force, it might be expected that the interaction of an incident neutron on a nucleus should be strongly absorptive, with only a small contribution from elastic scattering. Thus, the earliest model for neutron scattering

described the nucleus as a constant-density sphere that interacts strongly with incident neutrons approaching within a nuclear radius [13]. In this “strongly-absorbing sphere” (SAS) picture devoid of nuclear structure or shell effects, σ_{tot} depends only on size scaling of the interacting bodies:

$$\sigma_{\text{tot}}(E) = 2\pi(R + \lambda)^2 \quad (1.4)$$

where $R = r_0 A^{\frac{1}{3}}$ and λ is the reduced de Broglie wavelength of the incident neutron in the center of mass [14, 15].

As neutron scattering experiments expanded to higher energies in the 1950s, neutron total cross section data emerged that challenged this picture. The total cross section, σ_{tot} , is simply the sum of elastic and inelastic cross sections. Due to the infinite range of the Coulomb force, σ_{tot} is a sensible quantity only for neutral particles. In Fig. 1.1, neutron σ_{tot} data are shown from 2-500 MeV for nuclides from $A=12$ to $A=208$ [16, 17, 18, 19, 20]. Predictions for σ_{tot} given by Eq. 1.4 are shown as thin dashed lines for each nucleus. Regular oscillations about the SAS model are clearly visible, as is the trend for the oscillation maxima and minima to shift to *higher* energies as A is increased. At low energies, resonance structures are visible especially for light nuclides where the density of states is smallest. Note that at higher neutron energies, the experimental cross sections drop below those predicted by the SAS model, illustrating a increase in nuclear transparency. These hallmark oscillations in the neutron σ_{tot} can be explained as the result of a phase shift between neutron waves passing around the nucleus (unshifted) and waves passing through the the nucleus, where they experience refraction (illustrated in Fig. 1.2). This explanation was termed the “nuclear Ramsauer effect” by Peterson [21], based on the analogous effect seen in electron scattering on noble gases.

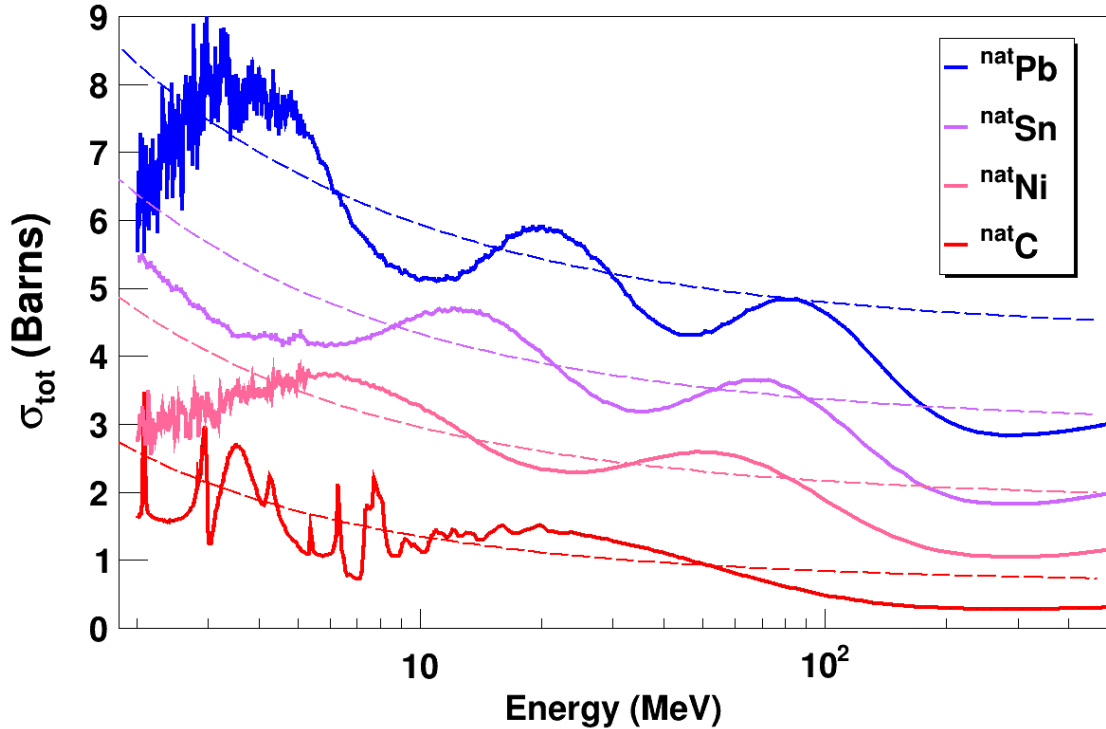


Figure 1.1: Experimental neutron σ_{tot} data on several natural samples (solid lines) from 2-500 MeV. The predictions of the crude strongly-absorbing-sphere model (Eq. 1.4) are shown as dashed lines. Resonance structures are clearly visible in the $^{\text{nat}}\text{C}$ neutron σ_{tot} below 20 MeV.

Following Angeli [22], these considerations can be incorporated by imbuing the strongly-absorbing sphere relations (equation 1.4) with an additional sinusoidal term:

$$\sigma_{\text{tot}} = 2\pi(R + \lambda)^2[1 - \rho \cos(\delta)] \quad (1.5)$$

where $\rho = e^{-\text{Im}(\Delta)}$, and $\delta = \text{Re}(\Delta)$, with Δ the phase difference between the wave traveling around and traveling through the nucleus. Thus, the amplitude of the oscillation provides the elastic removal, or inelastic, phase shift and the period of oscillation provides the elastic phase shift. As can be seen from Eq. 1.5, the large magnitude of the oscillations means that inelastic scattering (from $\text{Im}(\Delta)$) accounts for only a fraction of the total cross section, in

turn implying a much larger mean free path for neutrons through the nucleus than would be expected in the absence of Pauli blocking [23].

If the nucleus presents a spherical potential of radius R and depth U , the total phase shift δ is:

$$\delta = \frac{\bar{C} \left(\left[\frac{E+U}{E} \right]^{\frac{1}{2}} - 1 \right)}{\lambda} \quad (1.6)$$

where $\bar{C} = \frac{4}{3}R$ is the average chord length through the sphere [22]. Rearranging Eq. 1.6 in terms of A and E and discarding leading constants yields:

$$\delta \propto A^{\frac{1}{3}} \times \left(\sqrt{E+U} - \sqrt{E} \right) \quad (1.7)$$

This form reveals an important relation: as A is increased, to maintain constant phase δ , E must also increase [15, 21]. This is contrary to a typical resonance condition where an integer number of wavelengths are fit inside a potential; in that case, to maintain constant phase as size is increased, E must be decreased. Thus these σ_{tot} oscillations have been referred to as “anti-resonances” or “echoes” [15, 24]. It should be noted that this simple Ramsauer picture is illustrative only, as it fails to account for interference between the partial waves of the incident nucleon and cannot be extrapolated to high energies without conspicuous deficiencies [25].

A new type of nuclear model is thus at hand: by replacing the intractable many-body problem of the target nucleus by a complex, refractive potential, both elastic scattering (from the real part of the potential) and inelastic scattering (from the imaginary part) can be neatly explained. The existing mathematical machinery for calculating scattering of light from refractive materials can then be repurposed for nuclear scattering, giving birth to the “optical model” of the nucleus [24, 26]. Instead of a single central optical potential, a

series of potential terms may be used, centered on the nuclear surface and nuclear volume, corresponding to differing physics thought to be relevant for these areas (much as in the Droplet Model). Many comprehensive overviews of optical models are available [27, 28] that explore various potential forms and connect optical models to other approaches.

Global OMs have been developed to simultaneously reproduce single nucleon, heavy ion, and other hadron scattering data on targets across the chart of nuclides up to several hundred MeV [29, 30]. Because the proton-proton, proton-neutron, and neutron-neutron scattering cross sections are not identical, OM potentials are expected to differ for protons and neutrons. Isoscalar terms, which respect isospin symmetry and thus treat protons and neutrons identically, account for most of the observed scattering, but do not include the *asymmetry-dependent* interactions known to exist between nucleons, such as charged meson exchange. Thus isovector and isotensor terms, which depend on the difference between the proton and neutron density distributions in the nucleus, are needed. As experimental facilities like the Facility for Radioactive Isotope Beams (FRIB) come online and produce extremely asymmetric nuclei, knowing the asymmetry-dependence of optical potentials will become increasingly important for predicting nucleon scattering on exotic nuclei. Isovector considerations are not unique to full-blown optical models and can be introduced to simpler Ramsauer-like models as well. For example, building on the addition of spin-spin terms to a Ramsauer model by Gould et al. [31], Anderson and Grimes added an explicit isovector term to analyze isotone and isotope shifts in neutron total cross sections [32]. They concluded that “although [their] model may give semiquantitative agreement with some aspects of the data, optical-model calculations should be used for quantitative comparison”.

Despite their excellent reproduction of experimental data, OMs involve the interaction of many sometimes-opaque parameters with many incident partial waves, blurring the intuitive

picture of the underlying physics. OMs are unabashedly phenomenological so a wide variety of experimental data types and energies are required to constrain the potential. When data are absent, model predictions are poor. Without a clearer connection to formal many-body methods, the empiricism of optical models does not clarify the connection between nuclear reactions and nuclear structure. A major step forward was taken by Mahaux and Sartor [33], who linked the nucleon self-energy to the optical potential by means of a dispersion relation, allowing for a more-direct comparison between scattering data and mean-field nuclear structure calculations. We employ a descendant of their dispersive optical model, generalized to include a fully non-local potential, to treat nuclear structure and reactions on the same footing.

A long-standing difficulty in optical-model analyses is in constraining the isovector dependence of the real and imaginary parts of the potential [32, 34]. Improving constraints on the isovector terms in particular requires data on asymmetric nuclei, preferably on highly-asymmetric nuclei or isotopic chains, where the imbalance of protons and neutrons makes any isovector effects most visible. The isovector strength of the nuclear potential is directly connected to a host of open problems in nuclear physics, including fixing the density-dependence of the symmetry energy, L , locating the neutron dripline, and understanding how high-momentum content is distributed between neutrons and protons. Making progress in this area requires improved experimental data sets, a topic explored in the following section.

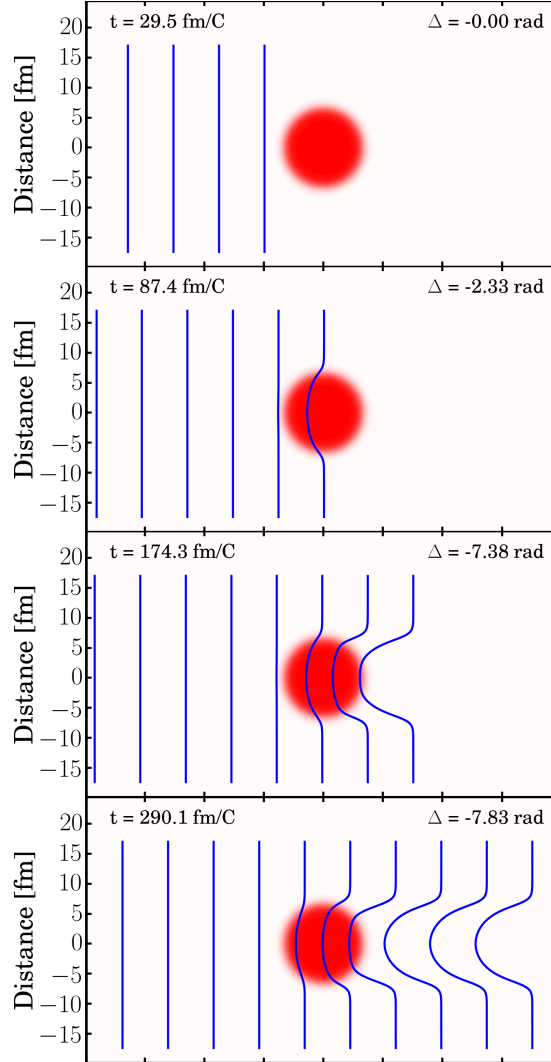


Figure 1.2: In this Ramsauer logic illustration, a neutron plane wave (series of blue lines) impinges from the left on a real Woods-Saxon potential centered at the origin (diffuse red circle). The potential refracts the neutron wave, retarding the phase of the wavefront as it passes through the potential. After escaping the potential, a phase difference Δ between the wave component passing *around* and *through the center* of the potential persists, dictating the scattering amplitude. For the leading wavefront, Δ is indicated in the top right-hand corner of each panel. A differential version of Eq. 1.6 is used to calculate the phase shift for each step. In this figure, the neutron energy $E_n = 14$ MeV and nuclear mass $A = 25$. For the Woods-Saxon potential, we used a potential depth $U = 42.8$ MeV (following Angeli and Csikai's analysis of σ_{tot} data at 14 MeV [22]), with nuclear radius $R = r_0 A^{\frac{1}{3}}$, $r_0 = 1.4$ fm, and a diffuseness parameter a of 0.5 fm.

1.2 Relevant Experimental Nuclear Data

1.2.1 Nucleon Scattering Data

Elastic nucleon scattering cross sections, especially with protons, comprise the most extensively-measured sector of experimental scattering databases. The EXFOR experimental reaction database [35] contains thousands of proton and neutron differential elastic scattering and analyzing power data sets between 1-300 MeV, the domain relevant for this work. Optical model fits to these data, both regional and global [29, 30], have helped constrain nuclear radii and the strength of the spin-orbit coupling and have revealed the importance of an imaginary spin-orbit term.

Inelastic nucleon scattering data are more difficult to collect experimentally and much sparser in the literature record. By helping fix the strength and energy-dependence of the absorptive component of the nuclear potential, inelastic data serve a complementary role to elastic data. Isotopically-resolved data are particularly valuable for constraining nuclear models, as they avoid averaging over multiple isotopes naturally present in many elemental samples. Unfortunately, many pure isotopes are extremely expensive (>\$10,000 per gram) to separate, putting them out of reach for all but the most well-funded experiments. Indeed, as late as 1988, only a handful of neutron σ_{tot} measurement campaigns on multiple samples had been conducted, most of them elemental, not isotopic [36].

Figs. 1.3 and 1.4 illustrate the status of isotopically-resolved inelastic nucleon scattering data in the EXFOR nuclear reaction database as of 2019. Except for light isotopes and a few security-related actinides, coverage is sparse and has changed little since the early 2000s. Isotopic *proton* σ_{rxn} measurements over a broad energy range are particularly lacking

due to the paucity of suitable accelerators and the subtlety of such a measurement. Both high-energy (>100 MeV) neutron σ_{tot} and proton σ_{rxn} data are useful for understanding the asymmetry-dependence of the imaginary strength of the nuclear potential. In this work, we focus on isotopically-resolved neutron scattering, which is easier to measure and, when combined with proton *elastic* cross sections, also provides information on the asymmetry-dependence of the real part of the nuclear potential.

In the last few decades, a smattering of isotope-chain neutron total cross section analyses have been carried out [38, 32, 39]. The most sophisticated was conducted by Dietrich et al. [40] using new data they measured on the $^{182,184,186}\text{W}$ isotope chain (a conspicuous bright spot in Fig. 1.3). In their study, an expanded Ramsauer-type model performed quite well at reproducing the relative difference between ^{186}W and ^{182}W , apart from a phase mismatch – but only when the isovector components they introduced in the Ramsauer model are *suppressed* (see Fig. 1.5). Despite the dubiousness of ignoring isospin, the resulting Ramsauer model agrees better with the experimental data than does the Ohio global optical potential [41], shown in Fig. 1.6.

The authors also performed phenomenological coupled-channel calculations based on a dispersive optical model formalism [33] that showed similar behavior: it gave good agreement with the experimental σ_{tot} relative differences, but only when isovector terms in the calculations were explicitly *neglected*. As the authors point out, it is quite puzzling that “good agreement with the experimental data can be obtained at the expense of an incorrect physical picture”. Of the models they tested, only a deformed, semimicroscopic optical model potential (SMOMP), obtained by folding an energy- and density-dependent optical model potential from nuclear matter calculations over the deformed nuclear densities, was capable of satisfactorily describing the σ_{tot} isotope shift in W. From this case study on W

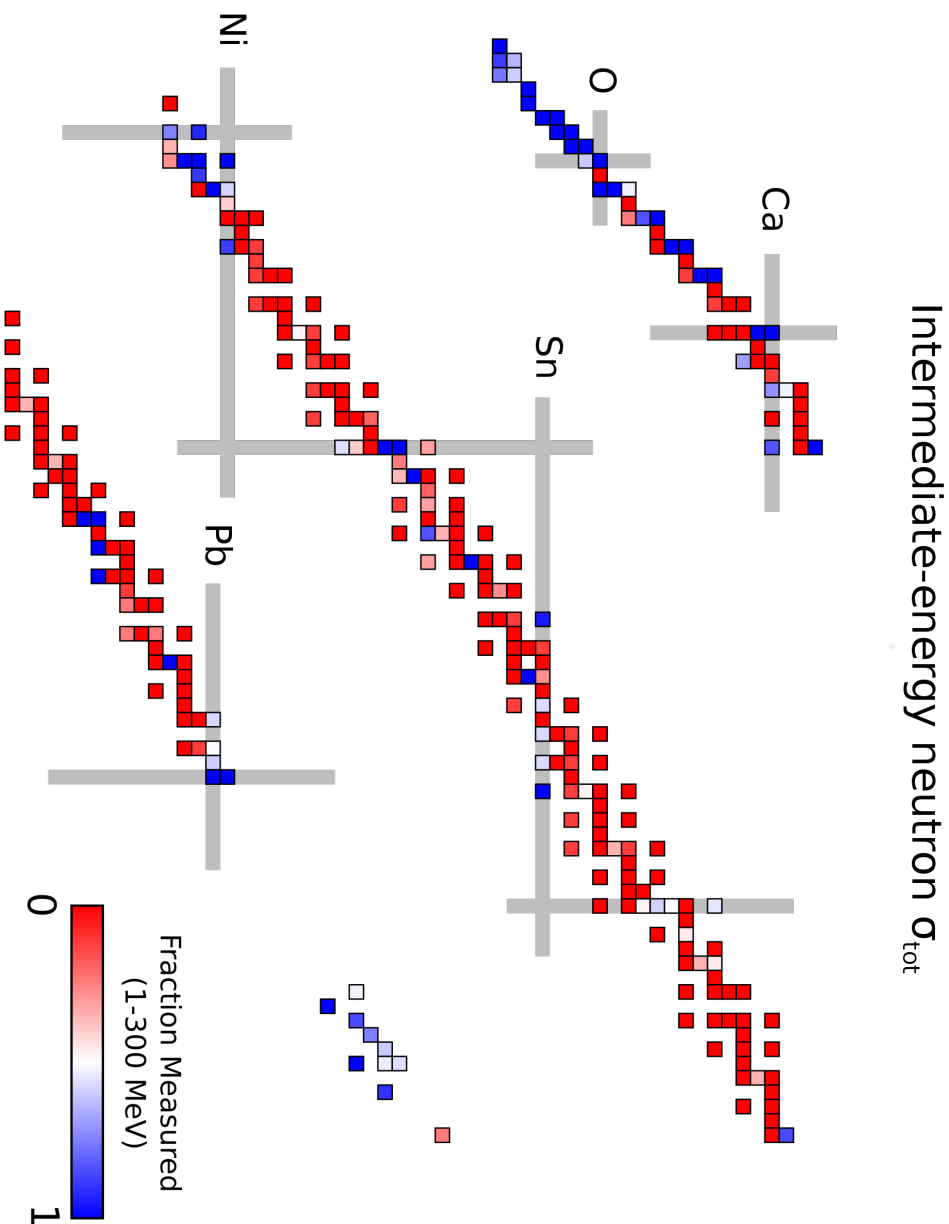


Figure 1.3: Isotopes are color-coded by the amount of neutron σ_{tot} data available in the EXFOR nuclear reaction datababase from 1-300 MeV, as accessed in 2018 and 2019. If data exist throughout the 1-300 MeV range, the isotope is colored blue. If no data exist, the isotope is colored red. For isotopes with partial coverage in this range, color varies by the degree of coverage. Except for the lightest isotopes (O and below) and a few security-related actinides, there is almost no coverage throughout the nuclear chart. Our newly-measured results on $^{16,18}\text{O}$, $^{58,64}\text{Ni}$, ^{103}Rh , and $^{112,124}\text{Sn}$ are included, as are a previous experiment by our group on $^{40,48}\text{Ca}$ [37].

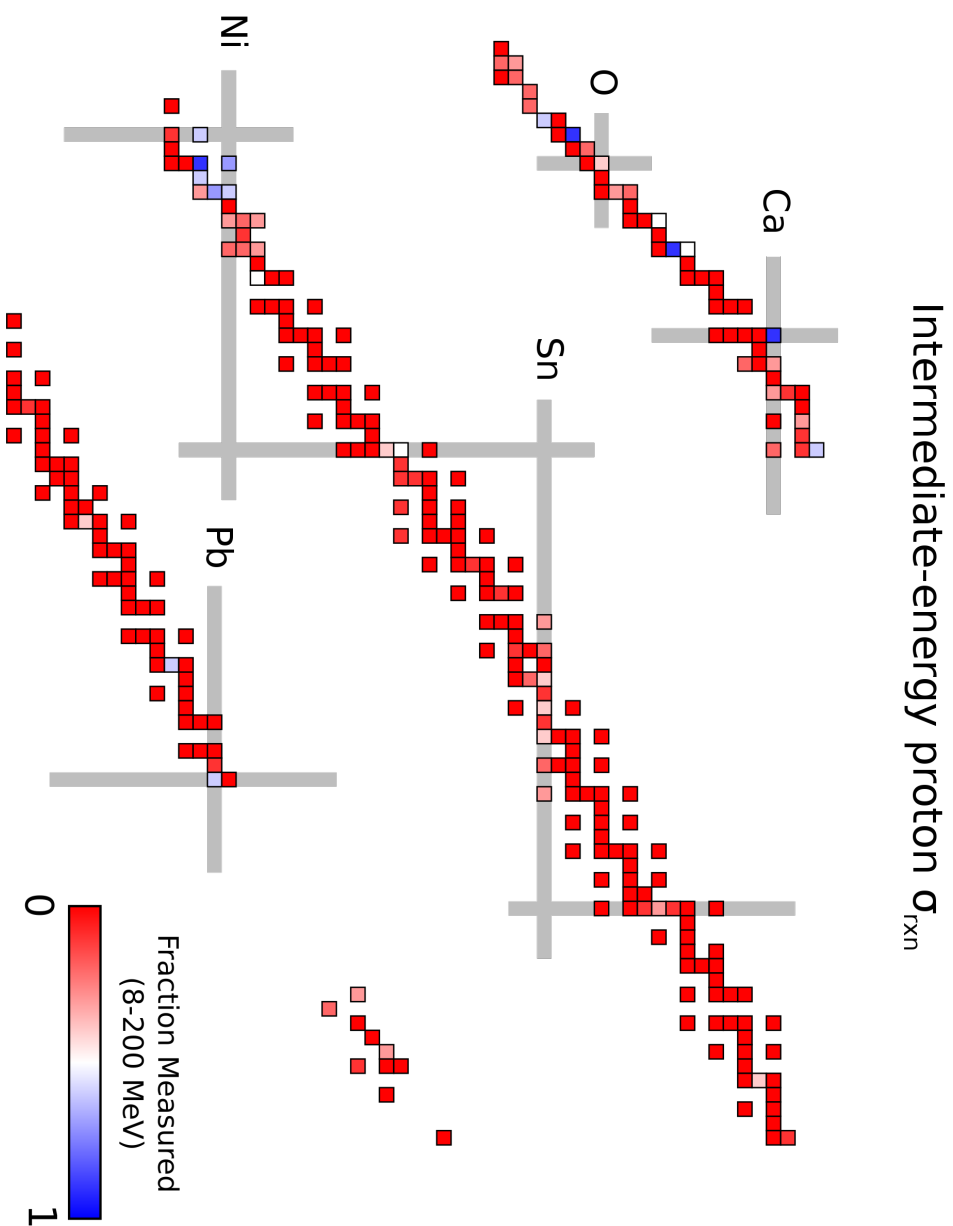


Figure 1.4: Isotopes are color-coded by the amount of proton σ_{rxn} data available in the EXFOR nuclear reaction database from 8-200 MeV, as accessed in 2018 and 2019. If data exist throughout the 8-200 MeV range, the isotope is colored blue. If no data exist, the isotope is colored red. For isotopes with partial coverage in this range, color varies by the degree of coverage. Coverage in this energy range is quite sparse, a testament to the difficulty of proton σ_{rxn} measurements.

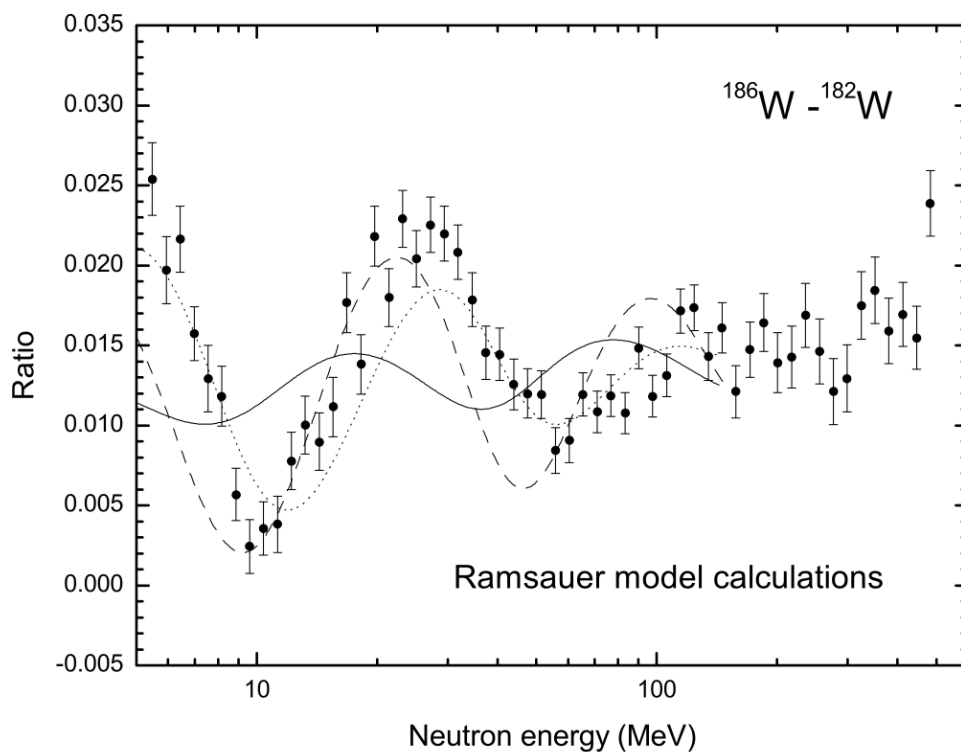


Figure 1.5: ^{186}W - ^{182}W neutron σ_{tot} relative difference and Ramsauer model predictions. Figure from [40]. If the standard isovector strength from optical-model treatments is used to dictate the Ramsauer isovector dependence (solid line), the model performs more poorly against the experimental data. When the isovector strength is suppressed, the correspondence to data improves (dashed line).

isotopes, several follow-up questions arise: is a microscopic knowledge of the proton and neutron matter densities important for reproducing the neutron σ_{tot} across an isotope chain? More fundamentally, what terms in an optical potential are the neutron σ_{tot} cross sections sensitive to, and are neutron σ_{tot} data connected to structural (i.e., bound-state) information in a consistent, transparent way?

Answers to these questions hinge on the availability of well-measured isotopic neutron σ_{tot} data sets across a broad energy range. Indeed, the $^{40,48}\text{Ca}$ neutron σ_{tot} data collected

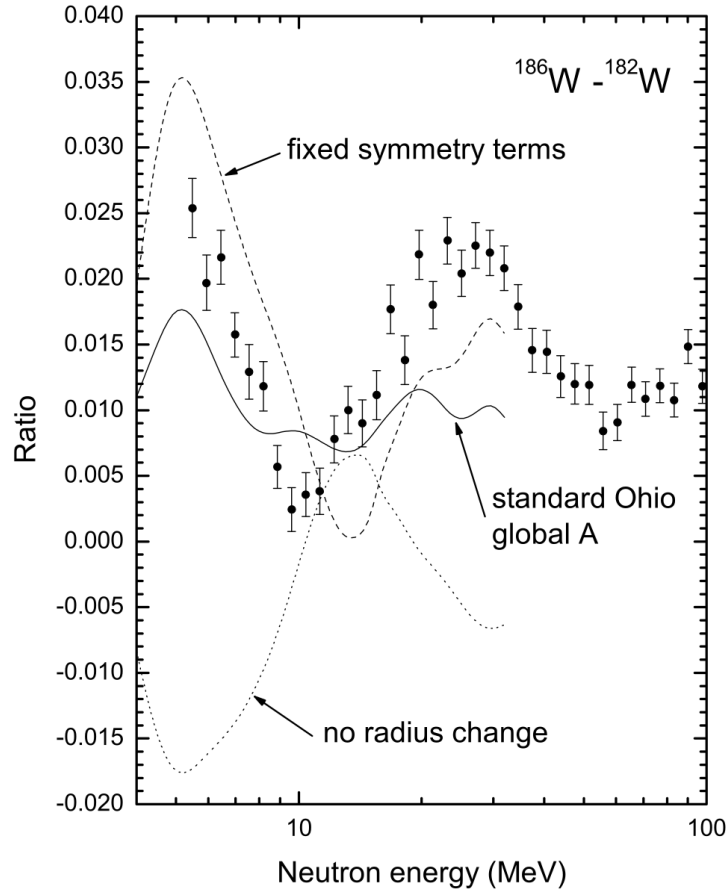


Figure 1.6: ^{186}W - ^{182}W neutron σ_{tot} relative difference and Ohio global optical potential predictions. Figure from [40].

by our group at LANSCE in 2009, in part inspired by the W measurements of [40], provided grist for a non-local Dispersive Optical Model (DOM) analysis in 2015 [42]. This non-local analysis revealed connections between the asymmetry-dependence of single-particle occupation numbers and high-energy scattering data. Providing experimental data on key nuclei, in particular for use with the DOM, is a primary motivation for the isotopically-resolved neutron σ_{tot} and $\frac{d\sigma}{d\Omega}$ results presented in this work. These new data are analyzed in Chapter 7 with an improved non-local DOM capable of fits to data on even-even nuclei.

Details on our DOM implementation are presented in chapter 6.

1.2.2 Nuclear Masses, Matter Radii, and Charge Radii

The mass and spatial extent of a nucleus are two of its most fundamental properties. Of all experimental data, nuclear masses are known to the highest precision, up to ten significant digits [43]. Connecting masses and radii is a central goal of the Liquid Drop Model and many other theoretical treatments over the last century (e.g., Hartree-Fock-BCS treatment of 700 nuclei to calculate proton and neutron RMS radii [44]). Extracting nuclear radii from optical models has been an active area of research for over fifty years [45].

Experimentally, a variety of techniques are available to probe the nuclear charge density distribution. On stable nuclei, x-ray energies from muonic atoms [46] are sensitive to deviations of the nuclear charge distribution from sphericity. Elastic electron scattering data on stable isotopes can be used (after a Fourier transform) to provide the full nuclear charge density profile at spatial resolutions between $2\pi/q_{min}$ and $2\pi/q_{max}$, where q is the momentum transfer associated with the elastic scattering [11]. On unstable nuclei, collinear laser spectroscopy [47] uses small shifts in electronic levels to extract the difference in RMS radii (δ_{RMS}) of the charge distributions along an isotope chain, the so-called “isotope shift”. The isotope shift is shown for the even- A Sn isotopes in Fig. 1.7 [48]. It has long been clear that the isotope shift is critically connected to the neutron and proton matter distributions. The difference in RMS radii between the protons and neutron point distributions (i.e., not including the finite size of the protons and neutrons) is commonly referred to as the “neutron skin” [49] and was first identified as an important nuclear quantity by Wilkinson over fifty years ago [50]. In a Droplet Model picture, the slope of the isotope shift is linked to the symmetry energy J , density dependence of the symmetry energy L , and surface stiffness coefficient Q^1 ,

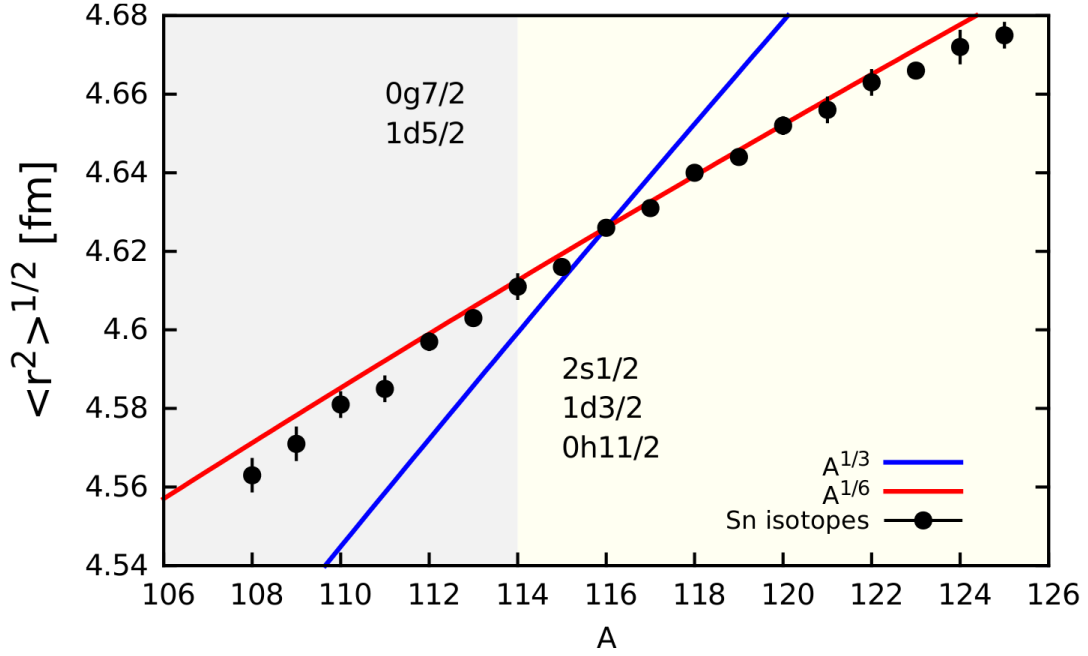


Figure 1.7: Root-mean-squared (RMS) charge radii in Sn isotopes. The $A=106-114$ region and $A=114-116$ region are shaded and labeled indicating the expected single-particle occupation of the valence neutrons. An isoscalar treatment that only accounts for size scaling predicts an $A^{1/3}$ slope as neutrons are added, but the data show a nearly-linear $A^{1/6}$ slope instead. The slope of the isotope shift is connected to the symmetry energy and its density dependence. Data from Anselment et al. [48].

the same bulk quantities that determine neutron-skin thickness [1, 51]. Without additional experimental constraints, the J , L , and Q parameters form an underdetermined system from which unique values cannot be recovered, even if the consensus value of $J \approx 30$ MeV is used

¹In [1], the J -, L -, and Q -dependent contributions to the binding energy are:

$$E(N, Z; \text{shape}) = [J\bar{\delta}^2 - \frac{1}{2}K\bar{\epsilon}^2 + \frac{1}{2}M\bar{\delta}^4]A + \frac{9}{4}(J^2/Q)\bar{\delta}^2 A^{\frac{2}{3}} B_s + CC(J, Q)$$

where $\bar{\delta}$ and $\bar{\epsilon}$ of Eq. 1.2 are fully parameterized as:

$$\bar{\delta} = I + \frac{3}{16}(c_1/Q)ZA^{-\frac{2}{3}}B_v/[1 + \frac{9}{4}(J/Q)A^{-\frac{1}{3}}B_s]$$

$$\bar{\epsilon} = [-2a_2A^{-\frac{1}{3}}B_s + L\bar{\delta}^2 + c_1Z^2A^{-\frac{4}{3}}B_c]/K$$

to reduce the parameter space. As was already pointed out 50 years ago by Myers [52], the single-particle configuration of a given nucleus may have a significant effect on the formation and size of such a skin.

Charge radius measurements have become sufficiently precise that models can no longer equate the proton matter distribution and the charge distribution; the non-uniform charge distributions of the proton and neutron must be accounted for as well. Constraining the neutron matter distribution experimentally is extremely difficult, as neutrons do not interact Coulombically with the electron and muonic probes used to determine the charge distribution. An on-going, multi-year experimental effort at Jefferson Laboratory aims to measure the ^{48}Ca and ^{208}Pb neutron and proton matter distributions directly using parity-violating electron scattering, taking advantage of the different weak charges of the proton and neutron [53]. The neutron skins of these and other neutron-rich nuclei are of immense theoretical and astrophysical interest, as they are closely correlated with the density-dependence of the symmetry energy, essential for the neutron star equation-of-state, and with many other bulk properties of nuclei, including the electric-dipole-polarizability (EDP) and the location of the pygmy and giant dipole resonances (PDR and GDR) [54, 55, 56, 57, 58]. Constraining L using these asymmetry-dependent properties is quite challenging: the properties of highly-asymmetric nuclei are most closely correlated with L , but harder to measure experimentally, and the properties of low-asymmetry nuclei are much more weakly correlated with L . One of the chief goals of the Dispersive Optical Model (detailed in Chapter 6) is to extract well-constrained values for the neutron skin thickness on a variety of nuclei (shown in Chapter 7).

In these equations, K is the compressibility coefficient, M accounts for anharmonicity of the binding-energy dependence on $\bar{\delta}$, and B_s accounts for shape dependence of the surface energy. $CC(J, Q)$ are corrections to the Coulomb term associated with deformation. The quantity $\frac{9}{4}(J^2/Q)\bar{\delta}^2$ is the correction to the binding energy from excess neutrons accumulating on the nuclear surface (i.e., neutron skin formation).

By judiciously applying all available scattering and bound-state data in the DOM approach, we hope to test the assertion that the EDP, GDR location, neutron skin, and L are as tightly correlated as it appears from mean-field models.

1.3 Motivation, Scope, and Dissertation Outline

Improved isotopically-resolved neutron scattering data are an essential ingredient for better nuclear reaction models and to test the asymmetry-dependence of the nuclear potential. The results from our campaign to collect these valuable σ_{tot} and $\frac{d\sigma}{d\Omega}$ data sets on cornerstone nuclei form the backbone of this dissertation. In addition to these experimental results, a suite of Dispersive Optical Model analyses that incorporates these new data is presented. From the DOM potentials, a variety of asymmetry-dependent nuclear-structure quantities, including neutron skins and relative momentum content, are extracted.

An overview of neutron σ_{tot} experimental considerations, the details of our σ_{tot} experiment, and analysis for our isotopically-resolved σ_{tot} measurements on $^{16,18}\text{O}$, $^{58,64}\text{Ni}$, ^{103}Rh , and $^{112,124}\text{Sn}$ are detailed in Chapters 2 and 3. Similarly, our elastic scattering measurements on $^{112,124}\text{Sn}$ are presented in Chapters 4 and 5. A brief summary of the Dispersive Optical Model formalism is given in Chapter 6 and the results from our DOM fits of $^{16,18}\text{O}$, $^{40,48}\text{Ca}$, $^{58,64}\text{Ni}$, $^{112,124}\text{Sn}$, and ^{208}Pb are presented in Chapter 7. A complete listing of the experimental data used in the DOM analyses, the parameter values of the DOM potentials, and figures showing the results of the DOM fits are provided in Appendices B, C, and D.

NEUTRON TOTAL CROSS SECTIONS: EXPERIMENTAL SETUP

2.1 Overview of Neutron σ_{tot} Experiments

Neutron scattering is a direct, Coulomb-independent tool for probing the nuclear environment. The simplest measurement of neutron interaction with a nucleus, the neutron total cross section σ_{tot} , provides fundamental information about nuclear size and the ratio of elastic-to-inelastic components of nucleon scattering. Additionally, σ_{tot} data are connected to a variety of nuclear properties of great interest including the neutron skin of neutron-rich nuclei [59] and thus the density dependence of the symmetry energy L , essential for an accurate neutron star equation-of-state (EOS) [56, 54, 55].

By scattering secondary radioactive beams off hydrogen targets in inverse kinematics, proton-scattering experiments are possible even on highly unstable nuclides. In contrast, because neutrons themselves must be generated as a secondary radioactive beam, neutron-scattering experiments are restricted to normal kinematics and σ_{tot} measurements are possible only for relatively stable nuclides that can be formed into a target. At present, σ_{tot} measurements above the resonance region on nuclides with short half-lives (shorter than the timescale of days) are technically infeasible for this reason, though a handful have been

carried out on samples with half-lives in the tens to thousands of years [18, 60, 61].

Traditionally, σ_{tot} measurements have relied on analog electronics for processing and recording events, techniques that suffer from a large per-event deadtime of up to several μs . For a state-of-the-art intermediate-energy σ_{tot} measurement with dozens or hundreds of energy bins, achieving statistical uncertainty at the level of 1% requires a thick sample to attenuate a sizable fraction of the incident neutron flux. For cross sections in the 1-10 barn range, this means sample masses of tens of grams [16, 20]. Producing an isotopically-enriched sample of this size is often prohibitively expensive. This explains the lack of data for isotopically-resolved σ_{tot} measurements from 1-300 MeV even for closed-shell isotopes of special importance like $^3,^4\text{He}$, ^{64}Ni , and ^{204}Pb (see Table 2.1).

In the 1990s, a comprehensive series of measurements were made at the Weapons Neutron Research (WNR) facility of the Los Alamos Neutron Science Center (LANSCE) on a wide battery of samples from Li to Pb [16, 20], some isotopically-separated. Twenty years later, the measurements on $^{40,48}\text{Ca}$ [37] were the first to employ newly-available digital-signal-processing technology to reduce the deadtime associated with processing each event and thus reduce the needed sample size. In 2015, we embarked on a systematic campaign to measure neutron σ_{tot} across the widest possible energy range for the heaviest and lightest stable isotopes in the $Z = 8$, $Z = 28$, and $Z = 50$ closed shells.

Table 2.1: Selected results from a literature search for isotopically-resolved σ_{tot} data using the EXFOR database [35]. For the heaviest and lightest stable nuclides in each closed shell in Z, all datasets falling at least partially within 1-500 MeV are shown. For elements whose natural abundance is $>90\%$ of a single isotope (e.g., 96.9% of $^{\text{nat}}\text{Ca}$ is ^{40}Ca), σ_{tot} data on the natural sample was included as “isotopic”.

Isotope	Nat. Abund. [%]	Energies [MeV]	Reference
^3He	2×10^{-4}	1.5 – 40	[62]
^4He	>99.9	0.7 – 30	[63]
		2 – 40	[62]
		77 – 151	[64]
^{16}O	99.8	0.2 – 49	[65]
		5 – 600	[16]
^{18}O	0.20	0.1 – 2.5	[66]
		2.5 – 19	[67]
^{40}Ca	96.9	<0.1 – 6.4	[68]
		5.3 – 560	[20]
^{48}Ca	0.187	0.6 – 5.2	[69]
		12 – 276	[37]
^{58}Ni	68.1	<0.1 – 68	[70]
^{64}Ni	0.926	14.1	[71]
^{112}Sn	0.97	<0.1 – 1.4	[72]
		14.1	[71]
^{124}Sn	5.79	0.3 – 5.0	[73]
		5.1 – 26	[74]
^{204}Pb	1.4	<0.1 – 27	[75]
^{208}Pb	52.4	<0.1 – 695	[76]
		5 – 600	[16]

2.2 Detector Construction

Because neutrons carry no charge, they penetrate materials much further than protons and do not deposit energy continuously along their path. Further, when neutrons do interact with nuclei in detector materials, the energy transferred does not correspond linearly to the neutron energy. Thus assigning the correct energy to a scattered neutron is far from trivial. The main approach to energy determination for fast neutrons is by time-of-flight (TOF) as evidenced by state-of-the-art neutron detector arrays including MoNA [77], VANDLE [78], and NeuLAND [79].

Figure 2.1 shows a TOF detector used in one of our neutron σ_{tot} measurements. A 2-inch x 2-inch x 1-inch block of BC-400 fast plastic scintillator is coupled to two transparent BC-800 adiabatic lightguides with RTV rubberized adhesive. The 2-inch x 2-inch face is perpendicular to the beam and the 1-inch dimension is parallel to the beam. These components were encased in an aluminum structural housing. On the distal end of the lightguides, Hamamatsu 1668 photomultiplier tubes were connected with optical grease and enclosed by μ -metal shielding, used to prevent external magnetic fields from affecting photoelectrons. Phototube signals and high voltage were supplied by a phototube base attached to the back of each phototube. To hold the phototubes, fitted black Delrin sleeves (shown on the left side of the CAD cutaway in Fig. 2.2) were custom-made to apply slight compression, keeping the optical surfaces in good contact. The entire assembly is 24 9/16 inch in length.

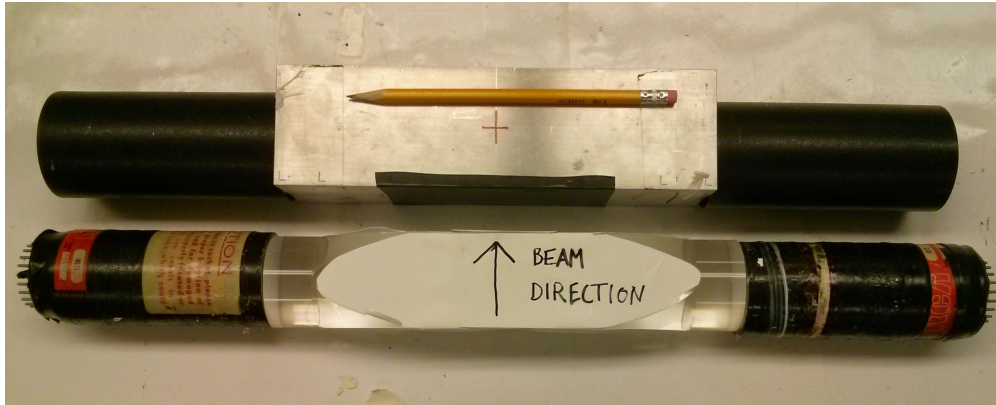


Figure 2.1: A TOF detector, partially assembled, with pencil for scale. The aluminum casing and Delrin phototube sleeves are at top, and the scintillator (beneath the beam direction arrow), lightguides, and phototubes, at bottom. The detector described in the text has a thinner scintillating plastic element (1 inch thick) and tapered lightguides to match.

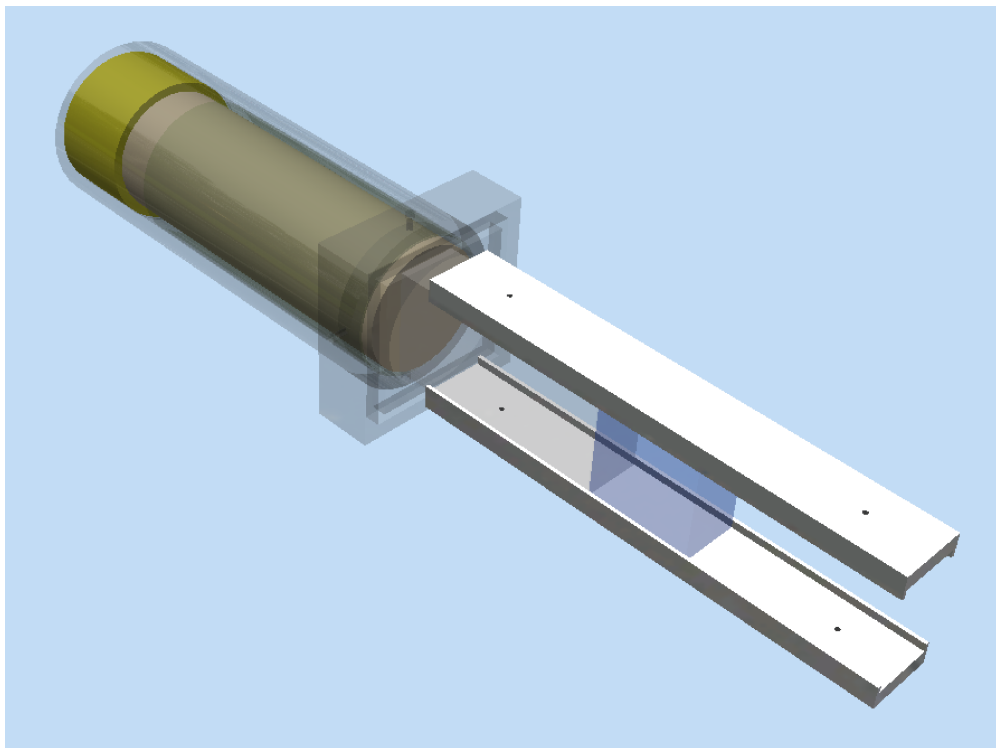


Figure 2.2: Cutaway CAD figure of TOF detector described in the text. The 1-inch-thick scintillating plastic element is visible in the middle of the aluminum housing brackets, and the light-tight sleeve for the phototube is visible on the left.

2.3 Sample Preparation

Where possible, the σ_{tot} samples were formed as right cylinders 8.25 mm in diameter and ranging from 10-27 mm in length (see Table 2.2 for sample characteristics and Fig. 2.3 for sample images). A natural-abundance sample was also prepared for each element to benchmark our results against already-existing literature neutron σ_{tot} data on natural samples. During the experiment, the samples were inserted into styrofoam sleeves and seated in the cradles of the sample changer, described below. This design minimizes the amount of non-target mass proximate to the neutron beam path that could cause unwanted neutron scattering. The areal density of atoms, the relevant quantity for cross section measurements, for each O, Ni, and Sn sample differs by less than 1% compared to the other samples of the same element.

For the oxygen isotopes, isotopically-enriched water samples were prepared to increase the areal density of O in the sample volume and for ease of handling. After measurement, the extremely-well-known neutron σ_{tot} on hydrogen could be subtracted to yield the O σ_{tot} values. This technique was also used by [66, 67]; cf. the use of ZnO and BeO [16]. Because the natural abundance of ^{16}O in H_2O is >99%, a sample of ordinary distilled water was used for the H_2^{16}O sample. For H_2^{18}O , we used distilled water enriched to 99.9% in ^{18}O purchased from Aldrich. Both samples were enclosed in brass vessels with thin (0.002 inch) brass endcaps, to minimize neutron attenuation. At the temperature and altitude of the experimental facility, the amount of dissolved gas and ions in the water samples were small enough to have no effect on the measurement.

The isotopic Sn samples were prepared by melting highly-enriched foils at 800 C in a tube furnace, cooling to ambient temperature, and pressing the ingots to the desired cylindrical

shape in a tempered die. To reduce formation of tin oxide during melting, the samples were melted in vitreous carbon crucibles and kept under a reducing atmosphere (90% Argon/10% H₂) while at elevated temperatures. Of the 4.9 grams of ¹¹²Sn used to prepare the sample, 3.9 grams were from a semi-permanent loan from the group of Lee Bernstein from LLNL and the remainder we purchased from Isoflex Corp. All of the 5.8 grams of ¹²⁴Sn were purchased from Isoflex. The ^{nat}Sn sample was prepared by melting and pressing analytical-grade Sn shot from Mallinckrodt Corp. Loss of isotopic material during the sample preparation process was minimal. The natural and isotopic Ni samples were prepared by Mike Zach at Oak Ridge National Lab (ORNL) to match the diameter of our Sn samples.

Due to its poor machining properties, the Rh sample was prepared by stacking a series of thin rhodium disks instead of manufacturing a fused cylinder. Four disks of 99.9% pure natural (monoisotopic) Rh metal were purchased from Goodfellow Corp. These were corralled inside a plastic sleeve with open ends, similar to the styrofoam sleeves used for the Ni and Sn samples, to match the $\frac{3}{4}$ -inch-diameter cradles of the sample changer (Fig. 2.4). This kept the discs snugly in series and perpendicular to the beam path.

Lastly, two natural-abundance graphite samples of different lengths and one natural-abundance Pb sample, all with the same diameter as the Sn and Ni samples, were prepared. These samples were used to benchmark the total cross sections measured at LANSCE by comparison with previous measurements of the C and Pb total cross sections available in the literature [16, 20]. In addition, the low-energy neutron σ_{tot} resonance structure of the C samples served a crucial role in fixing the exact distance of the TOF detector as detailed in Chapter 3. Before use, the C samples were baked in an oven for several hours to remove adsorbed water.

Appendix A lists the full composition of each isotopic sample as listed by the manufacturer

SAMPLE PREPARATION

or from mass spectrometer analysis.

Table 2.2: For isotopically-enriched samples, the natural abundance of the enriched isotope and the isotopic fraction of the sample are given. To calculate cross sections, the relevant “sample thickness” is the areal density of nuclei ρ_{areal} , equivalent to the (volumetric) density times the length of the sample. For liquid samples $\text{H}_2^{\text{nat}}\text{O}$, $\text{D}_2^{\text{nat}}\text{O}$, and H_2^{18}O , the length and diameter listed are for the interior of the vessels used to hold the samples and the masses given are calculated based on literature values for the density of each sample at 25 C. Our samples are generally much smaller than those used in previous measurements; for comparison, the Ni and Sn samples used in [20, 16] had areal densities of 1.515 and $0.5475 \frac{\text{mol}}{\text{cm}^2}$, respectively (12.7 and 6.5 times larger than our Ni and Sn samples). Columns 6 and 7 give the natural abundance of the isotope (NA) and the purity of our isotopic samples (SP).

Isotope	Len. [mm]	Diam. [mm]	Mass [g]	$\rho_{\text{areal}} [\frac{\text{mol}}{\text{cm}^2}]$	NA [%]	SP [%]
$^{\text{nat}}\text{C}$	13.66(2)	8.260(5)	1.2363	0.1921(1)	-	-
$^{\text{nat}}\text{C}$	27.29(2)	8.260(5)	2.4680	0.3835(2)	-	-
$\text{H}_2^{\text{nat}}\text{O}$	20.00(1)	8.92(1)	1.2461	0.1107(3)	-	-
$\text{D}_2^{\text{nat}}\text{O}$	20.00(1)	8.92(1)	1.3852	0.1107(3)	0.02	99.9
H_2^{18}O	20.00(1)	8.92(1)	1.3844	0.1107(3)	0.20	99.9
^{58}Ni	7.97(3)	8.18(2)	3.6438	0.1197(3)	68.1	99.6
$^{\text{nat}}\text{Ni}$	8.00(3)	8.20(2)	3.6898	0.1192(3)	-	-
^{64}Ni	7.96(2)	8.20(4)	3.9942	0.1192(6)	0.93	92.2
^{103}Rh	2.03(1)	10.20(2)	2.8359	0.02426(4)	100	99.9
^{112}Sn	13.65(3)	8.245(5)	4.9720	0.08332(5)	0.97	99.9
$^{\text{nat}}\text{Sn}$	13.68(3)	8.245(5)	5.3263	0.08414(5)	-	-
^{124}Sn	13.73(3)	8.245(5)	5.5492	0.08399(5)	5.79	99.9
$^{\text{nat}}\text{Pb}$	10.07(2)	8.27(1)	6.130	0.05508(6)	-	-

SAMPLE PREPARATION



Figure 2.3: $^{112,\text{nat},124}\text{Sn}$ (section a), $\text{H}_2^{\text{nat},18}\text{O}$ (section b), and $^{58,\text{nat},64}\text{Ni}$ samples (section c) used for neutron σ_{tot} measurements, with rulers for scale. Brass vessels were used to hold the water samples.

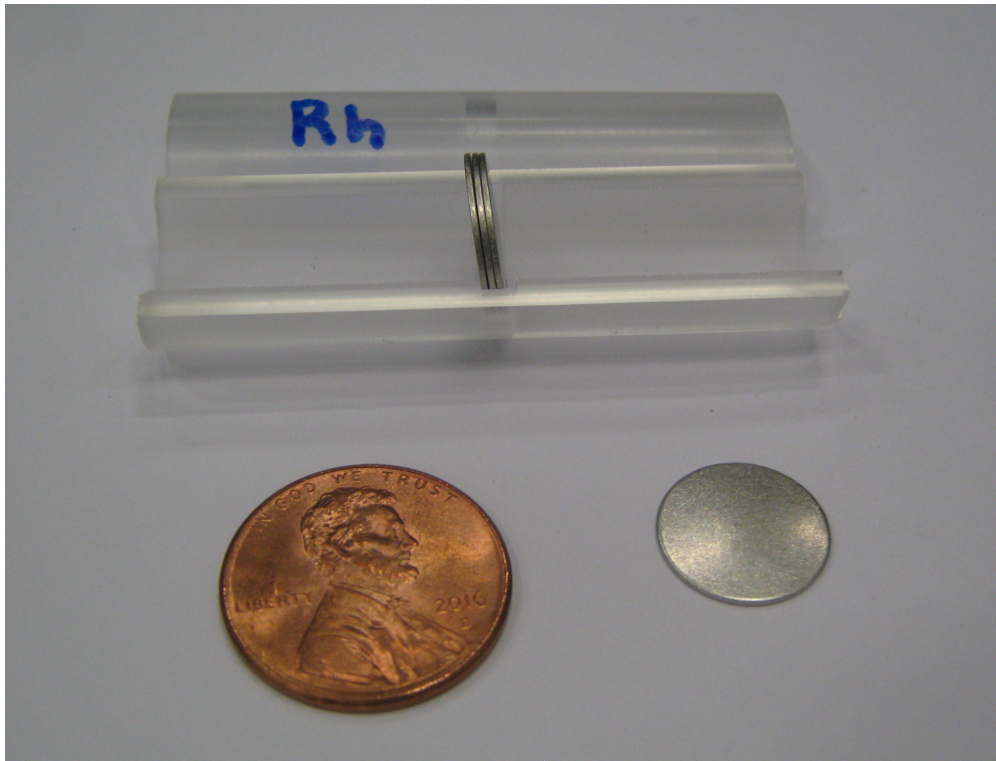


Figure 2.4: ^{103}Rh sample used for the neutron σ_{tot} measurements. One of the four Rh discs has been removed from the plastic sleeve to show detail.

2.4 Experimental Facility at LANSCE

All neutron σ_{tot} measurements were carried out at the 15R beamline of the Weapons Neutron Research (WNR) facility at the Los Alamos Neutron Science Center (LANSCE) over two run cycles (November 2016 and September 2017). At WNR, broad-spectrum neutrons up to 700 MeV are generated by impinging an 800-MeV proton beam onto a water-cooled, 7.5-cm-long tungsten target (see Fig. 2.5). A permanent magnet deflects all charged particles from the beam path, allowing only neutrons and γ rays to reach our samples. The neutron flux can be adjusted by the user with a pair of horizontal and vertical shutters upstream of the experimental vault. Based on beam divergence simulations, the beam was collimated to 0.200 inch at the entrance to the experimental vault using steel donuts with a total thickness of 24 inches. To reduce (but not eliminate) the γ -ray component of the beam, a $\frac{1}{2}$ -inch-thick plug of Hevimet (90% W, 6% Ni, 4% Cu by weight) was inserted at the upstream end of the stack of collimator donuts. After collimation, the beam passed successively through a flux monitor, the sample of interest held in a sample changer (see Fig. 2.6), a veto detector, and finally the TOF detector approximately 25 meters from the neutron source (see Fig. 2.7). The monitor detector and veto detector were constructed along similar principles to the TOF detector construction but only have one phototube each. The monitor and veto detectors each had scintillator thicknesses of $\frac{1}{4}$ inch. Figure 2.9 shows the entire experimental area, looking upstream from the perspective of the TOF detector. Figure 2.8 shows the same area, but looking downstream from the monitor detector.

The particular neutron beam structure at WNR dictates the energy range achievable for σ_{tot} measurements (see Fig. 2.10). Proton pulse trains, called “macropulses”, are delivered to the tungsten target at 120 Hz. Each macropulse consists of 350 individual proton pulses,

called “micropulses”, spaced 1.8 μs apart. Each micropulse consists of a single proton packet <1 ns wide when it arrives at the tungsten target that generates γ rays and neutrons within a tight temporal-spatial range. As neutrons from this micropulse travel along the beam path, high-energy neutrons separate in time from lower-energy neutrons so that neutron energy can be determined by standard TOF techniques described in Chapter 3 (see [80] for additional details). Because the γ rays and high-energy neutrons from later micropulses can overtake slower neutrons from an earlier micropulse, an important tradeoff exists between measuring low- and high-energy neutrons. The further the TOF detector is placed from the neutron source, the higher the minimum neutron energy that can be unambiguously resolved. However, placing the TOF detector closer to the neutron source increases the maximum instantaneous neutron flux at the start of each micropulse, increasing the digitizer-dead probability for the highest-energy neutrons. A balance must be struck between the detector thickness, the neutron flux, the γ -ray flux, the TOF detector distance, and the rate of data acquisition.

A programmable sample changer with six positions was used to cycle each sample into the beam at a regular interval of 150 seconds per sample. Once per macropulse, an analog signal from the sample changer was recorded to indicate its current position. The sample configuration for each run varied, but generally all six positions on the sample changer were used. For the solid targets, a typical configuration was to place an empty styrofoam sample sleeve in the first sample-changer cradle as the “blank”, the $^{\text{nat}}\text{C}$ and $^{\text{nat}}\text{Pb}$ samples in the second and third cradles, and the samples of interest (e.g., ^{58}Ni , $^{\text{nat}}\text{Ni}$, ^{64}Ni) in the fourth, fifth, and sixth cradles. For water samples, an empty brass vessel was placed in the first cradle to serve as the blank.

Due to beam divergence after collimation and the small diameter of the samples, precise

alignment of the sample changer was paramount. The sample changer was placed on an adjustable table and roughly aligned by laser. For precise alignment, a 2-inch aluminum cylinder with a $\frac{1}{16}$ -inch axial hole was placed in the first position of the sample changer and a radiographic film placed immediately posterior. The film was irradiated by the neutron beam for fifteen minutes and developed to show the alignment of the aluminum cylinder with the beam profile. The position of the target changer was adjusted to improve alignment, and the process was iterated until alignment was satisfactory, ensuring that all neutrons reaching the TOF detector had to pass through the in-beam sample. Figure 2.11 shows a radiogram confirming alignment of all sample changer positions within 1 mm.

The beam flux of each macropulse, required to normalize absolute cross sections, was continuously monitored by the flux monitor detector. The veto detector immediately upstream of the TOF detector was used to reject TOF events from charged-particle production in the samples and in air along the flight path. The left and right PMTs of the TOF detector were gain-matched and a 0.5-ns cable delay was introduced on the right PMT signal to improve the time-matching between the left and right signals.

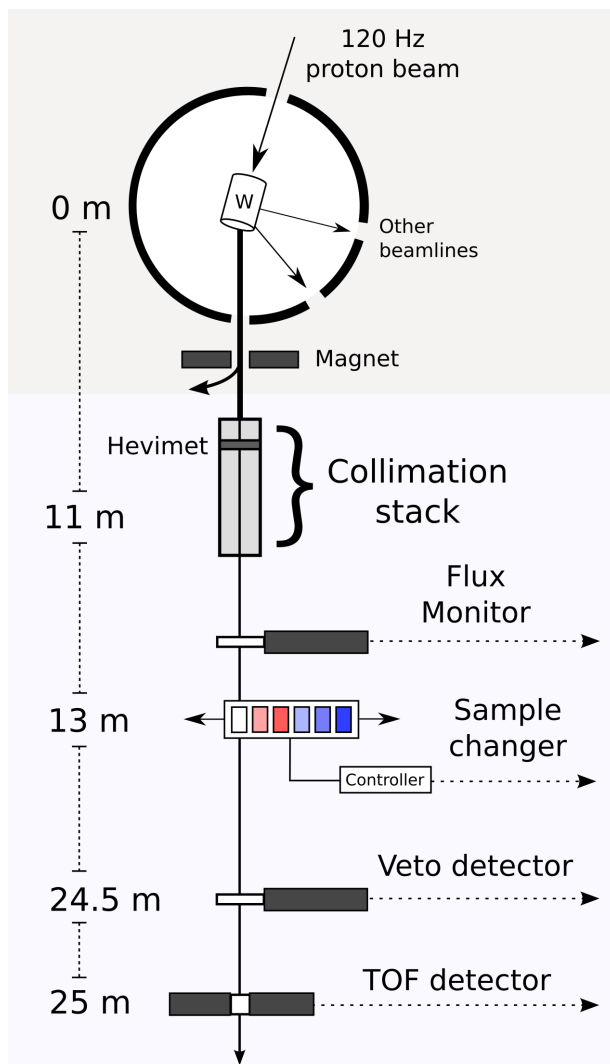


Figure 2.5: Layout of the 15R beamline at the WNR facility at LANSCE, with our experimental equipment indicated toward the bottom of the flight path. After a permanent magnet sweeps charged particles from the beam, neutrons and γ rays are collimated to 0.200 inch en route to the detectors used in the experiment. Samples are cycled into and out of beam using a linear actuator with a period of 150 seconds. Times-of-flight (TOFs) are determined by the TOF detector and used to calculate neutron energy.

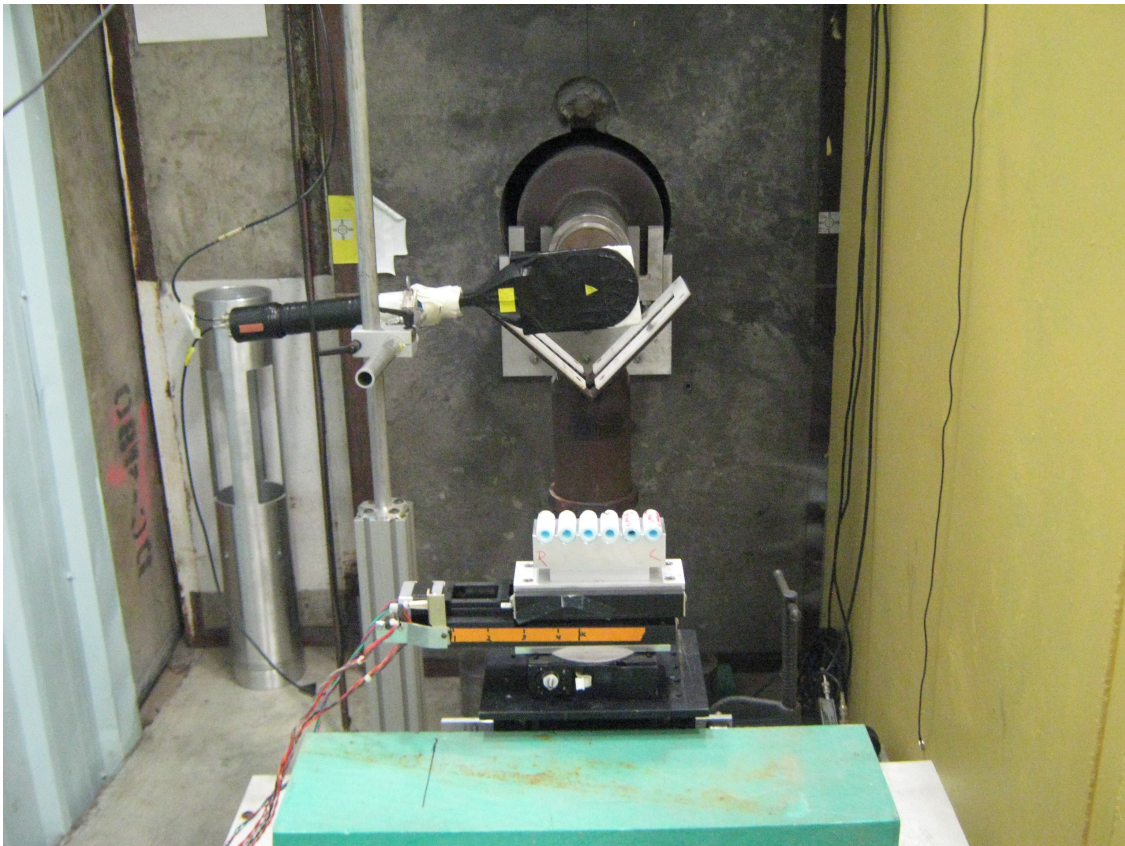


Figure 2.6: Upstream view of sample changer, monitor detector, and collimation stack.

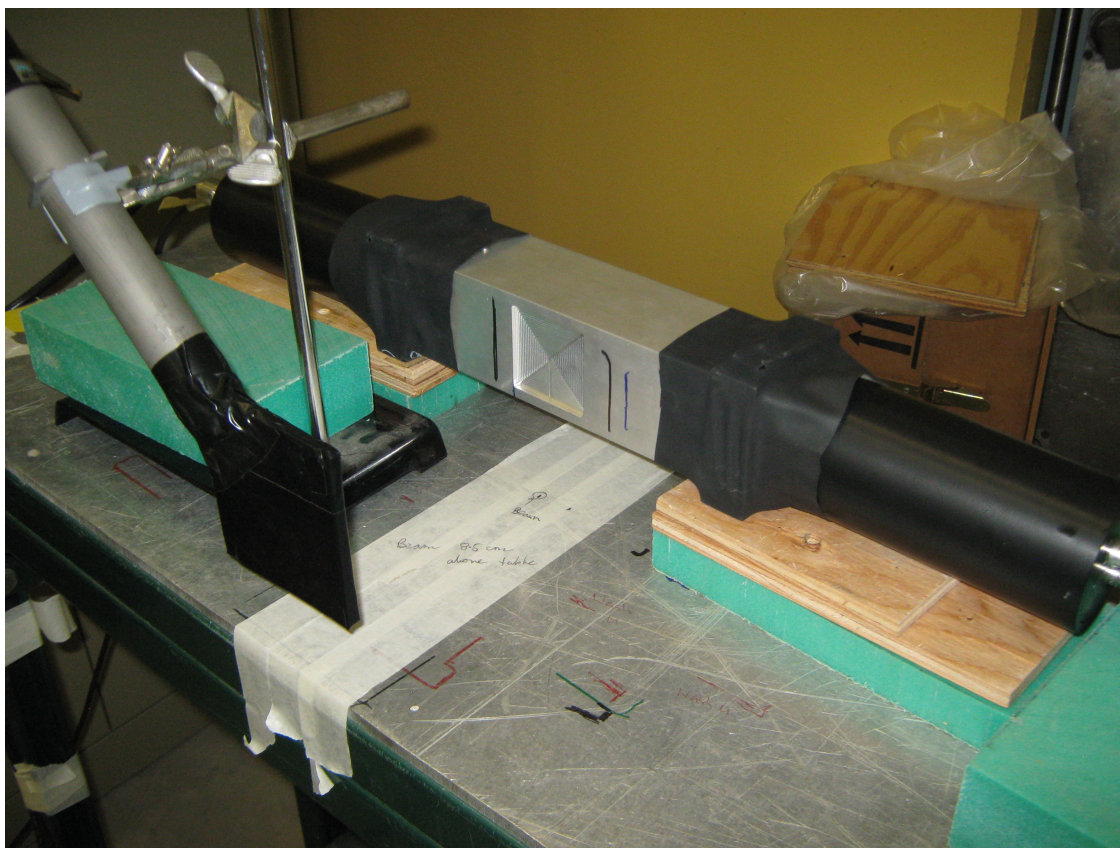


Figure 2.7: Veto and TOF detectors installed in the 15R beamline. Beam enters from the left.



Figure 2.8: Downstream view of monitor detector, sample changer and TOF detectors installed in the 15R beamline.



Figure 2.9: Upstream view of σ_{tot} experimental setup in the 15R beamline. In the foreground is the TOF detector (the veto detector is not pictured here). In the background, the sample changer and monitor detector are visible. The blue cart holds the coarse-alignment laser.

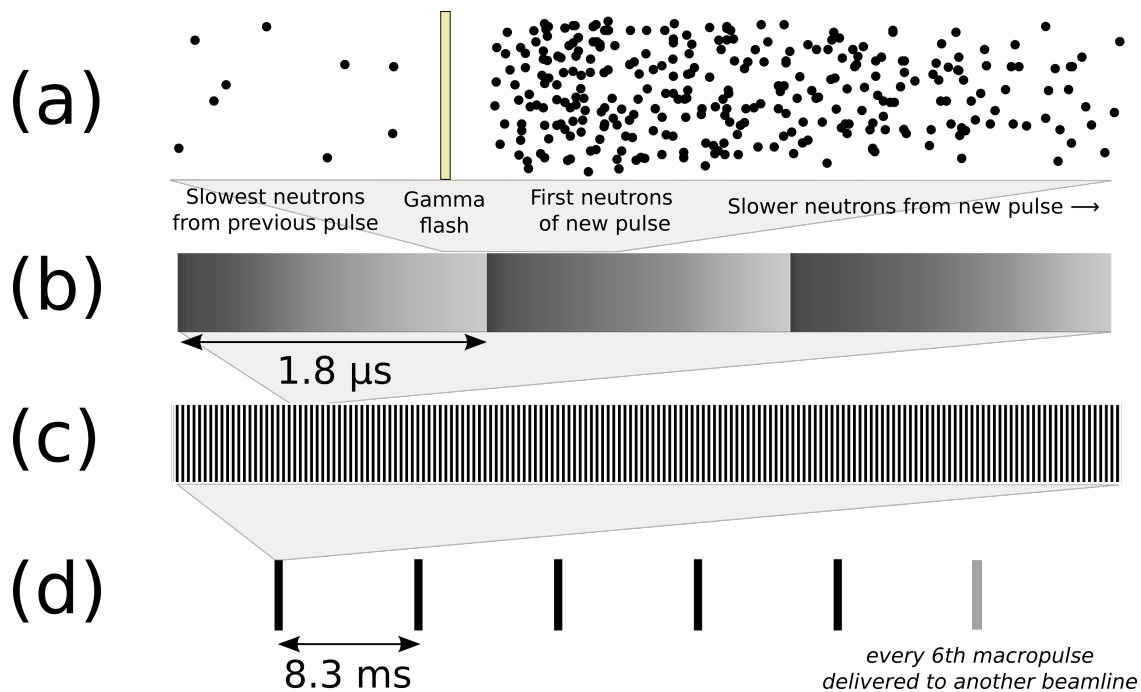


Figure 2.10: Neutron beam structure at WNR facility. “Macropulses” of protons (row d) are delivered to WNR’s tungsten Target 4, where they generate neutrons by spallation. Each macropulse consists of ≈ 350 proton “micropulses” (row c). Neutrons from each micropulse (row b) disperse in time as they travel along the flight path so that γ rays and high-energy neutrons catch up to low-energy ones from the previous pulse (row a).



Figure 2.11: Radiographic film showing precision alignment of the sample changer. When the high-intensity central region lies in the center of the diffuse halo, alignment is achieved. All six positions of the sample changer were tested.

2.5 Data Acquisition

Signals from all detectors and the sample changer were relayed to an 8-channel, 14-bit, 500-MHz CAEN DT-5730 waveform digitizer as shown in Fig. 2.12. Custom software was used to run the digitizer in two complementary modes, referred to as “DPP mode” and “Waveform mode”. In DPP mode, triggers were initiated by the digitizer’s onboard peak-sensing firmware. For each trigger, several quantities were recorded: the trigger timestamp, two charge integrals over the detected peak with different integration ranges (32 ns for the short integral, 100 ns for the long integral), and a 96-ns portion of the raw digitized waveform, referred to as a “wavelet”. The timestamp was stored as two components: a 48-bit timestamp with 2 ns resolution, and 10-bit “fine time” within the 2 ns coarse time bin period. DPP mode was used for the vast majority of the experiment and accounts for $\approx 99\%$ of the total data volume. In waveform mode, the digitizer performs no peak sensing and was externally triggered. Upon triggering, the trigger timestamp and a very long wavelet (60 μs) were recorded. While waveform mode data accounts for only $\approx 1\%$ of the total data, the instantaneous data rate is much higher than in DPP mode because hundreds of μs of consecutive waveform samples are stored. Roughly once every three seconds, the digitizer was switched to waveform mode for one macropulse, then switched back to DPP mode as quickly as possible (within 10-40 ms, depending on run configuration). When the buffer for any channel filled, all buffers were read out by optical link to a flash memory drive of the data acquisition computer, minimizing the downtime of the digitizer due to data readout.

Because we had fast digital-signal-processing technology available, we were able to perform event detection and processing in a fundamentally different way compared to analog-mediated approaches. This is worth mentioning here as it enabled a dramatic reduction,

over an order of magnitude, in the size of the samples required compared to previous measurements at the same facility. The reasons for our approach and tradeoffs are described in Section 3.2 of Chapter 3.

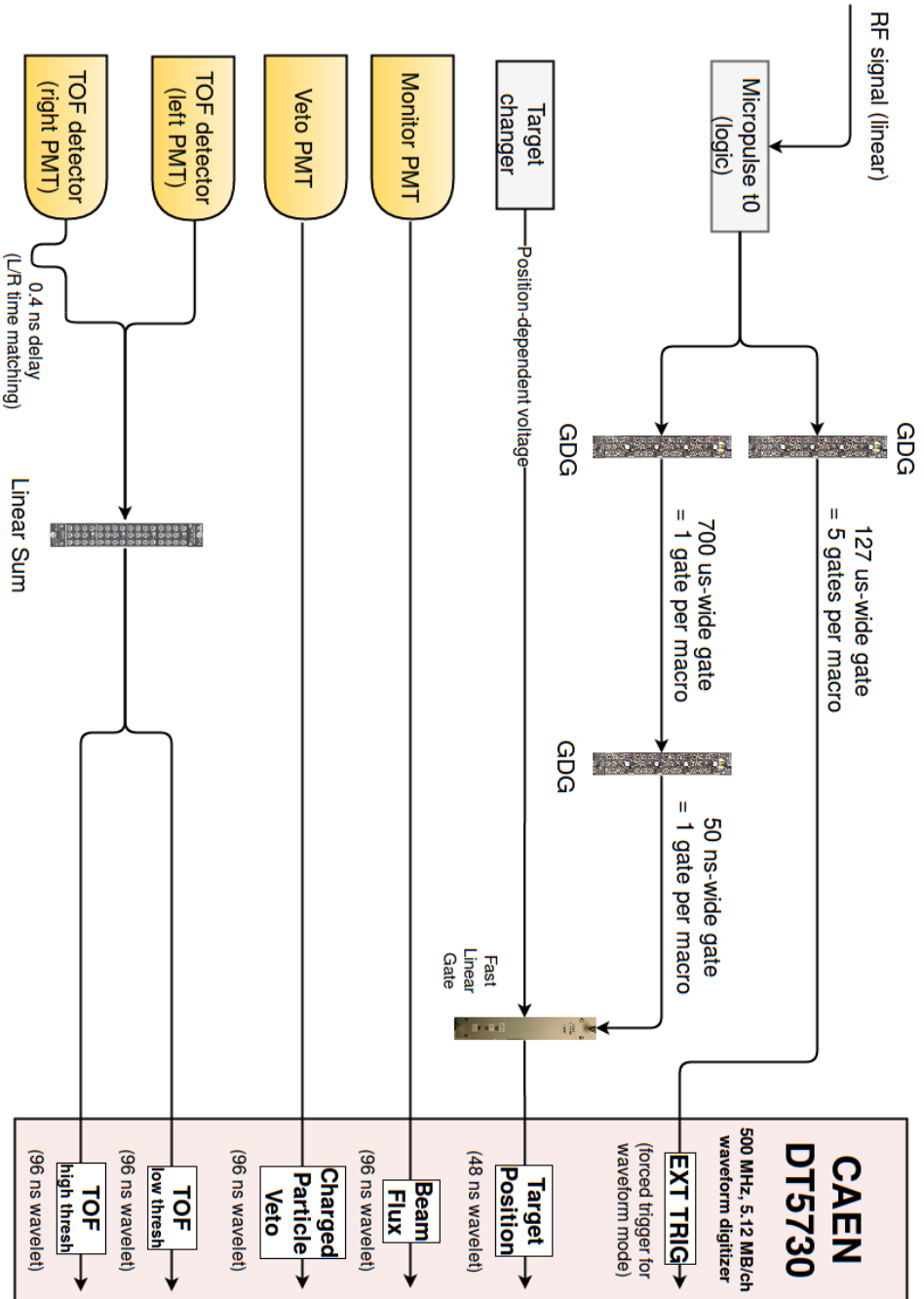


Figure 2.12: Logic diagram for neutron σ_{tot} data acquisition. An explanation is provided in the text on page 45.

NEUTRON TOTAL CROSS SECTIONS: ANALYSIS AND RESULTS

3.1 Timing Considerations

To assign correct neutron energies, the time resolution of the TOF detector is critical. Several tests and corrections were applied to improve timing resolution as much as possible.

The DT-5730 provides leading-edge discrimination (LED) and constant-fraction discrimination (CFD) modes for timing determination. In pre-experiment testing, we found that using the on-board CFD calculation increased the time required to process each event by 40 ns or more, an unacceptable increase in the per-event deadtime. Thus we chose to use the digitizer's faster LED option and to calculate precise event timing in software, after the experiment, by analyzing the digitized waveform for each event. Data taken from the left and right PMTs separately and gated by neutron energy are shown in Figs. 3.1 and 3.2. For each energy range, the FWHM of the distribution was calculated and a hyperbolic fit was performed, shown in Fig. 3.3. The inherent left-right timing resolution, independent of neutron energy, was identified as 0.34 ns FWHM. When folded over the actual beam energy profile (as during the experiment) the left-right time resolution degraded to 0.52 ns.

To calculate the TOF for each event, the “starting gun” of each micropulse had to be pre-

TIMING CONSIDERATIONS

cisely determined. All event times were first adjusted for cable and electronics delay so that each event was assigned to the correct macropulse. To reduce unnecessary data collection, we collected only the first T_0 , a logic signal, of each macropulse. Using this time and the precisely-known micropulse frequency, we identified all γ rays for a given macropulse and tabulated the average γ -ray TOF, as shown in Fig. 3.4. The uncertainty of our macropulse start time manifests as a spread in average γ -ray times-of-flight. Were the start time exactly known for each macropulse, and the micropulse period exactly known, the TOF for each γ ray would be exactly the same (if detector time resolution is ignored). The difference between the average calculated γ -ray times-of-flight (using the imprecise macropulse start time) and the *expected* TOF (given the TOF detector distance and speed of light) can be used to improve the macropulse start time. This γ -averaging procedure was applied to all events in each macropulse (see Fig. 3.6). We also examined the stability of the T_0 period and found that its day-to-day variation had a negligible effect on the calculated times-of-flight (see Fig. 3.5).

After these corrections, the total TOF resolution, taken as the FWHM of the γ -ray peak in the TOF spectrum, ranged from 0.60-0.90 ns over the series of σ_{tot} measurements. This is comparable to the resolution from our digitizer-mediated Ca experiment from 2008 [37], which used a similar γ -averaging technique. For a 100-MeV neutron and a TOF detector distance of 27 meters, an uncertainty of 0.80 ns translates to an energy resolution of ≈ 900 keV. For neutrons below ≈ 20 MeV, the TOF time resolution worsens as the traversal time through the 1-inch thickness of the scintillator becomes non-negligible. However, because the TOF of these neutrons is already several hundred ns or longer, the relative energy resolution ($\frac{\Delta E}{E}$) is superior at low energies. To wit, for a 5 MeV neutron with a 0.82 ns detector-traversal time and an inherent TOF resolution of 0.80 ns, ΔE is only 13 keV. These energy

uncertainties have been propagated through the subsequent analysis.

Precise determination of the TOF distance was done by comparing our measured σ_{tot} data for $^{\text{nat}}\text{C}$ with the precisely known resonance structure from 3-15 MeV (Fig. 3.7). The distance was determined as 2709 ± 1 cm for the Ni and Rh run configuration and 2554 ± 1 cm for the Sn and O run configuration. With all corrections applied, all events in the TOF detector channel were filtered against events in the veto detector to remove events caused by charged-particles created along the flight path.

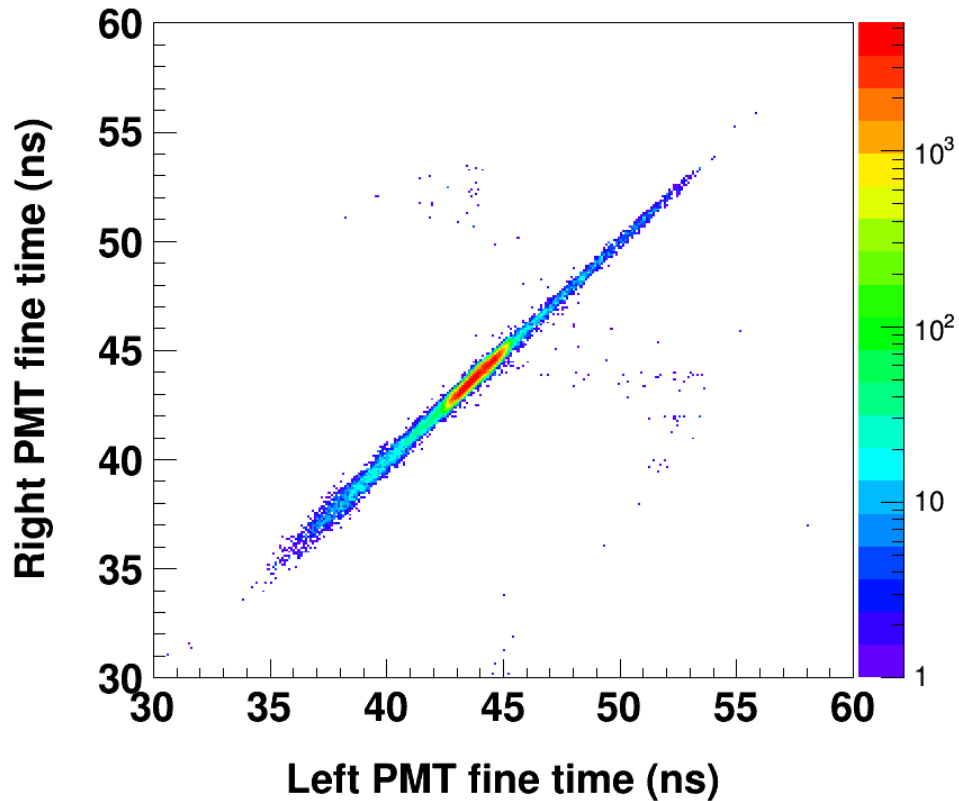


Figure 3.1: Fine times for left and right PMT events, taken separately, of the TOF detector as recovered by our software CFD algorithm. The times plotted are referenced to the start of each event waveform, which varied by several ns event-to-event. Thus the spread from 35-55 ns depends on where the digitizer initiated the waveform for each event and does not indicate timing resolution information.

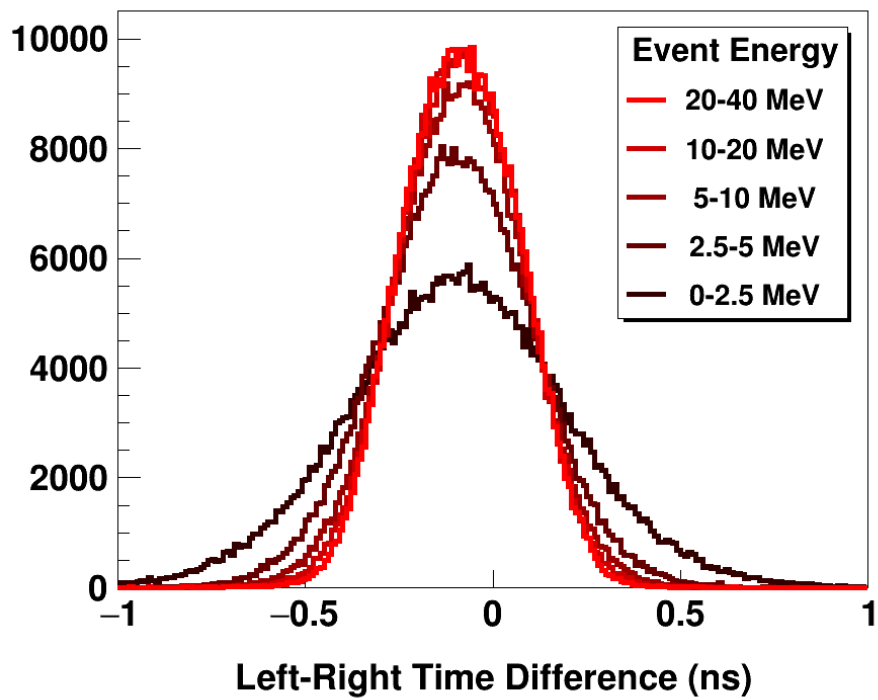


Figure 3.2: Effect of energy gating on the left/right PMT time difference. Higher-energy neutrons traverse also deposit more energy on average, slightly improving the precision of the software CFD. The same number of events were populated into each energy-range histogram.

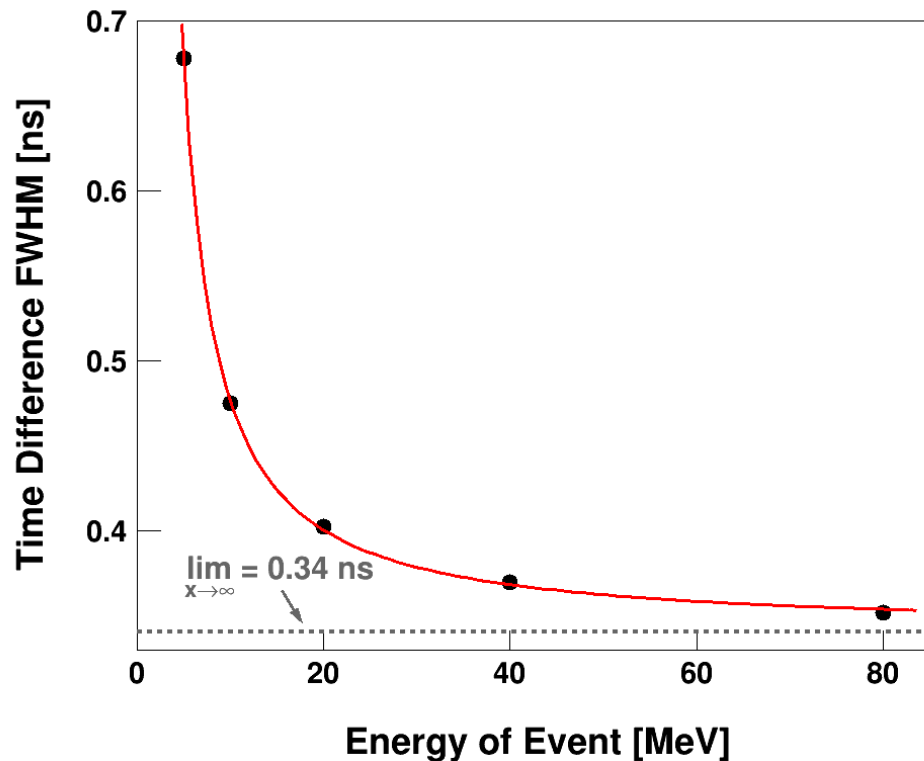


Figure 3.3: The time difference between the left and right PMTs of the TOF detector was calculated for all events in a diagnostic run. The FWHM of these time differences as a function of neutron energy are shown (black points) and fitted with a hyperbolic curve (red line). For low-energy events, the time resolution is poorer due to the lower signal amplitude. As energy increases, the FWHM time resolution asymptotically approaches 0.34 ns (grey dashed line).

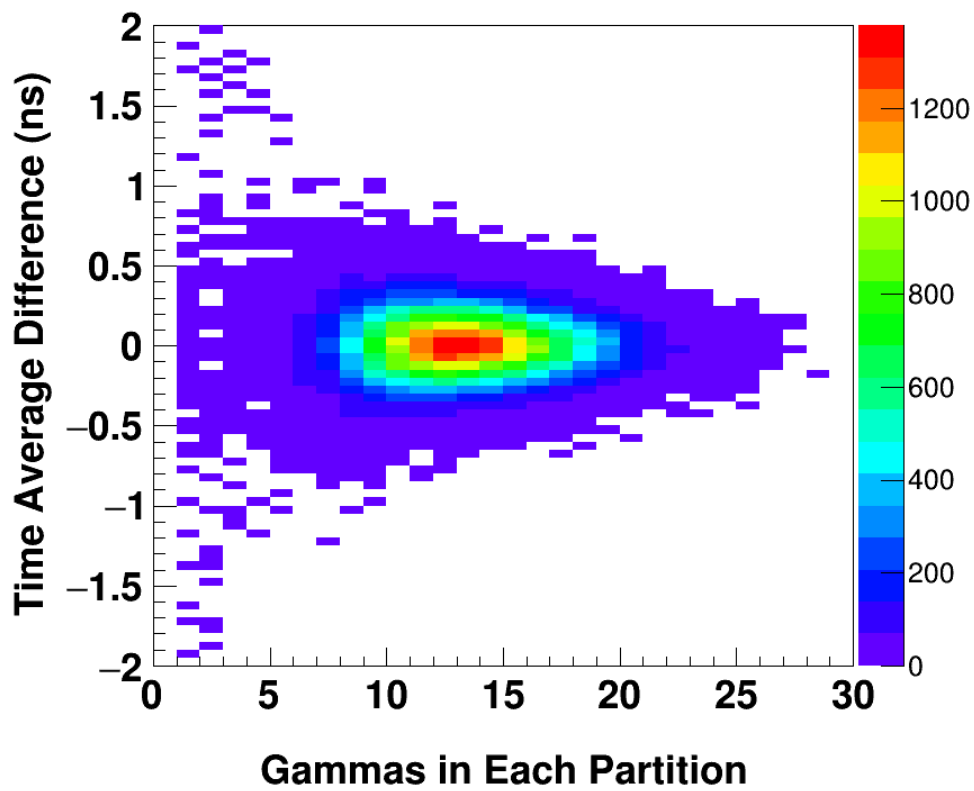


Figure 3.4: Deviation of the average γ -ray arrival time by macropulse.

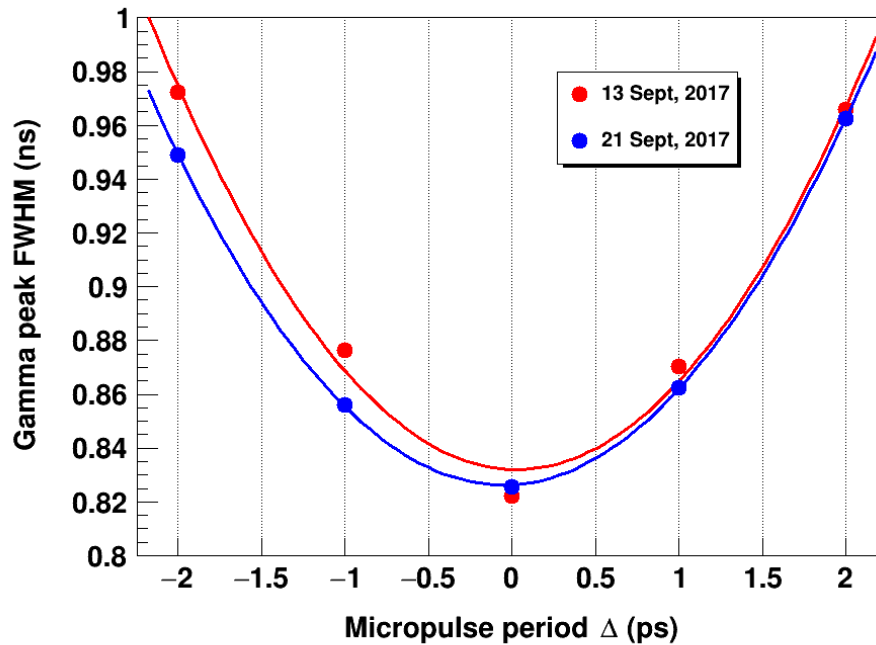


Figure 3.5: Results of a study of the micropulse frequency (T_0) stability. The T_0 period used in the analysis was varied in 1-picosecond increments to change the calculated arrival TOF of events in each micropulse. Within each micropulse, the FWHM of the time uncertainty in the γ -ray flash was tabulated. The variation of the γ -ray flash FWHM from varying the micropulse period was then fitted with a quadratic curve (solid lines). The true micropulse frequency was taken as the minimum of this curve. This procedure was repeated on data from different days throughout the experimental run, verifying that the observed drift in the micropulse frequency is small enough to have a negligible effect on the recovered times-of-flight.

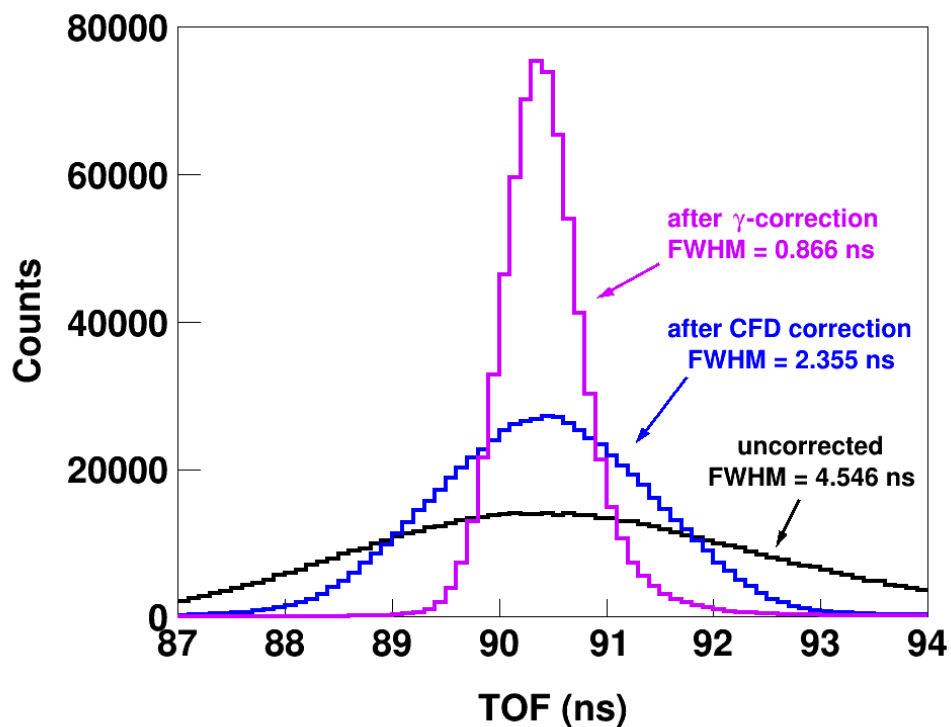


Figure 3.6: The effects of timing corrections on the γ -ray peak of a typical run are shown. The uncorrected spectrum is shown in black, the spectrum after correction with our software CFD is shown in blue, and the spectrum after correction with both our software CFD and γ -averaging is shown in pink. For this run, the final γ -ray peak FWHM after both corrections is 0.866 ns, comparable to the precision we achieved in our Ca study [37], which also employed γ -averaging.

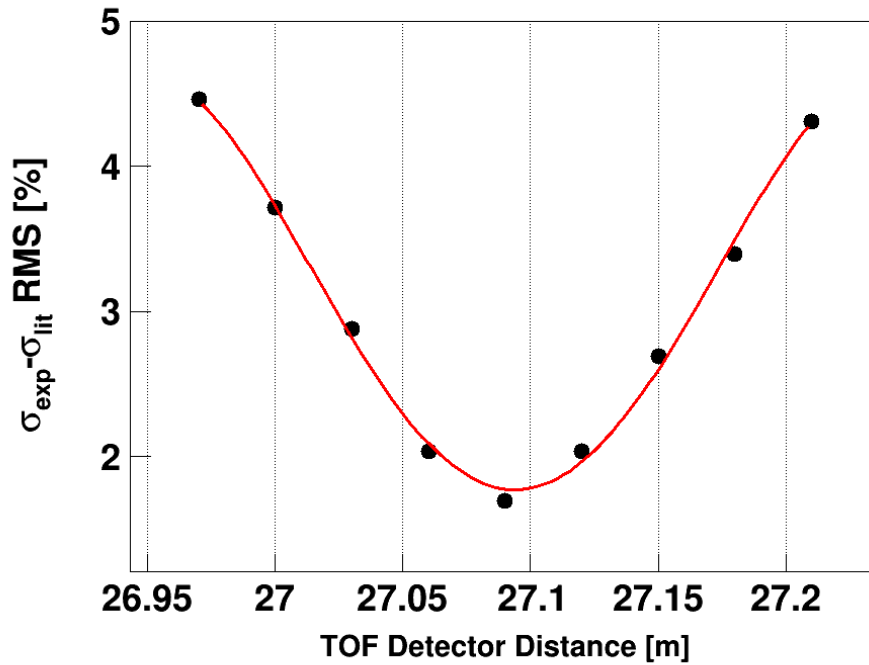


Figure 3.7: Results of a study to determine the distance between the neutron source and the TOF detector for the Ni/Rh running configuration are shown. First, a plausible range of flight path distances (26.97-27.21 m) was selected based on rough estimation during the experiment. Using each distance in this range, the σ_{tot} for natural carbon was calculated in the resonance region (3-15 MeV). The RMS difference between the cross section generated using that distance and literature data from Abfalterer [19, 20] was calculated (shown as black points in the figure). A quartic fit to these RMS data is shown (solid line). By minimizing the RMS difference, the flight path distance of 2709 ± 1 cm was determined for the Ni and Rh run configuration.

3.2 Deadtime Correction

Because events are not processed instantaneously, there is a brief period after each trigger during which the digitizer is busy processing that trigger. The busy period following each event is referred to as the “analytic” or “per-event” deadtime and can be corrected for according to standard techniques [80]. In an ideal experiment, the instantaneous flux at all times would be sufficiently low (and the amount of beam time available sufficiently high) that only very rarely would another event arrive at the TOF detector while a previous event was still being processed. In reality, given the low duty factor of the pulsed beam, the flux during each pulse must be high to achieve sufficient statistics over dozens or hundreds of energy bins within a few weeks of beam time. Given the extremely small areal density of our samples, this meant we required a rate of approximately one event per micropulse on average. Even with a flat TOF spectrum, a sizable fraction of events would arrive in the shadow of the previous event’s processing period, and thus be ignored by the pulse-processing firmware. In reality, the problem is far worse, as the instantaneous flux is much higher during the γ -ray flash and arrival of high-energy neutrons.

In [16, 20], this problem was addressed by using a “looking period” logic. Arriving T_0 signals were used to begin a “looking period” during which neutron and γ -ray events could be collected. At the time of the T_0 arrival, if the electronic modules were still busy from processing a previous event (as indicated by a “system busy” signal), the looking period was aborted. During a looking period, if a single neutron or γ -ray was detected, no subsequent events were allowed in the period. This logic is diagrammed in Fig. 3.8, reproduced from [20]. The fraction of T_0 signals that result in looking periods ($\frac{T_{0,live}}{T_0}$) is tabulated, as is the so-called “analytic deadtime”, i.e. the chance that the detector is busy for a given time

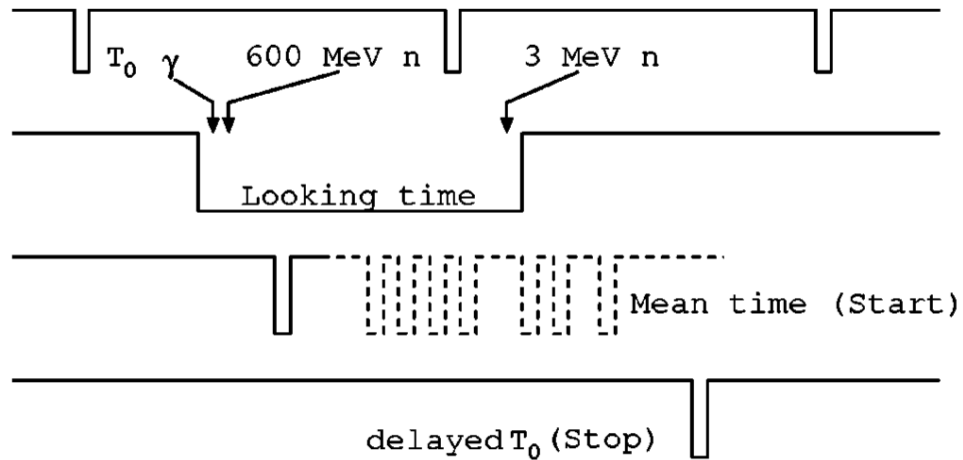


Figure 3.8: “Looking period” logic used by previous neutron σ_{tot} measurements at LANSCE [20]. Per the original caption: proton beam bursts arriving at evenly-spaced 1.8- μs time intervals define a time frame 1.4-1.6 μs long. For each time frame, a delayed copy of the T_0 defining it was used as a stop signal on the TDC clocks. In contrast, the event processing logic of our experiment dispensed with looking periods to maximize the number of neutrons detected.

within each looking period. TOF histograms are then scaled by these fractions to recover the true number of events per unit flux. This approach is useful if the analytic deadtime is commensurate with the micropulse period, as it means that only one event can be detected per micropulse anyway. For this approach to be successful, the analytic deadtime must be very precisely known, as corrections can soar to over 100% if the beam flux is high.

Due to the extremely low areal density of our samples, we could not afford to discard any neutron events and still acquire sufficient statistics. Thanks to the dramatically-reduced analytic deadtime of the digitizer algorithm, we could use a more straightforward deadtime correction logic and minimize the number of lost events. Assuming negligible variation in beam flux between micropulses (an assumption investigated below), the fraction of time $F[i]$

that the digitizer is dead for a given time bin i can be calculated:

$$F_i = \sum_{j=0}^{N-1} R_{(i-j) \bmod N} \times P_j \quad (3.1)$$

where N is the number of time bins in the micropulse, R_x is the rate of detected events per micropulse in bin x , and P_j is the probability that the digitizer is still busy from a trigger j bins ago. Moore [80] also provides a more general formula to calculate the appropriate deadtime correction in cases where the variation in beam flux is significant. However, an examination of our flux-per-micropulse data showed almost no variance in the flux per micropulse, except during the first 10% of each macropulse when flux was “ramping up”. In our final analysis, we have discarded the first 40 micropulses of each macropulse and used the simpler Eq. 3.2 to calculate the deadtime fraction.

To model P_j , we employed a logistic function and fitted it to the observed spectrum for time differences between consecutive events (see Fig. 3.9). For a given bin i , the fraction of time that the digitizer is dead, F_i , is in essence a discrete convolution of the *measured* TOF spectrum with P_j . Note that except for the first and last micropulses in a macropulse, micropulses are consecutive and thus deadtime effects can “wrap around” from the end of one micropulse to the next. For these wrap-around contributions (that is, $j > i$), the (mod N) term ensures that the bin referred to by $(i - j)$ is non-negative and has physical meaning as a time bin from the previous micropulse.

By optimizing trigger processing in digitizer firmware, we were able to reduce the per-event deadtime to between 160-230 ns, depending on the digitizer configuration. For a 230 ns per-event deadtime, the dead-probability F_i of our time bins is given in Fig. 3.10, showing that the probability-dead never exceeds 25%, much smaller than the 50-80% typical in the

DEADTIME CORRECTION

approach described above [16, 20]. Once the fraction dead was identified for each time bin, the total number of events detected in that bin, $N_d[i]$, was corrected to the *true* number of events in that bin $N_t[i]$ that would have been detected in the absence of a per-event deadtime:

$$N_t[i] = -\ln \left[1 - \frac{\frac{N_d[i]}{M}}{(1 - F_i)} \right] \times M \quad (3.2)$$

where M is the total number of micropulse periods. The difference between uncorrected and analytic-deadtime-corrected TOF spectra is shown in Fig. 3.11. At large TOFs (low energies) the correction is as low as a few percent, but at small TOFs (high energies) when the digitizer is still dead from the γ -ray flash and high-energy neutrons, the correction is significant ($\approx 20\%$ for our Ni/Rh runs, and $\approx 40\%$ for our Sn/O runs). Again, these corrections are themselves far lower than the correction required when using the previous approaches [16, 20], which could be over 100% for the lowest-energy neutrons, depending on beam flux. It is important to keep in mind that in these experiments the probability that the data acquisition electronics are busy is not a fixed number but a function of the neutron energy.

During analysis, it was noted that occasionally (1 in 400 macropulses), one or two adjacent macropulses would have an abnormally small number of flux monitor events or TOF events. The frequency of these “data dropouts” was similar to the rate of switching between DPP and waveform modes and we suspect it is related to edge case behavior right before or after a mode switch. To mitigate this issue, any macropulse that had less than 50% of the average event rate in either the flux monitor or TOF detector channel was ignored.

After applying these corrections, the veto and integrated charge gates are applied to all events and surviving events are populated into TOF spectra (see Fig. 3.12). From these spectra, room background was subtracted (responsible for 0.1% to 1% of event rate,

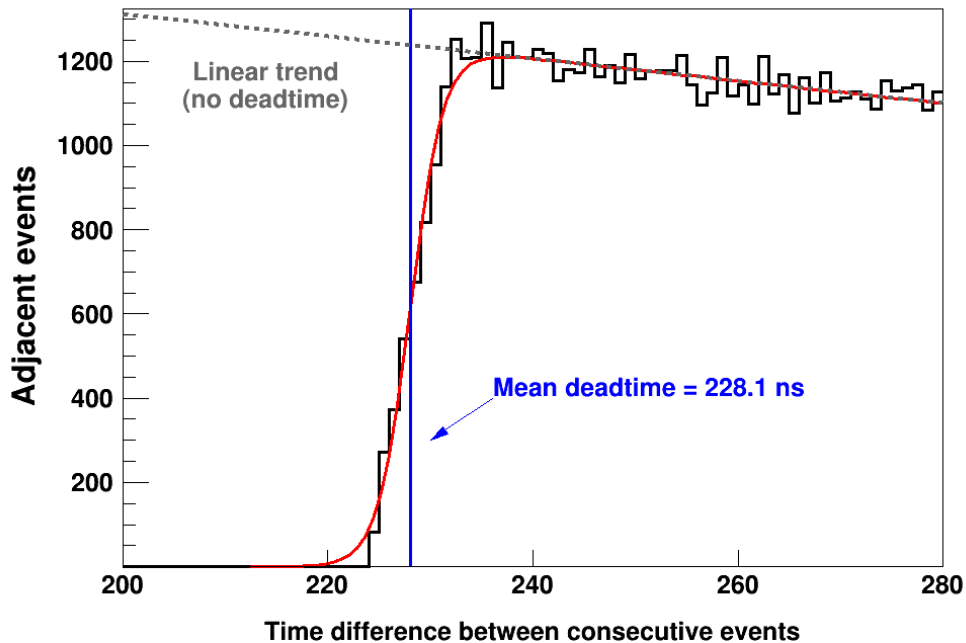


Figure 3.9: The time difference between adjacent TOF-detector events for a single run is plotted (black histogram). Below a certain minimum time difference (the “deadtime”), no events are recorded. A logistic fit (red) models the detector’s deadtime response and is used to generate a deadtime correction. The underlying linearly-decreasing count rate (gray dashed line) is incorporated into the logistic model. From the fit, a mean deadtime of 228.1 ns was extracted for the Sn and O run configuration (a similar procedure was used to recover a deadtime of 159.7 ns for the Ni and Rh run configuration).

depending on energy) and events were mapped to the energy domain.

It is worth mentioning two additional systematic differences between our configuration and those of previous LANSCE measurements [16, 20, 37], namely the flight path length and sample diameters. Flight path lengths of 37.70 meters, 38.14 meters, and 45 meters were used in [16], [20], and [37] respectively, much longer than the 25-27 meters position of our TOF detector. Had these lengths been available for our experiment, it would have reduced the high-energy instantaneous neutron flux by $\frac{1}{3}$, potentially affecting our results for the highest-energy neutrons. Future experimental work at the 90 meter flight path station at

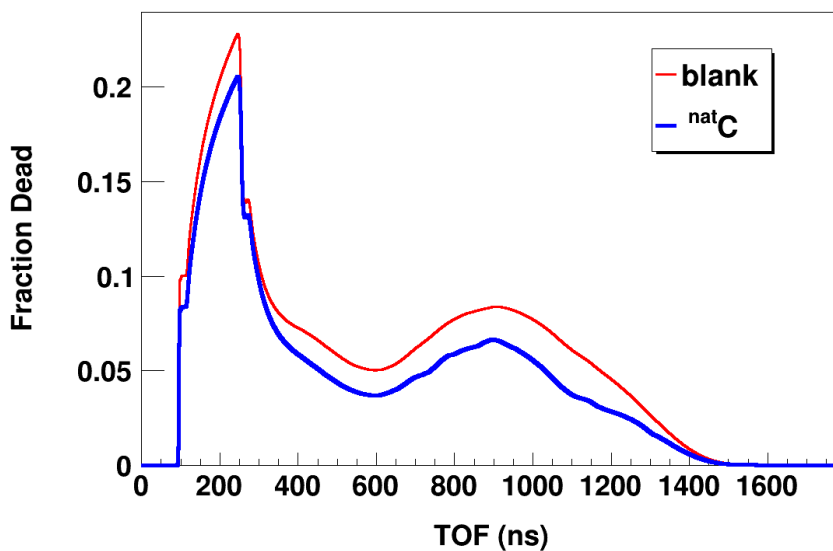


Figure 3.10: Using TOF data from a typical run, the fraction of time that a given TOF bin is “dead” is shown for the blank sample (red line) and the ^{nat}C sample (blue line). The sharp rise at 90 ns is the response to the γ -ray flash, the gradual increase from 90-245 ns is the response to the arrival of high-energy neutrons, and the sharp fall at 245 ns is the elapse of the γ -ray “shadow”. Only high-energy neutrons have a probability-dead exceeding 10%.

LANSCE would be ideal: the instantaneous neutron flux would be reduced by more than half compared to our experiment and neutrons as low as 10 MeV could still be unambiguously identified before micropulse wraparound. The other major difference, the sample diameters, affects the diameter of the collimation used. Diameters of 2.2-2.9 cm, 2.3-3.8 cm, and 1.3 cm were used for [37], [16], and [20], respectively, much larger than the 0.8 cm diameter of our samples. As sample (and thus collimator) size decreases, the cross-sectional area of the collimation pipe decreases compared to its circumference. At some point, neutrons scattering at very small angles on the interior of the collimation could become significant compared to the number of neutrons passing through the collimation freely, distorting results. While we see no evidence of this phenomenon affecting our results, a collimation-scattering simulation

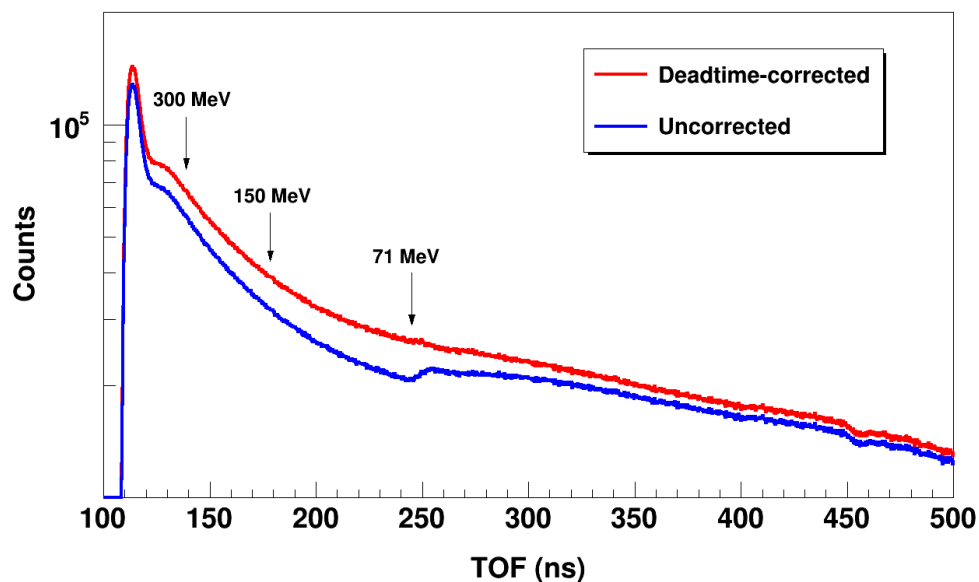


Figure 3.11: A typical TOF spectrum from the Ni/Rh run configuration is shown, before (in blue) and after (in red) analytic deadtime correction. Relevant neutron energies are indicated above the spectra. For this digitizer configuration, the mean deadtime was 155 ns (see Fig. 3.9 for details on mean deadtime determination). Note that at 245 ns, there is an obvious defect in the uncorrected spectrum that is repaired in the corrected spectrum. The defect corresponds to the elapse of the 155-ns-long deadtime “shadow” from the γ -ray flash, which arrived at 90 ns (not shown).

may be warranted for experiments with even smaller sample diameters.

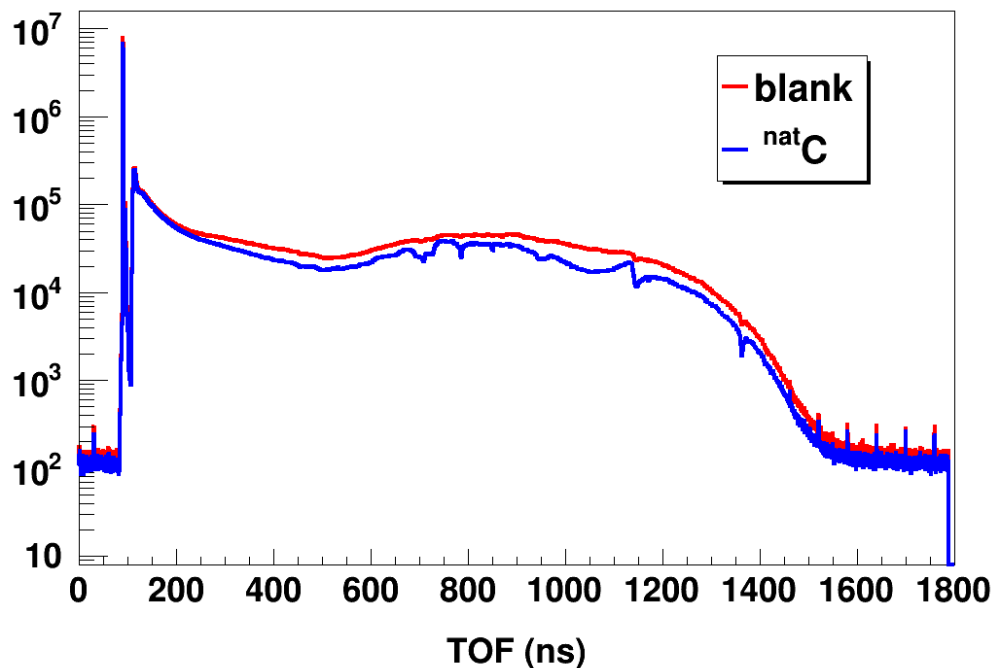


Figure 3.12: Typical TOF spectra after analytic deadtime correction and veto and integrated charge gating. A spectrum from the blank sample is shown in red and a spectrum for the $^{\text{nat}}\text{C}$ sample is shown in blue, both from the Ni/Rh experiment configuration. The γ -ray peak presents as a sharp spike at 90 ns, followed by the highest-energy neutrons at 130 ns. The small spikes spaced 60 ns apart (visible before 90 ns and after 1500 ns) are γ -ray peaks from a low-level, continuous “drip” of protons onto the tungsten target caused by mistuning of the proton buncher; their effect on the calculated cross sections is negligible. Low-energy carbon resonances are visible above 600 ns.

3.3 Cross Section Calculation

The fundamental quantity of interest, σ_{tot} , is related to the flux loss through a sample by:

$$I_t = I_0 e^{-\ell \rho \sigma_{\text{tot}}} \quad (3.3)$$

or, equivalently,

$$\sigma_{\text{tot}} = -\frac{1}{\ell \rho} \ln \left(\frac{I_t}{I_0} \right) \quad (3.4)$$

where I_0 is the neutron flux entering the sample, I_t is the neutron flux transmitted through the sample without interaction, ρ is the number density of nuclei in the sample, and ℓ is the sample length. For thin or low-density samples, flux attenuation through the sample will be small (e.g., 13% for our Ni samples at 100 MeV) and a large number of counts will be required to determine the cross section to high precision.

From these energy spectra, the raw cross sections were calculated, bin-wise, as follows:

$$\sigma_{\text{tot}} = -\frac{1}{\ell\rho} \ln \left(\frac{I_0}{I_s} \times \frac{M_s}{M_0} \right) \quad (3.5)$$

where $\frac{I_0}{I_s}$ is the ratio of counts in the energy spectra between the blank and sample, $\frac{M_s}{M_0}$ is the ratio of counts in the monitor detector between the sample and blank (for flux normalization), ℓ is the length of the sample, and ρ is the number density of atoms in the sample.

A series of small corrections were applied to the raw cross sections to produce the final results. First, because the blank sample contains air and not vacuum, the cross section of air must be added to each other sample's cross section (scaled by the ratio of areal densities of air in the blank and the sample of interest). For the ^{103}Rh sample, which had the smallest areal density, this correction was approximately 2 mb at energies above 100 MeV. The cross section for ^{64}Ni was corrected for the isotopic enrichment of our sample (92.2%) using our measured $^{\text{nat}}\text{Ni}$ cross section. All other isotopes were sufficiently pure such that the isotopic impurities contributed <0.1% to the final cross section.

Oxygen cross sections were calculated by subtracting the well-known hydrogen cross section from the raw H_2O result (we used H σ_{tot} data sets from Clement et al. [81] and Abfaltrer et al. [20], which together cover the range $0.5 \leq E_n \leq 500$ MeV and are in excellent agreement where their energy ranges overlap). In light of the additional uncertainty

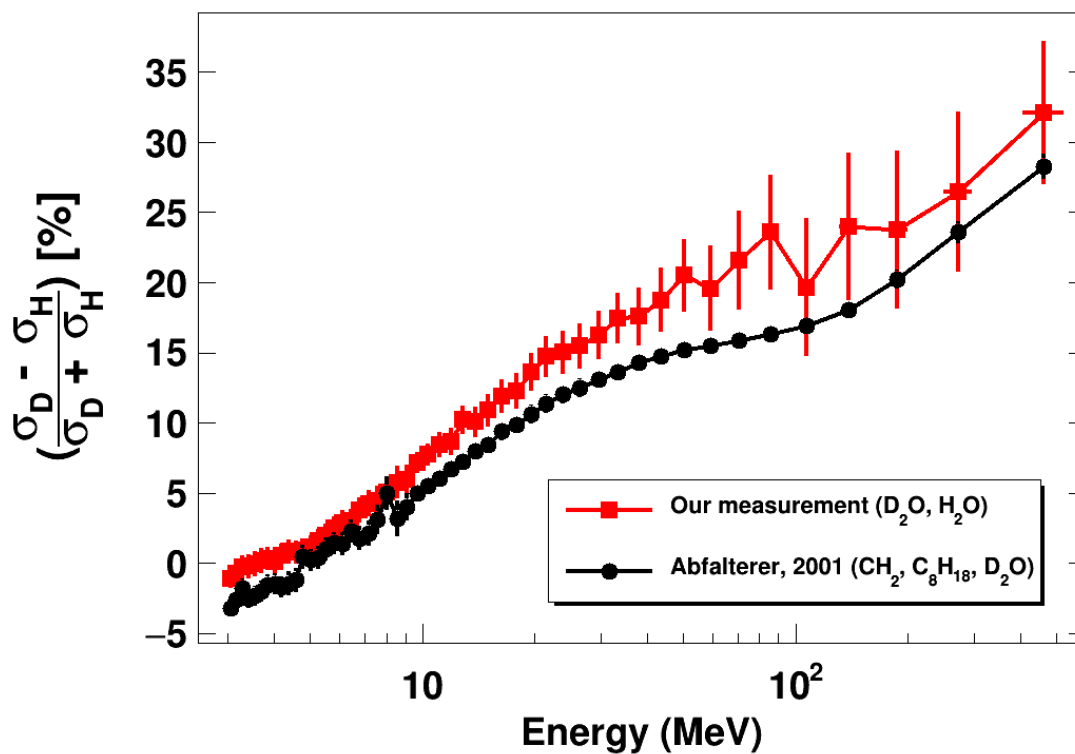


Figure 3.13: The σ_{tot} relative difference between deuterium and hydrogen, as calculated by subtraction of our O σ_{tot} results from D₂O and H₂O. Data from our measurement are shown as red squares; the data of Abfalterer et al. [82] are shown as black circles.

inherent to this kind of subtractive σ_{tot} determination, a D₂^{nat}O sample from which the literature σ_{tot} for D₂ could be subtracted was prepared as an additional cross-check. The results of the deuterium-to-hydrogen relative difference are shown in Fig. 3.13.

3.4 Results

3.4.1 Benchmarking σ_{tot} Results with Natural Samples

To validate our analysis, we first compared our σ_{tot} measurements on $^{\text{nat}}\text{C}$, $^{\text{nat}}\text{Ni}$, $^{\text{nat}}\text{Sn}$, $^{\text{nat}}\text{Pb}$ against the high-precision data sets on natural samples from Finlay et al. [16] and Abfalterer et al. [20], shown in Fig. 3.14. From 3-100 MeV, our measurements are in excellent agreement, within statistical error, with these previous data sets. Above 100 MeV, our results on natural samples diverge from the previous measurements up to a relative difference of 5% at 300 MeV for all samples, suggesting a small systematic effect at high energies when the instantaneous neutron flux is highest. To investigate this discrepancy, we analyzed data from multiple digitizer thresholds during data production, applied various software thresholds, gated events by low- and high-integrated charge, and varied our software CFD logic, among other diagnostic tests. Throughout these exercises, the agreement at <100 MeV and the discrepancy >100 MeV persisted. To ensure the shift was not related to imprecision in the areal density of the targets, we compared both our short and long natural carbon targets against each other (see Fig. 3.15) and found excellent agreement: the relative difference was within 1% throughout our energy domain, comparable to a similar test conducted by Abfalterer et al. [20]. From Eq. 3.5, it is clear that changes in flux ratio and sample areal density can shift the calculated cross section up or down across the entire energy range measured, but cannot change the *slope* of the cross section as energy is increased. Thus, the high-energy discrepancy is unlikely to be from an incorrect monitor flux. Further, it was not dependent on the nuclear mass of the sample nor with any other physical characteristics of the samples, suggesting that backshine of neutrons into the flux

RESULTS

monitor from the samples, or another physical mechanism, was not the cause.

Interestingly, we did not see any energy-dependent discrepancy in the ^{16}O results (see Fig. 3.16). Both our measurement and previous measurements on O isotopes used compound samples (H_2O , D_2O , BeO , ZnO), so it is possible that the subtraction of the positive-ion species (D and H for us, Be and Zn for [16]) eliminated the energy-dependent systematic difference in our measurements.

At neutron times-of-flight corresponding to energies >100 MeV, the number of counts in the spectrum rises sharply as one moves to higher energies. In this region, even a sub-nanosecond timing difference between the spectrum for the blank and for the sample of interest is amplified into a large error in the cross section calculation. Thus the event timing and data storage routines must be kept completely ignorant of which target is currently in-beam so as to avoid sample-dependent timing effects. In practice, this is difficult, as acquisition with the blank sample is naturally associated with a higher data rate as fewer neutrons are absorbed or scattered in-flight than when samples are in the beam path. By reducing the rate of data acquisition by an order of magnitude or more, the analog-electronics approach reduces the absolute data rates of both the blank and the samples, mitigating this effect. However, because much larger samples are required with the overall reduced data rate, the relative data rate between the blank and samples is increased, amplifying any effect on the electronics. Without a study of digital and analog systems running simultaneously with input from the same detectors, it is not clear which approach suffers more from this effect. Such a follow-up, especially with multiple digitizers from differing manufacturers, would help resolve the high-energy discrepancy we see between all of our σ_{tot} data sets and literature data.

Our absolute σ_{tot} results for all isotopic targets are shown in Figs. 3.16, 3.18, 3.20, and

3.21. All previous isotopic σ_{tot} measurements (where they exist) are shown alongside our results for comparison, and residuals between our data and literature data are provided in the lower panels. To make comparison meaningful, the literature data sets shown have been modified to have the same bins as our data via a simple linear interpolation of the original data bins. This rebinning washes out the fine structure of the cross section data where the density of states for a given sample is low and individual resonances are visible (e.g., $^{\text{nat}}\text{C}$ below 10 MeV). In all figures, error bars are indicated on data points or are smaller than the size of the markers used.

Relative differences of our measured σ_{tot} between $^{16,18}\text{O}$, $^{58,64}\text{Ni}$, and $^{112,124}\text{Sn}$ are shown in Figs. 3.17, 3.19, and 3.22, respectively. By examining relative differences between isotopes, any systematic errors of our approach (besides the areal density uncertainties) are divided out.

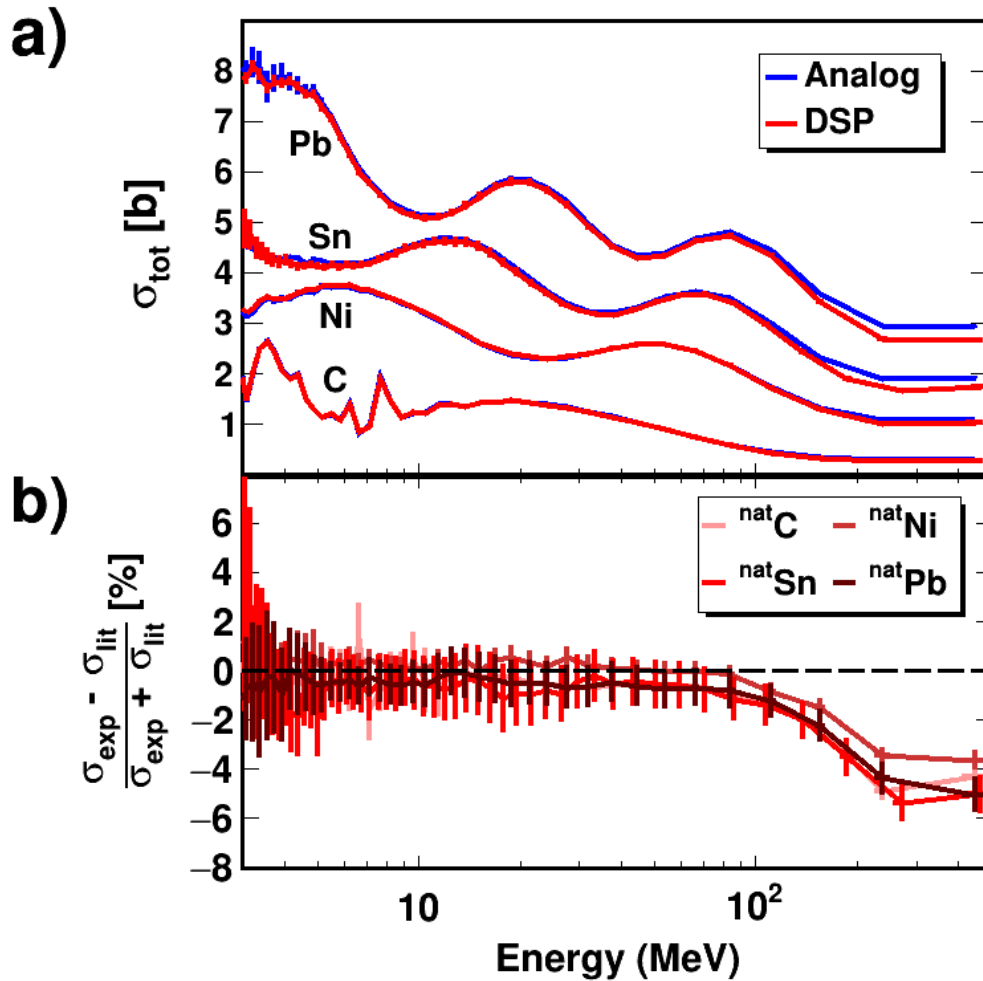


Figure 3.14: A comparison of literature data (taken with analog techniques) and our results (signals processed with a digitizer, or “DSP”) for natural C, Ni, Sn, and Pb. In panel (a), the absolute cross sections are shown from 3-500 MeV; in panel (b), the relative differences between the literature data and our data are shown in percent. From 3-100 MeV, our data are fully consistent with the literature datasets but above 100 MeV, a relative difference arises, peaking at $\approx 5\%$ at 300 MeV.

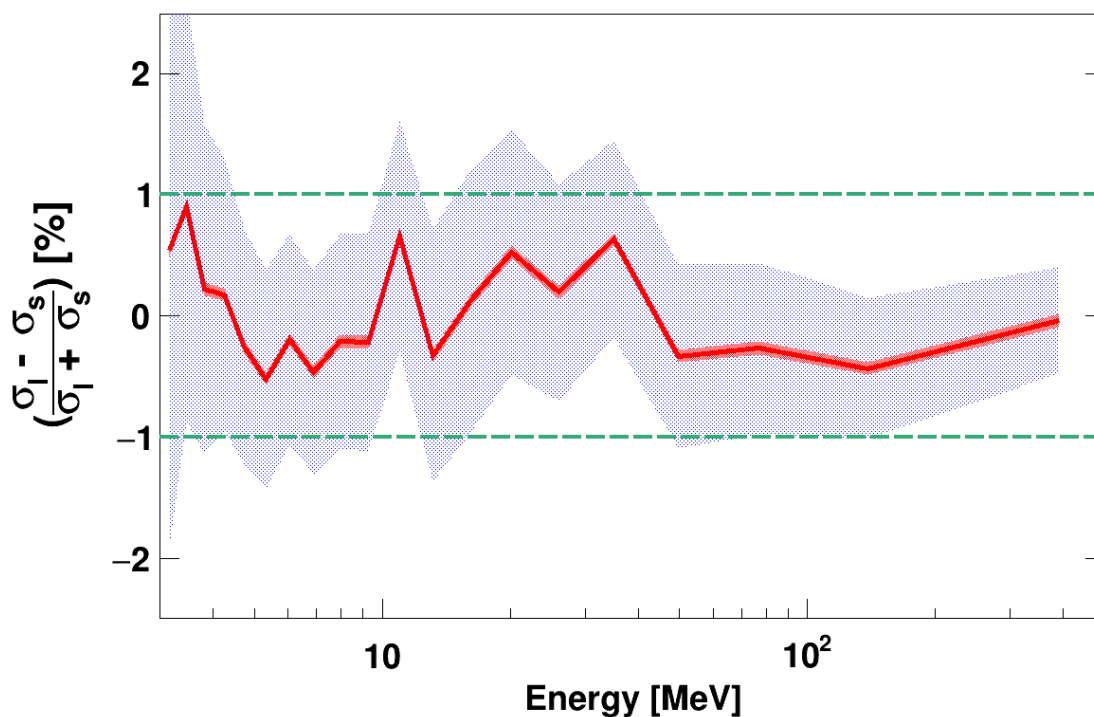


Figure 3.15: Relative difference of cross sections (red line) of our two lengths of ^{nat}C, (27.3 mm and 13.7 mm), shown from 3-400 MeV. Total error (including statistical and systematic) is indicated by the blue shaded region. Systematic error only (due to uncertainty in the areal density) is shown by the red shaded region (very small and immediately adjacent to the red line). Clearly, statistical error dominates for this relative difference. Despite the low statistics of this diagnostic run (only 1.5 hours beam-on-target for each sample), the high efficiency of the digitizer-enabled approach means that the relative difference can be resolved to $\pm 1\%$ for most of the energy range.

3.4.2 $^{16,18}\text{O}$ σ_{tot} Results

Above 5 MeV, our ^{16}O σ_{tot} results are within 5% of those from [16], where ZnO and BeO were used rather than H₂O. Below 5 MeV, the rapidly-rising (n,p) cross section and resonance structure of Zn, Be, and ^{16}O contribute to increased relative differences. Our measurement on ^{18}O extends the known neutron σ_{tot} by over an order of magnitude and shows reasonable agreement to the previous measurements taken over 50 years ago by [66, 67]. Above 200 MeV, the ^{18}O σ_{tot} is smaller than the ^{16}O σ_{tot} , a consequence of the larger neutron elastic phase shift in ^{18}O compared to ^{16}O , which pushes the σ_{tot} minimum to higher energies in ^{18}O .

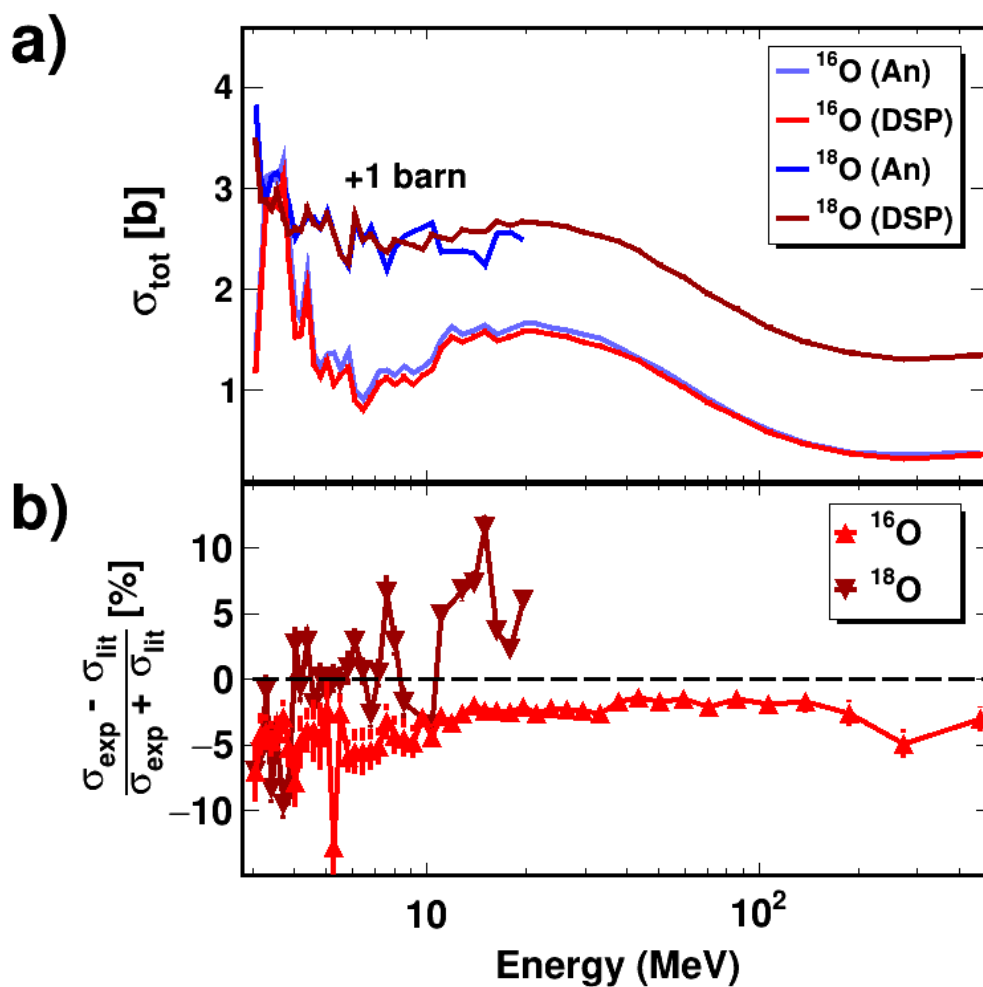


Figure 3.16: Neutron σ_{tot} for $^{16,18}\text{O}$: our results and literature data. (a) shows our digitizer-measured isotopic results (in shades of red) and corresponding analog-measured literature data [16, 65, 66, 67] (in shades of blue). The data for ^{18}O have been shifted up by 1 barn for visibility. (b) shows the relative difference between our data and literature data that are shown in panel (a).

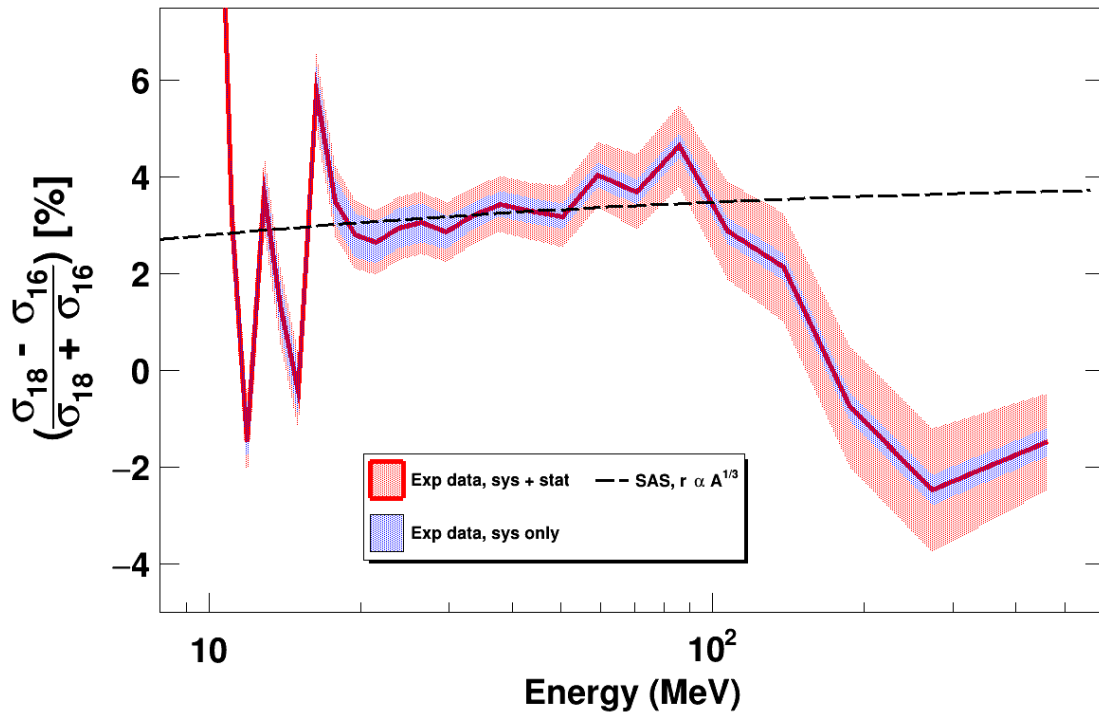


Figure 3.17: $^{16,18}\text{O}$ neutron σ_{tot} relative difference, from our newly-measured data sets (in red). Assuming a simple $A^{\frac{1}{3}}$ size scaling for the nuclear radius of ^{18}O from ^{16}O , the strongly-absorbing-sphere model Eq. 1.4 prediction for the $^{16,18}\text{O}$ neutron σ_{tot} relative difference is shown (black dashed line). From 10-100 MeV, the SAS model is surprisingly successful at reproducing the relative difference, though it fails above 100 MeV as the ^{18}O neutron σ_{tot} drops below that of ^{16}O .

3.4.3 $^{58,64}\text{Ni}$ σ_{tot} Results

In contrast to the case of O, no isotopic Ni data were available at all above 100 MeV and high-precision literature data were only available up to 15 MeV for ^{58}Ni [70] and at only one point, 14.2 MeV, for ^{64}Ni [71]. Our results extended the energy range to 400 MeV and are in good agreement with the previous results when their errors are included.

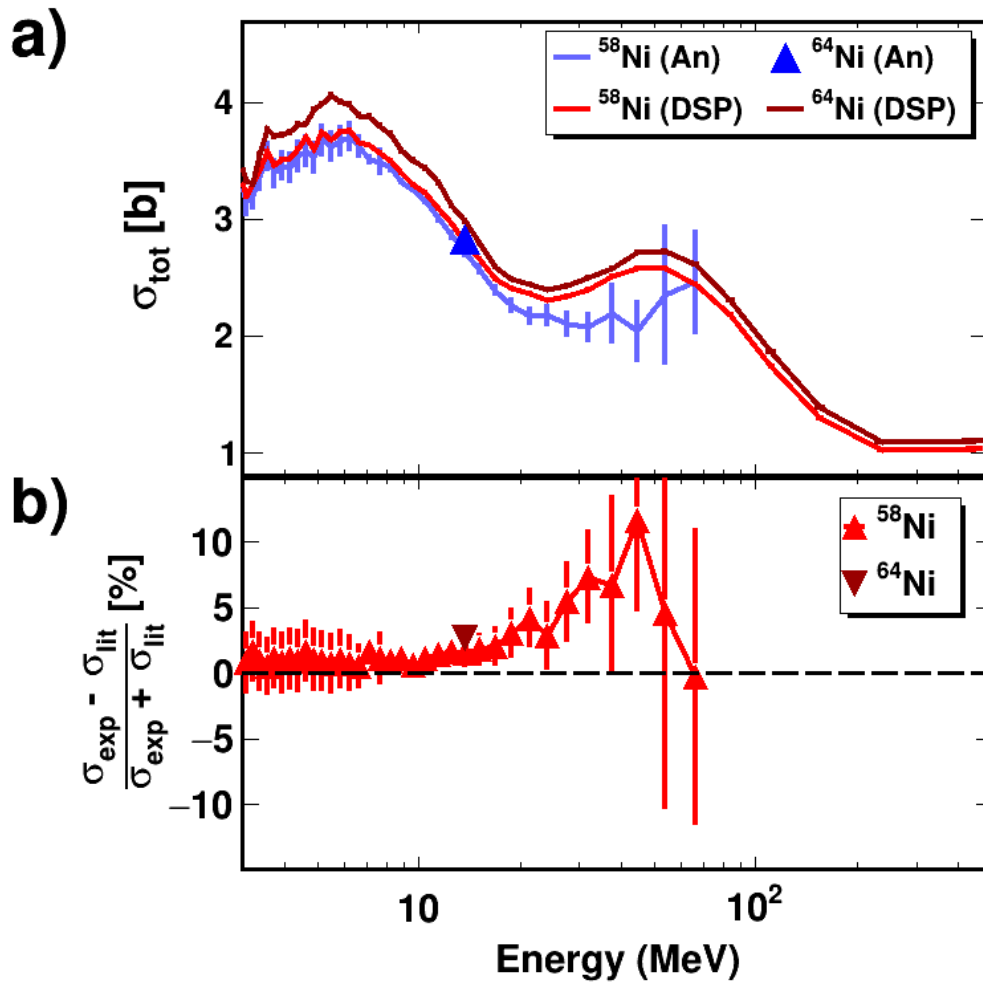


Figure 3.18: Neutron σ_{tot} for $^{58,64}\text{Ni}$: our results and literature data. (a) shows our digitizer-measured isotopic results (in shades of red) and corresponding analog-measured literature data [70, 71] (in shades of blue). (b) shows the relative difference between our data and literature data that are shown in panel a).

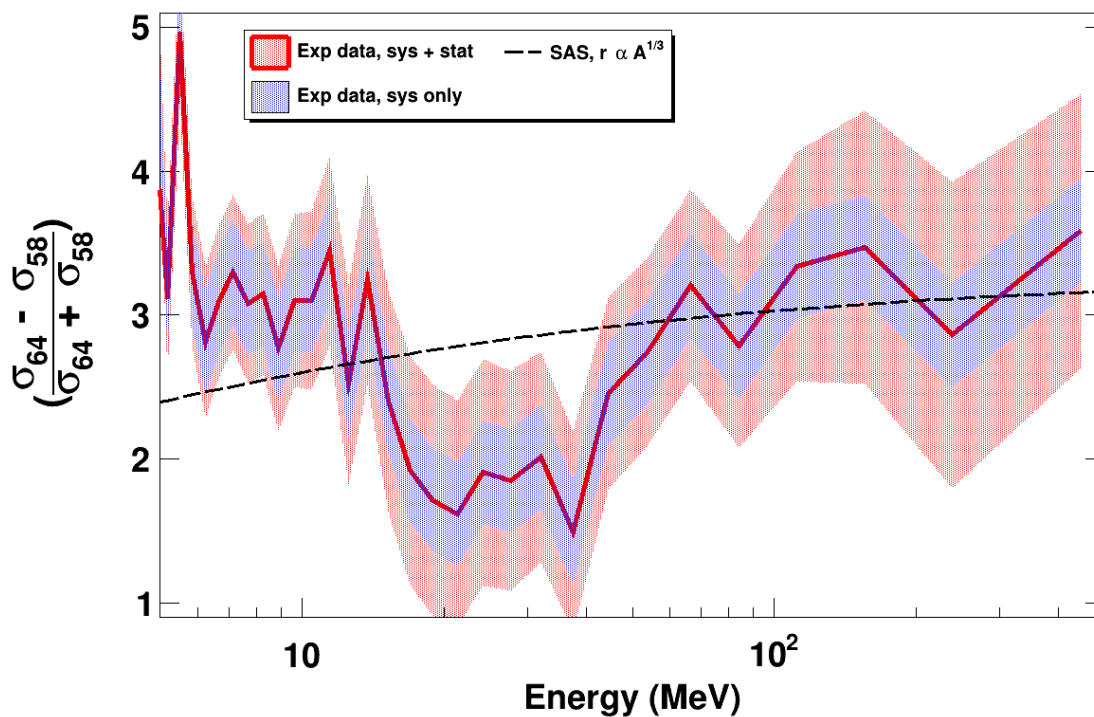


Figure 3.19: $^{58,64}\text{Ni}$ neutron σ_{tot} relative difference, from our newly-measured data sets (in red). Total error (including statistical and systematic) is indicated by the red shaded region. Systematic error only (due to uncertainty in the sample areal density) is shown by the blue shaded region. Assuming a simple $A^{\frac{1}{3}}$ size scaling for the nuclear radius of ^{64}Ni from ^{58}Ni , the simple strongly-absorbing-sphere model Eq. 1.4 prediction for the $^{58,64}\text{Ni}$ neutron σ_{tot} relative difference is shown (black dashed line).

3.4.4 ^{103}Rh σ_{tot} Results

The extremely small areal density and the reduced beam time allotted for our ^{103}Rh sample made it difficult to acquire sufficient statistics. Nevertheless, by reducing the energy range and number of bins slightly, we were able to achieve 1% statistics for all bins and our results agree with those of [18] up to 20 MeV. Our results extend the known energy range by over an order of magnitude up to 400 MeV.

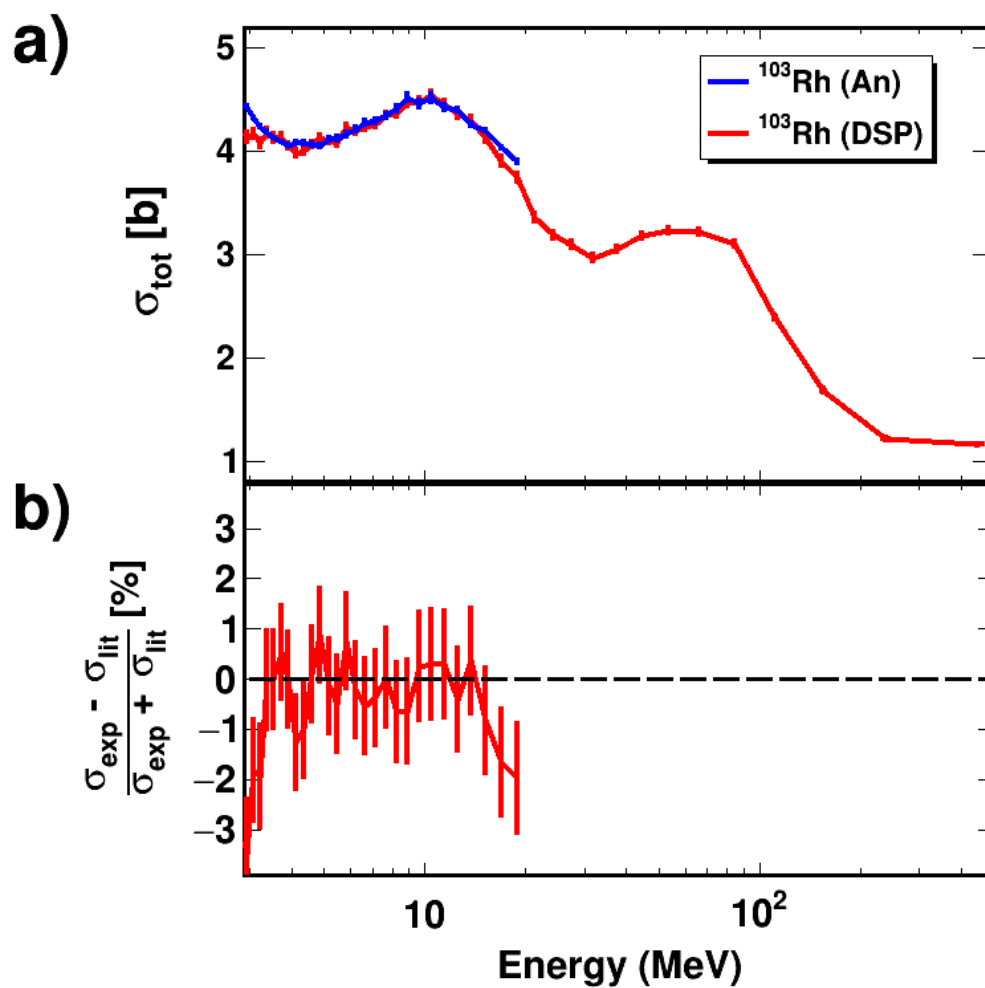


Figure 3.20: Neutron σ_{tot} for ^{103}Rh : our results and literature data. (a) shows our digitizer-measured isotopic results (in red) and corresponding analog-measured literature data [18] (in blue). (b) shows the relative difference between our data and literature data that are shown in panel (a).

3.4.5 $^{112,124}\text{Sn}$ σ_{tot} Results

Similar to Ni isotopes, the only existing Sn isotope neutron σ_{tot} data were below 25 MeV for both ^{112}Sn and ^{124}Sn [73, 72, 74, 71]. Our results extended the energy range to 400 MeV and are in excellent agreement, $\approx 1\%$ difference, with the previous results.

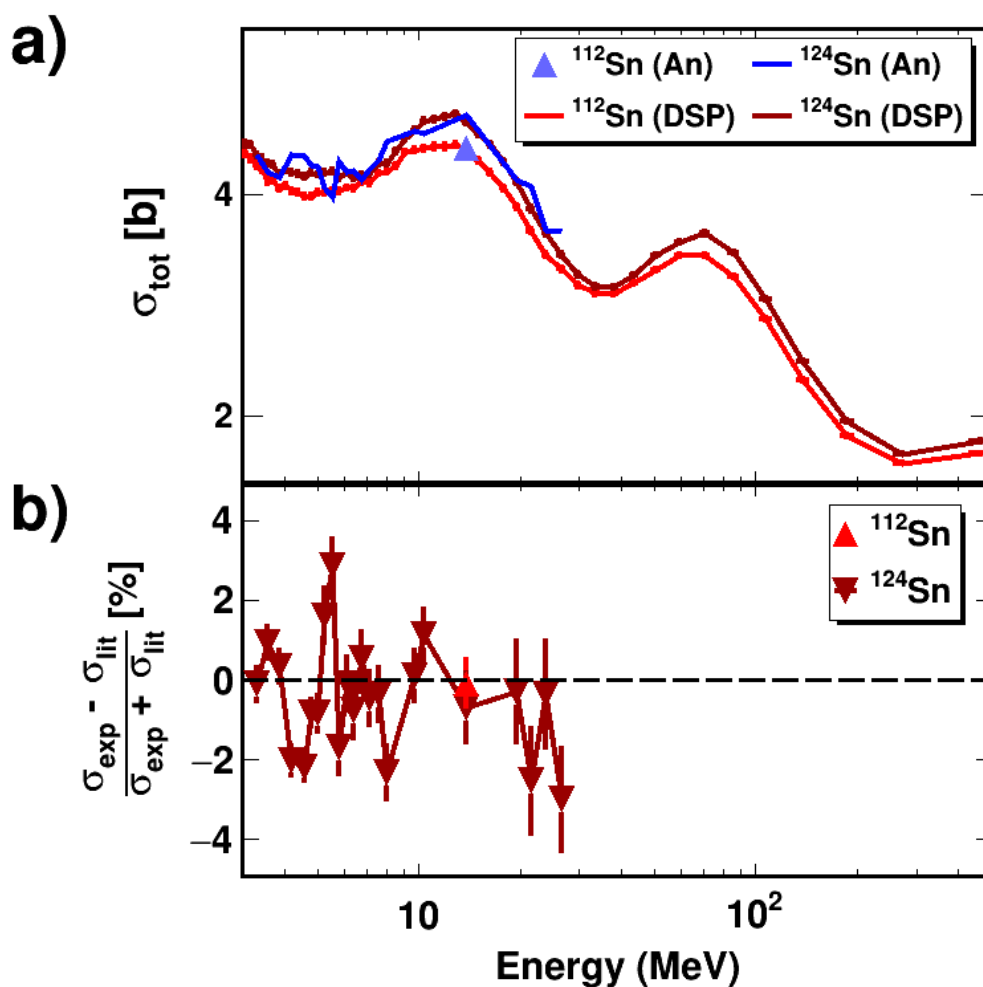


Figure 3.21: Neutron σ_{tot} for $^{112,124}\text{Sn}$: our results and literature data. (a) shows our digitizer-measured isotopic results (in red) and corresponding analog-measured literature data [73, 72, 74, 71] (in shades of blue). (b) shows the relative difference between our data and literature data that are shown in panel (a). The data sets are in excellent agreement where literature data exist, up to 20 MeV.

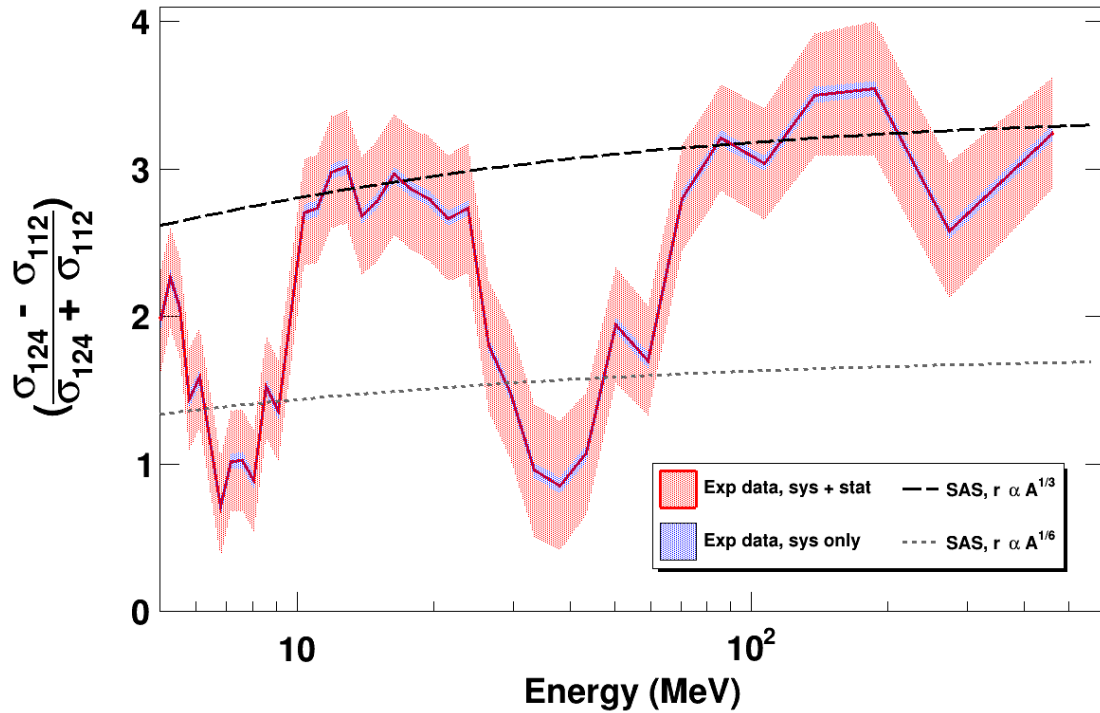


Figure 3.22: $^{112,124}\text{Sn}$ neutron σ_{tot} relative difference, from our newly-measured data sets (in red). Total error (including statistical and systematic) is indicated by the red shaded region. Systematic error only (due to uncertainty in the sample areal density) is shown by the blue shaded region. The predictions of the simple strongly-absorbing-sphere model of Eq. 1.4 for the $^{112,124}\text{Sn}$ neutron σ_{tot} relative difference are shown for two nuclear radius size scalings: $r \propto A^{1/3}$ (black dashed line) and $r \propto A^{1/6}$ (cf. the observed $A^{1/6}$ scaling of the Sn isotope shift in Fig. 1.7).

NEUTRON ELASTIC DIFFERENTIAL CROSS SECTIONS: EXPERIMENTAL SETUP

4.1 Overview of Neutron $\frac{d\sigma}{d\Omega}$ Experiments

In neutron elastic scattering measurements, the same time-of-flight techniques are used: given a “starting gun” when neutrons are produced and the neutron arrival time at a time-of-flight detector, the neutron energy can be calculated. However, in contrast to total cross section measurements, neutron elastic scattering measurements require a monoenergetic neutron beam so that elastically-scattered neutrons can be isolated. Unlike transmission measurements (e.g., total cross sections), which measure the neutron scattering integrated over all solid angles, neutron $\frac{d\sigma}{d\Omega}$ cross sections are measured differentially with respect to solid angle. To measure the angular dependence, one or more time-of-flight detectors are moved around the scattering sample on a large goniometer. As the differential cross section drops precipitously at large scattering angles, more beam time must be spent at large angles to generate sufficient statistics.

In transmission measurements, the time-of-flight detector is typically placed very far from the scattering sample so that it subtends an extremely small solid angle and thus only unscattered particles are detected. For example, in the neutron σ_{tot} experimental setup

described in Chapter 2, the scintillator of the time-of-flight detector subtended 4.5×10^{-6} steradians from the point of view of the samples. Thus, the contribution to background from isotropic γ -ray production in the samples is negligible. In differential measurements, background from γ -ray production in the samples may exceed the signal from elastically-scattered neutrons, especially at backward angles where the elastic cross section is lowest. Pulse-shape discrimination (PSD) techniques must be used to filter out γ rays, leaving only events from elastically-scattered neutrons.

4.1.1 Pulse-Shape Discrimination (PSD)

To identify neutron- and γ -ray-induced detector events, pulse-shape discrimination relies on the different energy-deposition modes of neutrons and γ rays. The scintillator used should exhibit both prompt fluorescence with a lifetime of a few ns (from a singlet state) and delayed phosphorescence with much longer lifetime in the μ s range or longer (from a triplet state). Figure 4.1 shows the relevant level structure for molecules of such a scintillator. During a scattering experiment, incident neutrons deposit energy by collision with scintillator nuclei. These recoiling nuclei (mostly protons) decelerate rapidly in the scintillating medium via Coulombic interactions with all electrons in the vicinity, exciting many scintillator molecules in the ion track. In contrast, incident γ rays interact primarily with single atomic electrons, which, during their recoil, produce a lower excitation energy density. For the same total energy deposition, neutron-initiated events produce a higher concentration of excited scintillator molecules than do γ -ray-initiated events.

In each population of excited scintillator molecules, most molecules are in a singlet excited state, and they decay promptly by fluorescence back to the ground state. A small fraction remain in a triplet excited state, either due to their initial excitation to a triplet state

or because of intersystem crossing from a singlet state. Kept isolated, these triplet-state molecules have lifetimes that are orders of magnitude longer (μs to ms) than the those in a singlet state because of the required spin flip to return to the singlet ground-state. If, however, two nearby triplet-state molecules collide and exchange a unit of spin, they can convert to two singlet-state molecules, one in the ground-state manifold and one in an excited-state manifold. The excited singlet-state molecule will decay promptly (ns), freed of quantum-mechanical forbiddeness. Thus, after the initial prompt fluorescence, delayed light output will appear tens of ns later from these triplet-triplet fusion events. The amount of light will be dependent on the rate of triplet-triplet collision, a second-order kinetics process associated with the diffusion of excited scintillator molecules in the medium. For neutron-initiated events, where the concentration of excited molecules is higher, the delayed light output is correspondingly higher than for γ -ray-initiated events. By comparing the tail of the light output signal to the prompt fluorescence peak, neutrons and γ -rays can be distinguished. Typically, the differences in light output are quantified by comparing the integrated charge of the prompt fluorescence peak with the integrated charge of a section of the delayed fluorescence. Machine learning techniques have also been applied to light output data to further improve discrimination [83] beyond the simple charge-gate-ratio method. Recently, pulse-shape discrimination has been shown to be possible in certain solid organic crystals (e.g., para-terphenyl, which is also used in laser dyes).

In our $^{112,124}\text{Sn}$ neutron $\frac{d\sigma}{d\Omega}$ cross section measurements presented below, we used both PSD information and the pulse height of each event to differentiate neutrons from γ -rays (see Figure 5.1 in Chapter 5). Our approach follows similar neutron $\frac{d\sigma}{d\Omega}$ measurements conducted at the Triangle University Nuclear Laboratory (TUNL) over the last three decades, including a measurement on ^{120}Sn at 17 MeV conducted by Guss et al. [85, 86] to which we later

OVERVIEW OF NEUTRON $\frac{d\sigma}{d\Omega}$ EXPERIMENTS

compare our results on $^{112,124}\text{Sn}$.

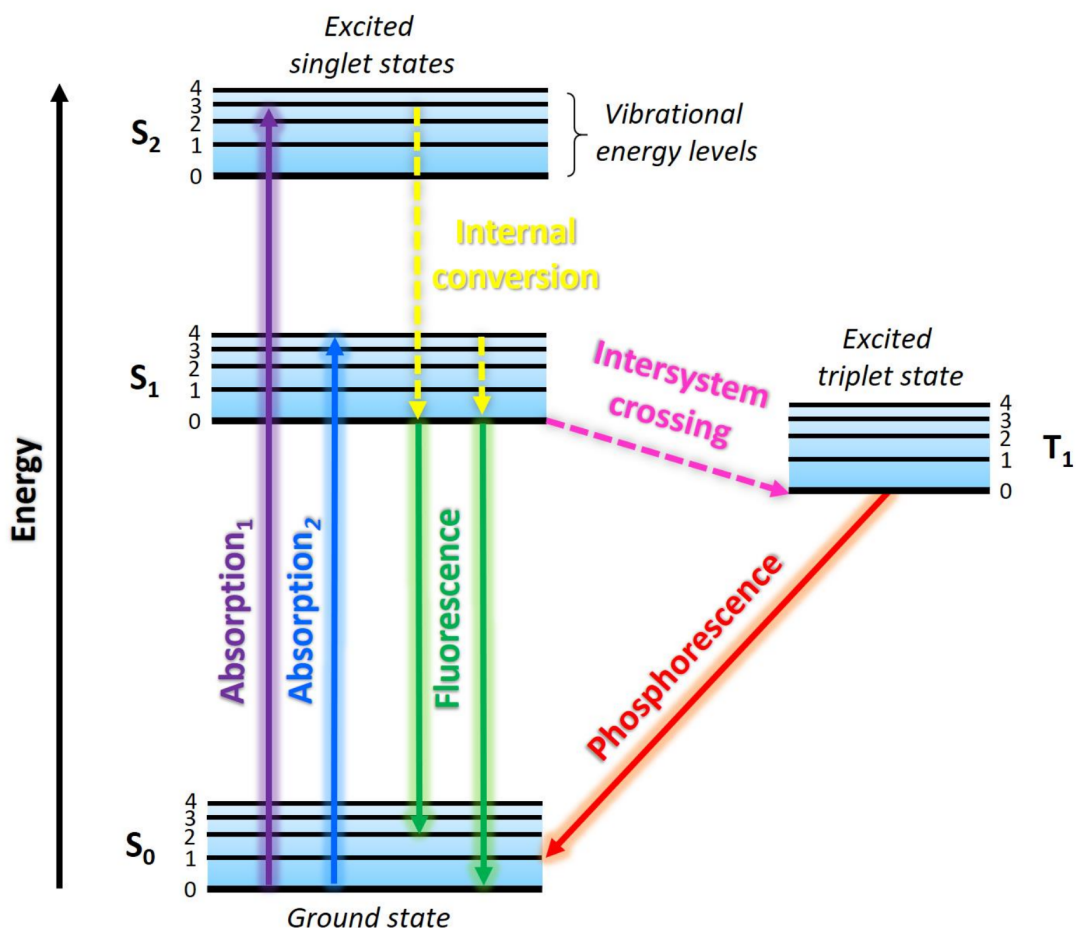


Figure 4.1: Example Jablonski diagram for an organic scintillator used for pulse-shape discrimination. After initial excitation to a higher electronic manifold, energy is shed non-radiatively by internal conversion on the picosecond timescale. If the first vibrational state of the S_1 manifold is reached, rapid decay to the S_0 manifold occurs on the ns timescale. Alternatively, the system may undergo intersystem crossing to the T_1 manifold, where it reaches the lowest vibrational state. The T_1 - S_0 transition is quantum-mechanically forbidden, dramatically increasing the lifetime of the T_1 state and leading to delayed light output from triplet-triplet fusion, as detailed in the text. Figure used with permission from J. Kang [84].

4.2 Sample Preparation

The same $^{112,\text{nat},124}\text{Sn}$ samples used in the neutron σ_{tot} experiment (see Chapter 2) were used for our neutron $\frac{d\sigma}{d\Omega}$ measurements without modification. Two additional samples, one of graphite and one polyethylene, were provided by the TUNL facility in order to normalize our $\frac{d\sigma}{d\Omega}$ results using the extremely-well-known (n,p) elastic cross section. The details of this normalization are given in Chapter 5. The physical characteristics of all the samples are given in Table 4.1.

Isotope	Len. [mm]	Diam. [mm]	Mass [g]	NA [%]	SP [%]
$^{\text{nat}}\text{C}$	23.58	9.39	2.924	-	-
$(\text{CH}_2)_n$	22.70	14.18	3.389	-	-
^{112}Sn	13.65(3)	8.245(5)	4.9720	0.97	99.9
$^{\text{nat}}\text{Sn}$	13.68(3)	8.245(5)	5.3263	-	-
^{124}Sn	13.73(3)	8.245(5)	5.5492	5.79	99.9

Table 4.1: Physical characteristics of samples used for the neutron $\frac{d\sigma}{d\Omega}$ measurements. For isotopically-enriched samples, the natural abundance of the enriched isotope and the isotopic fraction of the sample are given. Columns five and six give the natural abundance of the isotope in question (NA) and the isotopic purity of our samples (SP).

4.3 Experimental Facility at TUNL

We conducted our neutron $\frac{d\sigma}{d\Omega}$ measurements at the neutron TOF beamline at TUNL (diagrammed in Fig. 4.2) in 2017 and 2018. Incident deuterons, supplied by the facility’s variable-energy tandem Van de Graaff accelerator, impinged on a deuterium gas cell to produce a forward-focused neutron beam via the $\text{d}(\text{d},\text{n})^3\text{He}$ reaction. This exothermic reaction has a Q-value of 3.269 MeV. Two measurements, one for 11 MeV neutrons and one for

17 MeV neutrons, were conducted. The gas cell pressure varied between 35-40 psi during our measurement. Per [86], we estimate a neutron beam energy spread at the sample position of 350 keV, mostly from deuterium beam straggling in the gas cell prior to reacting. The deuterium gas cell was backed with a fresh tantalum beam stop to prevent unreacted deuterons from reaching the samples. Based on the number of counts collected during the normalization runs described below, we estimated that the average neutron flux incident on the sample was $\approx 5 \times 10^6$ neutrons per second for the 11 MeV run in 2017 and $\approx 1 \times 10^7$ neutrons per second for the 17 MeV run in 2018. Of course, the instantaneous neutron flux is much higher due to the pulse structure of the beam.

The production samples (^{112}Sn , ^{124}Sn , and a blank) were suspended several cm downstream of the gas cell in a vertically-aligned wire basket apparatus. In addition to the production runs, a few normalization runs were taken with the TUNL-supplied samples (graphite, polyethylene, and a blank). Between runs, samples were rotated into position with a hand-actuated pulley. Sample alignment with the gas cell was confirmed by transit. Neutrons scattering off the samples were recorded by one of the two main time-of-flight detectors, designated “4M” and “6M”, roughly 4 and 6 meters away from the target. These detectors were mounted on large, movable carriages, or “arms”, that could be rotated to different angles independently so that two angular measurements could be conducted simultaneously. By recessing the detectors deep within the arms’ heavy shielding, only neutrons entering the arm at a precise angle were counted. The active volumes of the 4M and 6M detectors were composed of NE218 organic liquid scintillator capable of PSD.

To further reduce room background and to shield detectors from direct, unscattered neutrons, an ensemble of “shadow bars” (wedge-shaped tungsten bricks) were arranged near the entrance to the detector arms. After an arm’s angle was changed, the shadow bars were

aligned by hand so that the detector had no line-of-sight to the gas cell or the shielding of the other arm. Any configuration in which the arms were in opposition (i.e., the angle between the arms was 180 ± 20 degrees) could allow neutrons scattered from one arm to enter the detector of the other arm, so these configurations were avoided.

Besides the time-of-flight detectors installed in the arms, a ceiling monitor detector (CMON) and zero-degree detector aligned with the beam (ZDEG) were used to record beam flux. In addition, a capacitive pickoff signal from the accelerator was collected to serve as a time-of-flight (TOF) stop signal any time an event was recorded on one of the four neutron detectors. Prior to production, detectors were gain-matched and calibrated with ^{137}Cs and ^{22}Na sources using the Compton edges produced from these γ -ray sources. For the 4M (6M) detector, a time resolution of 2 ns (3 ns) was achieved for elastically-scattered neutrons. An exhaustive description of the TUNL TOF room geometry, detector characteristics, gas cell, and other apparatus considerations is provided in [86].

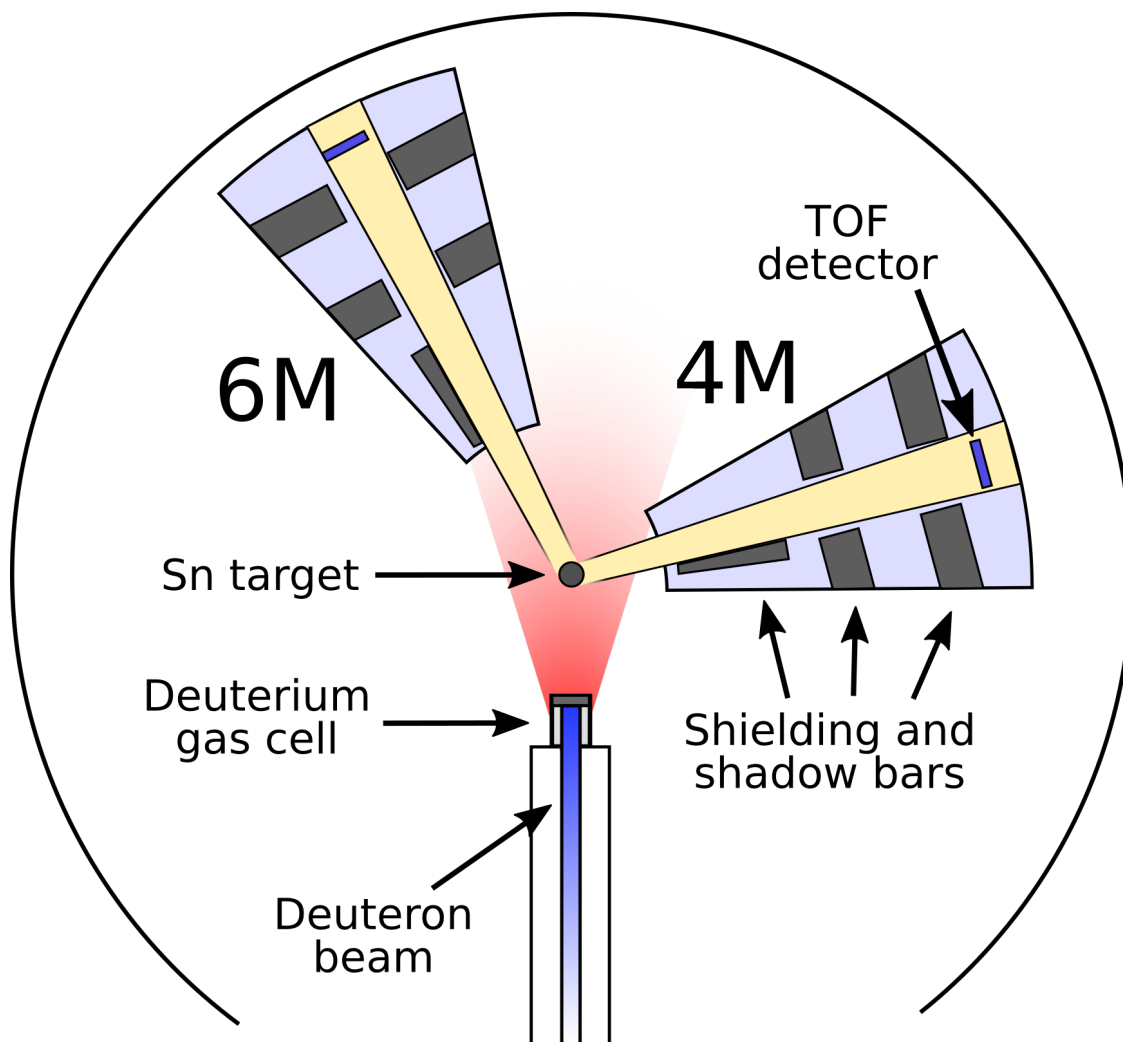


Figure 4.2: Diagram of the neutron TOF room at TUNL. Neutrons are produced by $d(d,n)^3\text{He}$ reaction in a small gas cell, forming a forward-focused cone (in red). They scatter off the sample into one of the detector arms, labeled 4M and 6M, where the neutron times-of-flight are recorded. Another shielded detector (not pictured), suspended from the ceiling, serves as a flux monitor so that absolute cross sections can be recovered. The angle of each detector arm is read from a goniometer in the center of the room.

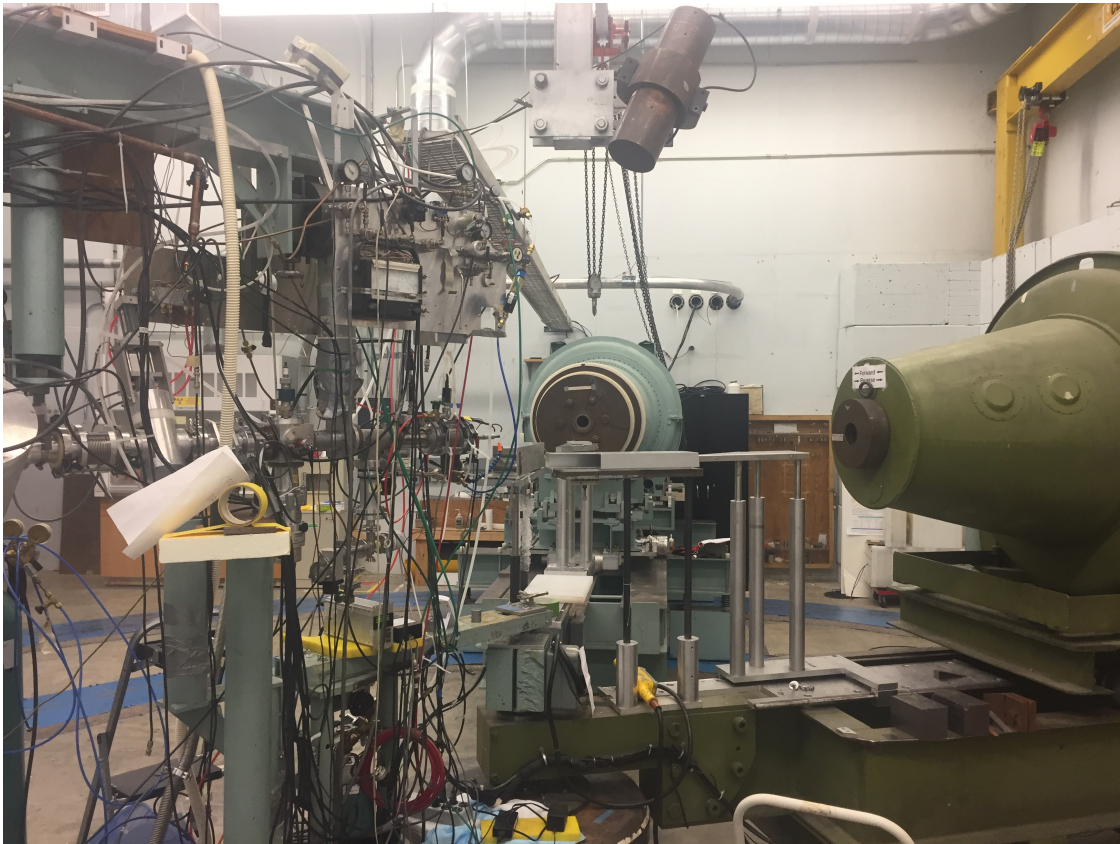


Figure 4.3: Image of the neutron TOF room at TUNL. The deuteron beam pipe is visible on the left and terminates in a small deuteron gas target in the middle of the image, where neutrons are produced. The two detector arms are shown at center (6M) and right (4M). The ceiling monitor detector (CMON), which records beam flux, is visible at the top of the image.

4.4 Data Acquisition

Timing, pulse-shape discrimination, and pulse height information were extracted by the analog signal processing logic laid out in Fig. 4.4. Raw signals from each neutron detector were processed by Mesytec MPD-4 pulse-shape-discrimination modules. The pulse tail length was converted to an amplitude via a time-to-analog converter (TAC), providing neutron-gamma discrimination. The pulse amplitude was measured by a separate analog-to-digital converter (ADC). Event times (labeled “Gate” from each MPD-4) were passed as logic signals to a single time-to-digital converter (TDC) so that event times were recorded using a single clock. Pulse counts (“scalers”) are collected at each step and the TDC, ADC, and data acquisition computer busy signals were used to arrest the TDC when the system was already busy processing, avoiding event pile-up.

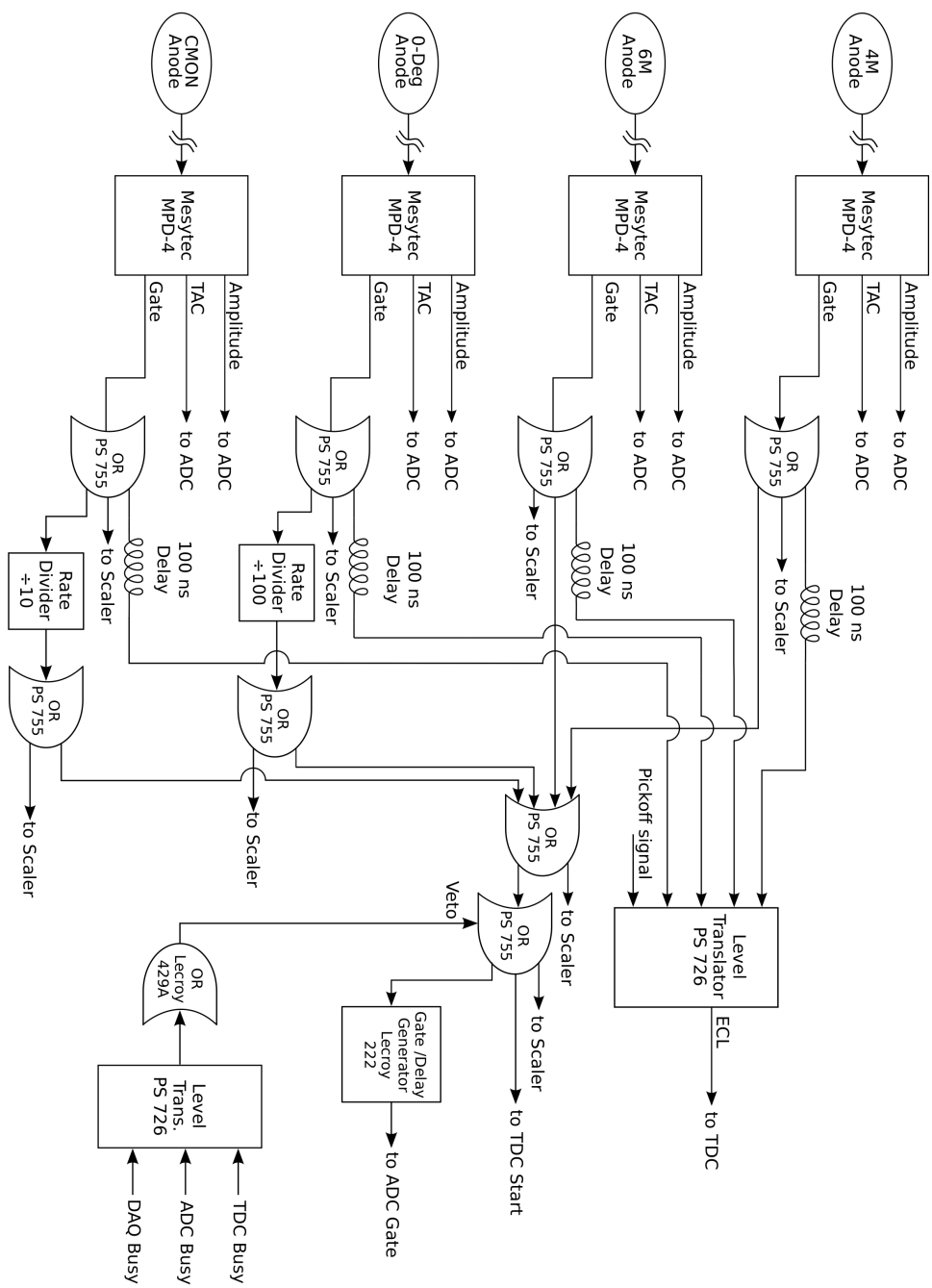


Figure 4.4: Logic diagram for neutron $\frac{d\sigma}{d\Omega}$ data acquisition at the TUNL time-of-flight room. Details are given in the text. Figure courtesy Ron Malone at TUNL.

NEUTRON ELASTIC DIFFERENTIAL CROSS SECTIONS: ANALYSIS AND RESULTS

5.1 Event Identification

During production, runs were taken in batches of three, one each with ^{112}Sn , ^{124}Sn , and the blank samples. Because the distance to each time-of-flight detector was already measured, the time-of-flight for elastically-scattered neutrons could be directly calculated and used to determine the delay from electronics and cabling. The timestamp of each event was thus adjusted by a fixed amount so that the first peak of the neutron spectrum aligned with the expected time-of-flight. Next, background γ -ray events were separated from relevant neutron events by a pulse-shape discrimination analysis, shown in Fig. 5.1.

After scaling histogram counts by detector efficiency, histograms were normalized by the total neutron flux (i.e., total counts in the CMON detector for that run) and summed by detector angle. Then, blank-run histograms were subtracted from the isotopic-run histograms to yield the neutron scattering events from the isotopic samples. Figure 5.2 provides example results for the 4M detector. For the 4M detector and at forward angles for both detectors, the elastic and first-inelastic scattering peaks are closer together in time and cannot be cleanly resolved. Measurements in this kinematic regime are the most challenging as the increased

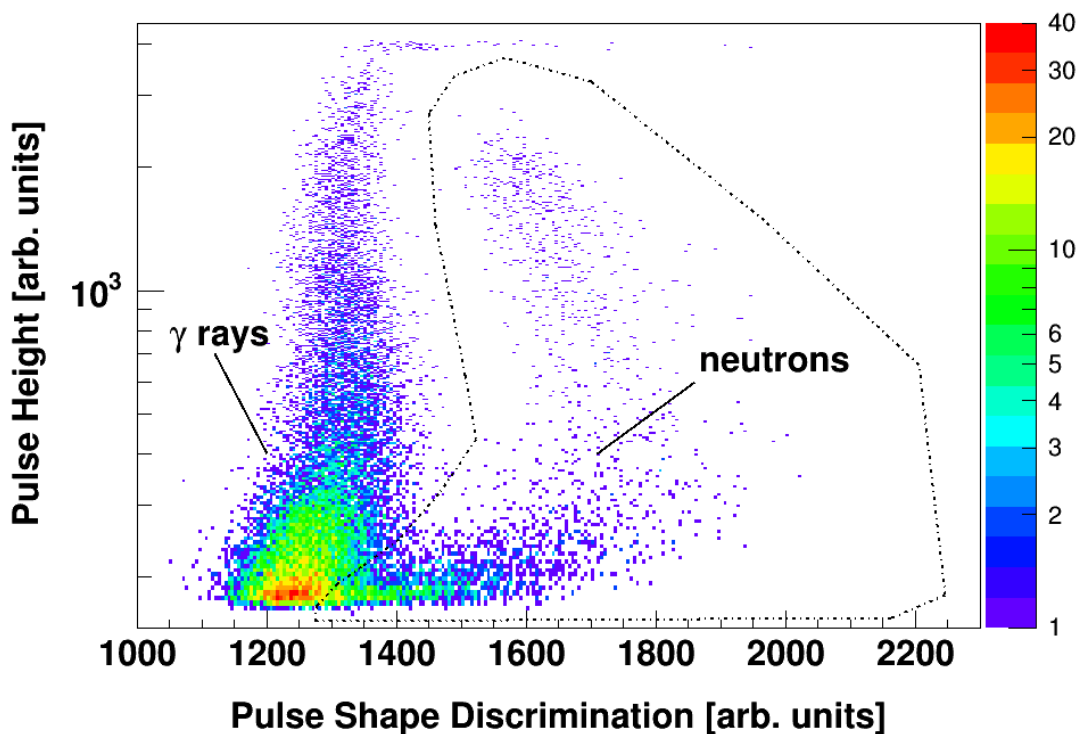


Figure 5.1: Event pulse height (PH) vs. pulse-shape-discrimination (PSD) for a typical run. A gate (dashed line) isolates neutron events, which are used for subsequent analysis. At low pulse heights, the PSD output from the MPD-4 module is non-linear, making neutron- γ -ray separation more difficult (bottom-left of the figure).

overlap between these peaks increases the uncertainty of the number of counts in the elastic peak. We fit the amplitudes of two Gaussian distributions to the elastic and first-inelastic peaks while fixing the width and centroid of each Gaussian according to our time-of-flight resolution and the expected time-of-flight. The integral of the first Gaussian provides the number of counts in the elastic peak.

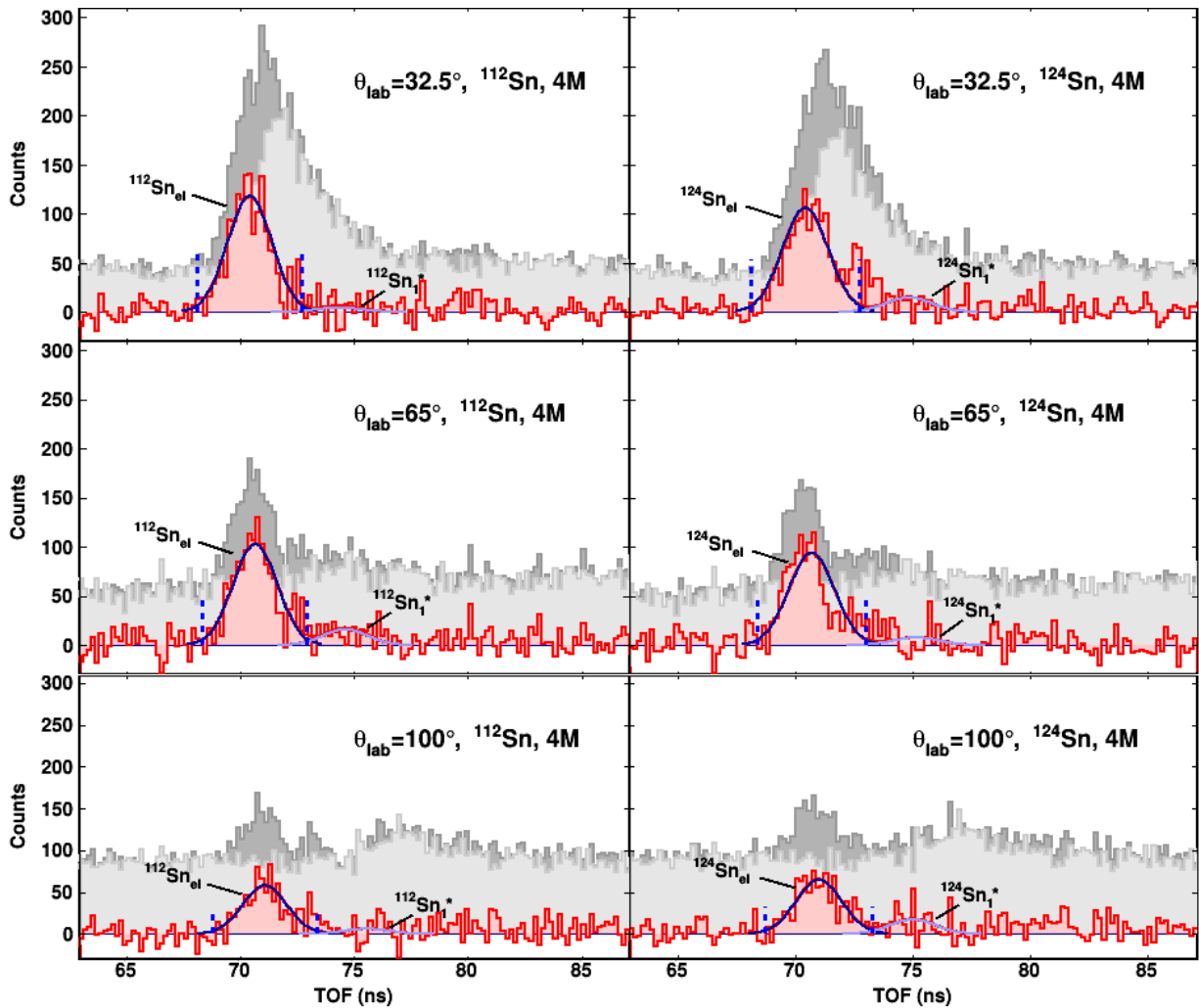


Figure 5.2: Scaled event histograms showing neutron elastic scattering and first-inelastic scattering peaks from the 4M detector for a few representative angles. The histograms for isotopic-sample runs (dark gray bottom layer), blank-sample runs (light gray middle layer), and the difference (red top layer) are shown. For each difference histogram, a double-Gaussian function was constructed with the centroid and width of each Gaussian fixed according to the expected time-of-flight for the elastic and first inelastic peaks and the detector resolution. The heights of each Gaussian were fitted to the difference histogram and the fitted Gaussians are shown in dark blue (elastic peak) and light blue (first-inelastic peak). The blue dashed lines bracketing the elastic-scattering peak depict the gates used to find the number of elastic-scattering counts for the cross section calculation. In the top two panels, the significant background peak is from neutron elastic scattering on atmospheric N_2 .

5.2 Normalization

To normalize the cross sections, a reference point is needed that connects the neutron flux (as measured by the monitor detector) to a known cross section. We took several reference runs using a graphite, a polyethylene, and a blank sample at both the beginning and end of our experiments. Figure 5.3 shows histograms for the 4M and 6M detectors for one set of these runs, taken at 30° in the lab frame. The same coloring conventions from Fig. 5.2 are used, except that now the light blue arrows correspond to the elastic and first-excited states of ^{12}C . In addition, the anticipated location of the peak from neutron elastic scattering on atmospheric N_2 is indicated by a green arrow. The dark gray histogram (back histogram layer) shows the elastic and first-excited states of ^{12}C and also a broad peak from elastic scattering on H. After scaling for the number of moles in the graphite and polyethylene samples, stoichiometry, and neutron flux, the graphite spectrum (light gray, middle histogram layer) was subtracted from the polyethylene spectrum, yielding neutron events only from elastic scattering on protons (area of the red histogram between the blue dashed lines). As the cross section for (n,p) scattering is extremely well-known, the number of counts in the time-of-flight detectors in the reference run can be pegged to the absolute differential cross section. We used the Scattering Analysis Interactive Database (SAID) code [87] to provide the (n,p) cross section at the energies and angles of the reference runs, and using the reference cross section, the $^{112,124}\text{Sn}$ $\frac{d\sigma}{d\Omega}$ were normalized as:

$$\frac{d\sigma}{d\Omega}(\theta) = \frac{d\sigma}{d\Omega_{ref}}(\theta) \times \frac{X_{sample}}{X_{ref}} \times \frac{N_{sample}}{N_{ref}} \quad (5.1)$$

where $\frac{d\sigma}{d\Omega_{ref}}(\theta)$ is the (n,p) cross section at lab angle θ , X_{sample} and X_{ref} are number of counts

in the flux-normalized elastic scattering peak for the sample and the reference runs, respectively (see Figs. 5.2 and 5.3), and N_{sample} and N_{ref} are the number of atoms in the sample of interest and the number of hydrogen atoms in the polyethylene sample, respectively.

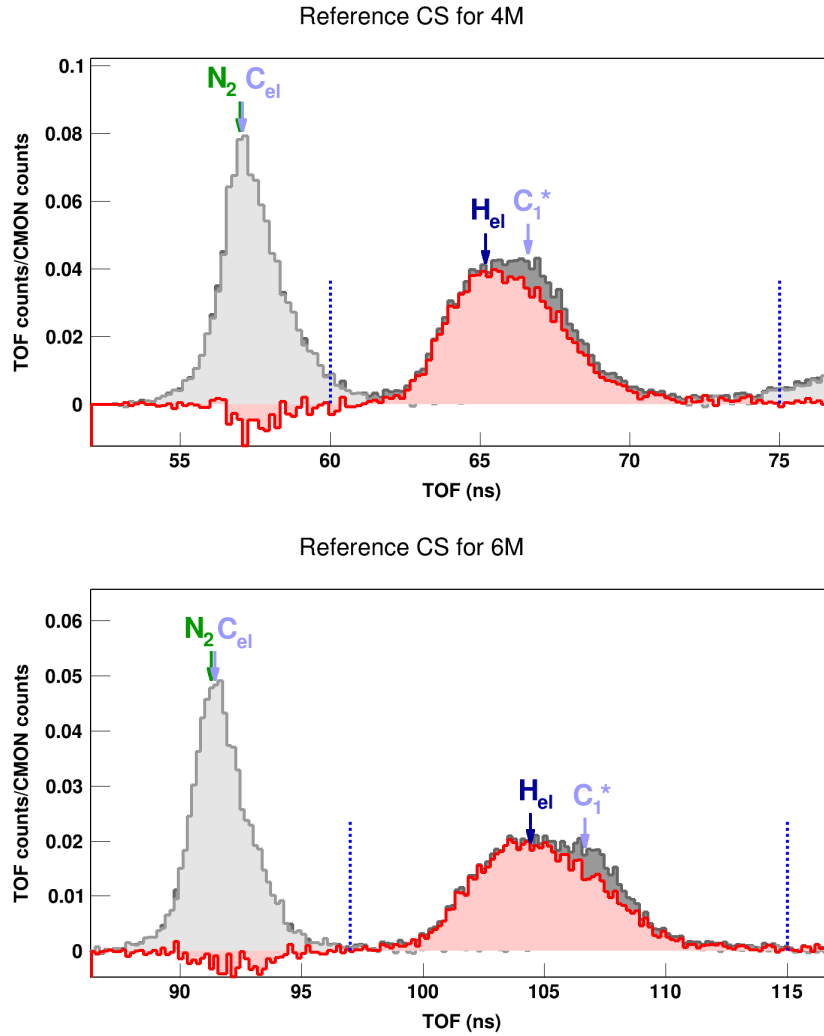


Figure 5.3: Reference runs of neutron scattering on C and $(CH_2)_n$. The $(CH_2)_n$ run (back histogram, in dark gray) and C run (middle histogram, in light gray) are scaled by beam flux and number of atoms in each sample. Their difference (front histogram, in red) shows a broad peak corresponding to neutron-proton elastic scattering. The expected time-of-flight for neutrons elastically scattered from protons is shown by the blue arrow and aligns with the observed peak. Similarly, the light blue arrows indicate the expected times-of-flight associated with neutron elastic and first-excited-state inelastic scattering on C. The green arrow indicates the expected time-of-flight of neutrons elastically scattered on atmospheric N_2 .

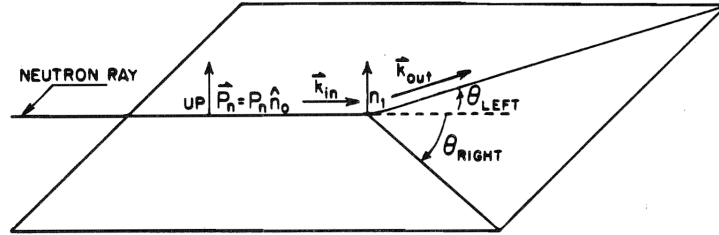
5.3 Finite-Size Corrections

In an idealized differential cross section measurement, the sample and neutron detectors can be treated as point objects. In reality, the neutron beam, samples, and detectors occupy a finite size (as illustrated in Fig. 5.4), leading to so-called finite-size effects that distort the measured cross sections. The experimenter is responsible for applying appropriate corrections to make results size- and apparatus-independent. The finite-size analysis for a similar TUNL-based neutron $\frac{d\sigma}{d\Omega}$ measurement on $^{116,120}\text{Sn}$ is described in detail in [86]. In that analysis, Monte Carlo simulations using the EFFIGY code were prepared to generate a correction for geometric uncertainty of the neutron scattering track, the possibility of multiple scattering in the samples, and flux attenuation in the samples. For the isotopic Ni and Sn samples they studied, they generated finite-size corrections of roughly 1-10% depending on the scattering angle. As seen in Fig. 5.5, the biggest effect is on the depth of the diffraction minima. However, their samples were an order of magnitude larger than our samples: 42.59 g and 44.73 g for their ^{116}Sn and ^{120}Sn samples, respectively, compared to 4.97 g and 5.55 g for our ^{112}Sn and ^{124}Sn samples. Thus we anticipated a significantly smaller correction would be required for our measurement. Figure 5.4 illustrates the potential for multiple scattering in the samples and the small degree of angular uncertainty in the neutron scattering path. The effect of this angular uncertainty on the measured cross sections is to “wash out” the sharp diffraction minima expected to be present in the true cross section. To assess the magnitude of this effect from our samples, an iterative simulation was prepared in which a uniform beam of neutrons impinged on the sample volume and was scattered into the time-of-flight detectors. To select each neutron’s scattering path, we took the raw cross section from our measurement to be the true cross section and allowed neutrons to propagate through the

sample and scatter up to twice. After scattering, neutrons were scored in simulated detectors with the same dimensions used in the real experiment and an “output” cross section was generated. The output is thus a weighted convolution of the input cross section over the finite-size effects of the samples and detectors. In addition to running a simulation with the sample sizes used in the experiment, we performed additional simulations with exaggerated sizes for the sample to make finite-size effects more visible. A comparison between the input and output cross sections shows the effects of beam attenuation and angular uncertainty, seen in Figs. 5.6 and 5.7. To calculate correction factors, we divided the simulation’s input cross section by the output cross section for each angle and multiplied our experimental results by this factor. In principle, this procedure to generate the correction should be repeated iteratively, with the new corrected cross section plugged back into the simulation, but in practice the corrections for our data were so small that only the first iteration was required.

IDEAL EXPERIMENTAL SETUP

1. POINT GEOMETRY



CONVENTION FOR NORMAL VECTOR

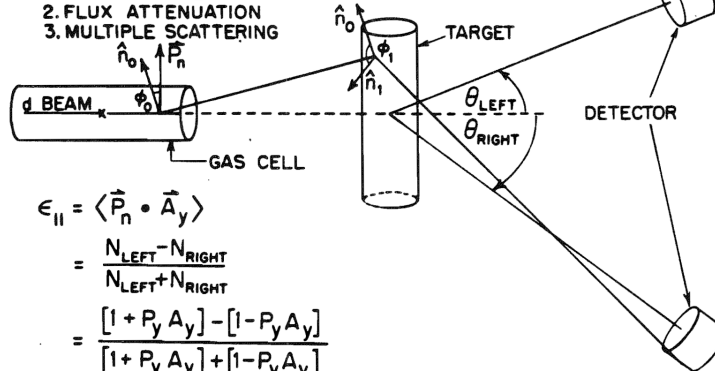
$$\hat{n} \equiv \frac{\vec{k}_{in} \times \vec{k}_{out}}{|\vec{k}_{in} \times \vec{k}_{out}|}$$

ASYMMETRY

$$\epsilon_{||} \equiv \frac{N_{LEFT} - N_{RIGHT}}{N_{LEFT} + N_{RIGHT}}$$

ACTUAL EXPERIMENTAL SETUP

1. FINITE GEOMETRY
2. FLUX ATTENUATION
3. MULTIPLE SCATTERING



$$\begin{aligned} \epsilon_{||} &= \langle \vec{P}_n \cdot \vec{A}_y \rangle \\ &= \frac{N_{LEFT} - N_{RIGHT}}{N_{LEFT} + N_{RIGHT}} \\ &= \frac{[1 + P_y A_y] - [1 - P_y A_y]}{[1 + P_y A_y] + [1 - P_y A_y]} \\ &= P_y A_y \end{aligned}$$

Figure 5.4: Illustration of finite-size effects relevant for $\frac{d\sigma}{d\Omega}$ cross section measurements, from the PhD thesis of P. Guss [86]. Due to the uncertainty in the exact path taken by neutrons during scattering and the possibility of multiple scattering in the sample, a series of finite-size corrections must be applied to recover the true cross section.

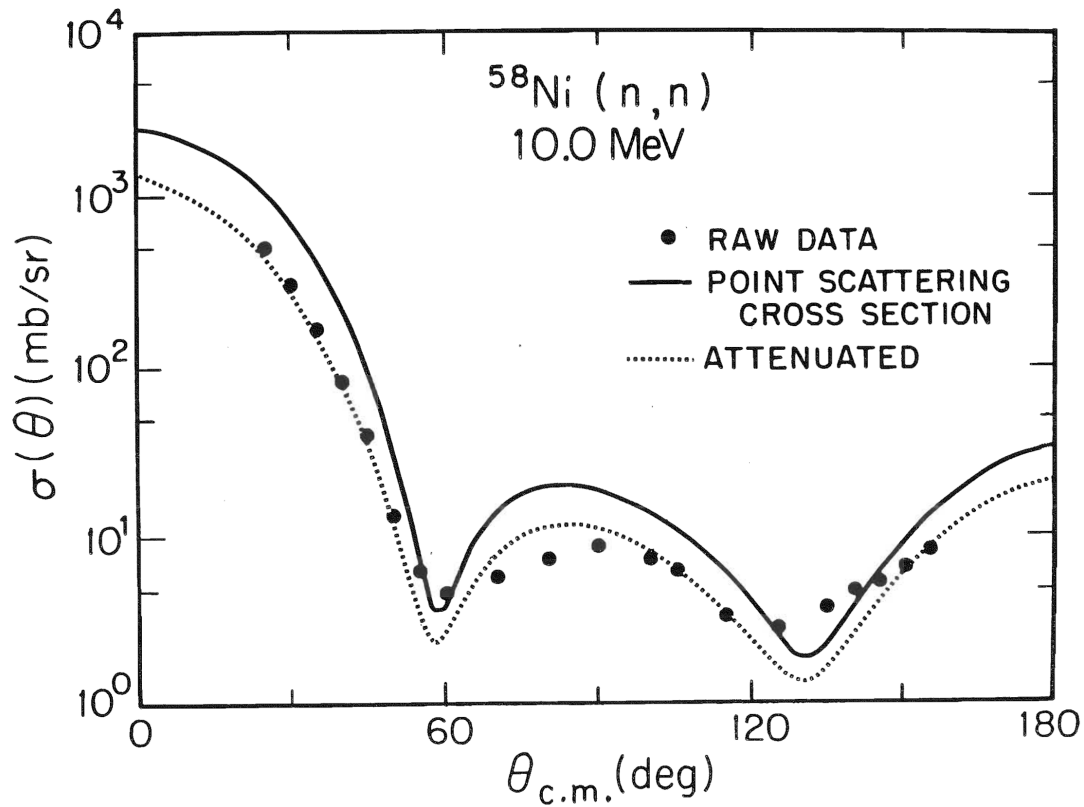


Figure 5.5: The extent of finite-size correction on a previous neutron $\frac{d\sigma}{d\Omega}$ measurement at TUNL are shown. Figure is from the PhD thesis of P. Guss [86]. The raw data from this measurement on Ni isotopes are shown as data points. Using a Monte Carlo simulation, the authors of the previous study generated a correction accounting for multiple scattering in their samples and the angular uncertainty due to the finite volume of their samples, resulting in the dashed curve. With beam attenuation also considered, the cross section is uniformly increased across the angular range, giving the solid curve, which they take to be the “true” cross section. Because our targets are approximately an order of magnitude smaller, we see smaller finite-size effects in our simulation (see Figs. 5.6 and 5.7).

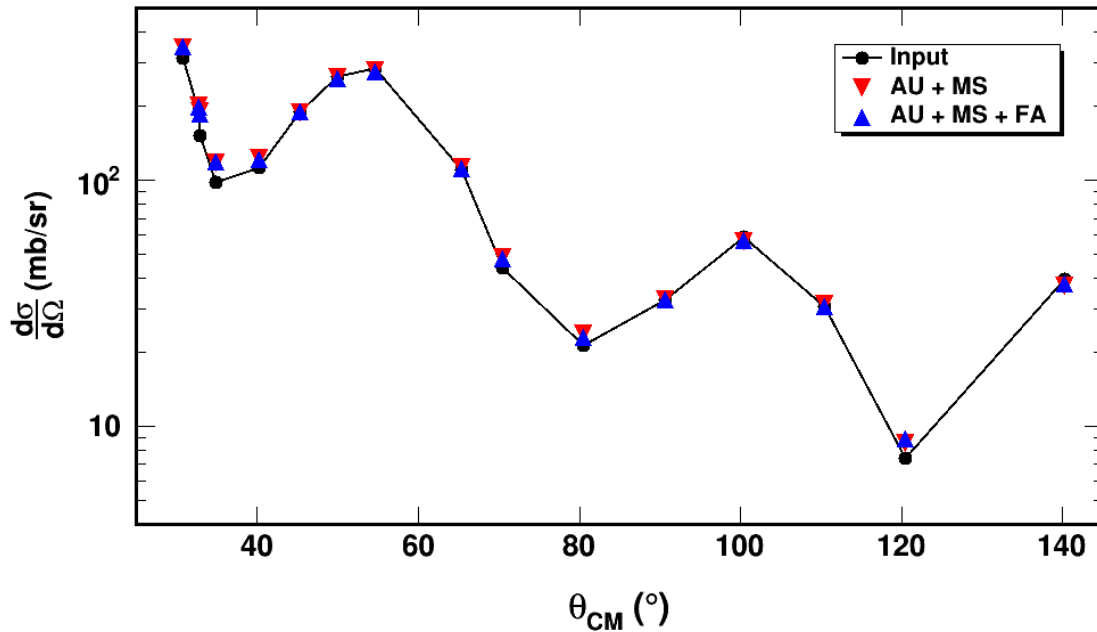


Figure 5.6: The extent of our finite-size corrections are shown, per the output of a typical finite-size simulation. Our raw 11 MeV ^{124}Sn $\frac{d\sigma}{d\Omega}$ data are shown as black points (connected with lines to guide the eye) and were used as the input cross section for the finite-size simulation. The simulation scattered neutrons according to the input distribution that were scored on an array of detectors with the same geometry as in the experiment. “Output” cross sections were calculated based on the number of detector hits. The results of two simulations are shown: one including only the effects of angular uncertainty (AU) and multiple scattering (MS), shown by red triangles, and the other also including flux attenuation in the target (FA), shown as blue triangles. For our targets, the finite-size effects were an order of magnitude smaller than those shown in Fig. 5.5, as anticipated given the smaller size of our targets.

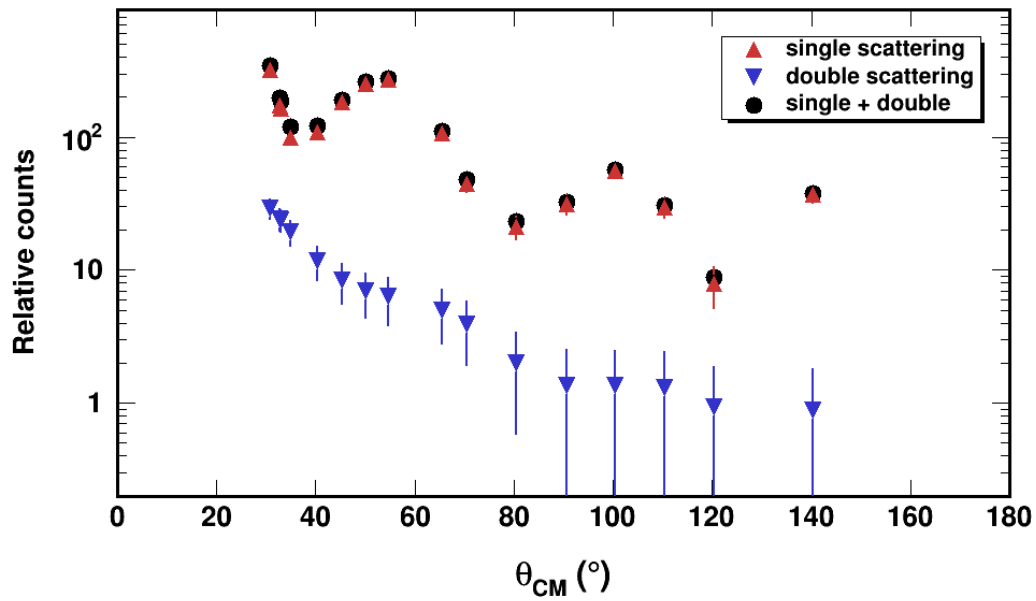


Figure 5.7: Relative counts due to single scattering and double scattering in the sample volume, per our finite-size simulation on ^{124}Sn . The measured data from our experiment include scattering to all orders. Our simulation shows that the contribution from double scattering (and higher orders) is quite small and makes an appreciable difference only in the depth of the diffraction minima.

5.4 Results

5.4.1 $^{112,124}\text{Sn}$ $\frac{d\sigma}{d\Omega}$ at 11 MeV

Figure 5.8 shows our final results for $^{112,124}\text{Sn}$ $\frac{d\sigma}{d\Omega}$ at 11 MeV after applying the corrections described above. Our data on ^{124}Sn at 11 MeV are in reasonable agreement with those of Rapaport et al. [74], which were taken using a much larger enriched sample ($\approx \frac{1}{3}$ mol) at the University of Ohio neutron time-of-flight facility. At angles just less than diffraction minima (e.g., at angles of 65-70°), the ^{112}Sn $\frac{d\sigma}{d\Omega}$ is seen to be larger than that of ^{124}Sn , a consequence of nuclear size differences leading to a phase mismatch, similar to the effect in the $^{16,18}\text{O}$ σ_{tot} relative difference of Fig. 3.17. This same phase-mismatch trend is visible in the $^{116,118,120,122,124}\text{Sn}$ $\frac{d\sigma}{d\Omega}$ collected by Rapaport et al., though the effect is less dramatic as the isotopic range is smaller. Due to our small $^{112,124}\text{Sn}$ sample sizes, our statistics in the 80° and 120° diffraction minima are limited, leading to a large uncertainty in the $\frac{d\sigma}{d\Omega}$ relative difference between $^{112,124}\text{Sn}$.

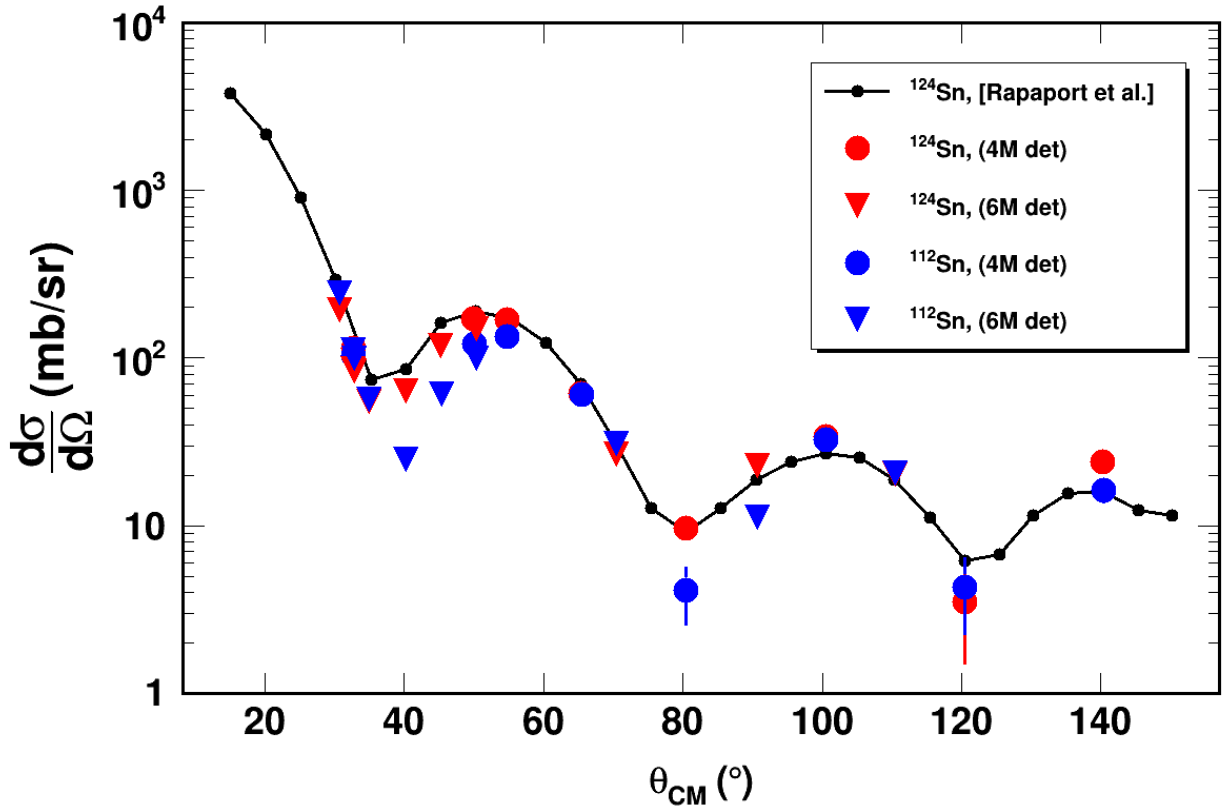


Figure 5.8: Neutron $\frac{d\sigma}{d\Omega}$ on $^{112,124}\text{Sn}$ at 11 MeV: our results and data on ^{124}Sn from Rapaport et al. [74]. The data collected with the 4M detector are shown as circles, and the data collected with the 6M detector are shown as triangles. At 32.5° and 50° , data were taken with both 4M and 6M detectors independently and results from the two detectors are in reasonable agreement.

5.4.2 $^{112,124}\text{Sn}$ $\frac{d\sigma}{d\Omega}$ at 17 MeV

Figure 5.9 shows our final results for $^{112,124}\text{Sn}$ $\frac{d\sigma}{d\Omega}$ at 17 MeV after applying the corrections described above. Our data on ^{124}Sn at 17 MeV are in reasonable agreement with those on ^{120}Sn of Guss et al. [85, 86], which were taken at the same TUNL neutron time-of-flight facility using an enriched sample roughly ten times larger than ours. The same phase-mismatch effect is visible to the left of the diffraction minima (e.g., at 70°). Above 100° , we were unable to collect sufficient statistics to recover a precise $^{112,124}\text{Sn}$ $\frac{d\sigma}{d\Omega}$ relative difference, a

consequence of the reduced cross section at 17 MeV compared to 11 MeV. Whereas in the 11 MeV dataset, the 4M and 6M detectors were in good agreement, in the 17 MeV dataset, our results from the 4M detector appear to be systematically slightly lower than those from the 6M detector, likely due to the increased difficulty in resolving the elastic from the inelastic scattering peaks in the 4M detector at 17 MeV, especially at low angles. As with the σ_{tot} results presented in Chapter 3, the relative difference between isotopes (relevant for fixing the isovector strength) should be insensitive to any systematic errors in our measurement.

As with the 11 MeV dataset, the biggest difference between the $^{112,124}\text{Sn}$ $\frac{d\sigma}{d\Omega}$ data is at the first diffraction minimum from 30-40°. The cross section in this low-angle region is expected to be sensitive to the interaction of the incident neutron with the nuclear surface rather than with the nuclear core, which is better probed with backward-angle scattering. Connecting the shape and magnitude of these $\frac{d\sigma}{d\Omega}$ results with the shape and magnitude of the nuclear potential is the subject of Chapter 7.

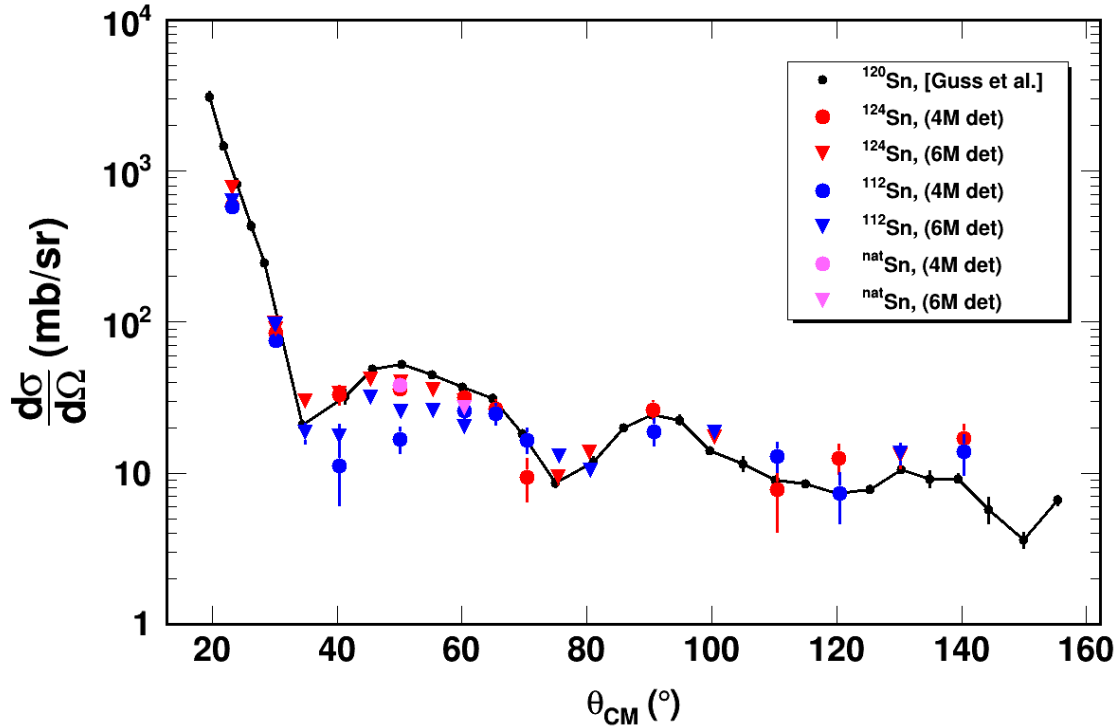


Figure 5.9: Neutron $\frac{d\sigma}{d\Omega}$ cross sections on $^{112,124}\text{Sn}$ at 17 MeV: our results and data on ^{120}Sn from Guss et al. [85]. The data collected with the 4M detector are shown as circles, and the data collected with the 6M detector are shown as triangles. In addition to data on $^{112,124}\text{Sn}$, we collected data on $^{\text{nat}}\text{Sn}$ at 50° and 60° , shown in pink. The data on $^{\text{nat}}\text{Sn}$ lie halfway between our data on ^{112}Sn and ^{124}Sn , adding confidence that the relative difference between $^{112,124}\text{Sn}$ is accurate. At 30° , 40° , and 50° , data were taken with both 4M and 6M detectors at separate times, and results from the two independent detectors are in rough agreement, though results from the 4M detector appear to be systematically slightly lower at low angles.

DISPERSIVE OPTICAL MODEL: OVERVIEW

This chapter provides a brief summary of the Dispersive Optical Model (DOM). A few motivating concepts and definitions, sourced from more extensive treatments [42, 88], are followed by an explicit parameterization of the optical potential used for the DOM fits of Chapter 7. For all sectors of experimental data used in said fits, the formulae connecting the optical potential to the scattering data are given. For detail on the development of the DOM formalism, the seminal work of Mahaux and Sartor [33] and a recent review [27] are recommended. The goal here is to connect the terms of the potential to different sectors of experimental data. In addition, several computational improvements to our implementation of the DOM, important for expanding the reach of the fully non-local DOM of [42] to all even-even systems, are pointed out. In most cases, the notation used conforms to [88], which also provides an introduction to second quantization and historical background for relevant many-body concepts.

6.1 The Single-Particle Propagator

The central project of the Dispersive Optical Model (like any optical model) is to understand how nucleons move about in a nuclear many-body system as parameterized by a

potential. Specifically, we wish to know how a nucleon with energy E and quantum numbers α (position, momentum, spin, isospin, etc.) at time t_0 will be measured at a later time t with quantum numbers β after interaction with the potential. Given a Hamiltonian that models this interaction, the Schrödinger equation relates the Hamiltonian to the time evolution of this state:

$$i\hbar \frac{\partial}{\partial t} |\alpha, t_0; t\rangle = H |\alpha, t_0; t\rangle, \quad (6.1)$$

where $|\alpha, t_0; t\rangle$ is the state at time t , given an initial state $|\alpha, t_0\rangle$. Simple substitution into Eq. 6.1 shows that the initial state propagates in time according to:

$$|\alpha, t_0; t\rangle = e^{-\frac{i}{\hbar}H(t-t_0)} |\alpha, t_0\rangle. \quad (6.2)$$

In position space, the wavefunction of the particle at a given time, $\psi(\mathbf{r}, t)$, is the sum over all contributions from the propagation of the initial state up to that time, a direct application of Huygens principle:

$$\psi(\mathbf{r}, t) = \langle \mathbf{r} | \alpha, t_0; t \rangle = \int d\mathbf{r}' \langle \mathbf{r} | e^{-\frac{i}{\hbar}H(t-t_0)} | \mathbf{r}' \rangle \langle \mathbf{r}' | \alpha, t_0 \rangle. \quad (6.3)$$

The integrand of Eq. 6.3 is referred to as the “single-particle propagator”, denoted $G(r, r'; t - t_0)$ in the time domain, as it determines how the wavefunction of a single particle propagates over time. Crudely speaking, the propagator can be interpreted as the probability that a given initial state will evolve into a final state according to the wave equation.

To conduct practical scattering calculations, the energy-domain representation of the propagator may be more useful than the time-domain representation. Applying a Fourier transform to the propagator (and omitting the intermediate algebraic steps) moves us to the

energy domain, bringing the mathematical structure of the propagator into focus:

$$\begin{aligned}
 G(\mathbf{r}, \mathbf{r}'; E) &= \int_{-\infty}^{\infty} d(t-t') e^{\frac{i}{\hbar} E(t-t')} G(\mathbf{r}, \mathbf{r}'; t-t') \\
 &= \langle 0 | a_{\mathbf{r}} \frac{1}{E - H + i\eta} a_{\mathbf{r}'}^{\dagger} | 0 \rangle \\
 &= \langle \mathbf{r} | \frac{1}{E - H + i\eta} | \mathbf{r}' \rangle,
 \end{aligned} \tag{6.4}$$

where $a_{\mathbf{r}}$ and $a_{\mathbf{r}'}^{\dagger}$ are the particle removal and addition operators in the second-quantization picture, respectively, and $|0\rangle$ is the vacuum state. Equation 6.4 contains the same information as Eq. 6.3: that the wavefunction $\psi(\mathbf{r})$ is the sum of the weighted contributions from all \mathbf{r}' and the weights are determined by the difference between the energy E and the evaluation of H on each of the \mathbf{r}' contributions. Of course, we need not privilege \mathbf{r} -space; G can be written using any suitable single-particle basis. For example, the momentum-space representation for a spinless, non-interacting free particle of mass m and momentum \mathbf{k} reads:

$$G^0(\mathbf{k}, \mathbf{k}'; E) = \delta(\mathbf{k} - \mathbf{k}') \frac{1}{E - \frac{\hbar^2 k^2}{2m} + i\eta}. \tag{6.5}$$

If the independent-particle model was exact and the mean-field potential could be perfectly known, calculating the propagation of nucleons through the nucleus would be as simple as calculating single-particle scattering off a potential well. Such a calculation involves little more than a matrix inversion of the Hamiltonian in the denominator of Eq. 6.4. Real nucleon-nucleus scattering involves the possibility of excitations in the nucleus from the incident nucleon so that the wavefunction of the compound system may be very different from that of the nuclear ground state. The single-particle propagator must include these possibilities as well. The propagator from the $|\alpha\rangle$ state at time t to the state $|\beta\rangle$ at a later

time t' is:

$$G(\alpha, \beta; t, t') = -\frac{i}{\hbar} \langle \Psi_0^N | \mathcal{T}[a_{\alpha_H}(t) a_{\beta_H}^\dagger(t')] | \Psi_0^N \rangle. \quad (6.6)$$

Here, $|\Psi_0^N\rangle$ is the normalized Heisenberg ground state for the N-particle system with eigenvalue E_0^N :

$$\hat{H} |\Psi_0^N\rangle = E_0^N |\Psi_0^N\rangle \quad (6.7)$$

The time-ordering operator \mathcal{T} ensures that operators with later time appear to the left of operators with earlier time¹, important for the perturbative treatment to follow. In short, this expression includes contributions from both particle propagation, already seen Eq. 6.3, and hole propagation, new behavior only pertinent for a many-particle system capable of particle excitation/hole production. We can expand Eq. 6.6 and once again apply a Fourier transform to make interpretation easier:

$$\begin{aligned} G(\alpha, \beta; E) &= \int_{-\infty}^{\infty} d(t-t') e^{\frac{i}{\hbar} E(t-t')} G(\alpha, \beta; t-t') \\ &= \sum_m \frac{\langle \Psi_0^N | a_\alpha | \Psi_m^{N+1} \rangle \langle \Psi_m^{N+1} | a_\beta^\dagger | \Psi_0^N \rangle}{E - (E_m^{N+1} - E_0^N) + i\eta} + \frac{\langle \Psi_0^N | a_\beta | \Psi_n^{N-1} \rangle \langle \Psi_n^{N-1} | a_\alpha^\dagger | \Psi_0^N \rangle}{E - (E_0^N - E_n^{N-1}) + i\eta} \\ &= \langle \Psi_0^N | a_\alpha \frac{1}{E - (\hat{H} - E_0^N) + i\eta} a_\beta^\dagger | \Psi_0^N \rangle + \langle \Psi_0^N | a_\beta^\dagger \frac{1}{E - (E_0^N - \hat{H}) - i\eta} a_\alpha | \Psi_0^N \rangle \end{aligned} \quad (6.8)$$

$|\Psi_{m(n)}^{N\pm 1}\rangle$ are the normalized Heisenberg states for the $N\pm 1$ particle systems. The $|\Psi_m^{N+1}\rangle$ have

¹The time-ordering operator \mathcal{T} is defined as:

$$\mathcal{T}[a_{\alpha_H}(t) a_{\beta_H}^\dagger(t')] = \theta(t-t') a_{\alpha_H}(t) a_{\beta_H}^\dagger(t') - \theta(t'-t) a_{\beta_H}^\dagger(t') a_{\alpha_H}(t)$$

eigenvalues E_m^{N+1} and the $|\Psi_n^{N-1}\rangle$ have eigenvalues E_n^{N-1} :

$$\begin{aligned}\hat{H} |\Psi_m^{N+1}\rangle &= E_m^{N+1} |\Psi_m^{N+1}\rangle \\ \hat{H} |\Psi_n^{N-1}\rangle &= E_n^{N-1} |\Psi_n^{N-1}\rangle\end{aligned}\tag{6.9}$$

in keeping with Eq. 6.7. The second line of Eq. 6.8 is referred to as the ‘‘Lehmann representation’’. To reach the third line of Eq. 6.8, the complete bases of $|\Psi_m^{N+1}\rangle$ and $|\Psi_n^{N-1}\rangle$ have been removed from the corresponding terms on the second line. The particle and hole contributions to the propagator are neatly separated and each possesses the relevant energy weighting in the denominator, sandwiched between the fermion creation and annihilation operators. Neither the ground-state wavefunction of the correlated many-body system Ψ_0^N or the full Hamiltonian \hat{H} are known at this stage, but they are now amenable to a perturbation expansion, the subject of the next section.

6.1.1 Perturbation Expansion and The Dyson Equation

The full single-particle propagator G can be calculated via perturbation expansion by starting with a non-interacting (unperturbed) propagator G_0 and adding interaction terms, \hat{V} , that bring G_0 closer to the real G . This expansion requires a change from the Heisenberg picture of the previous section to the Interaction picture². First, the full Hamiltonian H is broken up into the non-interacting and interacting parts:

$$\hat{H} = \hat{H}_0 + \hat{H}_1,\tag{6.10}$$

where \hat{H}_0 contains the kinetic energy operator \hat{T} and possibly a one-body auxiliary potential \hat{U} , and \hat{H}_1 collects all residual interactions (the hard part of the problem). Broken up in this way, the non-interacting propagator reads:

$$G^{(0)}(\alpha, \beta; t - t') = -\frac{i}{\hbar} \langle \Phi_0^A | \mathcal{T}[a_{\alpha I}(t) a_{\beta I}^\dagger(t')] | \Phi_0^A \rangle, \quad (6.11)$$

where the fully-correlated many-body ground state $|\Psi_0^A\rangle$ has been replaced by $|\Phi_0^A\rangle$, the uncorrelated ground-state associated with H_0 . Through algebraic manipulation and employing the Interaction version of all operators, the *full* single-particle propagator, including the contribution from the interactions buried in \hat{H}_1 , is:

$$G(\alpha, \beta; t - t') = \frac{Num}{Denom}, \quad (6.12)$$

where

$$\begin{aligned} Num &= -\frac{i}{\hbar} \sum_n \left(\frac{i}{\hbar}\right)^n \frac{1}{n!} \int_{-\infty(1-i\eta)}^{\infty(1-i\eta)} dt_1 \int_{-\infty(1-i\eta)}^{\infty(1-i\eta)} dt_2 \cdots \int_{-\infty(1-i\eta)}^{\infty(1-i\eta)} dt_n \\ &\quad \times \langle \Phi_0^N | \mathcal{T}[\hat{H}_1(t_1) \hat{H}_1(t_2) \cdots \hat{H}_1(t_n) a_{\alpha I}(t) a_{\beta I}^\dagger(t')] | \Phi_0^N \rangle, \\ Denom &= \sum_m \left(\frac{-i}{\hbar}\right)^m \frac{1}{m!} \int_{-\infty(1-i\eta)}^{\infty(1-i\eta)} dt'_1 \int_{-\infty(1-i\eta)}^{\infty(1-i\eta)} dt'_2 \cdots \int_{-\infty(1-i\eta)}^{\infty(1-i\eta)} dt'_m \\ &\quad \times \langle \Phi_0^N | \mathcal{T}[\hat{H}_1(t_1) \hat{H}_1(t_2) \cdots \hat{H}_1(t_m)(t')] | \Phi_0^N \rangle. \end{aligned}$$

²Operators in the Interaction picture are related to those in the Schrödinger picture by:

$$O_I(t) = e^{\frac{i}{\hbar} \hat{H}_0 t} O_S e^{-\frac{i}{\hbar} \hat{H}_0 t}$$

Appendix A of [88] provides a complete description of these different quantum-mechanical pictures.

Despite the extra ink, the mathematical structure of the Lehmann representation (Eq. 6.8) is still visible: the numerator contains the contributions from the creation and annihilation operators attaching to the uncorrelated ground-state, and the denominator provides an energy weighting. We have generated an infinite series of terms with increasing order in the number of \hat{H}_1 interactions permitted. Aside from arbitrary counting indices, the only differences between the numerator and denominator are a factor of $-\frac{i}{\hbar}$ and the fermion annihilation and creation operators responsible for moving from $|\alpha\rangle$ to $|\beta\rangle$. Wick's theorem³ can be applied to remove contributions to the propagator that appear in both the numerator and the denominator and do not survive the division. This dramatically reduces the number of terms at each level of the perturbation expansion, and when the dust settles, the propagator reads:

$$G(\alpha, \beta; t - t') = -\frac{i}{\hbar} \sum_n \left(\frac{i}{\hbar}\right)^n \frac{1}{n!} \int dt_1 \int dt_2 \cdots \int dt_n \quad (6.13)$$

$$\times \langle \Phi_0^A | \mathcal{T}[\hat{H}_1(t_1) \hat{H}_1(t_2) \cdots \hat{H}_1(t_n) a_{\alpha I}(t) a_{\beta I}^\dagger(t')] | \Phi_0^A \rangle_{connected}.$$

Physically speaking, the full propagator is the infinite sum of the expectation value of \hat{H}_1 iteratively applied to the non-interacting ground state. The non-interacting ground state is modified by each interaction and thus all the many-body correlations of $|\Psi_0^N\rangle$ are encoded by the repeated operation of \hat{H}_1 . The subscript “connected” indicates that only terms corresponding to fully-connected Feynman diagrams should be included in the full propagator, as all non-connected diagrams appear in both the numerator and denominator of Eq. 6.12 and do not survive the division. We can represent the perturbation expansion of Eq. 6.13 diagrammatically to clarify the physical meaning of the expansion terms. Figure 6.1 shows

³See section 8.4 of [88] for the full procedure.

THE SINGLE-PARTICLE PROPAGATOR

several diagrams from the first few orders of the expansion. To zeroth-order, the

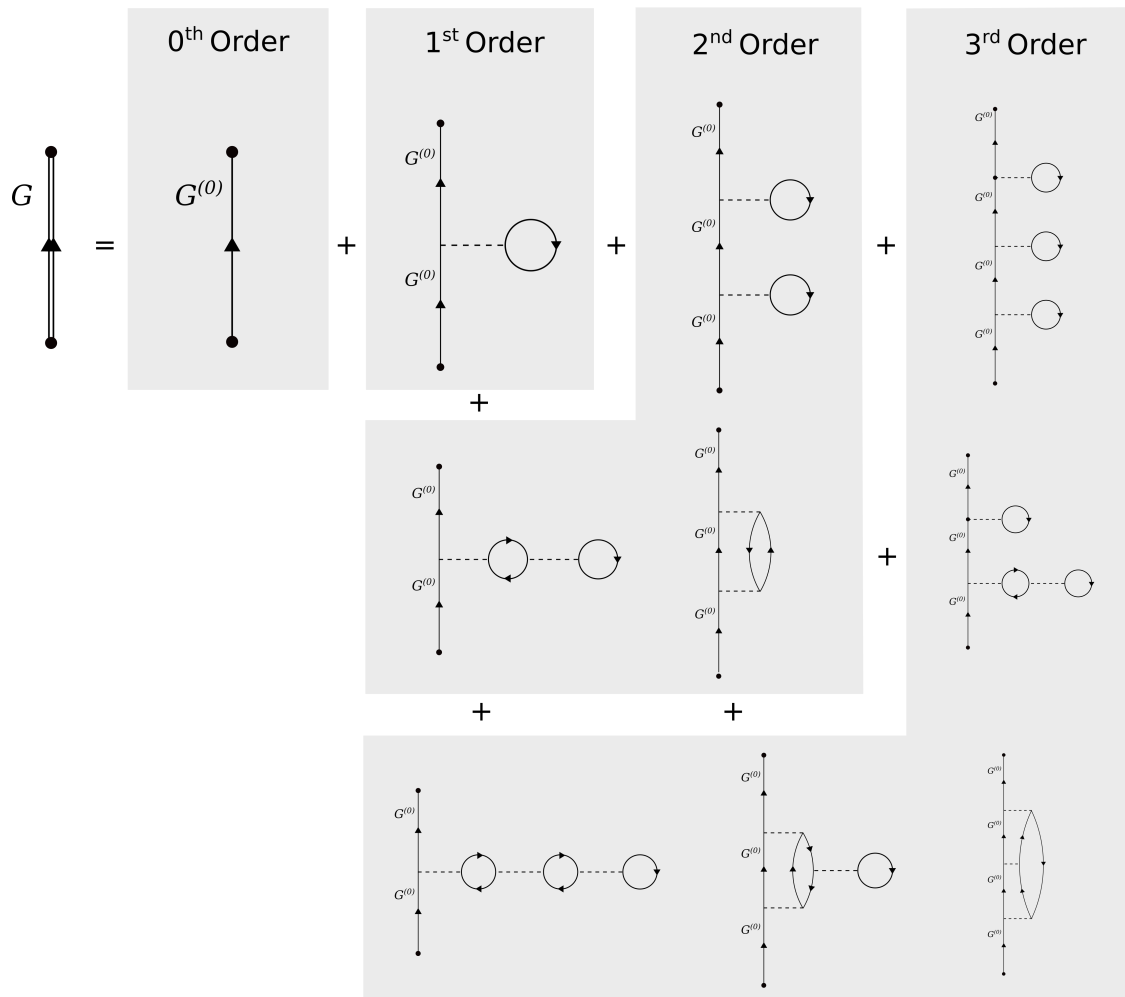


Figure 6.1: A subset of the diagrams from the first few orders that contribute to the single-particle propagator perturbation expansion. The interaction \hat{V} is represented by the horizontal dashed line and is taken to be two-body only in this treatment.

expansion is only one non-interacting term, which is just the free single-particle propagator. At each higher order, one more interaction is permitted to enter the diagram and can attach at any fermion line (i.e., into any propagator line). By grouping and rearranging the terms, we can condense the full perturbation expansion to a self-consistent equation called the

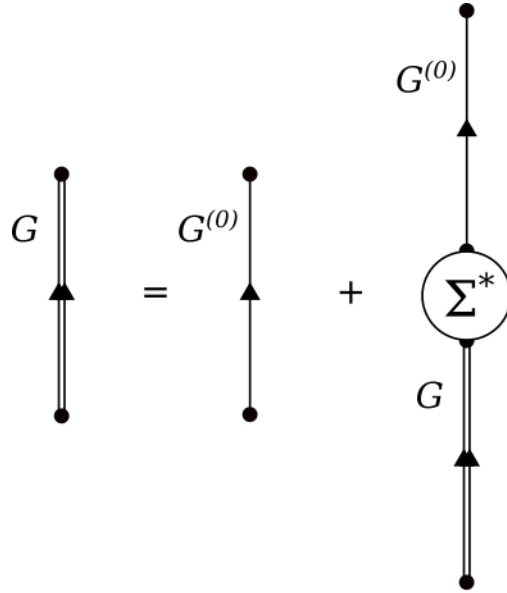


Figure 6.2: The Dyson equation in diagrammatic form.

Dyson equation:

$$G(\alpha, \beta; E) = G^{(0)}(\alpha, \beta; E) + \sum_{\gamma, \delta} G^{(0)}(\alpha, \gamma; E) \Sigma^*(\gamma, \delta, E) G(\delta, \beta; E). \quad (6.14)$$

A diagrammatic representation of the Dyson equation is given in Fig. 6.2. The two summation variables γ and δ label states internal to the diagrams that are accessed during the particle's excitation of the many-body system⁴. The Dyson equation introduces a new term, the irreducible nucleon self-energy Σ^* , that connects the free single-particle propagator to the full single-particle propagator that incorporates all the in-medium effects of traveling through the nuclear environment. The self-energy serves the role of the potential – the optical potential – experienced by a particle in the medium. This makes the Dyson equation

⁴While there are only two additional summation variables in Eq. 6.14, if a three-body interaction was included, an additional summation variable would be needed.

the equivalent of the Schrödinger equation, but for particles *embedded in the medium* rather than propagating in free space. Calculating the full self-energy explicitly remains impossible in practice, as it involves a (countably) infinite number of diagrams and the underlying nuclear interactions are only approximately known. *Rather than solve this problem analytically, the DOM solves it empirically by identifying the full self-energy as equivalent to the optical potential.* By fitting the self-energy to experimental data, we cut the Gordian knot of making an analytic calculation to all orders. As already discussed in Chapter 1, the optical potential is readily connected to a host of experimental data: elastic cross sections, analyzing powers, and inelastic reactions for both protons and neutrons. From a well-constrained optical-potential/self-energy, additional important quantities, like overlap functions and neutron skins, can be extracted. This phenomenological approach is the heart of the Dispersive Optical Model.

6.1.2 The Dispersion Relation

State-of-the-art optical models [29, 30] typically restrict their potentials to the positive-energy domain relevant for nucleon-nucleus scattering. From the previous section, though, it is clear that the self-energy must have a negative-energy component if it is to describe the correlated many-body ground state: bound nucleons experience the same potential as scattering nucleons, albeit at negative energies. It has been recognized for over fifty years [89, 90] that the real and imaginary parts of the self-energy should obey a dispersion relation: if the real part is known at all energies (positive and negative), the imaginary part can be deduced and vice-versa. Optical models that obey this relation may be called dispersive optical models.

The real part of the self-energy can be shown to have two components: one independent

of energy (equal to the correlated Hartree-Fock term) and an energy-dependent part that can be calculated from the imaginary part:

$$\text{Re}(\Sigma^*(\alpha, \beta; E)) = \text{Re}(\Sigma_s(\alpha, \beta)) + \text{Re}(\Sigma_d(\alpha, \beta; E)). \quad (6.15)$$

The relevant dispersion relation to calculate the real energy-dependent part is:

$$\text{Re}(\Sigma_d(\alpha, \beta; E)) = -\mathcal{P} \int_{\epsilon_T^+}^{\infty} \frac{dE'}{\pi} \frac{\text{Im}(\Sigma_d(\alpha, \beta; E'))}{E - E'} + \mathcal{P} \int_{-\infty}^{\epsilon_T^-} \frac{dE'}{\pi} \frac{\text{Im}(\Sigma_d(\alpha, \beta; E'))}{E - E'}. \quad (6.16)$$

\mathcal{P} is the Cauchy principle value and the integration limits ϵ_T^\pm are selected to be just below the lowest-lying imaginary strength in the positive-energy domain (for ϵ_T^+) and just above the highest-lying imaginary strength in the negative-energy domain (for ϵ_T^-). Between these thresholds, the imaginary component of the potential vanishes, so the self-energy is entirely real. After some algebraic rearrangement, it can be shown that:

$$\begin{aligned} \text{Re}(\Sigma(\alpha, \beta; E)) &= \text{Re}(\Sigma(\alpha, \beta; \epsilon_F)) \\ &\quad - \mathcal{P} \int_{\epsilon_T^+}^{\infty} \frac{dE'}{\pi} \frac{\text{Im}(\Sigma_d(\alpha, \beta; E'))}{E - E'} \left[\frac{1}{E - E'} - \frac{1}{\epsilon_F - E'} \right] \\ &\quad + \mathcal{P} \int_{-\infty}^{\epsilon_T^-} \frac{dE'}{\pi} \frac{\text{Im}(\Sigma_d(\alpha, \beta; E'))}{E - E'} \left[\frac{1}{E - E'} - \frac{1}{\epsilon_F - E'} \right] \end{aligned} \quad (6.17)$$

which is referred to as the “subtracted dispersion relation”. The integral of the imaginary component of the self-energy over the entire energy domain determines the dynamic (energy-dependent) part of the real component, ensuring that the potential is self-consistent and that reactions and structure calculations take place on equal footing. This is the form of the dispersion relation employed in the subsequent analysis.

6.2 Connection to Experimental Observables

6.2.1 Elastic and Inelastic Nucleon Scattering

For nucleon-nucleus scattering, the momentum basis is a natural choice. The scattering amplitude can be directly calculated using the reducible self-energy Σ^5 :

$$f_{m'_s, m_s}(\theta, \phi) = -\frac{4m\pi^2}{\hbar^2} \langle \mathbf{k}' m'_s | \Sigma(E) | \mathbf{k} m_s \rangle \quad (6.19)$$

where $\mathbf{k} m_s$ are the wave vector and spin quantum number of the incident nucleon and $\mathbf{k}' m'_s$ are for the exiting nucleon. The matrix structure of the right side can be split into spin-independent and spin-dependent portions \mathcal{F} and \mathcal{G} :

$$f(\theta, \phi) = \mathcal{F}(\theta)I + \sigma \cdot \hat{\mathbf{n}}\mathcal{G}(\theta), \quad (6.20)$$

where

$$\begin{aligned} \mathcal{F}(\theta) &= \frac{1}{2ik} \sum_{l=0}^{\infty} [(l+1)e^{2i\delta_{l+}} - 1 + l(e^{2i\delta_{l-}} - 1)] P_l(\cos\theta) \\ \mathcal{G}(\theta) &= \sigma \cdot \hat{\mathbf{n}} \left[\frac{\sin\theta}{2k} \sum_{l=1}^{\infty} [e^{2i\delta_{l+}} - e^{2i\delta_{l-}}] P'_l(\cos\theta) \right]. \end{aligned} \quad (6.21)$$

Here, P_l are Legendre polynomials of degree l , P'_l is the derivative of the Legendre polynomial, and $\delta_{l\pm} \equiv \delta_{l\pm\frac{1}{2}}$, corresponding to the spin being parallel or antiparallel to the orbital angular

⁵The reducible self-energy is related to the irreducible self-energy of Eq. 6.14 by:

$$\Sigma = \Sigma^* + \Sigma^* G^{(0)} \Sigma \quad (6.18)$$

. See [42] for details.

momentum. From the scattering amplitude, the unpolarized cross section is simply:

$$\left(\frac{d\sigma}{d\Omega}\right)(\theta) = |\mathcal{F}(\theta)|^2 + |\mathcal{G}(\theta)|^2 \quad (6.22)$$

and the analyzing power is:

$$A(\theta) = \frac{2\mathcal{F}(\theta)(\mathcal{G}(\theta))^*}{\frac{d\sigma}{d\Omega}(\theta)}. \quad (6.23)$$

The complex phase shift (equivalently, the S-matrix elements) for each partial wave associated with the nucleon under investigation can be calculated directly from the reducible self-energy:

$$\begin{aligned} e^{2i\delta_{lj}} &\equiv \langle \mathbf{k} | \mathcal{S}_{lj}(E) | \mathbf{k} \rangle \\ &= 1 - 2\pi i \left(\frac{mk}{\hbar^2} \right) \langle \mathbf{k} | \Sigma_{lj}(E) | \mathbf{k} \rangle, \end{aligned} \quad (6.24)$$

where k is the center-of-mass momentum of the nucleon, m is the nucleon mass, and E is the center-of-mass energy. The reaction cross section at a given energy is the sum of the partial reaction cross section over all partial waves:

$$\sigma_{rxn} = \sum_{l=0}^{\infty} \frac{\pi}{k^2} [(2l+1) - (l+1)|e^{2i\delta_{l+}}|^2 - l|e^{2i\delta_{l-}}|^2], \quad (6.25)$$

and the total cross section simply a sum of the reaction and elastic over all partial waves:

$$\sigma_{tot} = \sigma_{el} + \sigma_{rxn} \quad (6.26)$$

where

$$\begin{aligned}
 \sigma_{el} &= \int d\theta \int d\phi \frac{d\sigma}{d\Omega}(\theta) \\
 &= \sum_{l=0}^{\infty} \frac{\pi}{k^2} \frac{|(l+1)(e^{2i\delta_{l+}} - 1) + l(e^{2i\delta_{l-}} - 1)|^2}{2l+1} \\
 &\quad \times \frac{l(l+1)|e^{2i\delta_{l+}} - e^{2i\delta_{l-}}|^2}{2l+1}.
 \end{aligned} \tag{6.27}$$

6.2.2 Bound-state Properties

To compare the bound-state information of the propagator with experimental data, we first define the spectral functions for holes and particles:

$$\begin{aligned}
 S_h(\alpha; E) &= \frac{1}{\pi} \text{Im}(G(\alpha, \alpha; E)) \quad \text{for } E \leq \epsilon_F^- \\
 &= \sum_n |\langle \Psi_n^{N-1} | a_\alpha | \Psi_0^N \rangle|^2 \delta(E - (E_0^N - E_n^{N-1})),
 \end{aligned} \tag{6.28}$$

$$\begin{aligned}
 S_p(\alpha; E) &= -\frac{1}{\pi} \text{Im}(G(\alpha, \alpha; E)) \quad \text{for } E \geq \epsilon_F^+ \\
 &= \sum_n |\langle \Psi_n^{N+1} | a_\alpha^\dagger | \Psi_0^N \rangle|^2 \delta(E - (E_n^{N+1} - E_0^N)).
 \end{aligned}$$

In this expression, ϵ_F^\pm are the lowest-unoccupied and highest-occupied single-particle levels, which yield the Fermi energy ϵ_F when averaged. Physical speaking, the hole spectral function at the energy E is the probability density for plucking out a particle with quantum numbers α from the ground state and leaving the residual nucleus with the energy $E_0^N - E$. The particle spectral function provides the same information, but for *adding* a particle, leaving the nuclear system with energy $E_0^N + E$. From the spectral functions, the occupation of a

state is simply

$$\begin{aligned}
 n(\alpha) &= \langle \Psi_0^N | a_\alpha^\dagger a_\alpha | \Psi_0^N \rangle \\
 &= \int_{-\infty}^{-\epsilon_F} S_h(\alpha; E).
 \end{aligned}
 \tag{6.29}$$

Numerically, this integral can be difficult to compute near ϵ_F where peaks in the spectral function (from bound quasi-hole states just below ϵ_F) become δ -function-like. This is a consequence of the vanishing imaginary strength near ϵ_F . Thus, we use a piecemeal procedure where the spectral function is integrated up to an arbitrary threshold near (but below) the δ -function-like behavior, and the spectroscopic factor of any quasi-holes between the threshold and ϵ_F^- is added to account for the remaining occupation. The spectroscopic factor is calculated:

$$S = \left(1 - \left. \frac{\partial \Sigma^*(\alpha_{qh}, \alpha_{qh}; E)}{\partial E} \right|_{\epsilon_n^-} \right)^{-1},
 \tag{6.30}$$

where qh indicates the quasi-hole nature of the single-particle state indicated by α and $\epsilon_n^- = E_0^N - E_n^{N-1}$ is the eigenvalue associated with the quasi-hole state. It should be noted that if the self-energy has a significant imaginary component at ϵ_n^- , the quasi-hole normalization will be incorrect and the validity of Eq. 6.30 degraded. Hence, this expression should only be used in the vicinity of the Fermi energy where the imaginary strength is negligible.

Previous DOM analyses (e.g., [42]) dealt only with doubly-closed shell nuclei such as ^{40}Ca and ^{48}Ca . For these nuclei, the above procedure to calculate the occupation number is sufficient. The present analysis includes nuclei with open neutron subshells (e.g., the $\nu 0d_{5/2}$ in ^{18}O and $\nu 0f_{5/2}$ in ^{58}Ni)⁶, motivating a new procedure. Per standard treatments of nucleon pairing [91], an additional pairing parameter Δ was added to account for open subshells'

fractional occupation n_{\pm} . This parameter splits these subshells' occupants into upper and lower sublevels with energies E_{\pm} :

$$E_{\pm} = \mu \pm [(\epsilon_F - \mu)^2 + \Delta^2]^{\frac{1}{2}}, \quad (6.31)$$

where μ is the energy of the open subshell before pairing is considered and ϵ_F is the Fermi energy. The magnitude of Δ corresponds to the energy difference between adding/removing a nucleon to/from that subshell. The subshell is split between the upper and lower sublevels. The occupancy of these sublevels is calculated via:

$$n_{\pm} = \frac{1}{2} \left(1 - \frac{\chi}{E_{\pm}} \right), \quad (6.32)$$

where $\chi = |E_{\pm} - \mu| - (\epsilon_F - \mu)$. Only occupation in the lower sublevel is counted toward the total particle number. For each open-shell nucleus with neutron number N and proton number Z , Δ was fixed according to:

$$\Delta(N, Z) = \frac{1}{4} [B(N - 2, Z) - 3B(N - 1, Z) + 3B(N, Z) - B(N + 1, Z)], \quad (6.33)$$

where $B(N, Z)$ is the nuclear binding energy [91].

In addition to the total occupation of each state with quantum numbers α , the density distribution of particles in that state in r-space can be calculated. By summing the single-particle position-space distributions, the total point distributions for protons and neutrons can be calculated. After folding this distribution with an appropriate form factor associated with the internal charge density distribution for protons and neutrons [12], the final distri-

⁶The standard notations π and ν refer to proton and neutron subshells, respectively.

bution can be compared to the experimental charge density distribution calculated in (e,e) scattering experiments.

The total binding energy of the nucleus may be calculated directly from the spectral function and the kinetic energy operator \hat{T} :

$$\begin{aligned} E_0^N &= \langle \Psi_0^N | \hat{H} | \Psi_0^N \rangle \\ &= \frac{1}{2} \left[\sum_{\alpha, \beta} \langle \alpha | \hat{T} | \beta \rangle n_{\alpha, \beta} + \sum_{\alpha} \int_{-\infty}^{\epsilon_F^-} dE E S_h(\alpha; E) \right] \end{aligned} \quad (6.34)$$

and the discrete single-particle energy levels can be calculated by diagonalizing the Hamiltonian. It should be noted that while previous DOM treatments have calculated binding energies after fitting was complete, the present DOM treatment is the first to explicitly include the binding energy as part of the fitting process. The PhD thesis of M. Atkinson [92], published simultaneously with this work, includes an in-depth discussion of the energy density and presents fit results for $^{40,48}\text{Ca}$ and ^{208}Pb using an alternative DOM parameterization.

6.3 Parameterization of the Potential

As discussed earlier in this chapter, the irreducible nucleon self-energy is composed of both real and imaginary parts that govern elastic and inelastic processes, respectively. If the real part is broken into a static component Σ_s with no energy dependence and a dynamic part Σ_d with energy dependence, the self-energy reads:

$$\Sigma^*(\alpha, \beta; E) = \Sigma_s(\alpha, \beta) + \Sigma_d(\alpha, \beta; E) + \text{Im}(\Sigma^*(\alpha, \beta; E)). \quad (6.35)$$

No confusion should arise between Σ , the reducible self-energy introduced in Section 6.2.1, and the static and dynamic real irreducible self-energy components Σ_s and Σ_d of this equation. To parameterize the real and imaginary terms, functional forms are selected to conform with general physical intuition about the nuclear many-body problem and past experience with optical potentials. Accordingly, the self-energy should be, *non-local*, *complex*, and *dispersively correct*. Before the full parameterization is provided, a few standard mathematical forms need to be introduced. The free parameters that are fitted to data during the DOM procedure we **denote in bold**. Thus the bolded variables in this section do not denote vector quantities (which is a common notation in the literature). After the basic functional forms are introduced, all bolded free parameters are assigned numbers to facilitate comparison with the list of parameter values of Appendix C.

6.3.1 Functional Forms

We use two standard form factors to describe the radial dependence of components associated with the nuclear volume (a Woods-Saxon shape) and the nuclear surface (a derivative of the Woods-Saxon shape):

$$f_{vol}(r; \mathbf{r}_0, \mathbf{a}) = \frac{-1}{1 + e^{(r-\mathbf{R})/\mathbf{a}}}, \tag{6.36}$$

$$f_{sur}(r; \mathbf{r}_0, \mathbf{a}) = \frac{1}{r} \frac{d}{dr} f_{vol}(r; \mathbf{r}_0, \mathbf{a}).$$

\mathbf{R} is the nuclear radius, calculated as $\mathbf{R} = \mathbf{r}_0 A^{\frac{1}{3}}$, with A the total number of nucleons in the nucleus. The diffuseness term \mathbf{a} determines how quickly the potential tends to zero in the nuclear surface region. The sign of the potential is such that the Woods-Saxon form provides

an attractive interaction. To approximate the non-locality, equivalent local potentials [33] with an additional energy dependence may be used, but their additional energy-dependence violates the dispersion relation and thus makes local-equivalent potentials unsuitable for a comprehensive treatment at both positive and negative energies unless certain corrections are applied [33]. The self-energy/optical potential used in our treatment is based on that of [42], which was the first to fully implement the non-locality in the potential forms alongside the dispersion relation. For simplicity, we use a Gaussian non-locality first proposed by [93]:

$$N(r, r'; \boldsymbol{\beta}) = \frac{1}{\pi^{\frac{3}{2}} \boldsymbol{\beta}^3} e^{-|r-r'|^2/\boldsymbol{\beta}^2}, \quad (6.37)$$

where $\boldsymbol{\beta}$ is a free parameter that sets the Gaussian width. The energy-dependence of the imaginary components is based on the functional form of [94]:

$$\omega_n(E; \mathbf{A}, \mathbf{B}, \mathbf{C}) = \Theta(X) \mathbf{A} \frac{X^n}{X^n + \mathbf{B}^n} \quad (6.38)$$

where

$$X = |E - \epsilon_F| - \mathbf{C}$$

and $\Theta(X)$ is the Heaviside step function.

We are now ready to give the full parameterization. The parameterization for symmetric nuclei is simpler as the same potential is used for protons and neutrons, excepting Coulomb. For asymmetric systems, we introduce a handful of asymmetry-dependent additional terms. All calculations are non-relativistic with a first-order relativistic correction and do not explicitly account for nucleon excitations (e.g., the Δ resonance). Accordingly, the potential is not expected to be valid outside the domain $-300 \text{ MeV} < E < 200 \text{ MeV}$, which we used

during fitting.

6.3.2 Real Part

The energy-independent real part of the self-energy consists of a nonlocal Hartree-Fock and a spin-orbit component (plus a local Coulomb term if the nucleon in question is a proton):

$$\Sigma_s(r, r') = \Sigma_{HF}(r, r') + V_{so}(r, r') + \delta(r - r') \times V_C(r). \quad (6.39)$$

The Coulomb term is calculated using the same experimentally-derived charge density distributions (see [11]) used in fitting. Figure 6.3 shows the radial dependence of the Hartree-Fock and spin-orbit components of the real part of the potential. The Hartree-Fock component V_{HF} has two subcomponents:

$$\Sigma_{HF}(r, r') = V_{vol}(r, r') + V_{wb}(r), \quad (6.40)$$

where the non-local Hartree-Fock volume term $V_{vol}(r, r')$, is defined as a Woods-Saxon form coupled to a Gaussian non-locality:

$$V_{vol}(r, r') = \mathbf{V}_1 \times f_{vol}(r; \mathbf{r}_1, \mathbf{a}_1) \times N(r, r'; \beta_1). \quad (6.41)$$

The local Hartree-Fock wine-bottle term V_{wb} , named for resemblance to the dimple at the bottom of a wine bottle, is defined as a Gaussian centered at the nuclear origin:

$$V_{wb}(r) = \mathbf{V}_2 \times e^{r^2/\sigma_2^2}. \quad (6.42)$$

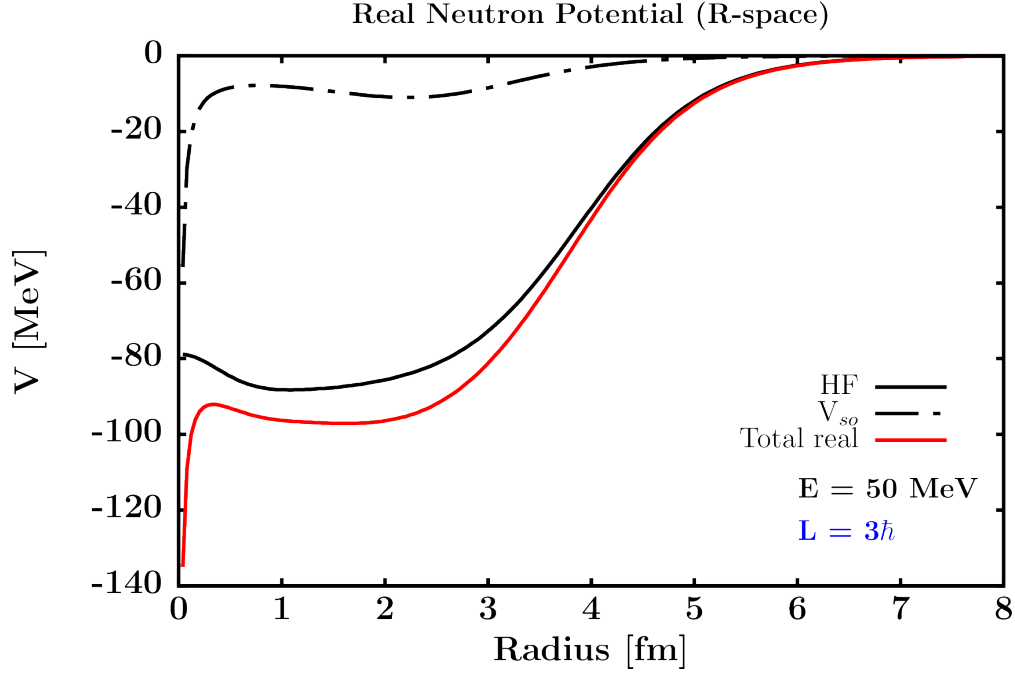


Figure 6.3: The local radial dependence of the real part of the neutron optical potential is shown for ^{58}Ni at 50 MeV for $l = 3\hbar$. The central Hartree-Fock term is the dominant component of the real potential and has a small wine-bottle contribution at the nuclear core (see Eq. 6.40). Per Eq. 6.43, the Woods-Saxon form of the real spin-orbit component is allowed to have a different radius and diffuseness compared to the Hartree-Fock Woods-Saxon form. In this fit, the radial component of the spin-orbit Woods-Saxon is smaller than that from the Hartree-Fock Woods-Saxon. The hyperbolic asymptotic growth of the real spin-orbit component at the origin is a consequence of the $\frac{1}{r}$ term in Eq. 6.43 but contributes negligibly to the volume integral of the real part of the potential.

The real spin-orbit component V_{so} is defined using a derivative-Woods-Saxon shape in keeping with the expectation that the spin-orbit coupling is strongest near the nuclear surface:

$$V_{so}(r, r') = \left(\frac{\hbar}{m_{\pi}c} \right)^2 \mathbf{V}_3 \times \frac{1}{r} f_{sur}(r; \mathbf{r}_3, \mathbf{a}_3) \times N(r, r'; \beta_3) \times (\ell \cdot \sigma). \quad (6.43)$$

The leading constant $\left(\frac{\hbar}{m_{\pi}c} \right)^2$ is taken to be 2.0 fm^2 [42]. The energy-dependent part of the real component of the potential, $\text{Re}(\Sigma_{\Delta}(\alpha, \beta; E))$, is generated using the imaginary component of the potential, according to the dispersion relation (Eq. 6.17). Figure 6.5 shows

the energy-dependent behavior of the dispersively-generated real part. This completes the parameterization of the real component.

6.3.3 Imaginary Part

The imaginary part of the potential is comprised of independent surface and volume terms both above and below the Fermi surface:

$$\text{Im}(\Sigma^*(r, r', E)) = \text{Im}(\Sigma_{vol}^\pm(r, r', E)) + \text{Im}(\Sigma_{sur}^\pm(r, r', E)), \quad (6.44)$$

where the volume and surface components are:

$$\begin{aligned} \text{Im}(\Sigma_{vol}^\pm(r, r', E)) &= W_{vol}^\pm(E) \times f_{vol}(r; \mathbf{r}_4, \mathbf{a}_4) \times N(r, r'; \boldsymbol{\beta}_4), \\ \text{Im}(\Sigma_{sur}^\pm(r, r', E)) &= 4\mathbf{a}_4 W_{sur}^\pm(E) \times f_{sur}(r; \mathbf{r}_4, \mathbf{a}_4) \times N(r, r'; \boldsymbol{\beta}_4). \end{aligned} \quad (6.45)$$

The terms labeled with + determine the potential above ϵ_F , and the terms labeled with – determine the potential below ϵ_F . Note that in this equation, the same Woods-Saxon variables and nonlocality are used for both imaginary surface and imaginary volume, both at positive and negative energies. Figure 6.4 shows the radial dependence of the imaginary components of the potential. Compared to parameterizations used in previous DOM treatments, the parameterization given here reduces by nine the number of r-space parameters used for the imaginary surface and volume terms. The energy dependence of the imaginary volume term reads:

$$W_{vol}^\pm(E) = \mathbf{A}_5^\pm \left[\frac{(E_\Delta)^4}{(E_\Delta)^4 + (\mathbf{B}_5^\pm)^4} + W_{NM}^\pm(E) \right], \quad (6.46)$$

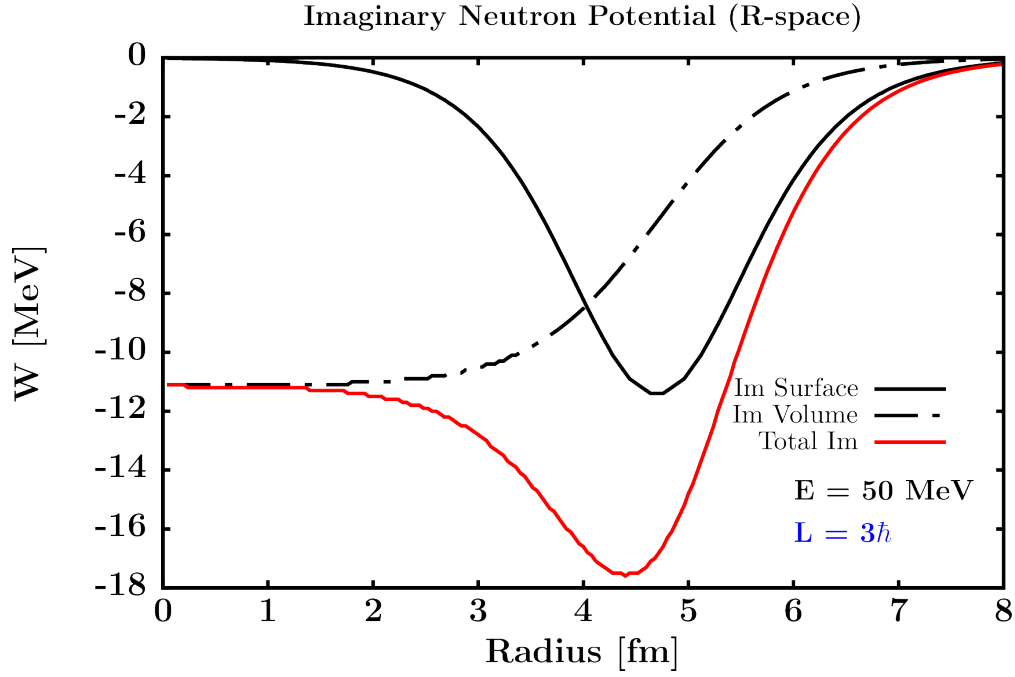


Figure 6.4: The local radial dependence of the imaginary part of the neutron optical potential is shown for ^{58}Ni at 50 MeV for $l = 3\hbar$. At this energy, there are significant contributions from both the surface- and volume-associated terms.

where $E_\Delta = |E - \epsilon_F|$ and

$$\begin{aligned}
 W_{NM}^+(E) &= \alpha_6 \left[\sqrt{E} + \frac{(\epsilon_F + \mathbf{E}_6^+)^{\frac{3}{2}}}{2E} - \frac{3}{2} \sqrt{\epsilon_F + \mathbf{E}_6^+} \right], \\
 W_{NM}^-(E) &= \frac{(\epsilon_F - E - \mathbf{E}_6^-)^2}{(\epsilon_F - E - \mathbf{E}_6^-)^2 + (\mathbf{E}_6^-)^2}.
 \end{aligned} \tag{6.47}$$

The terms W_{NM}^\pm are asymmetric above and below the Fermi surface and are modeled after nuclear-matter calculations. They account for the decreasing phase space at negative energies and the increasing phase space at positive energies. The imaginary surface terms read:

$$W_{sur}^\pm(E) = \omega_4(E, \mathbf{A}_7^\pm, \mathbf{B}_7^\pm, 0) - \omega_2(E, \mathbf{A}_7^\pm, \mathbf{B}_7^{\prime\pm}, \mathbf{C}_7^\pm) + \mathbf{W}_7 \times (\ell \cdot \sigma), \tag{6.48}$$

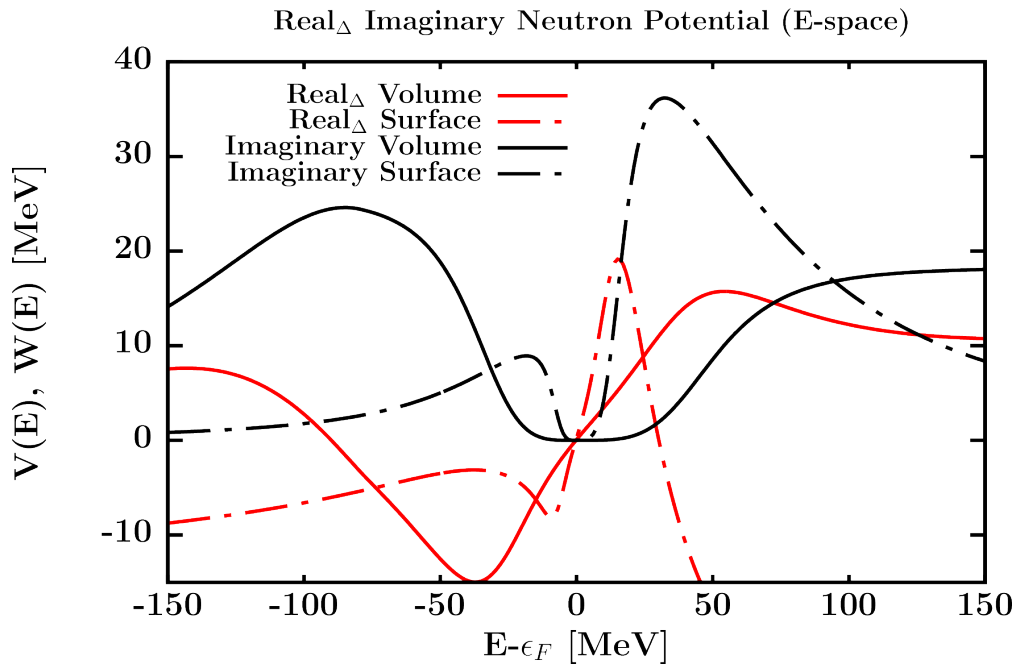


Figure 6.5: Typical energy dependence of the imaginary part and the dispersion-relation-generated energy-dependent real part of the neutron optical potential are shown for ^{58}Ni .

where ω_n was defined in Eq. 6.38, and \mathbf{W}_7 represents the change in the imaginary surface strength due to an imaginary spin-orbit force. An imaginary spin-orbit contribution has been seen to be useful in previous optical-model treatments in order to reproduce the high-energy analyzing power data. Figure 6.5 depicts the energy-dependence of the imaginary terms in the potential and the energy-dependence of the dispersive correction to the real part of the potential. For comparison to other models and to compare the potential between nuclei, the volume integral of the potential is the most useful. An example for the neutron imaginary potential ^{58}Ni is shown in Fig. 6.6. This completes the parameterization of the potential for symmetric nuclei.

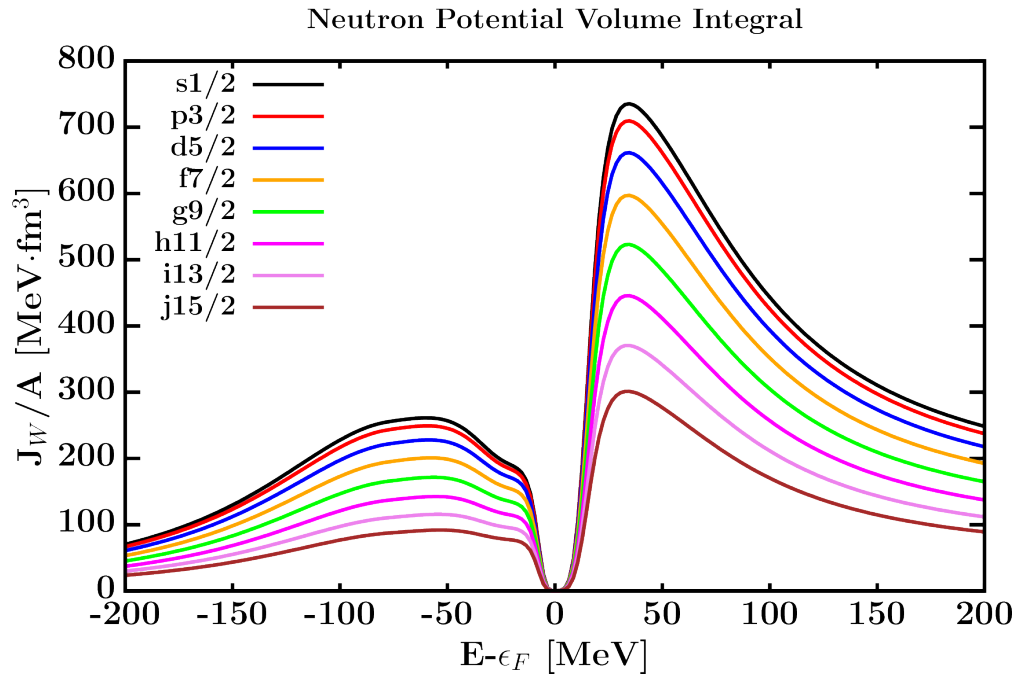


Figure 6.6: Volume integrals of imaginary part of the neutron optical potential are shown for ^{58}Ni for the relevant LJ quantum numbers. At this energy, there are significant contributions from both the surface- and volume-associated terms.

6.3.4 Parameterization of Asymmetry Dependence

For asymmetric nuclei, the parametric forms must be modified to account for the different potential experienced by protons and neutrons. Previous DOM treatments have created entirely separate proton and neutron potentials, each having all the free parameters used in the symmetric parameterization presented above. For example, the fit of ^{48}Ca in [42] used over sixty unique parameters. Such an abundance of parameters risks overfitting, which can hamper interpretation and predictive power. To reduce this risk, in this analysis we allowed only a select handful of parameters to differ between neutrons and protons. Of the ten free parameters used for the real potential in the symmetric parameterization above, only the

depth of the central potential, V_1 from Eq. 6.41, is allowed to vary with asymmetry:

$$V_1 \Rightarrow \begin{cases} V_1 + V_{asym} \times \frac{N-Z}{A} & \text{for protons} \\ V_1 - V_{asym} \times \frac{N-Z}{A} & \text{for neutrons.} \end{cases} \quad (6.49)$$

Of the nineteen free parameters used for the imaginary potential in the asymmetric parameterization above, the magnitude of the energy-dependence for the imaginary surface and volume, A_5^\pm and A_7^\pm from Eqs. 6.46 and 6.48, are allowed to vary with asymmetry:

$$A_5^\pm \Rightarrow \begin{cases} A_5^\pm + A_{vol,asym}^\pm \times \frac{N-Z}{A} & \text{for protons} \\ A_5^\pm - A_{vol,asym}^\pm \times \frac{N-Z}{A} & \text{for neutrons,} \end{cases} \quad (6.50)$$

$$A_7^\pm \Rightarrow \begin{cases} A_7^\pm + A_{sur,asym}^\pm \times \frac{N-Z}{A} & \text{for protons} \\ A_7^\pm - A_{sur,asym}^\pm \times \frac{N-Z}{A} & \text{for neutrons.} \end{cases} \quad (6.51)$$

There should be no confusion between $A_{5,7}^\pm$, A (the total number of nucleons), and the analyzing power. With these four additional asymmetric imaginary terms, the total number of free parameters used for fitting asymmetric nuclei in the present work comes to thirty-four: eleven real, twenty-three imaginary.

6.4 Computational Considerations

As with any high-dimensional optimization problem, the fitter must be vigilant against the overfitting of data. In practice, this requires:

- parsimony with the number of parameters used in the model,

- checking “under the hood” during optimization to verify that parameter values are sensible, given the assumptions that undergird the model,
- understanding of what the value function is (i.e., the function being optimized) and whether certain experimental data are being privileged over others, and
- that the cross-correlation between parameters is understood.

As was pointed out by Koning and Delaroche [30], large-scale fitting to experimental data is part science, part art: fits should deviate as little as possible from the experimental values but also be aesthetically acceptable to the eye of the fitter. Thus the preconceptions of the fitter play a major role in the definition of the potential forms, the starting values of the parameters, and the conclusion that a fit is “good enough” to stop fitting. For an extrapolation from a fit to be well-justified, the fitted potential should be physically reasonable throughout its domain and each parameter used in the fit should be well-constrained by the data.

To conclude this chapter, we briefly mention a few preconceptions that guided our expectations on how the nuclear potential should look. Based on countless optical model analyses over the last fifty years, the Woods-Saxon radius parameters r_0 and diffuseness parameters a were expected to be 1.1-1.2 fm and 0.5-0.7 fm, respectively. As non-local behavior is at least partially associated with Pauli-exclusion-principle arguments, our fitted non-localities β are expected to stay between 0.5-1.5 fm, commensurate with the size of the nucleon. In the energy domain, above the Fermi level, the imaginary strength is expected to be dominated by the surface-associated term from 0-50 MeV and by the volume-associated term from 50 MeV upward, keep flat beyond 200 MeV to agree with measurements of inelastic nucleon-nucleon scattering in the GeV regime. Below the Fermi surface, the imaginary strength is at first largely symmetric to that of the positive-energy regime, then tapers off as the phase

space is reduced. Especially for smaller nuclei like ^{16}O and even for ^{40}Ca , it is difficult to cleanly separate the negative-energy imaginary surface and imaginary volume terms, and this separation may not be physically meaningful anyway. These general trends comport with the expectation that low-lying excitations (surface phonons and collective modes) and two-particle-one-hole excitations should be responsible for most surface imaginary strength.

6.4.1 Fitting Procedure

The Powell minimization method, outlined in Numerical Recipes in C [95], was used to minimize the χ^2 between experimental data points and the values calculated from the DOM potential. A weighting scheme was assigned to the data points according to the number of data sets for each sector of experimental data (e.g., $\frac{d\sigma}{d\Omega}$, binding energies) and to their relative importance, guiding the fit to reproduce the most essential data. From fit to fit, the weighting scheme was adjusted as necessary to escape local minima and reproduce the broadest range of experimental data.

The radial grid, energy grid, size of the Lagrange and Laguerre bases, partial wave angular momentum cutoff, and various integration cutoffs used in calculating the potential and observable quantities were varied to ensure that results were not distorted by rounding or truncation errors.

**DISPERSIVE OPTICAL MODEL:
RESULTS ON $^{16,18}\text{O}$, $^{40,48}\text{Ca}$, $^{58,64}\text{Ni}$, $^{112,124}\text{Sn}$, ^{208}Pb**

The DOM fits on $^{16,18}\text{O}$, $^{40,48}\text{Ca}$, $^{58,64}\text{Ni}$, $^{112,124}\text{Sn}$, and ^{208}Pb presented in this chapter are the culmination of the new σ_{tot} and $\frac{d\sigma}{d\Omega}$ experimental results (Chapters 3 and 5) and new computational improvements in our DOM code (Chapter 6). Previous DOM treatments have either used a local equivalent potential [94, 96] or only provided results on one or two nuclei [59, 97]. All nine fits detailed here use the same fully-non-local approach (outlined in chapter 6) and lay the groundwork for a comprehensive DOM treatment across the chart of nuclides.

Beginning with ^{40}Ca , results from our new analyses of $^{40,48}\text{Ca}$ are compared to the previous DOM analyses of [42] and [97]. Highlights from our results on $^{16,18}\text{O}$, $^{58,64}\text{Ni}$, $^{112,124}\text{Sn}$, and ^{208}Pb are then presented; a complete picture of the fits on these nuclei is reserved for Appendix D. Last, general trends are identified across all nine nuclei and successes and deficiencies of the present DOM treatment are pointed out. A complete list of experimental data used to constrain the fits is provided in Appendix B. The best-fit parameter values for each nucleus are given in Appendix C.

7.1 Results for $^{40,48}\text{Ca}$

As doubly-closed, mid-A nuclei, $^{40,48}\text{Ca}$ are heavy enough for both density functional theory (DFT) calculations [57] and light enough for certain *ab initio* treatments [98]. As such, they have long been cornerstone nuclei for nuclear modeling. The size of the neutron skin of ^{48}Ca (along with that of ^{132}Sn and ^{208}Pb) is of great theoretical interest as it is expected to be tightly correlated with the density-dependence of the symmetry energy [56]. A model-independent determination of the neutron skin thickness of ^{48}Ca is the goal of the upcoming parity-violating electron scattering measurement CREX [53]. Given this degree of interest in Ca isotopes, optical models have been applied to $^{40,48}\text{Ca}$ more than almost any other nuclei. Thanks to the great deal of high-quality $^{40,48}\text{Ca}$ elastic and inelastic nucleon scattering data, quasi-free scattering data, and elastic electron scattering data available, $^{40,48}\text{Ca}$ are ideal candidates to test the DOM approach. To orient the reader and facilitate a comparison to previous DOM treatments, the $^{40,48}\text{Ca}$ fit results are presented in greater detail than are the fit results on $^{16,18}\text{O}$, $^{58,64}\text{Ni}$, $^{112,124}\text{Sn}$, and ^{208}Pb presented in later sections.

7.1.1 Results for ^{40}Ca

As with previous DOM treatments of ^{40}Ca [42, 99], the present fit quickly converged on proton and neutron elastic and inelastic scattering data from 10-200 MeV (shown in Figs. 7.1 and 7.2). Because the ^{40}Ca proton σ_{rxn} has been measured up to 200 MeV, the energy-dependence of the imaginary volume potential, W_{vol}^+ , was well-constrained, expediting the fitting process and lending confidence to the quality of our fit. Inelastic scattering data for protons and neutrons on ^{40}Ca are shown in Figs. 7.3 and 7.4.

Table 7.1 shows the nucleon occupancy associated with each set of quantum numbers

Table 7.1: ^{40}Ca proton and neutron occupancies by orbital angular momentum L and total angular momentum J from our DOM analysis. While most of the particle occupancy resides in states completely filled in an independent-particle-model ($0s_{\frac{1}{2}}$, $0p_{\frac{3}{2}}$, $0p_{\frac{1}{2}}$, $0d_{\frac{5}{2}}$, $0d_{\frac{3}{2}}$, and $1s_{\frac{1}{2}}$ for ^{40}Ca), more than 10% of the occupancy appears in higher-angular-momentum states.

LJ	$s_{\frac{1}{2}}$	$p_{\frac{3}{2}}$	$p_{\frac{1}{2}}$	$d_{\frac{5}{2}}$	$d_{\frac{3}{2}}$	$f_{\frac{7}{2}}$	$f_{\frac{5}{2}}$	$g_{\frac{9}{2}}$	$g_{\frac{7}{2}}$	$\ell > 4$	Total
π_{occ}	3.455	3.628	1.807	5.265	3.391	0.426	0.246	0.295	0.195	1.374	20.08
ν_{occ}	3.452	3.624	1.803	5.257	3.39	0.421	0.244	0.291	0.192	1.351	20.02

LJ as calculated from our ^{40}Ca fit. We see slightly less depletion of the proton $1s_{\frac{1}{2}}$ and $0d_{\frac{3}{2}}$ occupancy than the treatments of [42, 59], but there is qualitative agreement. In both treatments, the correct total proton and neutron numbers were achieved within 1% of the real values. From Fig. 7.8, it is clear that without significant depletion of the proton $0s_{\frac{1}{2}}$ and $1s_{\frac{1}{2}}$ shells, the charge density at the core of ^{40}Ca would be too high, a characteristic failure of mean-field models that do not account for depletion. The spectral functions of ^{40}Ca nucleons that we extract from the fit (Fig. 7.6) show spectral peak broadening compared to the mean-field expectation, in keeping with (e,e'p) and (p,2p) measurements [9, 10].

From the spectral functions, the momentum-space distribution for protons and neutrons was calculated (shown in Figs. 7.9 and 7.10). The amount of “high-momentum content” of these distributions is of great interest, as significant high-momentum content indicates deviation from the mean-field picture due to short-range correlations (SRCs). SRCs arise even in very light nuclear systems (e.g., ^4He) and are associated with an altered quark distribution in nucleons [100, 101, 102]. Tensor-force interactions in neutron-proton pairs are thought to be a dominant source of SRCs [103]. Thus in symmetric nuclei like ^{12}C and ^{40}Ca , the high-momentum content is expected to be nearly the same for protons and neutrons, whereas in asymmetric nuclei like ^{208}Pb , the minority nucleon species is expected to have

a larger high-momentum tail in the momentum distribution. In [104], the ^{12}C proton and neutron momentum distributions showed that $\approx 10\%$ of the nucleon density has momentum above roughly 270 MeV/c. We recover high-momentum fractions of 13.9% and 14.6% for protons and neutrons in ^{40}Ca , respectively.

The total binding energy for ^{40}Ca is readily calculated using Eq. 6.34. Its radial dependence is shown in Fig. 7.14 and the contributions to the binding energy from each single-particle LJ are shown in 7.13. Per our fit, even though the $0s_{\frac{1}{2}}$ nucleons are only about 9% of the total nucleons in ^{40}Ca , they provide a significant share of the binding energy (35%). As the spectral functions (Fig. 7.6) reveal, $0s_{\frac{1}{2}}$ nucleons spend a small but significant portion of their time at very negative energies (< -100 MeV), pulling the weighted average binding energy closer to 8.5 MeV/A, the experimentally-known binding energy for ^{40}Ca . Even in our fits that possess a large negative-energy tail, we still underpredict the binding by roughly 2 MeV/A. It appears that a better description of nucleon-nucleon correlations at extreme negative energies is required to locate the remaining binding energy.

Lastly, from the proton and neutron point distributions generated by our fit, we calculate a ^{40}Ca neutron skin for of -0.056 fm (see Fig. 7.12). This is in good agreement with the skin calculated in previous DOM treatments [42] and with the expectation that the neutron skin should be slightly negative in symmetric nuclei, a consequence of Coulomb repulsion nudging proton density toward the surface.

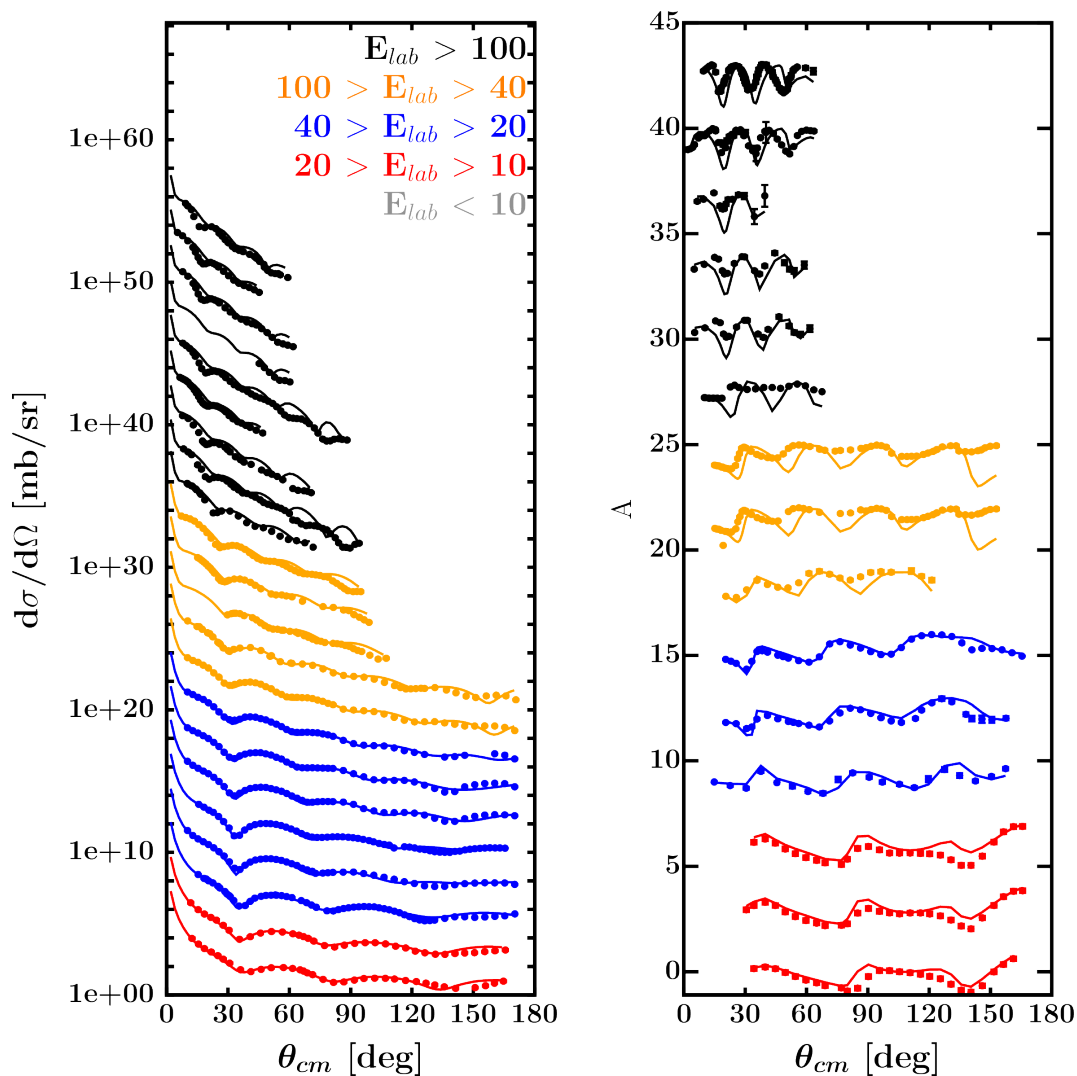


Figure 7.1: Proton elastic scattering cross sections on ^{40}Ca : experimental data and results from DOM fit. Experimental data are shown as points and calculated values from the DOM fit of these data are shown as lines. Differential cross sections ($\frac{d\sigma}{d\Omega}$) are shown in the left panel and analyzing powers are shown in the right panel. For visual clarity, the data have been offset along the ordinate axis so that the highest-energy data appear at the top of the figures. Data are colored according to the energy ranges shown in the left panel. References to all experimental data are listed in Appendix B.

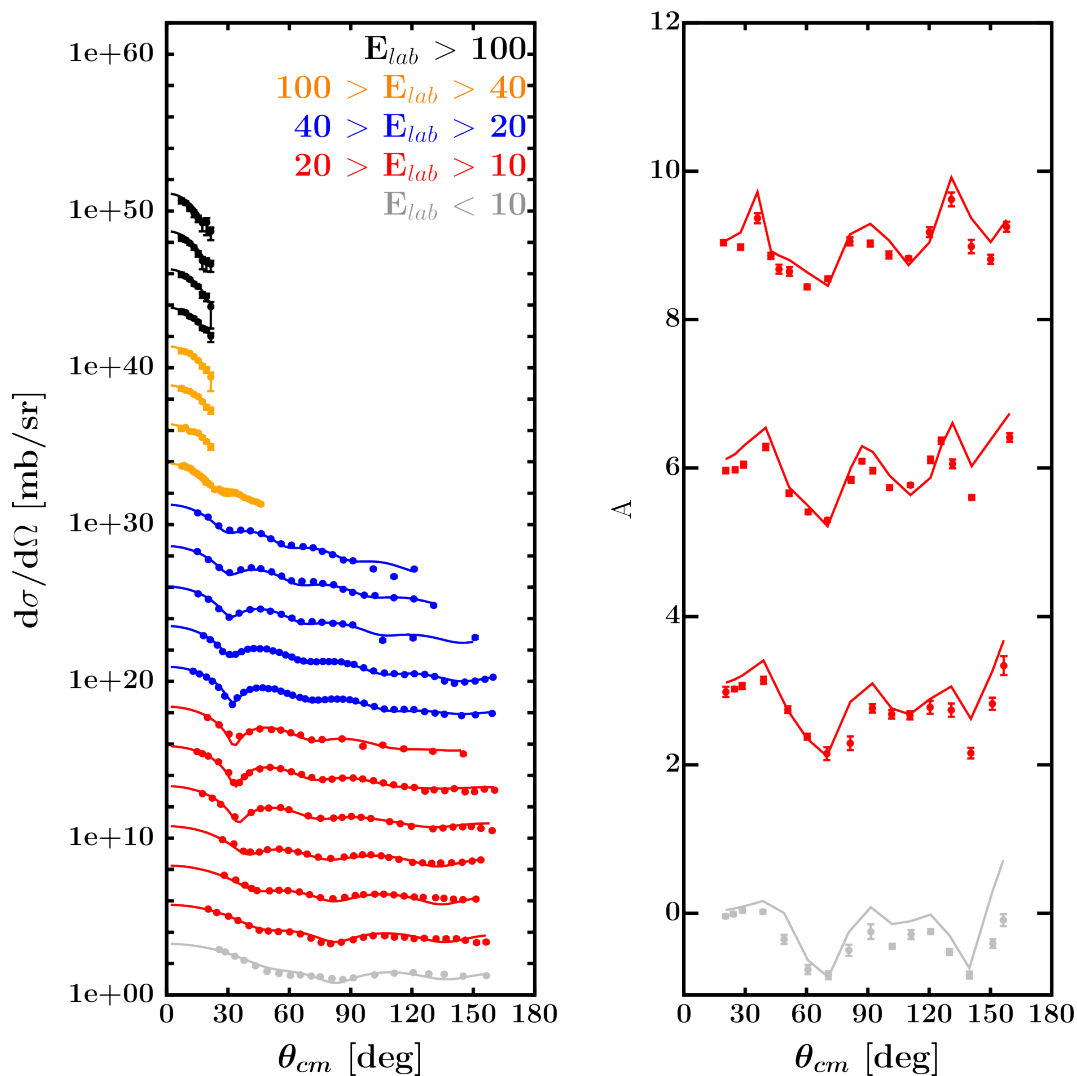


Figure 7.2: Neutron elastic scattering cross sections on ^{40}Ca : experimental data and results from DOM fit. Experimental data are shown as points and calculated values from the DOM fit of these data are shown as lines. Differential cross sections ($\frac{d\sigma}{d\Omega}$) are shown in the left panel and analyzing powers are shown in the right panel. For visual clarity, the data have been offset along the ordinate so that the highest-energy data appear at the top of the figures. Data are colored according to the energy ranges shown in the left panel. References to all experimental data are listed in Appendix B.

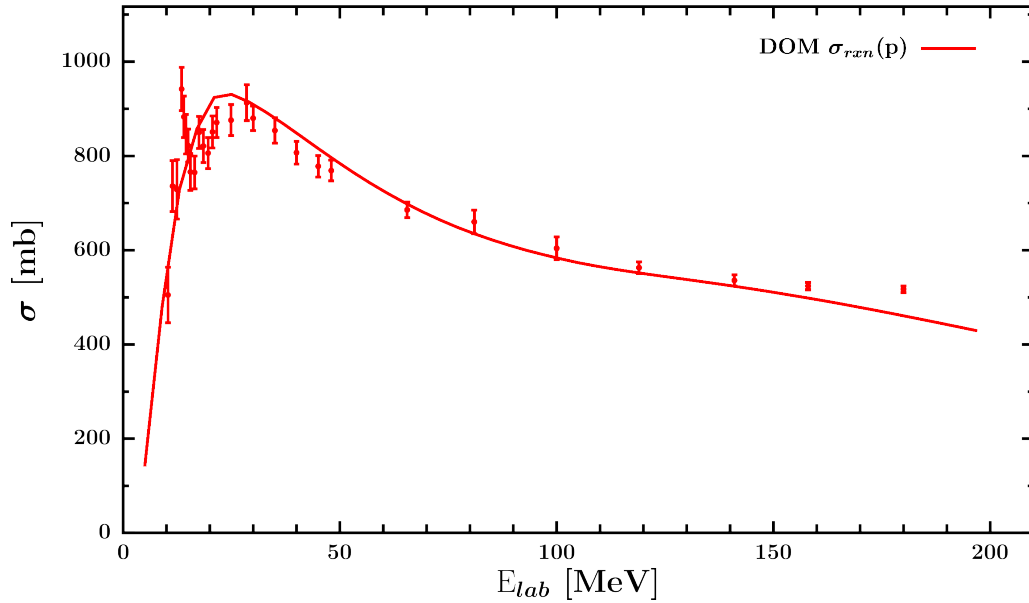


Figure 7.3: Proton reaction cross sections on ^{40}Ca : experimental data and DOM predictions. Experimental data are shown as points and calculated values from our DOM fit of these data are shown by the line. References to all experimental data are listed in Appendix B.

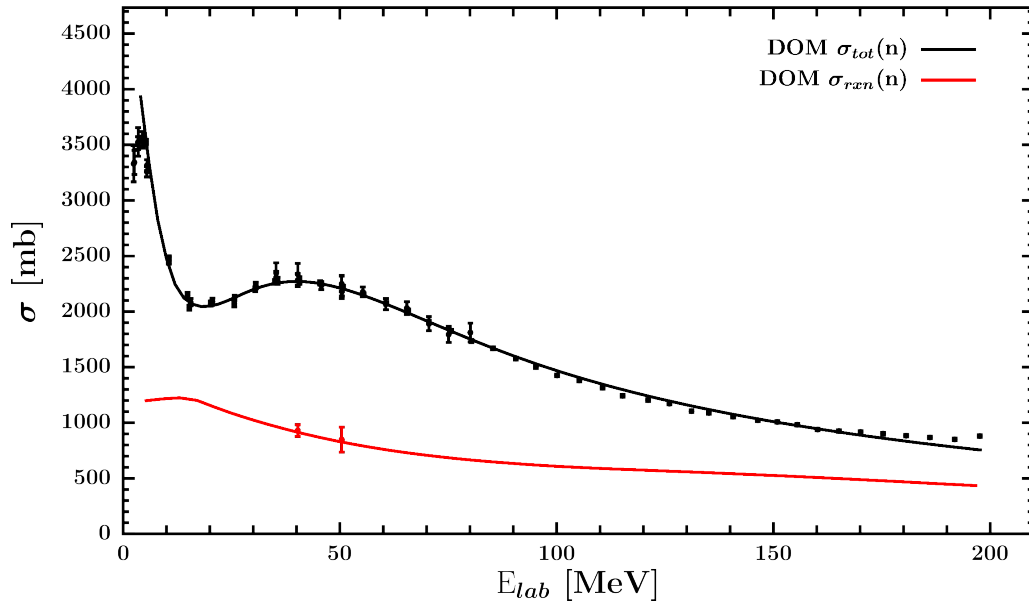


Figure 7.4: Neutron reaction and total cross sections on ^{40}Ca : experimental data and DOM predictions. Experimental data are shown as points and calculated values from our DOM fit of these data are shown by the line. References to all experimental data are listed in Appendix B.

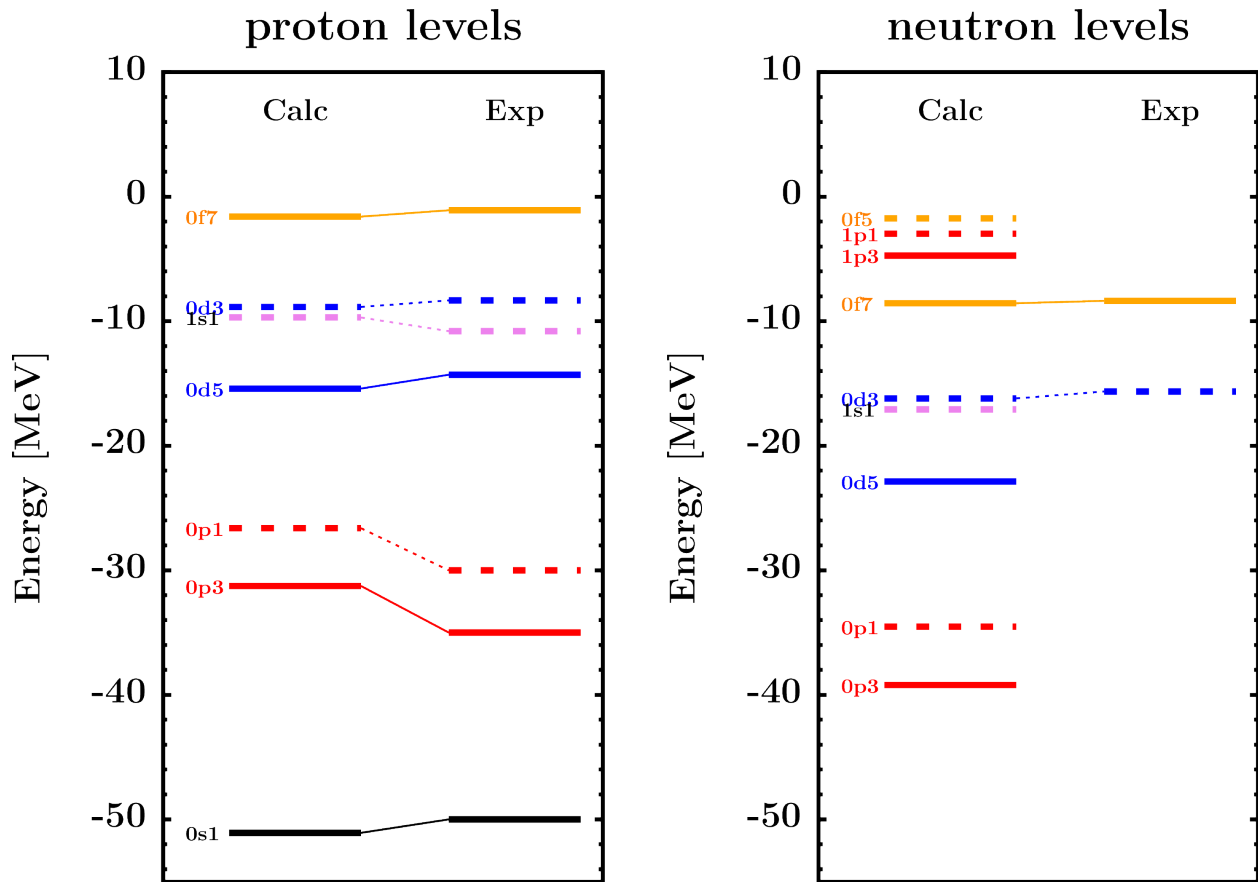


Figure 7.5: Single-particle energy levels in ^{40}Ca for protons and neutrons. In each panel, calculated energies are shown on the left and experimental energies are shown on the right. References to all experimental data used to estimate these energy levels are listed in Appendix B.

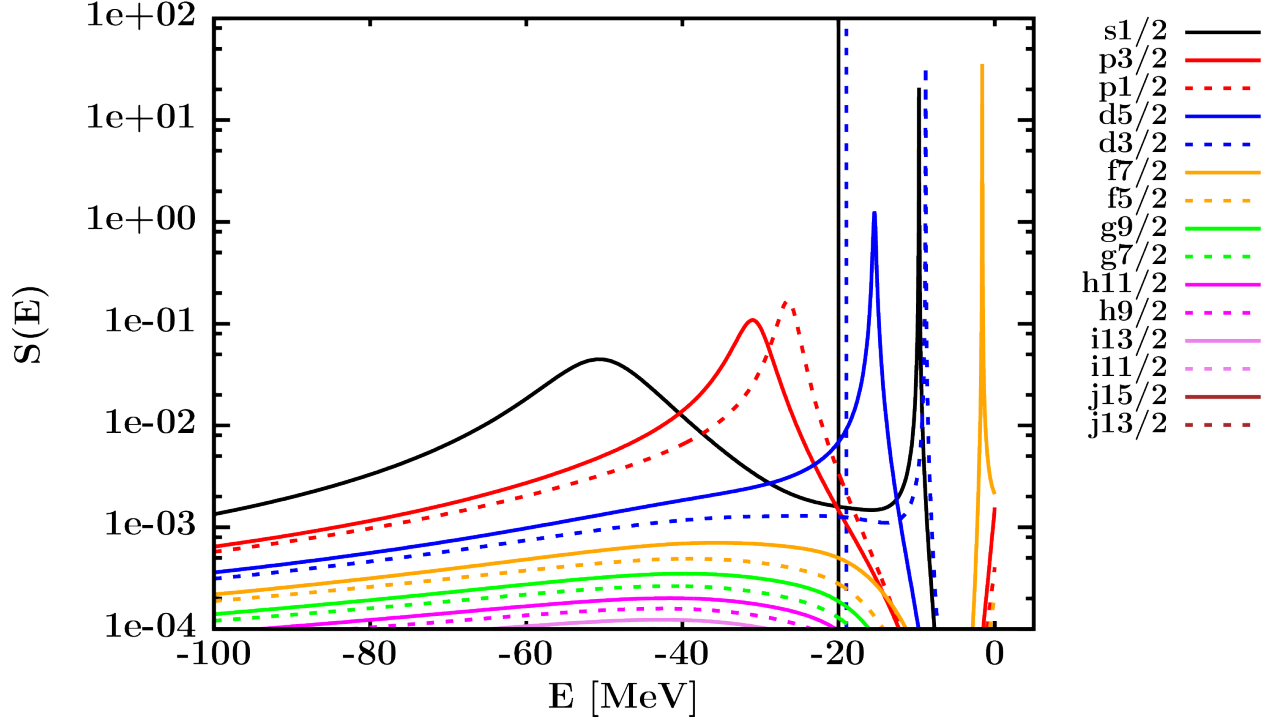


Figure 7.6: Proton spectral functions by orbital angular momentum L and total angular momentum J in ^{40}Ca , as generated by our DOM fit. In deeply-bound shells, spectral peak broadening is obvious, a consequence of increased imaginary strength in the self-energy at energies far from the Fermi energy. The shape and location of the *neutron* spectral functions in ^{40}Ca are similar except for a Coulomb shift. The general shape and degree of occupation depletion associated with our spectral functions agree with results of (p,2p) and (e,e'p) scattering and former DOM treatments [42]. The vertical lines at 20 MeV show the threshold used to calculate particle numbers in the $s_{\frac{1}{2}}$ and $d_{\frac{3}{2}}$ shells, per the discussion following Eq. 6.29.

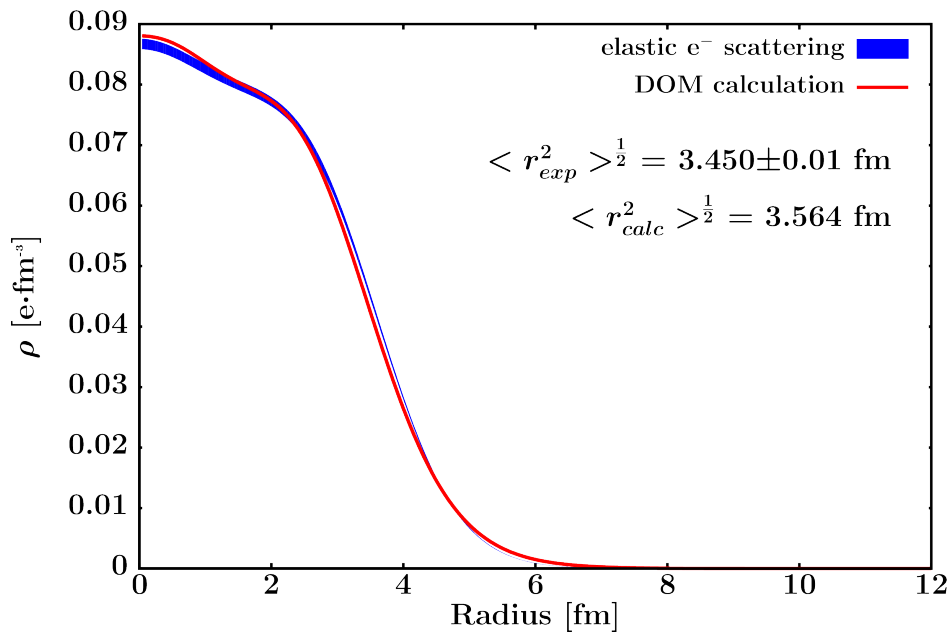


Figure 7.7: Charge density distribution of ^{40}Ca , as generated by our DOM fit (in red) and as generated from experimental elastic electron scattering [11]. No error bars are reported in the compilation of [11]; we show an arbitrary uncertainty range of 1% (blue shaded region).

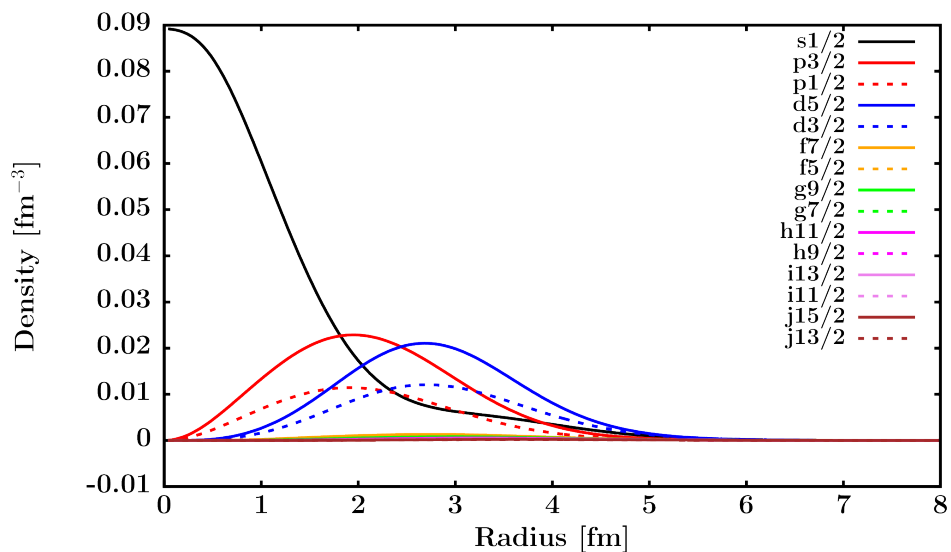


Figure 7.8: Proton single-particle density distributions in ^{40}Ca , as generated by our DOM fit. Only the $s_{1/2}$ has density at the origin, which means that to recover the correct charge density at the origin, the occupation of the proton $0s_{1/2}$ and $1s_{1/2}$ in ^{40}Ca must be depleted by 20-30%. That the bound LJs are significantly depleted indicates the importance of accounting for short- and long-range correlations when extracting structural information.

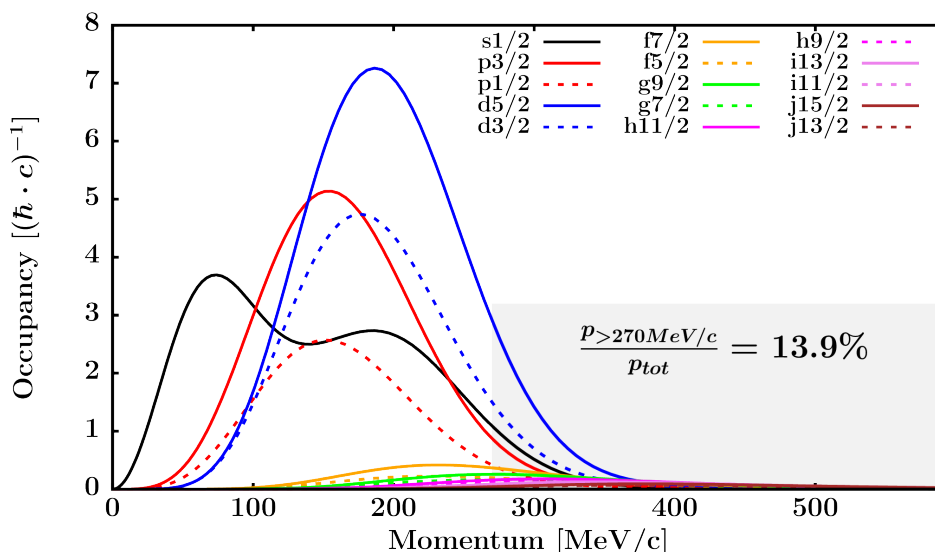


Figure 7.9: Integrated proton momentum distribution in ^{40}Ca , as generated by our DOM fit. For the slightly-occupied proton $f_{7/2}$, $f_{5/2}$, and $g_{9/2}$ and higher shells (which are completely vacant in an independent-particle model), a significant fraction of their density lies above 270 MeV/c (indicated by the shaded gray region). The fraction of proton high-momentum content (i.e., above 270 MeV/c) is listed.

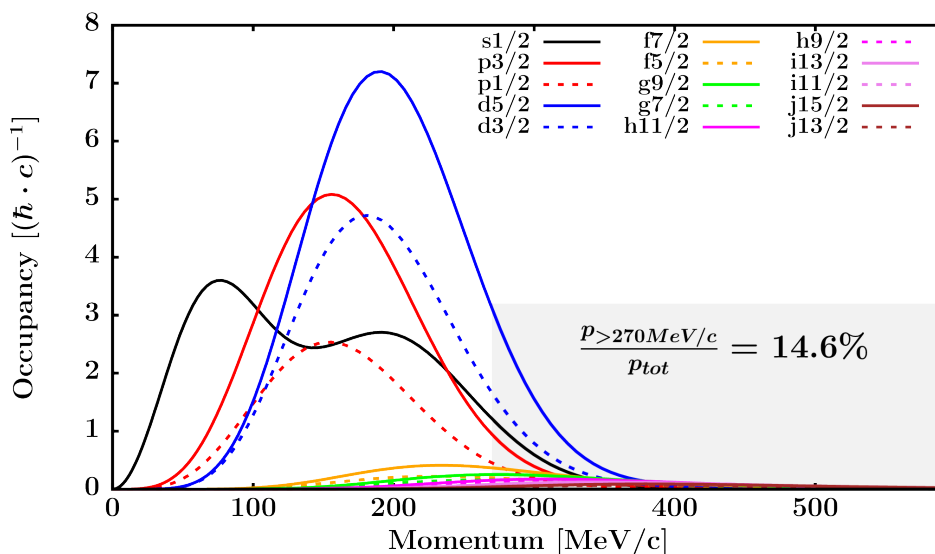


Figure 7.10: Integrated neutron momentum distribution in ^{40}Ca , as generated by our DOM fit. The slightly-occupied neutron $f_{7/2}$, $f_{5/2}$, and $g_{9/2}$ shells make a significant contribution to the high-momentum content above 270 MeV/c (indicated by the shaded gray region), as is true for the protons in the figure at top of the page. The fraction of neutron density with momentum above 270 MeV/c is listed.

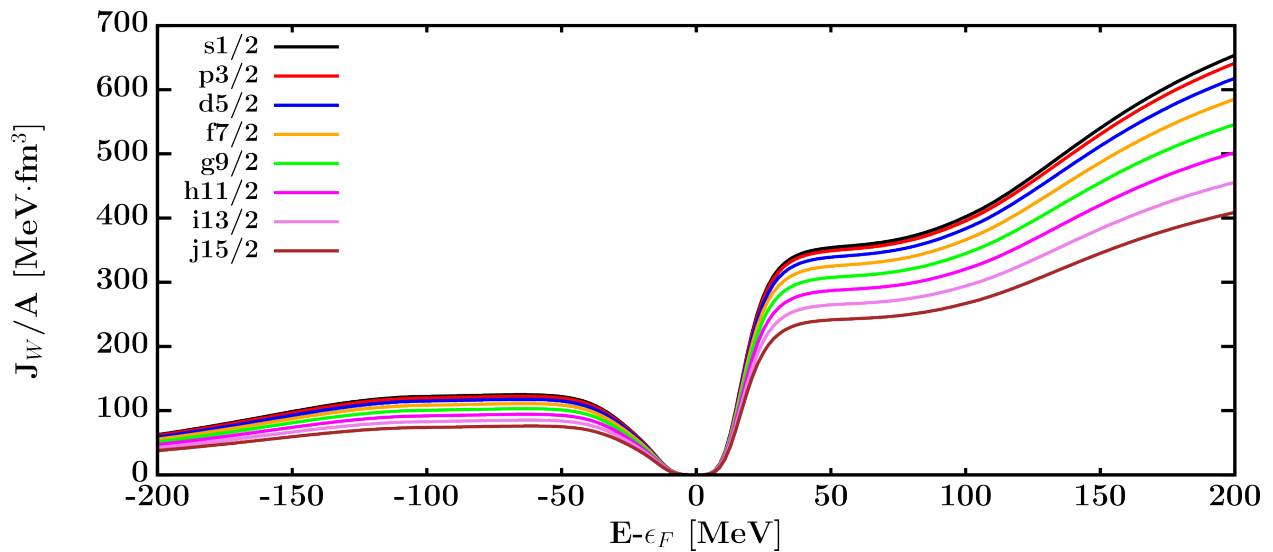


Figure 7.11: Volume integral of proton imaginary potential in ^{40}Ca . Above the Fermi energy, the surface-associated and volume-associated strength are clearly identifiable around 40 MeV and above 100 MeV, respectively. Near the Fermi energy, the potential is symmetric. Below the Fermi energy, the reduction of phase space reduces the magnitude of imaginary strength, but even at very negative energies, there is some strength. The small – but significant – occupation at very negative energies make an outsized contribution to the total binding energy.

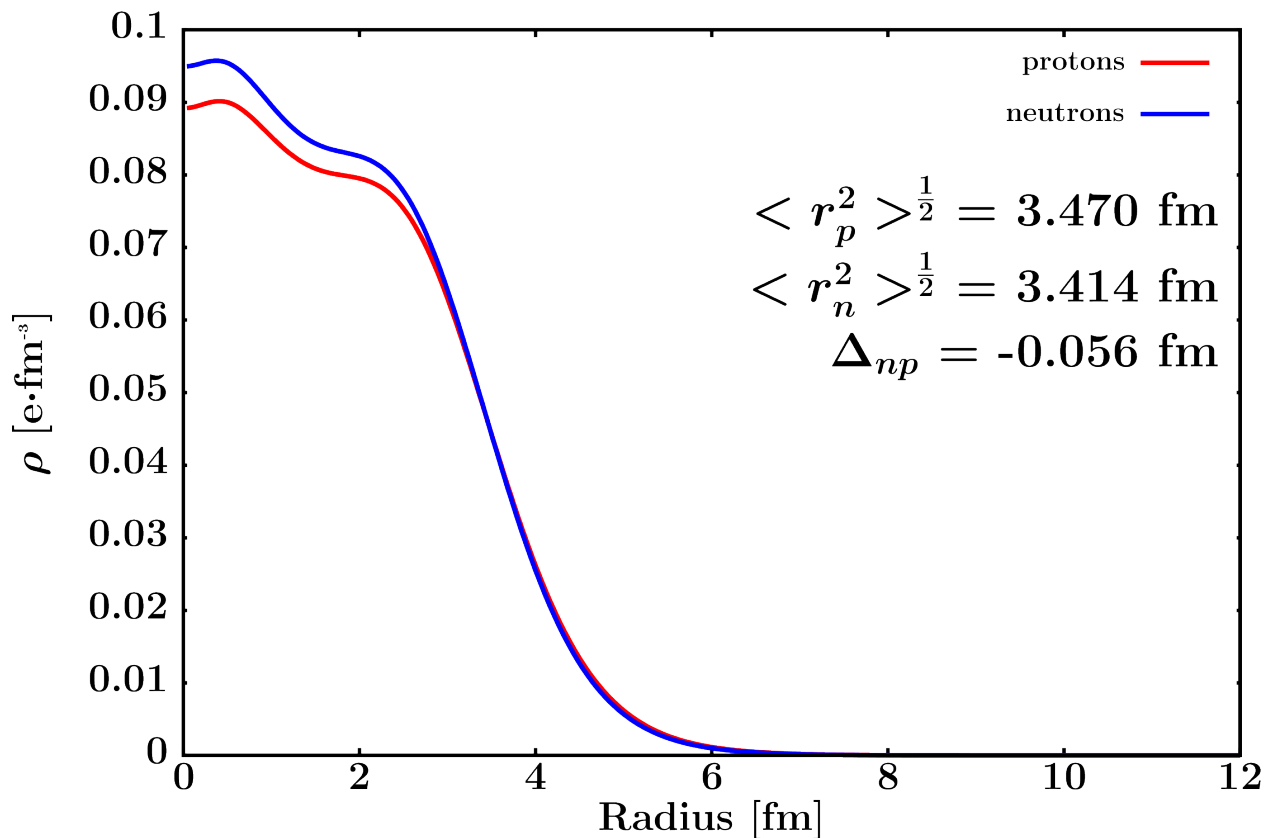


Figure 7.12: Proton and neutron point density distributions in ^{40}Ca , as generated by our DOM fit. The RMS radii of the distributions and their difference (the neutron skin) are provided. In a symmetric system like ^{40}Ca , the neutron skin is expected to be slightly negative as a consequence of slight reduction of proton density in the core from Coulomb repulsion. The neutron skin we extract is in good agreement with the previous DOM fit of [42]. A comparison to the experimental ^{40}Ca charge density distribution is shown in Section D.3 of Appendix D.

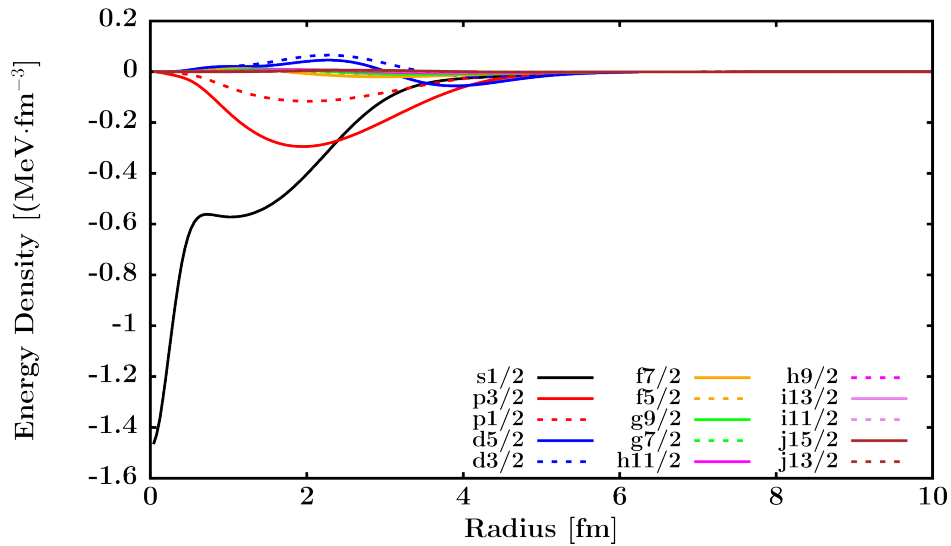


Figure 7.13: Energy density distribution for protons in ^{40}Ca , as generated by our DOM fit. Valence nucleons (e.g., in the proton $1s_{\frac{1}{2}}$ and $0d_{\frac{3}{2}}$ subshells in ^{40}Ca) contribute only slightly to the binding energy.

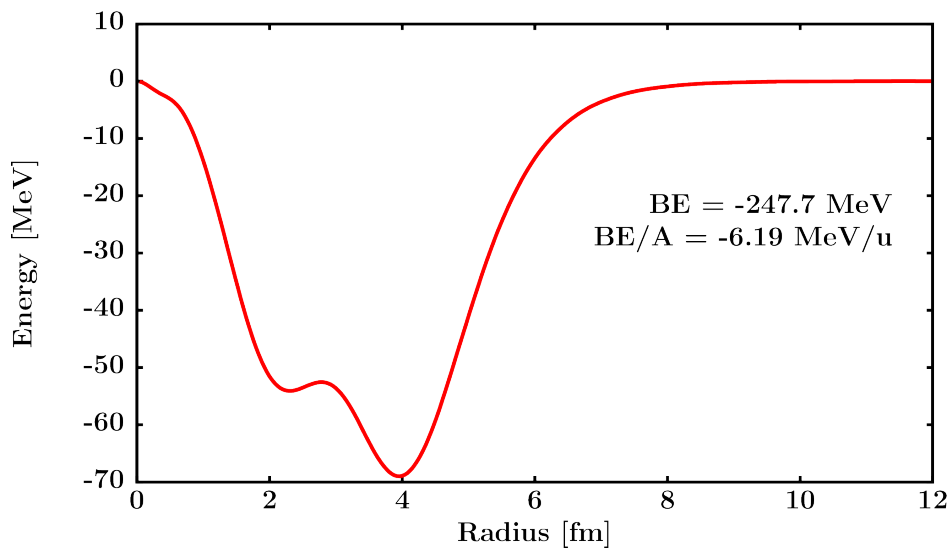


Figure 7.14: Total energy density integral in ^{40}Ca , as generated by our DOM fit. The total binding energy and binding energy per nucleon are given.

7.1.2 Results for ^{48}Ca

The recent non-local DOM treatment of Mahzoon et al. [59] was able to reproduce a wide variety of experimental data on ^{48}Ca and recovered a ^{48}Ca neutron skin of 0.249 ± 0.023 fm. This neutron skin value is significantly higher than the 0.132 fm calculated by the *ab initio* treatment of [98]. Mahzoon et al. found that when the smaller *ab initio* neutron skin size was forcibly applied to their fit, it disturbed the fit's reproduction of experimental ^{48}Ca neutron σ_{tot} data, implying that the neutron σ_{tot} might be sensitive to the neutron skin thickness. In this work, our fit on ^{48}Ca uses essentially the same experimental data used by Mahzoon et al. but less than half as many potential parameters.

There are fewer available elastic nucleon scattering data sets for ^{48}Ca compared to ^{40}Ca , so it was somewhat more difficult to nail down the real terms of the potential. Still, with both proton elastic scattering data sets and a complete neutron total cross section data set in hand, we did not have too much trouble converging on a reasonable asymmetry-dependence for the depth of the real central potential V_{asym} . This term sets the relative depth of the central potential for protons and neutrons and thus is moderately important for the size of the neutron skin. A more serious problem was the lack of proton σ_{rxn} data above 48 MeV, as it meant that the magnitude parameter of the imaginary volume asymmetry $A_{\text{vol,asym}}^{\pm}$ was very difficult to constrain. In our final optimization, we have a rather low value of W_{vol}^+ for ^{48}Ca compared to that of ^{40}Ca (compare Fig. 7.11 with Fig. 7.15).

Figure 7.16 shows the matter density distribution of ^{48}Ca per our fit. Compared to ^{40}Ca , the difference in proton and neutron distributions is more apparent, as the valence $\nu 0f_{7/2}$ shell goes from mostly empty in ^{40}Ca (0.42 neutrons, per our fit) to mostly full in ^{48}Ca (6.84 neutrons, per our fit). We extract a neutron skin of 0.150 fm, significantly lower than the

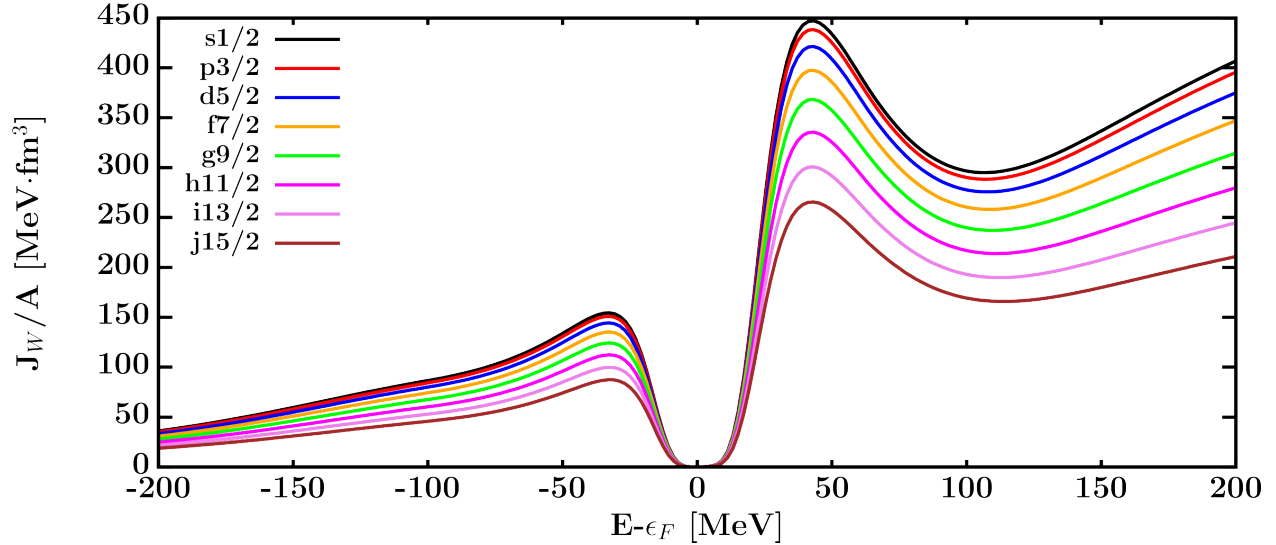


Figure 7.15: Volume integral of proton imaginary potential in ^{48}Ca . Compared to ^{40}Ca , the magnitude and slope above 100 MeV is significantly lower, likely because there were no proton σ_{rxn} data available for ^{48}Ca above 48 MeV to constrain this regime.

0.249 ± 0.023 fm of the previous DOM treatment and only slightly larger than the *ab initio* result. Without a covariance analysis of the DOM parameters, it cannot be clear which DOM result is more reliable. If most of the additional parameters of [42] are well-constrained, then our present treatment with fewer parameters is likely deficient, as we would have discarded relevant physics. If the previous DOM treatment was underconstrained, their result may be a consequence of overfitting. We await the results of the CREX measurement to provide a model-independent indication of the ^{48}Ca neutron skin size.

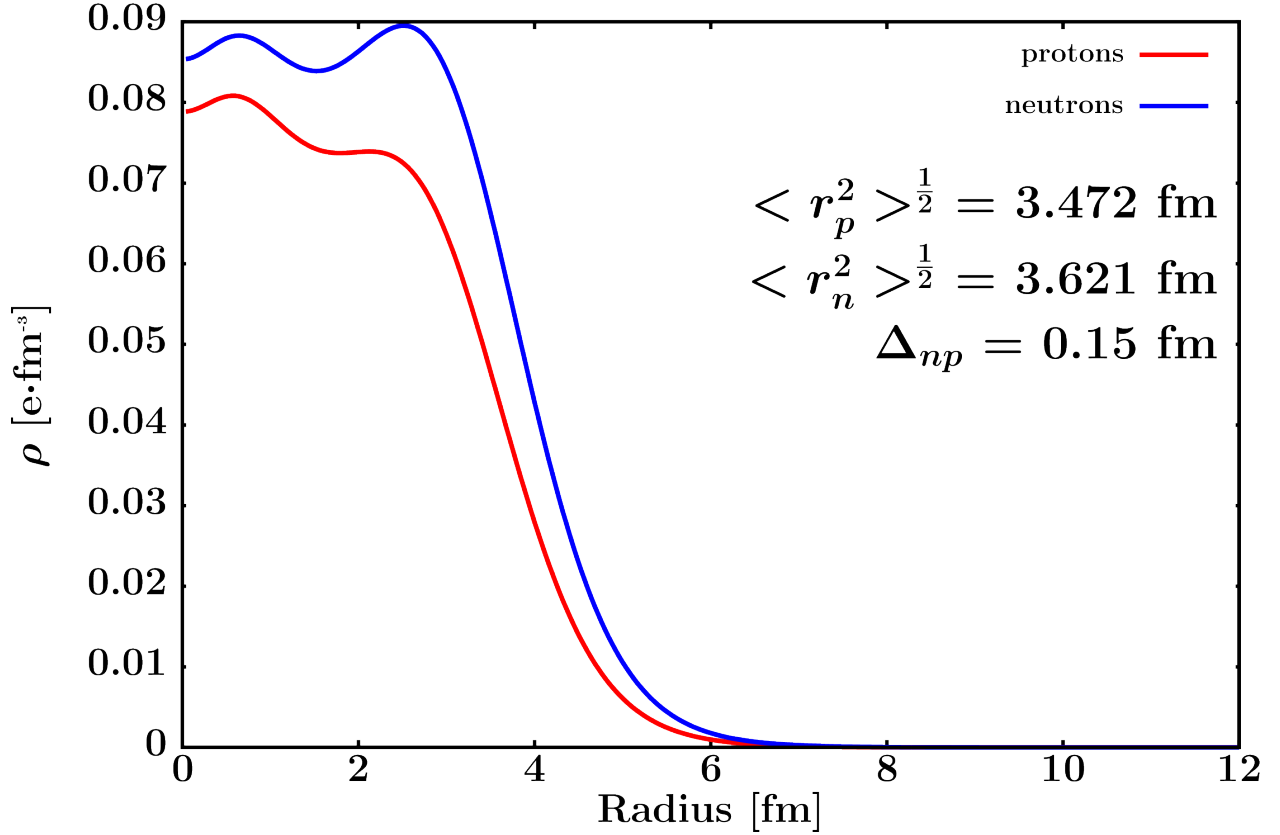


Figure 7.16: Proton and neutron point density distributions in ^{48}Ca , as generated by our DOM fit. The RMS radii of the distributions and their difference (the neutron skin) are provided. The neutron skin we extract is significantly smaller than that of the previous DOM fit of [42] and is only slightly larger than the skin extracted from the *ab initio* treatment of [98]. A comparison with the experimental ^{48}Ca charge density distribution is shown in Section D.4 of Appendix D.

7.2 Results for $^{16,18}\text{O}$

The lightest system analyzed in the DOM framework, ^{16}O is a valuable benchmark for χ -EFT, shell model, and *ab initio* approaches. A wealth of scattering and bound-state information have been collected on ^{16}O , making it a good test case for the validity of the DOM in light systems and helping to validate the choices of DOM potential forms.

Of the nuclides we chose for a DOM treatment, ^{18}O was one of most challenging due

to the paucity of available experimental data, the lightness of the system, and the neutron open shell. To constrain the negative-energy domain of the potential, the only unambiguous experimental data were the neutron and proton separation energies and the overall binding energy, adding to the uncertainty in the ^{18}O negative energy parameter values.

7.2.1 Results for ^{16}O

The large corpus of experimental data used to constrain the ^{16}O potential includes proton $\frac{d\sigma}{d\Omega}$ and analyzing powers up to 200 MeV, neutron $\frac{d\sigma}{d\Omega}$ and analyzing powers up to 100 MeV, proton σ_{rxn} cross section up to 65 MeV, and qualitative knowledge about the shape of the spectral functions of the bound $\pi s_{\frac{1}{2}}$, $p_{\frac{3}{2}}$, and $p_{\frac{1}{2}}$ subshells from (e,e'p) measurements. Reasonable agreement with all experimental data was achieved, excepting the highest-energy (> 150 MeV) proton differential elastic cross sections and analyzing powers, especially at backward angles.

For a system as light as ^{16}O , the density of states at low energies (i.e., below the neutron separation energy) is sufficiently low that a smoothly-varying potential will be a poor approximation of the resonance structure that dictates the strength of inelastic scattering. This deficiency is particularly acute in the doubly-closed-shell nuclei, where the level spacing is larger near the Fermi energy. We expect this to be a contributing factor to the slight overestimation of the RMS charge radius (see Fig. 7.17).

As with ^{40}Ca , we find that ^{16}O has a slightly negative neutron skin, -0.024 fm.

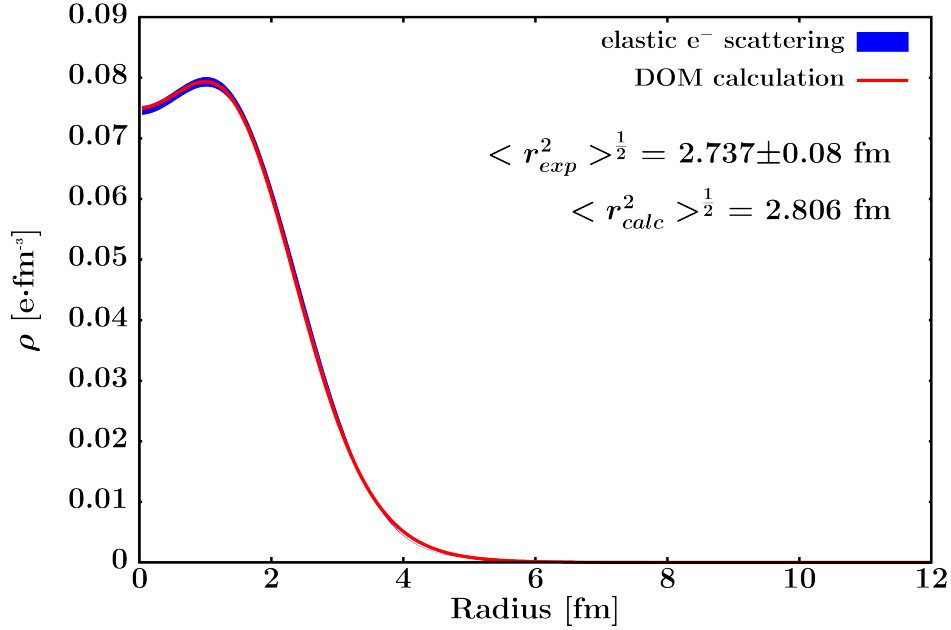


Figure 7.17: Charge density distribution of ^{16}O , as generated by our DOM fit (in red) and as generated from experimental elastic electron scattering [11]. No error bars are reported in the compilation of [11]; we show an arbitrary uncertainty range of 1% (blue shaded region).

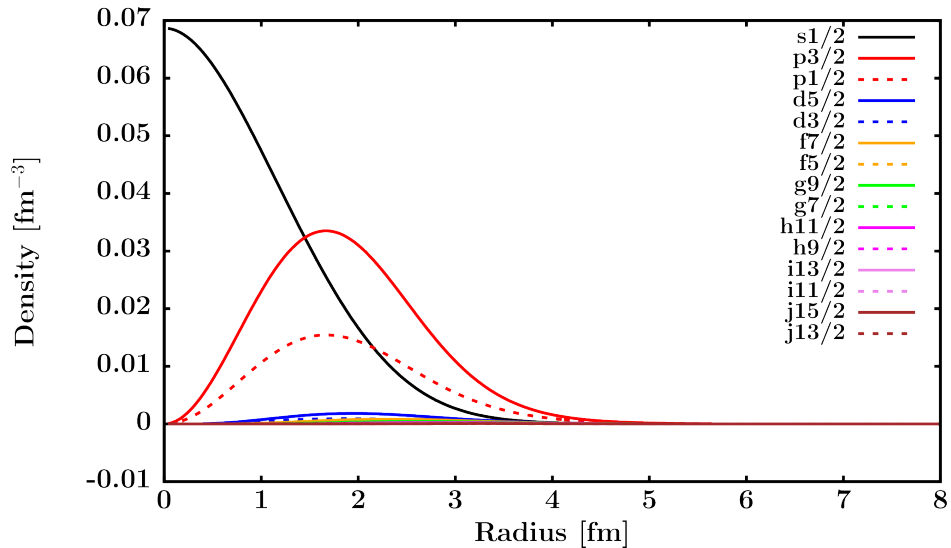


Figure 7.18: Proton single-particle density distributions in ^{16}O , as generated by our DOM fit.

7.2.2 Results for ^{18}O

For ^{18}O , a complete Fourier-Bessel-parameterized charge density distribution (used for ^{16}O , $^{40,48}\text{Ca}$, $^{58,64}\text{Ni}$, ^{124}Sn , and ^{208}Pb) was unavailable. To generate an approximate charge density distribution for ^{18}O we linearly scaled the ^{16}O charge density distribution to reproduce the ^{18}O - ^{16}O δ_{RMS} from [11] while maintaining a total charge of eight. The reported RMS charge radii of ^{16}O and ^{18}O differ by only 0.07 fm ($\approx 2.5\%$), so the ^{18}O charge density distribution we generated is barely distinguishable from the ^{16}O distribution. This same scaling procedure was also employed to generate a charge density distribution for ^{112}Sn , using the experimentally-derived ^{124}Sn charge density distribution.

To initiate the fit on ^{18}O , the ^{16}O best-fit parameter values were assigned to the ^{18}O parameter file and observables were calculated to compare with ^{18}O experimental data. The ^{16}O optimized parameter values were moderately successful at reproducing the ^{18}O scattering data without further adjustment, though almost no neutron scattering data was available for ^{18}O besides our newly-measured neutron σ_{tot} . Using the raw ^{16}O parameters, the DOM predictions for ^{18}O proton SP levels were underbound by several MeV per particle and the calculated particle number was too low, unsurprising given the insufficiency of the ^{16}O Hartree-Fock term in providing two additional nucleons' worth of binding in ^{18}O . Thus, before loosening any other parameters, the HF depth and HF depth asymmetry terms were allowed to vary, reducing the chi-square contribution from the charge density, particle number, and energy level sectors. Once a chi-square minimum had been reached with these two parameters, all other parameters were allowed to vary. Our optimum fit achieved good agreement with all experimental ^{18}O scattering data except the 24 MeV neutron elastic scattering data of Grabmayr et al. [105], where our fit somewhat underestimates the differential cross

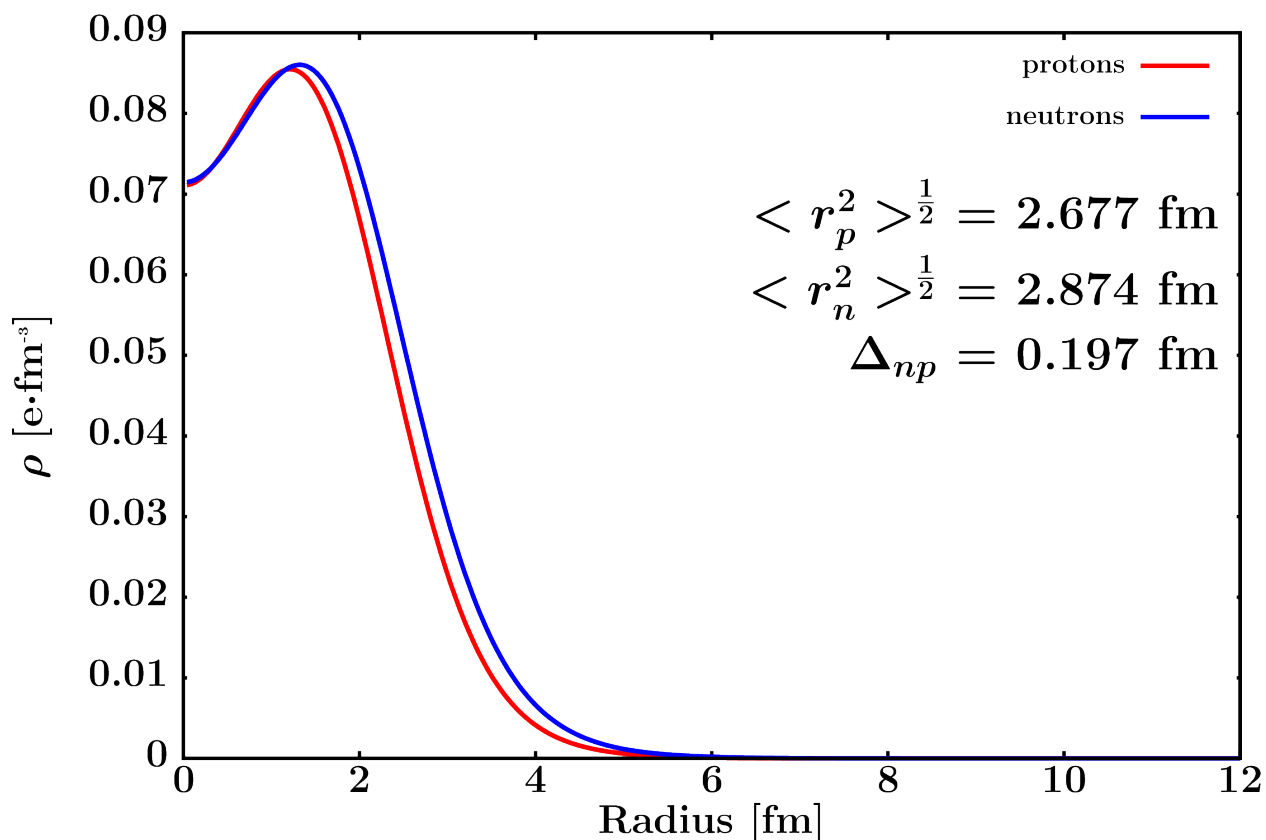


Figure 7.19: Proton and neutron point density distributions in ^{18}O , as generated by our DOM fit. The RMS radii of the distributions and their difference (the neutron skin) are provided. Adding two neutrons to ^{16}O dramatically increases the neutron skin, as most of the added neutron density settles into the $\nu 0d_{5/2}$ shell, outside the ^{16}O core. A comparison to the experimental ^{18}O charge density distribution is shown in Section D.2 of Appendix D.

section throughout its range.

Figure 7.19 shows the matter density distributions for protons and neutrons extracted from our fit on ^{18}O . We recover a large neutron skin of 0.197 fm, commensurate with the neutron skin of much heavier, more asymmetric nuclei. The reason is clear: most of density from the two extra neutrons in ^{18}O goes into the $\nu 0d_{5/2}$, which peaks at the nuclear surface, increasing the neutron RMS radius. To test our extracted neutron skin thickness for ^{18}O we considered the difference in RMS charge radii between mirror nuclei ^{18}Ne and ^{18}O . The

values of 2.97 fm for ^{18}Ne from [106] and 2.79 fm for ^{18}O from [11, 12] yield a difference of 0.18 fm, quite close to our extracted neutron skin for ^{18}O .

7.3 Results for $^{58,64}\text{Ni}$

Unlike $^{40,48}\text{Ca}$, both ^{58}Ni and ^{64}Ni have partially-occupied neutron shells in the independent-particle-model picture. Accordingly, Ni isotopes have increased level density near the Fermi level and should possess significant imaginary strength in this region, impacting low-energy elastic and inelastic nucleon cross sections. Recently, A. Brown has outlined a program to constrain the density dependence of the symmetry energy using RMS charge radii in mirror nuclei in the Fe and Ni region [107], heightening interest in accurate matter density distributions for these isotopes. While ^{60}Ni and ^{62}Ni were not analyzed here, the charge density distributions of both are well-known [11], making the even Ni isotopes an ideal target for a future DOM analysis along an isotope chain.

7.3.1 Results for ^{58}Ni

Like ^{40}Ca , ^{58}Ni enjoys abundant proton and neutron elastic scattering data. In our ^{58}Ni fit, the imaginary strength rises steeply just above the Fermi energy, understandable in light of the lower-lying excited states in ^{58}Ni compared to all the lighter closed-shell isotopes already presented. As with ^{48}Ca , the lack of high-energy proton σ_{rxn} data makes it difficult to unambiguously identify the high-energy imaginary strength (W_{vol}^+).

Figure 7.20 shows the matter distributions and neutron skin we extract for ^{58}Ni . In the case of ^{18}O , the addition of two neutrons compared to symmetric ^{16}O increased the neutron skin size dramatically. In ^{58}Ni , the two extra neutrons (with respect to symmetric ^{56}Ni)

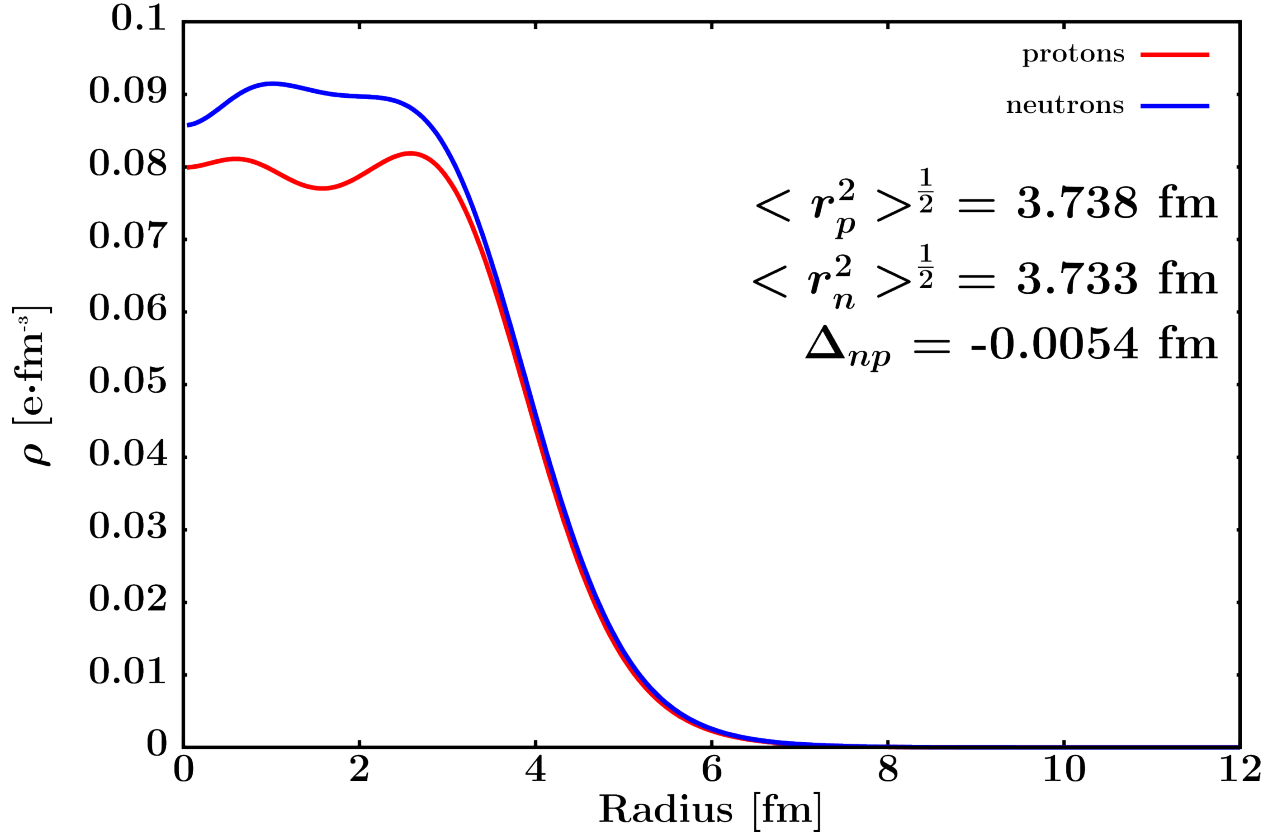


Figure 7.20: Proton and neutron point density distributions in ^{58}Ni , as generated by our DOM fit. The RMS radii of the distributions and their difference, the neutron skin, are provided. The two valence neutrons (with respect to a ^{56}Ni core) do little to increase the neutron skin, as most of the added neutron density populates the $\nu 1p_{3/2}$ shell close to the nuclear core. A comparison to the experimental ^{58}Ni charge density distribution is shown in Section D.5 of Appendix D.

join the p-shell, dwelling mostly near the nuclear core where they do little to change the neutron skin size. Per this rudimentary picture, it is clear that shell structure is critical for understanding the evolution of neutron skins along an isotope chain.

7.3.2 Results for ^{64}Ni

Due to its low natural abundance, ^{64}Ni is a dramatically more expensive target material than ^{58}Ni , making experimental coverage very sparse on this isotope. Our search of the

EXFOR database showed no ^{64}Ni elastic or inelastic neutron scattering data at all, except for a single study on $^{58,60,62,64}\text{Ni}$ from 5-7 MeV almost forty years old [108]. Without our new σ_{tot} data, a DOM analysis of this type would have been infeasible. Our fit of ^{64}Ni easily converged on our new neutron σ_{tot} and the experimental binding energy per nucleon, suggesting that the ^{64}Ni fit parameters are still significantly underconstrained. Accordingly, the neutron skin we extract for ^{64}Ni is expected to be less reliable but still worth reporting. Compared to ^{58}Ni , our fit suggests that much of the extra neutron density of ^{64}Ni adds to the occupation of the $\nu 0f_{7/2}$ and $\nu 0f_{5/2}$ subshells. The extra occupation in the high-angular-momentum f-shell grows the neutron skin substantially, to 0.15 fm (cf. -0.0054 fm for ^{58}Ni).

7.4 Results for $^{112,124}\text{Sn}$

Of the isotopic systems studied in this treatment, $^{112,124}\text{Sn}$ was the least characterized by experimental data. Our new neutron σ_{tot} and $\frac{d\sigma}{d\Omega}$ measurements provide a sizable fraction of the total available nucleon scattering data on $^{112,124}\text{Sn}$ from 1-200 MeV. Because of the lack of data, our Sn fits are likely the least well-constrained of all the fits presented here, with the possible exception of ^{64}Ni . Still, the structural information extracted from our fits on $^{112,124}\text{Sn}$ largely comports with the trends seen in the other isotopic systems and may be useful for extrapolating properties of the doubly-magic ^{100}Sn and ^{132}Sn . In addition, mid-shell Sn isotopes exhibit neutron superfluidity and help provide important information about deviations from the shell model outside shell closures.

7.4.1 Results for ^{112}Sn

For ^{112}Sn , the only neutron scattering data available from 10-200 MeV were the new data sets presented earlier in this work. Given this situation, it is encouraging that the momentum distributions we extract, shown in Figs. 7.21 and 7.22, are comparable to those of both the lighter ^{58}Ni and heavier ^{208}Pb , suggesting that our parameters for $^{112,124}\text{Sn}$ are reasonably well-constrained.

It should be noted that while ^{112}Sn and ^{18}O have almost the same asymmetry ($\frac{N-Z}{A}$), the valence neutrons in ^{112}Sn are spread more evenly over several shells, so it is sensible that the neutron skin we recover is nearly zero.

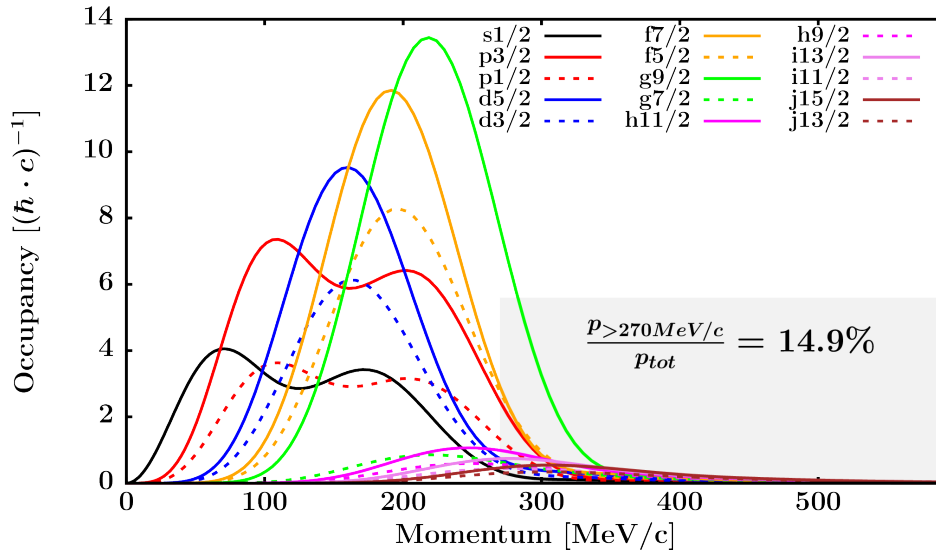


Figure 7.21: Integrated proton momentum distribution in ^{112}Sn , as generated by our DOM fit. The fraction of proton high-momentum content is comparable, but slightly lower than, that of neutrons (figure below).

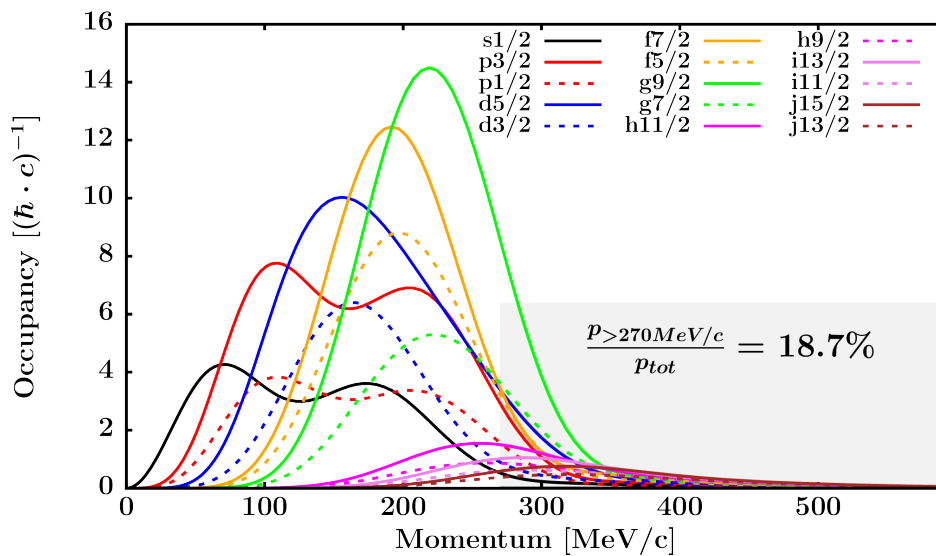


Figure 7.22: Integrated neutron momentum distribution in ^{112}Sn , as generated by our DOM fit. The fraction of neutron density with momentum above $270 \text{ MeV}/c$ is listed.

7.4.2 Results for ^{124}Sn

Figure 7.23 shows the matter distribution for protons and neutrons in ^{124}Sn and the neutron skin as generated by our fit. For both Sn isotopes, we had trouble reproducing the experimentally-derived charge density distributions with the same degree of accuracy as the nuclei presented above. Whether this difficulty stemmed from insufficient nucleon scattering data or from a deficiency in our parameterization, we do not know. To make up for the lack of data on any one Sn isotope, previous local DOM fits on the Sn isotopes [94, 96] had fit several members of the ten stable Sn isotopes simultaneously. The current non-local DOM version used in this work is not equipped for this strategy, but it is a promising direction that we hope to pursue in future work.

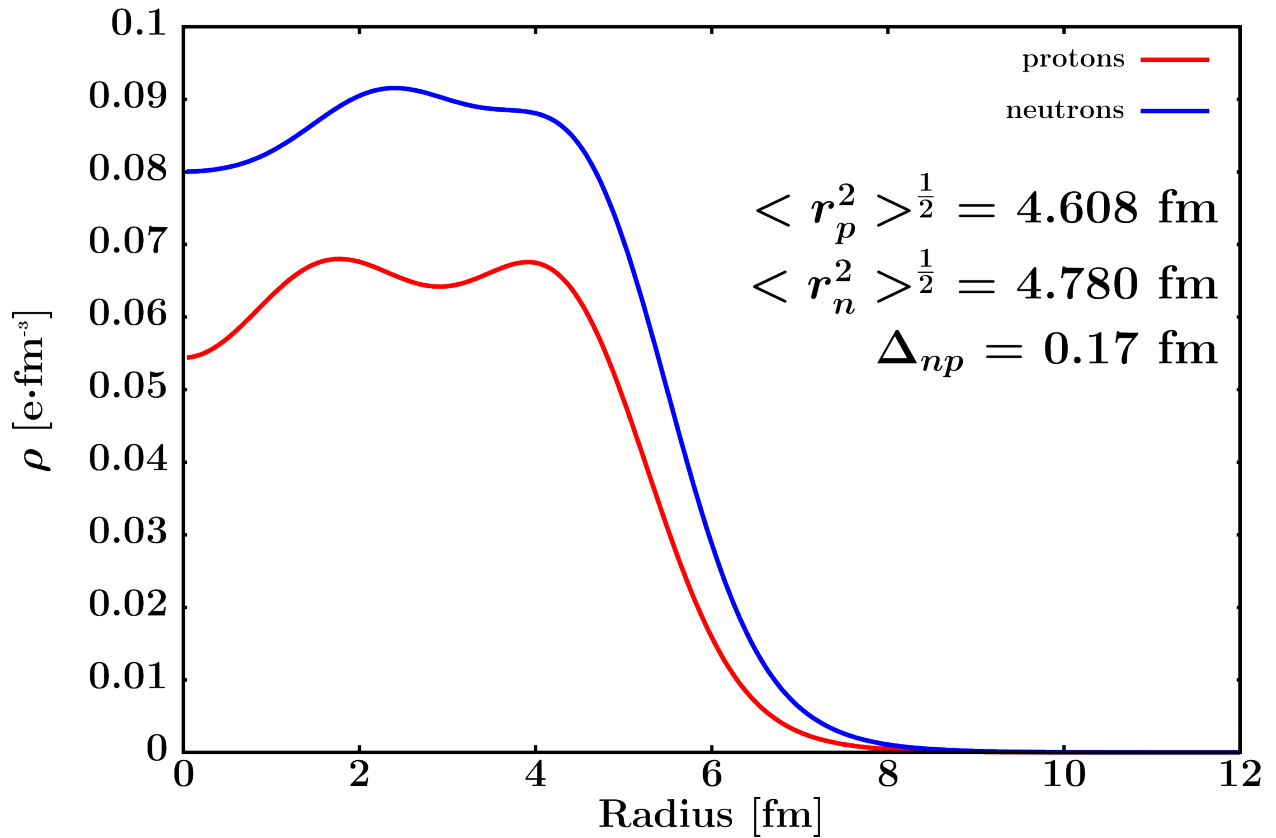


Figure 7.23: Proton and neutron point density distributions in ^{124}Sn , as generated by our DOM fit. The RMS radii of the distributions and their difference (the neutron skin) are provided. The neutron skin of neutron-rich systems like ^{124}Sn are expected to be strongly correlated with the size of the density-dependence of the symmetry energy, L .

7.5 Results for ^{208}Pb

Like ^{40}Ca and ^{16}O , ^{208}Pb occupies an important square on the chart of nuclides and has received a great deal of experimental and theoretical attention. The size of the neutron skin of ^{208}Pb has been identified by numerous studies as highly correlated with the density-dependence of the symmetry energy, L , a critical input for the neutron star equation-of-state. By employing parity-violating electron scattering to probe the weak charge distribution in ^{208}Pb , the PREX experiment at Jefferson Laboratory extracted a ^{208}Pb neutron skin value

of 0.33 ± 0.17 fm. A followup experiment with improved statistics, PREX II, is slated to run later in 2019 and is expected to provide a model-independent value for the ^{208}Pb neutron skin thickness to within 0.06 fm. Given the wide range of ^{208}Pb neutron skin thicknesses predicted by relativistic and non-relativistic mean-field models, this quantity is an excellent test for the value of the DOM as a predictive tool.

Figures 7.24 and 7.25 show the momentum distribution for protons and neutrons we extract from our ^{208}Pb fit. As with ^{48}Ca , the proton high-momentum content is lower than the neutron high-momentum content, a consequence of additional filling of higher-angular-momentum subshells for neutrons compared to protons, skewing the total momentum distribution upward. Figure 7.26 shows the nucleon matter distributions, which yield a neutron skin of 0.200 fm. Compared to previous DOM treatments, our value for the ^{208}Pb neutron skin is slightly smaller and more in line with the average of mean-field calculations [56]. An important difference in our DOM treatment is that only the depth of the Hartree-Fock potential is allowed to vary with asymmetry; previous treatments relaxed this restriction and equipped every real-term parameter with an asymmetry-dependence. We suspect that some of the difference in our extracted ^{208}Pb radii derives from this choice. Unfortunately, our present fit of ^{208}Pb fails to recover enough binding energy per nucleon and substantially underbinds the most deeply-bound proton levels (e.g., the $0p_{\frac{3}{2}}$), indicating that our description of very deep levels is inadequate. In the end, it is not clear which DOM parameterization is better-justified without a deeper analysis of the model-dependence of the results.

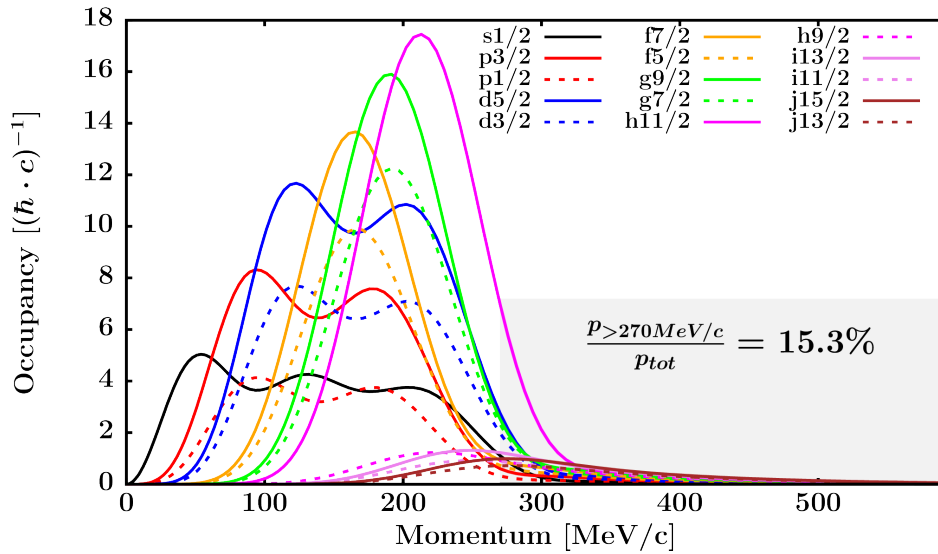


Figure 7.24: Integrated proton momentum distribution in ^{208}Pb , as generated by our DOM fit. The fraction of proton density with momentum above 270 MeV/c is listed.

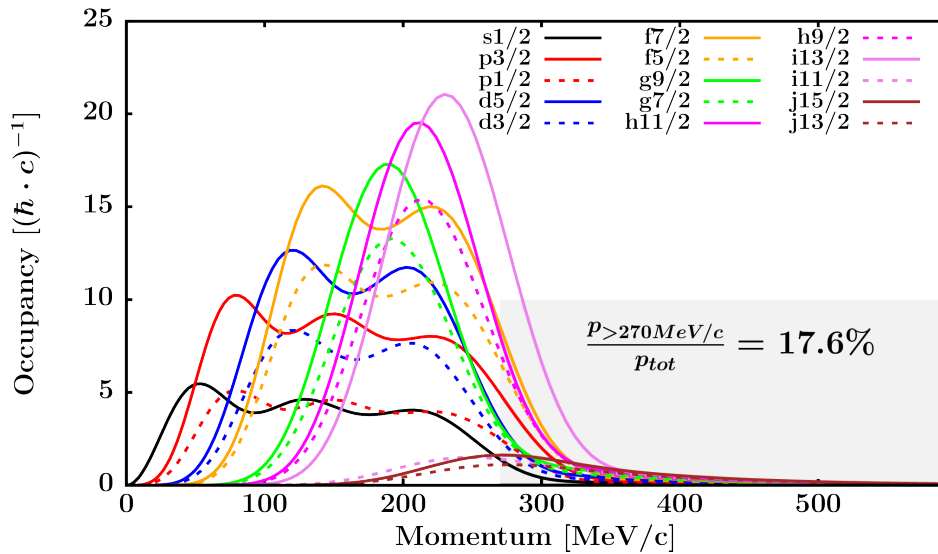


Figure 7.25: Integrated neutron momentum distribution in ^{208}Pb , as generated by our DOM fit. The fraction of neutron density with momentum above 270 MeV/c is listed.

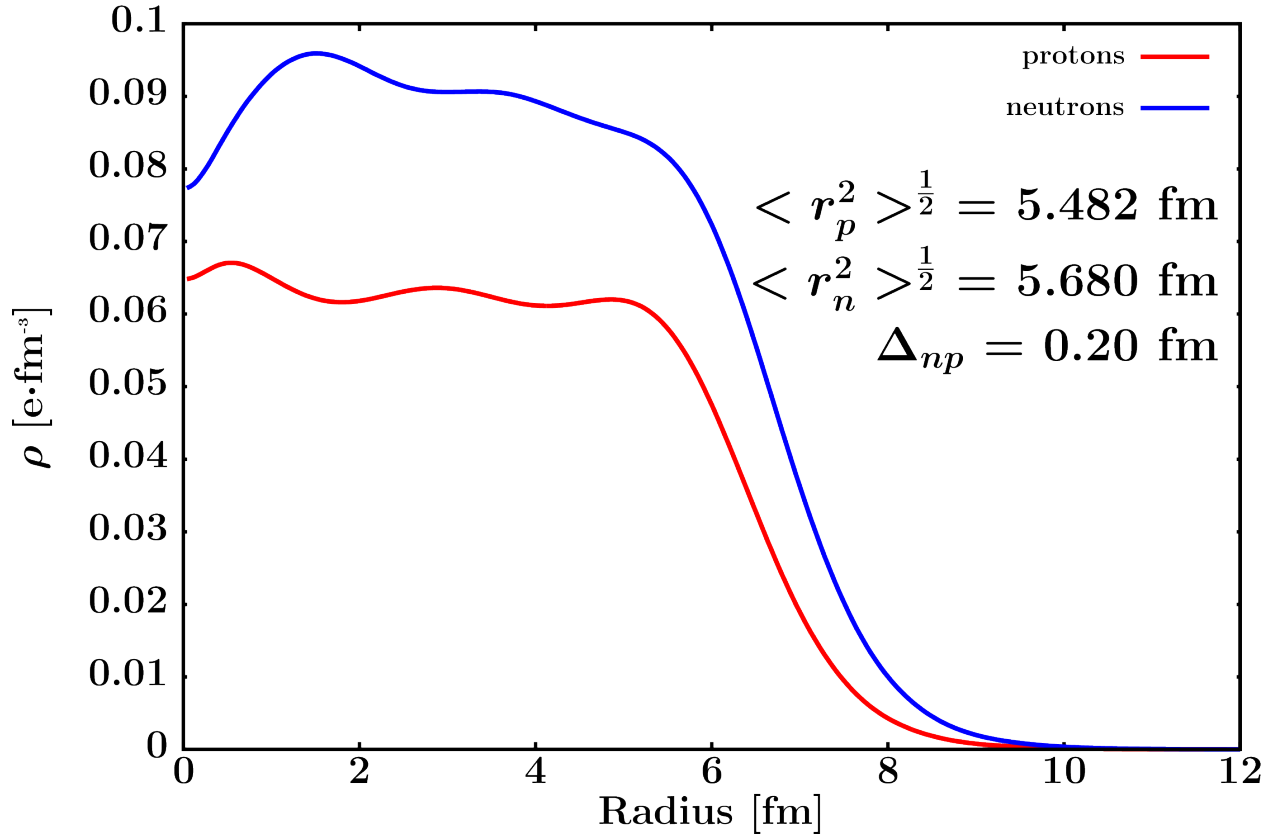


Figure 7.26: Proton and neutron point density distributions in ^{208}Pb , as generated by our DOM fit. The RMS radii of the distributions and their difference (the neutron skin) are provided. The neutron skin of neutron-rich systems like ^{208}Pb are expected to be strongly correlated with the size of the density-dependence of the symmetry energy, L .

7.6 General Trends

7.6.1 Neutron Skins Sensitive to Shell Structure

Table 7.2 presents the neutron skins we extracted from our optimized DOM fits on all nuclei under study. As anticipated, both the total degree of asymmetry and the specific shell structure affect the calculated skins.

Isotope	π r_{rms} [fm]	ν r_{rms} [fm]	Δ_{rms} [fm]
¹⁶ O	2.685	2.661	-0.024
¹⁸ O	2.677	2.874	0.197
⁴⁰ Ca	3.470	3.414	-0.056
⁴⁸ Ca	3.472	3.621	0.150
⁵⁸ Ni	3.738	3.733	-0.005
⁶⁴ Ni	3.828	3.977	0.150
¹¹² Sn	4.569	4.560	-0.009
¹²⁴ Sn	4.608	4.780	0.170
²⁰⁸ Pb	5.482	5.680	0.200

Table 7.2: Neutron skins (Δ_{rms}) extracted from DOM analysis. The skins are calculated as the difference between the proton and neutron point distribution root-mean-square (RMS) radii and thus do not include the nucleon-size form factor. All values are rounded, so the neutron skin reported in the last column may not exactly match the difference of proton and neutron RMS radii listed. The full calculated matter distributions for protons and neutrons for each nucleus are available in Appendix D.

7.6.2 Depletion, Momentum Content, and Deep Imaginary Strength

For over fifty years, (e,e'p) and (p,2p) measurements have shown that in real nuclei, single-particle spectroscopic factors are significantly reduced both near the Fermi surface and for deeply-bound subshells. Table 7.3 shows the spectroscopic factors for valence proton

and neutron subshell for each nucleus modeled in this work and indicates consistent reduction in spectroscopic factors by around 25-30%, for valence subshells.

Isotope	Protons		Neutrons	
	Level	SF	Level	SF
^{16}O	$0p_{\frac{1}{2}}$	0.75	$0p_{\frac{1}{2}}$	0.75
^{18}O	$0p_{\frac{1}{2}}$	0.78	$0d_{\frac{5}{2}}$	0.76
^{40}Ca	$0d_{\frac{3}{2}}$	0.76	$0d_{\frac{3}{2}}$	0.76
^{48}Ca	$1s_{\frac{1}{2}}$	0.75	$0f_{\frac{7}{2}}$	0.76
^{58}Ni	$0f_{\frac{7}{2}}$	0.70	$1p_{\frac{3}{2}}$	0.71
^{64}Ni	$0f_{\frac{7}{2}}$	0.74	$1p_{\frac{1}{2}}$	0.78
^{112}Sn	$0g_{\frac{9}{2}}$	0.70	$1d_{\frac{5}{2}}$	0.74
^{124}Sn	$0g_{\frac{9}{2}}$	0.72	$0h_{\frac{11}{2}}$	0.76
^{208}Pb	$2s_{\frac{1}{2}}$	0.67	$1f_{\frac{5}{2}}$	0.73

Table 7.3: Spectroscopic factors for protons and neutrons in the valence subshell (e.g., $\pi p_{\frac{1}{2}}$, $\nu d_{\frac{5}{2}}$ for ^{18}O) are listed for all nuclei considered in the present treatment. For some of the heavier systems with multiple, nearly-degenerate levels nears the Fermi surface (e.g., ^{124}Sn), we list only one representative level.

When examined in momentum space, the proton and neutron particle density distributions are expected to show significant enhancement of nucleon density at higher momentum than would be expected in an independent-particle shell model [109]. The amount of this so-called “high-momentum content” has been investigated by knockout reactions [104, 109] and shown to be significant even for very light nuclei such as ^{12}C ($\approx 10\%$ above 270 MeV/c). Table 7.4 shows the percentage of the proton and neutron densities with momentum above 270 MeV/c per our fits. The values we extract are roughly constant for all nuclei at around 12-15% for protons and 15-18% for neutrons. For ^{112}Sn and ^{124}Sn where experimental coverage is most sparse, we see deviations from the average, suggesting that our optimized fits

GENERAL TRENDS

Table 7.4: High-momentum content as extracted from DOM analysis. For protons and neutrons for each nucleus under study, the nucleon density distribution in momentum-space is calculated and the fraction of the density distribution above 270 MeV/c is tabulated. For comparison, [104] reported $\approx 10\%$ high momentum content for ^{12}C . The full momentum-space matter distributions for protons and neutrons for each nucleus are available in Appendix D.

Isotope	π $p_{>270}$ [%]	ν $p_{>270}$ [%]	p/n Ratio
^{16}O	15.3	15.7	0.97
^{18}O	14.3	13.8	1.03
^{40}Ca	13.9	14.6	0.95
^{48}Ca	12.4	15.5	0.80
^{58}Ni	12.3	14.8	0.83
^{64}Ni	14.7	16.0	0.92
^{112}Sn	14.9	18.7	0.80
^{124}Sn	10.9	15.8	0.69
^{208}Pb	15.3	17.6	0.87

require more experimental data for a clearer picture. For the symmetric nuclei ^{16}O and ^{40}Ca , we see that the neutron high-momentum content is slightly larger than the proton high-momentum content, ostensibly from a slight broadening of the momentum distribution for neutron subshells compared to proton subshells, which nudges more neutron density into the high-momentum regime.

For highly asymmetric nuclei (e.g., ^{124}Sn , ^{208}Pb), we might expect that, *all other things being equal*, the minority nucleon species should have a larger fraction of high-momentum content [103, 100], a consequence of the enhanced short-range correlations experienced by the minority-species nucleons. At first glance, our results appear to contradict this expectation: for example, in ^{48}Ca , we see a *reduction* in the percentage of proton high-momentum content compared to ^{40}Ca (12.4% for ^{48}Ca , 13.9% for ^{40}Ca). However, a closer look at the breakdown of momentum distributions by angular momenta (Fig. 7.27) shows that the story is more complicated. In going from ^{40}Ca to ^{48}Ca , the nuclear potential widens and the proton Fermi

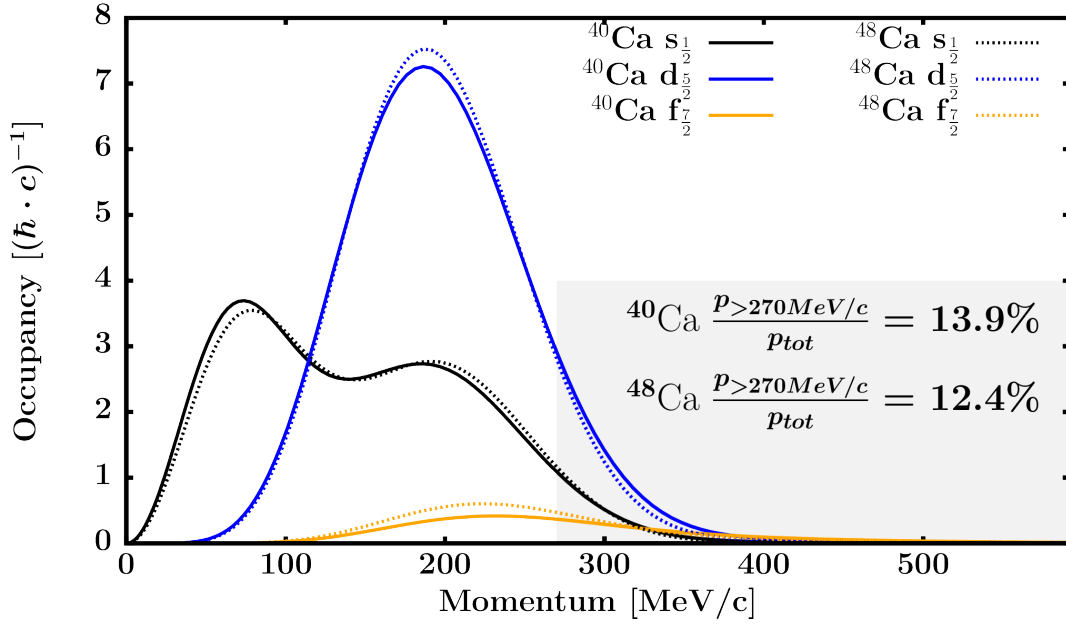


Figure 7.27: The proton $s_{\frac{1}{2}}$, $d_{\frac{5}{2}}$, and $f_{\frac{7}{2}}$ momentum distributions for $^{40,48}\text{Ca}$ are shown. Compared to ^{40}Ca , we see a slight reduction in the total ^{48}Ca proton high-momentum content over all subshells (the total fraction of protons with momentum above 270 MeV/c is listed in the gray box). This reduction is associated with a slight narrowing of the valence-region momentum distributions (e.g., $d_{\frac{5}{2}}$ and $f_{\frac{7}{2}}$) that are the dominant contributors to the total high-momentum fraction.

energy drops considerably, by almost 10 MeV. Per our fit, the first lobe of the proton $s_{\frac{1}{2}}$ momentum distribution appears to shift toward higher momentum slightly, but the second lobe (corresponding to the proton $1s_{\frac{1}{2}}$ level) narrows slightly. More importantly, the subshells that contribute the most to the proton high-momentum content (e.g., the proton $d_{\frac{5}{2}}$ and $f_{\frac{7}{2}}$) are also reduced in width, lessening the overall high-momentum fraction. It is plausible that the narrowing of the momentum-space peaks is due to the widening of the proton potential from the eight extra neutrons in ^{48}Ca , but it also may indicate that our parameterization is insufficiently flexible to reproduce the true potential. In any case, our results suggest that to connect short-range correlations with increased high-momentum content, a fixed momentum threshold (e.g., 270 MeV/c) may not be useful for comparing nuclei and a more nuanced

treatment may be needed. Of course, additional experimental data to constrain the deep negative-energy regime for ^{48}Ca , especially for neutrons, would be quite valuable.

The deep negative-energy realm is perhaps the most challenging sector for our fit, as our only direct constraint is the experimental binding energy. Because the binding energy does not differentiate between protons and neutrons, we have very limited sensitivity to the isovector-dependence of the potential in this area. As a result, the relative high-momentum content between protons and neutrons that we extract can only be taken qualitatively.

7.6.3 Overestimation of RMS Charge Radius

The charge density distributions extracted from our fits showed a slight excess of charge density on the extreme tail of the distributions (e.g., above 5 fm for ^{40}Ca). As the RMS charge radius is most sensitive to contributions from the tail, this excess led to chronic overestimation of the RMS charge radius of roughly 0.05-0.10 fm across nuclei. We found that density in the extreme tail of the matter distributions was very sensitive to the amount of imaginary strength just below the Fermi energy (W_{sur}^-); in fits with a high weight for the RMS charge radius, W_{sur}^- would tend toward zero or even cross into negative territory, which is unphysical. Especially in the lighter systems we studied, our fits routinely moved all the negative-energy imaginary strength into W_{vol}^- . We had no difficulties fitting W_{sur}^+ , largely due to the availability of proton σ_{rxn} and neutron σ_{tot} data from 20-50 MeV. Interestingly, the volume integral of the imaginary strength (an integration over the radial form factors) of our optimized fits shows the imaginary potential to be largely symmetric about the Fermi energy within roughly 30 MeV (see Fig. 7.11), in keeping with the expectations of [33] and many other theoretical treatments. Whether the partitioning of the negative-energy imaginary strength into W_{vol}^- over W_{sur}^- has real significance is unclear, but it suggests that subsequent

analyses may need more specialized treatment in the near-surface negative-energy regime.

Practically speaking, because the nuclear surface and volume overlap significantly in light systems like ^{16}O , we did not expect to see a unique best-fit for the negative-energy parameters. In real nuclei near the Fermi surface, imaginary strength should vary rapidly due to the discrete resonance structure of the nucleus. In this region, the optical potential corresponds quite poorly with this reality as it can only represent a smooth average. With these considerations in mind, it is perhaps not surprising that we had trouble getting the negative-energy surface parameters under control. In the end, for $^{16,18}\text{O}$ we fixed W_{sur}^- to zero for the final optimizations to avoid numerical problems and prevent any unphysical imaginary parameter values. In our fits, the W_{vol}^- term had no trouble providing imaginary strength where it was needed to recover correct particle numbers, charge density distributions, and, to some extent, binding energies.

It should be noted that while we produce RMS charge radii that are a tad high compared to experimental measurements, we had good success recovering the shape of the full charge density distribution profiles. As the neutron skin is the *difference* between proton and neutron matter radii, any systematic issues that affect both the neutron and proton matter distributions should have only a small effect on our neutron skin values.

CONCLUSIONS

8.1 Advancements in Digitizer-enabled Neutron σ_{tot} Measurements of Rare Isotopes

By applying newly-available digitizer technology to reduce per-event deadtime, we have advanced a program of isotopic σ_{tot} measurements valuable for constraining the isovector strength of the nuclear potential at positive energies. New data have been obtained on $^{16,18}\text{O}$, $^{58,64}\text{Ni}$, ^{103}Rh , and $^{112,124}\text{Sn}$ up to 450 MeV, dramatically expanding the coverage of these nuclei and laying the groundwork for subsequent optical model analyses. At the same time, we have identified shortcomings in the digital-signal-processing approach that must be rectified in future measurements, namely, the uncertainty in the true analytic deadtime and in the deadtime associated with digitizer buffer readout to the data acquisition computer. These effects depend on the proprietary digitizer firmware algorithms used for peak identification and buffer management, both of which are opaque to the end user. In an ideal experiment, DPP and raw waveform traces should be collected in parallel throughout the experiment and compared during data analysis to pinpoint any weaknesses in the peak-detection algorithm and identify variations in the analytic deadtime. Due to the ferocious data rate, we could

only collect small snippets of raw waveform data, insufficient for a full DPP-raw-waveform comparison. To resolve the discrepancy in our results above 100 MeV with those of [16] and [20], we suggest two types of benchmarking experiments in the future. First is a two-digitizer experiment: the same detector signals are fed into two separate time-synchronized digitizers, one running only in DPP mode, and one running in raw waveform mode. During analysis, a simulated DPP-mode peak sensing algorithm can be developed, applied to the real raw waveform-mode data, and its results compared with the real DPP-mode data, clarifying the DPP-mode behavior of the digitizer firmware. The second experimental setup would use both a digitizer and analog electronics: the same signals would be fed both into the digitizer, as in our experiment, and into analog-electronics logic utilizing a “looking period” (shown in Fig. 3.8).

8.2 Implications of DOM Results

Our DOM analyses of $^{16,18}\text{O}$, $^{40,48}\text{Ca}$, $^{58,64}\text{Ni}$, $^{112,124}\text{Sn}$, and ^{208}Pb have yielded new insight into the validity of the DOM approach and what experimental data are most needed for improved calculations of essential structural quantities. Our successful fits of $^{16,18}\text{O}$ show that even lighter systems (e.g., ^{12}C) may be amenable to a non-local DOM treatment, providing a bridge between ab initio calculations and phenomenological optical models. The shape of the imaginary potential above the Fermi energy is consistent across all our fits and agrees qualitatively with the state-of-the-art global optical model of [30]. Below the Fermi energy where experimental data are much sparser, we see significant variation in the shape of the potential between nuclei especially near the Fermi surface, where the magnitude of the imaginary potential changes rapidly. This is most conspicuous in the lighter nuclei where a

Table 8.1: Sensitivity of optical potential terms to the experimental nucleon scattering data types used in our fit. The typical range of available experimental data roughly corresponds to that used for our DOM treatments. Parameter terms are detailed in Section 6.3.

Data type	Protons		Neutrons	
	Typ. range [MeV]	Affected terms	Typ. range [MeV]	Affected terms
$\frac{d\sigma}{d\Omega}$	0 – 200	V_{vol}, V_{so}	0 – 100	V_{vol}, V_{so}
AP*	0 – 200	V_{vol}, V_{so}	0 – 100	V_{vol}, V_{so}
σ_{rxn}	0 – 100	$W_{sur}^+, W_{vol}^+, W_{NM}^+$	14.1	W_{sur}^+
σ_{tot}	–	–	10 – 200	$V_{vol}, V_{so}, W_{sur}^+, W_{vol}^+, W_{NM}^+$

*Analyzing Power

reduced level density makes a smooth optical potential a poor approximation. Heavy nuclei have sufficient phase space and level density on both sides of the Fermi energy that the nuclear potential is largely symmetric near the Fermi energy, in keeping with the expectations of Mahaux and Sartor [33].

Tables 8.1 and 8.2 summarize our understanding of the sensitivity of optical potential terms to the many experimental data types used in our fit. As discussed in Chapter 1 and shown in Appendix B, there is an abundance of nucleon elastic scattering data from 0-200 MeV on many isotopic targets. Equipped with these data, optical-model analyses have tightly constrained the magnitude and shape of the *real* components of the self-energy (in our treatment, the central potential and spin-orbit components). Unsurprisingly, the gaps in our knowledge of the self-energy are largest for *imaginary* terms, especially in areas where experimental data are sparsest. In our parameterization, this meant that the imaginary potential above 100 MeV (W_{vol}^+) and at all energies below the Fermi surface (W_{vol}^-) were difficult to constrain due to lack of data. At small positive energies, the imaginary strength

IMPLICATIONS OF DOM RESULTS

Table 8.2: Sensitivity of optical potential terms to the bound-state experimental data types used in our fit. The typical range listed here refers to the choice of incident particle momentum used to perform the measurement. Parameter terms are detailed in Section 6.3.

Data type	Typical range	Affected terms
(e,e)	q-range: 0.5 – 3.5 fm	$V_{vol}, V_{asym},$ W_{vol}^{\pm}, W_{NM}^-
(e,e'p)	p-range: 70 – 200 MeV/c	W_{sur}^-, W_{vol}^-
$\langle r^2 \rangle^{\frac{1}{2}}$	–	V_{vol}, W_{sur}^-
SP Levels	–	V_{vol}, V_{so}
Binding Energies	–	$V_{vol}, W_{vol}^-,$ W_{NM}^-

W_{sur}^{\pm} was relatively well-constrained by the handful of proton σ_{rxn} studies from 20-80 MeV all more than a decade old [110, 111, 112, 113]. These crucial mid-energy proton σ_{rxn} data streamlined the fitting process for ^{16}O , $^{40,48}\text{Ca}$, ^{58}Ni , and ^{208}Pb and added confidence in the quality of our fits. Unfortunately, proton σ_{rxn} data between 100-200 MeV were available only for ^{40}Ca and ^{208}Pb , so a chart-wide study of the evolution of the proton imaginary strength remains out of reach. To understand the asymmetry-dependence of the imaginary strength from 100-200 MeV, our new σ_{tot} results only contribute to the neutron half of the story. New proton σ_{rxn} measurements above 100 MeV would provide the other.

In preliminary fits that did not include the binding energy, we found that the deep negative imaginary strength, essentially W_{vol}^- , was very poorly constrained. These early fits gave far too small a binding energy, roughly 2-4 MeV/A. The inclusion of the binding energy as a fitting constraint had a dramatic impact on the imaginary terms in the potential: not only did W_{vol}^- grow considerably, but the imaginary non-locality β_4 grew from ≈ 0.6 fm to ≈ 0.9 fm, affecting the angular-momentum-dependence of the imaginary strength

at all energies. With the binding energy included, all our fits indicate that a significant fraction, as much as half, of the nuclear binding energy is generated by a small fraction of the total nucleon density at very negative energies (< -50 MeV). To understand why, a comparison to mean-field models is useful. In real nuclei near the Fermi surface, there is little absorptive strength and thus the spectral functions for nucleons are primarily discrete peaks. In this regime, mean-field models can give an excellent description of nuclear behavior as the assumption of independent particle motion (and a discrete spectrum) is appropriate. However, at very negative energies with larger imaginary strength, spectral peak broadening is dramatic and adds a small, but significant, single-particle occupation at very negative energies, occupation that plays an outsized role in binding. If our interpretation is correct, it would partially explain the underbinding of nuclei in shell models as a failure to account for spectral peak broadening beyond the valence space of the model. While our optimized fits produced a binding energy per nucleon roughly 2 MeV/A smaller than the experimental values, our results indicate that the binding energy is still quite useful for constraining the imaginary potential strength at negative energies.

By comparison to experimentally-measured charge density distributions, we see that significant depletion of s-shell occupation is needed to reproduce the proton density in the nuclear core. This depletion should occur in all bound shells as a consequent of short-range and long-range correlations and significantly alters the proton and neutron matter distributions. It is clear in our analysis that the matter distributions are sensitive to the proton and neutron single-particle configurations as anticipated by Wilkinson [50] and Myers [52] several decades ago. To wit, the neutron skin thickness we extract for ^{18}O (0.197 fm) appears to be as large or larger than that of ^{208}Pb (0.200 fm), even though the asymmetry ratio of ^{208}Pb (0.212) is almost twice as large as that of ^{18}O (0.111). In light of this result, we expect that the neutron

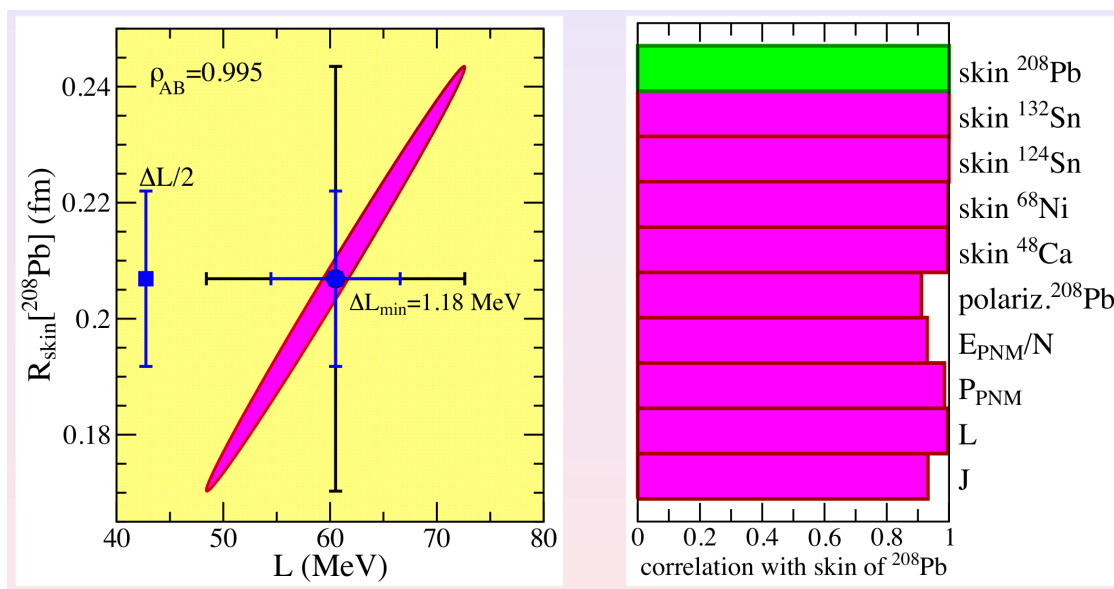


Figure 8.1: Correlation between the neutron skin of ^{208}Pb and several nuclear structure observables, per a relativistic mean-field calculation with the FSUGold interaction conducted by J. Piekarewicz. Many mean-field models recover a very strong correlation between the size of the neutron skin of several neutron-rich nuclides and the density-dependence of the symmetry energy, L . Figure used with permission.

skins may balloon in ^{52}Ar and ^{54}Ca with the filling of the $\nu f_{7/2}$ and $f_{5/2}$ subshells, but grow more slowly in even heavier Ar and Ca isotopes. Future experiments at FRIB and other radioactive beam facilities will probe this region and clarify the relative importance of the asymmetry ratio and high-spin intruder subshells in determining the neutron distribution near the dripline.

In relativistic and non-relativistic mean-field models, the neutron skin, electric dipole

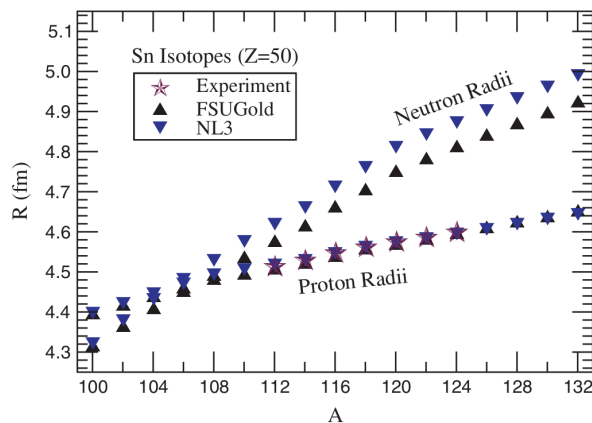


Figure 8.2: Proton and neutron RMS radii in the Sn isotopes computed in a relativistic mean-field approximation using the FSUGold and NL3 parameter sets, with experimental data for comparison. Figure and caption used with permission from [114].

polarizability, and dipole resonances of neutron-rich nuclei are shown to be tightly correlated with the density-dependence of the symmetry energy, L . While some of our neutron skin predictions are in agreement with those extracted from state-of-the-art mean-field models, the full story is not at all clear. As an example, Fig. 8.1 shows the results of a covariance analysis on a variety of nuclear structure quantities as calculated by a relativistic mean-field model that employs an FSUGold interaction [56]. The neutron skin for ^{208}Pb generated by our fit is in good agreement with this model. However, another treatment that uses the same interaction [114] gives a neutron skin for ^{112}Sn of roughly 0.09 fm (see Fig. 8.2), much *larger* than the -0.01 fm predicted by our fit. Understanding the model-dependence of these predictions, both from relativistic mean-field approaches and from the DOM, is critical for making progress on constraining L . As has been pointed out by other authors, a multi-pronged approach is warranted and should include electroweak measurements like PREX [53], comparison of charge radii in mirror nuclei [107], modeling of dipole polarizability [114], and multi-messenger astrophysical measurements on neutron stars. With the expanded scope of the DOM introduced in this work, we hope to add our new predictions to the mix.

Last, a few comments should be made about the DOM parameterization choices made in this work. While we have found that the neutron skin is inflated with the filling of the high-angular-momentum neutron subshells, we have also seen significant variation in the skin thickness depending on small changes in the parameter values. In the present treatment, to reduce the risk of overfitting, we reduced the total number of parameters to 34, less than half as many as used in other DOM analyses by our group. As a consequence, it appears that we have discarded some important physics: we were unable to recover, for example, the full binding energies and the experimentally-known RMS charge radii for most of the isotopes we analyzed. Further, the momentum distributions we generate for protons and neutrons likely

underestimate the amount of high-momentum content, especially for protons in neutron-rich systems. As mentioned earlier, the absence (and value) of high-energy proton σ_{rxn} plays an important role in resolving these discrepancies. A comprehensive error analysis is required to identify which parameters, if any, should be reintroduced to accommodate missing physics while keeping the total number of parameters to a minimum.

8.3 Additional Directions for Future Study

In light of the advances and limitations of this work, we identify several additional avenues of research worth pursuing. Besides the digitizer benchmarking experiments described earlier in this chapter, σ_{tot} measurements on the stable Fe and Cd isotopes would supplement our Ni and Sn isotope studies and provide much-needed information about optical-potential isovector dependence outside closed proton shells. Data for σ_{tot} on the intermediate stable isotopes $^{114,116,118,120,122}\text{Sn}$ would improve optical-model extrapolations to ^{100}Sn and ^{132}Sn , both of which are valuable for testing shell-model validity near the driplines. We reiterate the importance of new proton σ_{rxn} studies across the chart of nuclides, particularly on closed-shell isotope and isotone chains.

A major defect in the DOM treatment presented here is the lack of covariance analysis of DOM parameters. Without theoretical error bars associated both with uncertainty in the experimental data used and in the DOM's parameteric forms, comparisons between the DOM and other models cannot be complete. Such an analysis would also help reveal exactly which experimental data are most needed to clarify the murkier energy domains in our fits (e.g., the imaginary potential below -100 MeV and above 100 MeV). A first step toward this goal is publication of the DOM codebase, a priority of our group. Even in the absence of

appropriate error analysis, the single-particle densities and overlap functions generated by DOM fits can be immediately applied for calculations of coherent neutrino scattering [115] and scattering of potential dark matter candidates on common detector materials [116].

We close by noting that without a wide variety of fundamental experimental nuclear data on stable targets – at high and low energies, both for elastic and inelastic scattering, and probing both protons and neutrons – systematic analyses like that of the DOM are not possible. Even as radioactive beam facilities reach further toward the driplines, the capacity for basic scattering experiments on stable targets is vital for illuminating the relationship between nuclear structure and reactions.

BIBLIOGRAPHY

- [1] William D. Myers. *Droplet model of atomic nuclei*. IFI/Plenum, 1977.
- [2] V.M. Strutinsky. Shell effects in nuclear masses and deformation energies. *Nuclear Physics A*, 95(2):420 – 442, 1967.
- [3] P.A. Seeger and W.M. Howard. Semiempirical atomic mass formula. *Nuclear Physics A*, 238(3):491 – 532, 1975.
- [4] P. Möller and J.R. Nix. Nuclear masses from a unified macroscopic-microscopic model. *Atomic Data and Nuclear Data Tables*, 39(2):213 – 223, 1988.
- [5] Ning Wang, Min Liu, Li Ou, and Yingxun Zhang. Properties of nuclear matter from macroscopic–microscopic mass formulas. *Physics Letters B*, 751:553 – 558, 2015.
- [6] M. G. Mayer and J. H. D. Jensen. *Elementary theory of nuclear shell structure*. Structure of matter series. New York: Wiley, 1955.
- [7] R. B. Wiringa, V. G. J. Stoks, and R. Schiavilla. Accurate nucleon-nucleon potential with charge-independence breaking. *Phys. Rev. C*, 51:38–51, Jan 1995.
- [8] J. Mougey. The (e,e’p) Reaction. *Nuclear Physics A*, 335:35–53, 1980.
- [9] G. Jacob and Th. A. J. Maris. Quasi-Free Scattering and Nuclear Structure. *Reviews of Modern Physics*, 38(1):121–142, 1966.
- [10] G. Jacob and Th. A. J. Maris. Quasi-Free Scattering and Nuclear Structure. II. *Reviews of Modern Physics*, 45(1):6–21, 1973.
- [11] H. De Vries, C.W. De Jager, and C. De Vries. Nuclear charge-density-distribution parameters from elastic electron scattering. *Atomic Data and Nuclear Data Tables*, 36(3):495 – 536, 1987.

BIBLIOGRAPHY

- [12] B. A. Brown, S. E. Massen, and P. E. Hodgson. Proton and neutron density distributions for $A=16-58$ nuclei. *Journal of Physics G: Nuclear Physics*, 5(12):1655–1698, Dec 1979.
- [13] H. Feshbach and V. F. Weisskopf. A Schematic Theory of Nuclear Cross Sections. *Phys. Rev.*, 76:1550–1560, Dec 1949.
- [14] S. Fernbach, R. Serber, and T. B. Taylor. The Scattering of High Energy Neutrons by Nuclei. *Phys. Rev.*, 75:1352–1355, May 1949.
- [15] G. R Satchler. *Introduction to Nuclear Reactions*. John Wiley And Sons, 1980.
- [16] R. W. Finlay, W. P. Abfalterer, G. Fink, E. Montei, T. Adami, P. W. Lisowski, G. L. Morgan, and R. C. Haight. Neutron Total Cross Sections at Intermediate Energies. *Physical Review, Part C, Nuclear Physics*, 47:237, 1993.
- [17] R. B. Schwartz, R. A. Schrack, and H. T. Heaton II. MeV total neutron cross sections. Technical Report 138, National Bureau of Standards, 1974.
- [18] W. P. Poenitz and J. F. Whalen. NEUTRON TOTAL CROSS SECTION MEASUREMENTS IN THE ENERGY REGION FROM 47 KEV TO 20 MEV. Technical Report 80, Argonne National Laboratory, 1983.
- [19] W. P. Abfalterer, R. W. Finlay, and S. M. Grimes. Level widths and level densities of nuclei in the $32 < A < 60$ mass region inferred from fluctuation analysis of total neutron cross sections. *Phys. Rev. C*, 62:064312, Nov 2000.
- [20] W. P. Abfalterer, F. B. Bateman, F. S. Dietrich, R. W. Finlay, R. C. Haight, and G. L. Morgan. Measurement of Neutron Total Cross Sections up to 560 MeV. *Physical Review, Part C, Nuclear Physics*, 63:044608, 2001.
- [21] J. M. Peterson. Neutron Giant Resonances - Nuclear Ramsauer Effect. *Phys. Rev.*, 125:955–963, Feb 1962.
- [22] I. Angeli and J. Csikai. Total neutron cross sections and the nuclear Ramsauer effect. *Nuclear Physics A*, 158(2):389–392, 1970.
- [23] C B O Mohr. The Mean Free Path of Slow Neutrons in Nuclear Matter. *Proceedings of the Physical Society. Section A*, 68(4):340, 1955.
- [24] K.W. McVoy. Giant resonances and neutron-nucleus total cross sections. *Annals of Physics*, 43(1):91–125, 1967.

-
- [25] I. Ahmad, N. Bano, and A. N. Saharia. A semi-empirical formula for the neutron total cross section and the interpretation of the empirical formula for $A \geq 40$. *Pramana - J. Phys.*, 1:188–195, 1973.
- [26] H Feshbach. The Optical Model and Its Justification. *Annual Review of Nuclear Science*, 8(1):49–104, 1958.
- [27] W. H. Dickhoff and R. J. Charity. Recent developments for the optical model of nuclei. *Progress in Particle and Nuclear Physics*, 2018.
- [28] P E Hodgson. The nuclear optical model. *Reports on Progress in Physics*, 34(2):765–819, may 1971.
- [29] R. L. Varner, W. J. Thompson, T. L. McAbee, E. J. Ludwig, and T. B. Clegg. A global nucleon optical potential. *Physics Reports*, 201:57–119, 1991.
- [30] A.J. Koning and J.P. Delaroche. Local and global nucleon optical models from 1 keV to 200 MeV. *Nuclear Physics A*, 713(3):231 – 310, 2003.
- [31] C. R. Gould, D. G. Haase, L. W. Seagondollar, J. P. Soderstrum, K. E. Nash, M. B. Schneider, and N. R. Roberson. Spin-Spin Potentials in $^{27}\text{Al}_{\text{pol}} + n_{\text{pol}}$ and the Nuclear Ramsauer Effect. *Phys. Rev. Lett.*, 57:2371–2374, Nov 1986.
- [32] J. D. Anderson and S. M. Grimes. Nuclear Ramsauer effect and the isovector potential. *Phys. Rev. C*, 41:2904–2910, Jun 1990.
- [33] C Mahaux and R Sartor. Single-Particle Motion in Nuclei. *Advances in Nuclear Physics*, 20:1–225, 01 1991.
- [34] J. W. Holt, N. Kaiser, and G. A. Miller. Microscopic optical potential for exotic isotopes from chiral effective field theory. *Phys. Rev. C*, 93:064603, Jun 2016.
- [35] Experimental Nuclear Reaction Data (EXFOR). Accessed 2018-3-10 to 2019-4-1.
- [36] Neutron Cross section Curves For $Z = 1-100$. In Victoria McLane, Charles L. Dunford, and Philip F. Rose, editors, *Neutron Cross Sections*, pages 1–806. Academic Press, 1988.
- [37] R. Shane, R. J. Charity, J. M. Elson, L. G. Sobotka, M. Devlin, N. Fotiadis, and J. M. O'Donnell. Total neutron cross-sections for rare isotopes using a digital-signal-processing technique: Case study ^{48}Ca . *Nucl. Instrum. Methods in Physics Res., Sect.A*, 614:468, 2010.

BIBLIOGRAPHY

- [38] Tapan Mukhopadhyay, Joydev Lahiri, and D.N. Basu. Theoretical estimates of cross sections for neutron–nucleus collisions. *Annals of Nuclear Energy*, 38(7):1452–1457, 2011.
- [39] H. S. Camarda, T. W. Phillips, and R. M. White. Neutron absolute and total cross section difference measurements in the mass-140 region. *Phys. Rev. C*, 29:2106–2117, Jun 1984.
- [40] F. S. Dietrich, J. D. Anderson, R. W. Bauer, S. M. Grimes, R. W. Finlay, W. P. Abfalterer, F. B. Bateman, R. C. Haight, G. L. Morgan, E. Bauge, J.-P. Delaroche, and P. Romain. Importance of isovector effects in reproducing neutron total cross section differences in the W isotopes. *Phys. Rev. C*, 67:044606, Apr 2003.
- [41] J. Rapaport, V. Kulkarni, and R.W. Finlay. A global optical-model analysis of neutron elastic scattering data. *Nuclear Physics A*, 330(1):15 – 28, 1979.
- [42] Mohammadhossein Mahzoon. *Implications of a Fully Nonlocal Implementation of the Dispersive Optical Model*. PhD thesis, Washington University in St Louis, 2015.
- [43] Meng Wang, G. Audi, F. G. Kondev, W.J. Huang, S. Naimi, and Xing Xu. The AME2016 atomic mass evaluation (II). Tables, graphs and references. *Chinese Physics C*, 41(3):030003, mar 2017.
- [44] I Angeli, M Beiner, R J Lombard, and D Mas. Trends in nuclear radii from the energy density method. *Journal of Physics G: Nuclear Physics*, 6(3):303–317, 03 1980.
- [45] D F Jackson. Nuclear sizes and the optical model. *Reports on Progress in Physics*, 37(1):55–146, jan 1974.
- [46] G. Fricke and K. Heilig. *Nuclear Charge Radii*, volume 20 of *Elementary Particles, Nuclei and Atoms*. Springer-Verlag Berlin Heidelberg, 2004.
- [47] A. J. Miller, K. Minamisono, A. Klose, D. Garand, C. Kujawa, J. D. Lantis, Y. Liu, B. Maaß, P. F. Mantica, W. Nazarewicz, W. Nörtershäuser, S. V. Pineda, P.-G. Reinhard, D. M. Rossi, F. Sommer, C. Sumithrarachchi, A. Teigelhöfer, and J. Watkins. Proton superfluidity and charge radii in proton-rich calcium isotopes. *Nature Physics*, 2019.
- [48] M Anselment, K Bekk, A Hanser, H Hoeffgen, G Meisel, S Göring, H Rebel, and G Schatz. Charge radii and moments of tin nuclei by laser spectroscopy. *Physical review C: Nuclear physics*, 34:1052–1059, 10 1986.

-
- [49] Otten E. W. Nuclear Radii and Moments of Unstable Isotopes. In Bromley D. A., editor, *Treatise on Heavy Ion Science*. Springer, Boston, MA, 01 1989.
- [50] D. H. Wilkinson. Is the Surface of the Nucleus Neutron-Rich? *Comments Nucl. Particle Phys.*, 1:80–84, 03 1967.
- [51] D. Berdichevsky, R. Fleming, D. W. L. Sprung, and F. Tondeur. Charge and mass radii of the tin isotopes. *Zeitschrift für Physik A Atomic Nuclei*, 329(4):393–405, Dec 1988.
- [52] William D Myers and W.J Swiatecki. Average nuclear properties. *Annals of Physics*, 55(3):395 – 505, 1969.
- [53] C. J. Horowitz, K. S. Kumar, and R. Michaels. Electroweak measurements of neutron densities in CREX and PREX at JLab, USA. *The European Physical Journal A*, 50(2):48, Feb 2014.
- [54] X. Viñas, M. Centelles, X. Roca-Maza, and M. Warda. Density dependence of the symmetry energy from neutron skin thickness in finite nuclei. *The European Physical Journal A*, 50(2):27, Feb 2014.
- [55] B. Alex Brown. Neutron Radii in Nuclei and the Neutron Equation of State. *Phys. Rev. Lett.*, 85:5296–5299, Dec 2000.
- [56] F. J. Fattoyev and J. Piekarewicz. Neutron skins and neutron stars. *Phys. Rev. C*, 86:015802, Jul 2012.
- [57] Jorge Piekarewicz, B Agrawal, Gianluca Colò, Witold Nazarewicz, Nils Paar, P Reinhard, Xavier Roca-Maza, and D Vretenar. Electric dipole polarizability and the neutron skin. *Physical Review C*, 85:041302, 01 2012.
- [58] Zhen Zhang, Yeunhwan Lim, Jeremy W. Holt, and Che Ming Ko. Nuclear dipole polarizability from mean-field modeling constrained by chiral effective field theory. *Physics Letters B*, 777:73 – 78, 2018.
- [59] M. H. Mahzoon, M. C. Atkinson, R. J. Charity, and W. H. Dickhoff. Neutron Skin Thickness of ^{48}Ca from a Nonlocal Dispersive Optical-Model Analysis. *Phys. Rev. Lett.*, 119:222503, Nov 2017.
- [60] T. W. Phillips, B. L. Berman, and J. D. Seagrave. Neutron total cross section for tritium. *Phys. Rev. C*, 22:384–396, Aug 1980.
- [61] D. Graham Foster and Dale W. Glasgow. Neutron Total Cross Sections, 2.5-15 MeV. I. Experimental. *Phys. Rev. C*, 3:576–603, Feb 1971.

BIBLIOGRAPHY

- [62] B. Haesner, W. Heeringa, H. O. Klages, H. Dobiash, G. Schmalz, P. Schwarz, J. Wilczynski, B. Zeitnitz, and F. Kappeler. Measurement of the ^3He and ^4He Total Neutron Cross Sections up to 40 MeV. *Physical Review, Part C, Nuclear Physics*, 28(3):995, 1983.
- [63] C. A. Goulding, P. Stoler, and J. D. Seagrave. ^3He and ^4He Total Neutron Cross Sections in the MeV Region. *Nuclear Physics, Section A*, 215:253, 1973.
- [64] D. F. Measday and J. N. Palmieri. Neutron Total Cross Sections in the Energy Range 80 to 150 MeV. *Nuclear Physics*, 85:129, 1966.
- [65] F.G Perey, T. A. Love, and W. E. Kinney. Test of Neutron Total Cross-Section Evaluations from 0.2 to 20 MeV for C, O, Al, Si, Ca, Fe, and SiO. Technical Report 4823, Oak Ridge National Lab, 1972.
- [66] F. J. Vaughn, H. A. Grench, W. L. Imhof, J. H. Rowland, and M. Walt. The Total Neutron Cross Section of O^{18} from 0.14 to 2.47 MeV. *Nuclear Physics*, 64:336, 1965.
- [67] S. R. Salisbury, D. B. Fossan, and F. J. Vaughn. The Total Neutron Cross Section Of O^{18} From 2.45 To 19.0 Mev. *Nuclear Physics*, 64:343, 1965.
- [68] C.H. Johnson, J.L. Fowler, and N.W. Hill. Total neutron cross section of calcium. volume 1, page 525, 1973. Int.Conf.on Nuclear Physics,Munich 1973.
- [69] J. A. Harvey, C. H. Johnson, R. F. Carlton, and B. Castel. Single-Particle $2d_{5/2}$ Strength in the $^{48}\text{Ca} + n$ Reaction. *Physical Review, Part C, Nuclear Physics*, 32:1114, 1985.
- [70] C. M. Perey, F. G. Perey, J. A. Harvey, N. W. Hill, N. M. Larson, R. L. Macklin, and D. C. Larson. $^{58}\text{Ni} + n$ Transmission, Differential Elastic Scattering, and Capture Measurements and Analysis up to 813 keV. *Physical Review, Part C, Nuclear Physics*, 47:1143, 1993.
- [71] Y. V. Dukarevich, A. N. Dyumin, and D. M. Kaminker. Total Neutron Cross Sections Of Isotopes And The Isobaric Spin Term Of Nuclear Potential. *Nuclear Physics, Section A*, 92(2):433, 1967.
- [72] V. M. Timokhov, M. V. Bokhovko, A. G. Isakov, L. E. Kazakov, V. N. Kononov, G. N. Manturov, E. D. Poletaev, and V. G. Pronyaev. Neutron Capture, Total Cross Sections and Average Resonance Parameters for Tin Isotopes. *Yadernaya Fizika*, 50(3):609, 1989.

-
- [73] R. W. Harper, T. W. Godfrey, and J. L. Weil. Interaction of Neutrons with Even-A Tin Isotopes. I. Total Cross Section for $E(n) = 0.3\text{-}5.0$ MeV. *Physical Review, Part C, Nuclear Physics*, 26:1432, 1982.
- [74] J. Rapaport, M. Mirzaa, M. Hadizadeh, D. E. Bainum, and R. W. Finlay. Neutron Elastic Scattering from $^{116,118,120,122,124}\text{Sn}$. *Nuclear Physics, Section A*, 341:56, 1980.
- [75] R. F. Carlton, J. A. Harvey, and N. W. Hill. Neutron resonance spectroscopy for $n+^{204}\text{Pb}$: Total and differential elastic scattering cross sections. *Physical Review, Part C, Nuclear Physics*, 67:024601, 2003.
- [76] Experimental Nuclear Reaction Data (EXFOR). EXFOR cites private communication with J. A. Harvey, 1999.
- [77] B Luther, T Baumann, M Thoennessen, Jervon Brown, P Deyoung, J Finck, J Hinnefeld, R Howes, K Kemper, P Pancella, Graham Peaslee, W Rogers, and S Tabor. MoNA—The Modular Neutron Array. *Nuclear Instruments and Methods in Physics Research Section A: Accelerators, Spectrometers, Detectors and Associated Equipment*, 505:33–35, 06 2003.
- [78] W.A. Peters, S. Ilyushkin, M. Madurga, C. Matei, S.V. Paulauskas, R.K. Grzywacz, D.W. Bardayan, C.R. Brune, J. Allen, J.M. Allen, Z. Bergstrom, J. Blackmon, N.T. Brewer, J.A. Cizewski, P. Copp, M.E. Howard, R. Ikeyama, R.L. Kozub, B. Manning, T.N. Massey, M. Matos, E. Merino, P.D. O'Malley, F. Raiola, C.S. Reingold, F. Sarazin, I. Spassova, S. Taylor, and D. Walter. Performance of the Versatile Array of Neutron Detectors at Low Energy (VANDLE). *Nuclear Instruments and Methods in Physics Research Section A: Accelerators, Spectrometers, Detectors and Associated Equipment*, 836:122 – 133, 2016.
- [79] The R³B Collaboration. Technical Report for the Design, Construction, and Commissioning of NeuLAND: The High-Resolution Neutron Time-of-Flight Spectrometer for R³B. Technical report, Facility for Antiproton and Ion Research, 2011.
- [80] M.S. Moore. Rate dependence of counting losses in neutron time-of-flight measurements. *Nuclear Instruments and Methods*, 169(1):245 – 247, 1980.
- [81] J. M. Clement, P. Stoler, C. A. Goulding, and R. W. Fairchild. Hydrogen and Deuterium Total Neutron Cross Sections in the MeV Region. *Nuclear Physics, Section A*, 183:51, 1972.

BIBLIOGRAPHY

- [82] W. P. Abfalterer, F. B. Bateman, F. S. Dietrich, Ch. Elster, R. W. Finlay, W. Glöckle, J. Golak, R. C. Haight, D. Hüber, G. L. Morgan, and H. Witala. Inadequacies of the Nonrelativistic $3N$ Hamiltonian in Describing the $n + d$ Total Cross Section. *Phys. Rev. Lett.*, 81:57–60, Jul 1998.
- [83] E. Doucet, T. Brown, P. Chowdhury, C.J. Lister, C. Morse, P.C. Bender, and A.M. Rogers. Machine learning n/γ discrimination in CLYC scintillators. *Nuclear Instruments and Methods in Physics Research Section A: Accelerators, Spectrometers, Detectors and Associated Equipment*, 2018.
- [84] Ji-Hwan Kang. *Triplet Fusion Photon Upconversion Systems: Towards Low Threshold Applications*. PhD thesis, Georgia Institute of Technology, 2017.
- [85] P. P. Guss, R. C. Byrd, C. R. Howell, R. S. Pedroni, G. Tungate, R. L. Walter, and J. P. Delaroche. Optical model description of the neutron interaction with ^{116}Sn and ^{120}Sn over a wide energy range. *Phys. Rev. C*, 39:405–414, Feb 1989.
- [86] Paul Guss. *Cross Sections and Analyzing Powers For Elastic and Inelastic Neutron Scattering From ^{58}Ni , ^{60}Ni , ^{116}Sn , and ^{120}Sn* . PhD thesis, Duke University, 1982.
- [87] Richard A. Arndt, Igor I. Strakovsky, and Ron L. Workman. Updated resonance photodecay amplitudes to 2 GeV. *Phys. Rev. C*, 53:430–440, Jan 1996.
- [88] W. H. Dickhoff and D. Van Neck. *Many-Body Theory Exposed!* World Scientific, 2nd edition, 2008.
- [89] Herman Feshbach. Unified theory of nuclear reactions. *Annals of Physics*, 5(4):357 – 390, 1958.
- [90] G. Passatore. On a dispersion relation for the potential in the optical model. *Nuclear Physics A*, 95(3):694 – 704, 1967.
- [91] A. Bohr and B. R. Mottelson. *Nuclear Structure*, volume Vol. 1, Single-Particle Motion. W. A. Benjamin, 1969.
- [92] Mack Atkinson. *Developing nucleon self-energies to generate the ingredients for the description of nuclear reactions*. PhD thesis, Washington University in St Louis, 2019.
- [93] F. Perey and B. Buck. A non-local potential model for the scattering of neutrons by nuclei. *Nuclear Physics*, 32:353 – 380, 1962.
- [94] R. J. Charity, J. M. Mueller, L. G. Sobotka, and W. H. Dickhoff. Dispersive-optical-model analysis of the asymmetry dependence of correlations in Ca isotopes. *Phys. Rev. C*, 76:044314, Oct 2007.

- [95] William Press, Saul A. Teukolsky, William Vetterling, and Brian Flannery. *Numerical recipes in C. The art of scientific computing*. Cambridge: Cambridge University Press, 01 1992.
- [96] J. M. Mueller, R. J. Charity, R. Shane, L. G. Sobotka, S. J. Waldecker, W. H. Dickhoff, A. S. Crowell, J. H. Esterline, B. Fallin, C. R. Howell, C. Westerfeldt, M. Youngs, B. J. Crowe, and R. S. Pedroni. Asymmetry dependence of nucleon correlations in spherical nuclei extracted from a dispersive-optical-model analysis. *Phys. Rev. C*, 83:064605, Jun 2011.
- [97] M. C. Atkinson, H. P. Blok, L. Lapikás, R. J. Charity, and W. H. Dickhoff. Validity of the distorted-wave impulse-approximation description of $^{40}\text{Ca}(e, e'p)^{39}\text{K}$ data using only ingredients from a nonlocal dispersive optical model. *Phys. Rev. C*, 98:044627, Oct 2018.
- [98] G. Hagen, A. Ekström, C. Forssén, G. R. Jansen, W. Nazarewicz, T. Papenbrock, K. A. Wendt, S. Bacca, N. Barnea, B. Carlsson, C. Drischler, K. Hebeler, M. Hjorth-Jensen, M. Miorelli, G. Orlandini, A. Schwenk, and J. Simonis. Neutron and weak-charge distributions of the ^{48}Ca nucleus. *Nature Physics*, 12:186–190, 2016.
- [99] M. H. Mahzoon, R. J. Charity, W. H. Dickhoff, H. Dussan, and S. J. Waldecker. Forging the Link between Nuclear Reactions and Nuclear Structure. *Phys. Rev. Lett.*, 112:162503, Apr 2014.
- [100] O. Hen, E. Piassetzky, and L. B. Weinstein. New data strengthen the connection between short range correlations and the EMC effect. *Phys. Rev. C*, 85:047301, Apr 2012.
- [101] J. Arrington, A. Daniel, D. B. Day, N. Fomin, D. Gaskell, and P. Solvignon. Detailed study of the nuclear dependence of the EMC effect and short-range correlations. *Phys. Rev. C*, 86:065204, Dec 2012.
- [102] The CLAS Collaboration. Modified structure of protons and neutrons in correlated pairs. *Nature*, 566:354–358, 2019.
- [103] R. Subedi, R. Shneor, P. Monaghan, B. D. Anderson, K. Aniol, J. Annand, J. Arrington, H. Benaoum, F. Benmokhtar, W. Boeglin, J.-P. Chen, Seonho Choi, E. Cisbani, B. Craver, S. Frullani, F. Garibaldi, S. Gilad, R. Gilman, O. Glamazdin, J.-O. Hansen, D. W. Higinbotham, T. Holmstrom, H. Ibrahim, R. Igarashi, C. W. de Jager, E. Jans, X. Jiang, L. J. Kaufman, A. Kelleher, A. Kolarkar, G. Kumbartzki, J. J. LeRose, R. Lindgren, N. Liyanage, D. J. Margaziotis, P. Markowitz, S. Marrone, M. Mazouz, D. Meekins, R. Michaels, B. Moffit, C. F. Perdrisat, E. Piassetzky,

BIBLIOGRAPHY

- M. Potokar, V. Punjabi, Y. Qiang, J. Reinhold, G. Ron, G. Rosner, A. Saha, B. Sawatzky, A. Shahinyan, S. Širca, K. Slifer, P. Solvignon, V. Sulkosky, G. M. Urciuoli, E. Voutier, J. W. Watson, L. B. Weinstein, B. Wojtsekhowski, S. Wood, X.-C. Zheng, and L. Zhu. Probing Cold Dense Nuclear Matter. *Science*, 320(5882):1476–1478, 2008.
- [104] D. Rohe, C. S. Armstrong, R. Asaturyan, O. K. Baker, S. Bueltmann, C. Carasco, D. Day, R. Ent, H. C. Fenker, K. Garrow, A. Gasparian, P. Gueye, M. Hauger, A. Honegger, J. Jourdan, C. E. Keppel, G. Kubon, R. Lindgren, A. Lung, D. J. Mack, J. H. Mitchell, H. Mkrtchyan, D. Mocolj, K. Normand, T. Petitjean, O. Rondon, E. Segbefia, I. Sick, S. Stepanyan, L. Tang, F. Tiefenbacher, W. F. Vulcan, G. Warren, S. A. Wood, L. Yuan, M. Zeier, H. Zhu, and B. Zihlmann. Correlated Strength in the Nuclear Spectral Function. *Phys. Rev. Lett.*, 93:182501, Oct 2004.
- [105] P. Grabmayr, J. Rapaport, and R.W. Finlay. Elastic and inelastic scattering of 24 MeV nucleons from oxygen isotopes. *Nuclear Physics A*, 350(1):167 – 189, 1980.
- [106] K. Marinova, W. Geithner, M. Kowalska, K. Blaum, S. Kappertz, M. Keim, S. Kloos, G. Kotrotsios, P. Lievens, R. Neugart, H. Simon, and S. Wilbert. Charge radii of neon isotopes across the *sd* neutron shell. *Phys. Rev. C*, 84:034313, Sep 2011.
- [107] B. Alex Brown. Mirror Charge Radii and the Neutron Equation of State. *Phys. Rev. Lett.*, 119:122502, Sep 2017.
- [108] I.A.Korzsh, V.P.Lunev, V.A.Mishchenko, E.N.Mozhzhukhin, M.V.Pasechnik, and N.M.Pravdivyy. The Angular Distribution of Neutrons Elastically and Idealistically Scattered by Ni-58,60,62,64. *Yadernaya Fizika*, 31:13, 1980.
- [109] Daniela Rohe. *Spectral function at high energy and momentum from (e,e'p) experiment*. habilitation, University of Basil, 2004.
- [110] R. F. Carlson, A. J. Cox, J. R. Nimmo, N. E. Davison, S. A. Elbakr, J. L. Horton, A. Houdayer, A. M. Sourkes, W. T. H. van Oers, and D. J. Margaziotis. Proton total reaction cross sections for the doubly magic nuclei *O*16, *Ca*40, and *Pb*208 in the energy range 20-50 MeV. *Phys. Rev. C*, 12(4):1167–1175, 1975.
- [111] I. Šlaus, D. J. Margaziotis, R. F. Carlson, W. T. H. van Oers, and J. Reginald Richardson. Structure in the energy dependence of the proton total reaction cross section for C and Si in the energy region 20-40 MeV. *Phys. Rev. C*, 12:1093–1095, Sep 1975.

- [112] A. Ingemarsson, J. Nyberg, P.U. Renberg, O. Sundberg, R.F. Carlson, A. Auce, R. Johansson, G. Tibell, B.C. Clark, L. Kurth Kerr, and S. Hama. Reaction cross sections for 65 MeV protons on targets from 9Be to 208Pb. *Nuclear Physics A*, 653(4):341 – 354, 1999.
- [113] A. Auce, A. Ingemarsson, R. Johansson, M. Lantz, G. Tibell, R. F. Carlson, M. J. Shachno, A. A. Cowley, G. C. Hillhouse, N. M. Jacobs, J. A. Stander, J. J. van Zyl, S. V. Förtsch, J. J. Lawrie, F. D. Smit, and G. F. Steyn. Reaction cross sections for protons on C^{12} , Ca^{40} , Zr^{90} , and Pb^{208} at energies between 80 and 180 MeV. *Phys. Rev. C*, 71(6):064606, 2005.
- [114] J. Piekarewicz. Pygmy dipole resonance as a constraint on the neutron skin of heavy nuclei. *Phys. Rev. C*, 73:044325, Apr 2006.
- [115] J. L. Herraiz, M. C. Martínez, J. A. Caballero, and J. M. Udías. Overview of neutino-nucleus quasielastic scattering. *AIP Conference Proceedings*, 1189(1):125–132, 2009.
- [116] Nikhil Anand, A. Liam Fitzpatrick, and W. C. Haxton. Weakly interacting massive particle-nucleus elastic scattering response. *Phys. Rev. C*, 89:065501, Jun 2014.
- [117] K. J. R. Rosman and P. D. P. Taylor. Isotopic Compositions of the Elements 1997. Technical Report 4780, International Union of Pure and Applied Chemistry, 1997.
- [118] Shinsaku Kobayashi. Elastic and Inelastic Scattering of Protons by Oxygen in the Energy Region of 6.9 MeV to 15.6 MeV. *Journal of the Physical Society of Japan*, 15(7):1164–1174, 1960.
- [119] Chuin Hu, Ken Kikuchi, Shinsaku Kobayashi, Kazuhisa Matsuda, Yukio Nagahara, Yukiyasu Oda, Naoyuki Takano, Minoru Takeda, and Takashi Yamazaki. Elastic and Inelastic Scatterings of Protons from Ti, Cr, Ni, Zn, and O at 8 to 14 MeV. *Journal of the Physical Society of Japan*, 14(7):861–869, 1959.
- [120] Donald R. Maxson. $O^{16}(p, \alpha)N^{13}$ Angular Distributions at 13.5–18.1 MeV. *Phys. Rev.*, 123:1304–1309, Aug 1961.
- [121] G. M. Crawley and G. T. Garvey. Inelastic Scattering in the $2s - 1d$ Shell. II. Odd- A Nuclei. *Phys. Rev.*, 167:1070–1090, Mar 1968.
- [122] O. Karban, P.D. Greaves, V. Hnizdo, J. Lowe, N. Berovic, H. Wojciechowski, and G.W. Greenlees. The elastic scattering of protons by ^{16}O in the energy range 16–30 MeV. *Nuclear Physics A*, 132(3):548 – 560, 1969.

BIBLIOGRAPHY

- [123] J. M. Cameron, J. Reginald Richardson, W. T. H. van Oers, and J. W. Verba. Studies of the Energy Dependence of p - O^{16} Interactions between 20 and 50 MeV. I. Measurements of the Differential Cross Sections of Protons Elastically Scattered by O^{16} at 23.4, 24.5, 27.3, 30.1, 34.1, 36.8, 39.7, 43.1, and 46.1 MeV. *Phys. Rev.*, 167:908–914, Mar 1968.
- [124] J.A. Fannon, E.J. Burge, D.A. Smith, and N.K. Ganguly. Elastic and inelastic scattering of 50 MeV protons by ^{12}C and ^{16}O . *Nuclear Physics A*, 97(2):263 – 281, 1967.
- [125] F. E. Bertrand and R. W. Peelle. Complete Hydrogen and Helium Particle Spectra from 30- to 60-MeV Proton Bombardment of Nuclei with $A = 12$ to 209 and Comparison with the Intranuclear Cascade Model. *Phys. Rev. C*, 8:1045–1064, Sep 1973.
- [126] H. Sakaguchi. Systematic study on the elastic scattering of 65 MeV polarized protons. *Jour. Memoirs Faculty of Sci., A*, 36:305, 1982.
- [127] J. J. Kelly, W. Bertozzi, T. N. Buti, J. M. Finn, F. W. Hersman, C. Hyde-Wright, M. V. Hynes, M. A. Kovash, B. Murdock, B. E. Norum, B. Pugh, F. N. Rad, A. D. Bacher, G. T. Emery, C. C. Foster, W. P. Jones, D. W. Miller, B. L. Berman, W. G. Love, J. A. Carr, and F. Petrovich. Density dependence in the two-nucleon effective interaction at 135 MeV. *Phys. Rev. C*, 39:1222–1241, Apr 1989.
- [128] A.E. Taylor and E. Wood. Proton scattering from light elements at 142 MeV. *Nuclear Physics*, 25:642 – 655, 1961.
- [129] J. J. Kelly, J. M. Finn, W. Bertozzi, T. N. Buti, F. W. Hersman, C. Hyde-Wright, M. V. Hynes, M. A. Kovash, B. Murdock, P. Ulmer, A. D. Bacher, G. T. Emery, C. C. Foster, W. P. Jones, D. W. Miller, and B. L. Berman. Effective interactions and nuclear structure using 180 MeV protons. I. $^{16}O(p,p')$. *Phys. Rev. C*, 41:2504–2513, Jun 1990.
- [130] C. W. Glover, P. Schwandt, H. O. Meyer, W. W. Jacobs, J. R. Hall, M. D. Kaitchuck, and R. P. DeVito. Optical model analysis of 200 MeV $p \rightarrow ^{16}O$ elastic scattering data measured to large momentum transfers. *Phys. Rev. C*, 31:1–11, Jan 1985.
- [131] W. E. Kinney and F. G. Perey. Neutron elastic- and inelastic-scattering cross sections for oxygen in the energy range 4.34 to 8.56 MeV. Technical Report 4780, ORNL, 1972.
- [132] W. P. Bucher, C. E. Hollandsworth, D. McNatt, R. Lamoreaux, A. Niiler, and J. E. Youngblood. Small-Angle Scattering of 7.4- to 9.5-MeV Neutrons from Nitrogen and Oxygen. *Nuclear Science and Engineering*, 54(4):416–422, 1974.
- [133] S. G. Glendinning, S. El-Kadi, C. E. Nelson, F. O. Purser, C. R. Gould, and L. W. Seagondollar. Neutron Elastic Scattering Cross Sections for ^{16}O Between 9 and 15 MeV. *Nuclear Science and Engineering*, 82(4):393–399, 1982.

-
- [134] L. Anli, H. G. Pfutzner, C. R. Howell, and R. L. Walter. Measurements of analyzing power $A_y(\theta)$ for neutron elastic scattering from ^{14}N and ^{16}O . *Chinese J. of Nuclear Physics (Beijing)*, 11:1, 1989.
- [135] G. Boerker, R. Boettger, H. J. Brede, H. Klein, W. Mannhart, and R. L. Siebert. Elastic And Inelastic Differential Neutron Scattering Cross Sections Of Oxygen Between 6 And 15 MeV. page 193, 1988. Conf. on Nucl. Data for Sci. and Technol., Mito).
- [136] J. H. Dave and C. R. Gould. Optical model analysis of scattering of 7- to 15-MeV neutrons from $1 - p$ shell nuclei. *Phys. Rev. C*, 28:2212–2221, Dec 1983.
- [137] J. P. Delaroche, M. S. Islam, and R. W. Finlay. Giant resonance coupling and l -dependent potentials for ^{16}O . *Phys. Rev. C*, 33:1826–1829, May 1986.
- [138] S. T. Lam, W. K. Dawson, S. A. Elbakr, H. W. Fielding, P. W. Green, R. L. Helmer, I. J. van Heerden, A. H. Hussein, S. P. Kwan, G. C. Neilson, T. Otsubo, D. M. Sheppard, H. S. Sherif, and J. Soukup. Elastic scattering of polarized neutrons on ^{16}O , ^{59}Co , and Pb at 23 MeV. *Phys. Rev. C*, 32:76–82, Jul 1985.
- [139] P. Mermod, J. Blomgren, C. Johansson, A. Öhrn, M. Österlund, S. Pomp, B. Bergenwall, J. Klug, L. Nilsson, N. Olsson, U. Tippawan, P. Nadel-Turonski, O. Jonsson, A. Prokofiev, P.-U. Renberg, Y. Maeda, H. Sakai, A. Tamii, K. Amos, R. Crespo, and A. Moro. 95 MeV neutron scattering on hydrogen, deuterium, carbon, and oxygen. *Phys. Rev. C*, 74:054002, Nov 2006.
- [140] R. A. Blue and W. Haeberli. Polarization of Protons Elastically Scattered by Oxygen. *Phys. Rev.*, 137:B284–B293, Jan 1965.
- [141] R.M. Prior, K.W. Corrigan, E.D. Berners, and S.E. Darden. Proton polarization in $^{16}\text{O}(p, p)^{16}\text{O}$ and states in $^{17}\text{F}^*$. *Nuclear Physics A*, 167(1):143 – 156, 1971.
- [142] P.D. Greaves, V. Hnizdo, J. Lowe, and O. Karban. Elastic and inelastic scattering of 30.4 MeV polarised protons by ^{12}C , ^{16}O and ^{54}Fe . *Nuclear Physics A*, 179(1):1 – 22, 1972.
- [143] H. Ohnuma, N. Hoshino, K. Ieki, M. Iwase, H. Shimizu, H. Toyokawa, T. Hasegawa, K. Nisimura, M. Yasue, H. Kabasawa, T. Nakagawa, T. Tohei, H. Orihara, S.I. Hayakawa, K. Miura, T. Suehiro, S.K. Nanda, D. Dehnhard, and M.A. Franey. The $^{16}\text{O}(p, p')$ reaction at 35 MeV. *Nuclear Physics A*, 514(2):273 – 294, 1990.
- [144] L Alvarez and G Palla. Elastic scattering of ^3He by ^{12}C and ^{16}O at an energy of 40.9 MeV. *Journal of Physics G: Nuclear Physics*, 8(7):987–995, jul 1982.

BIBLIOGRAPHY

- [145] Peter Hillman, A. Johansson, and H. Tyrén. Polarization of high energy protons in elastic and inelastic scattering. *Nuclear Physics*, 4:648 – 661, 1957.
- [146] R. F. Carlson, A. J. Cox, J. R. Nimmo, N. E. Davison, S. A. Elbakr, J. L. Horton, A. Houdayer, A. M. Sourkes, W. T. H. van Oers, and D. J. Margaziotis. Proton total reaction cross sections for the doubly magic nuclei ^{16}O , ^{40}Ca , and ^{208}Pb in the energy range 20-50 MeV. *Phys. Rev. C*, 12:1167–1175, Oct 1975.
- [147] D. Meier, M.Brullmann, H.Jung, and P.Marmier. Elastische und Inelastische Streuung von 14,1-MeV-Neutronen an ^{16}O und ^{16}O . *Helvetica Physica Acta*, 42:813, 1969.
- [148] J. Stevens, H.F. Lutz, and S.F. Eccles. Elastic and inelastic scattering of protons by ^{18}O . *Nuclear Physics*, 76(1):129 – 144, 1966.
- [149] E. Fabrici, S. Micheletti, M. Pignanelli, F. G. Resmini, R. De Leo, G. D’Erasmus, A. Pantaleo, J. L. Escudié, and A. Tarrats. Proton elastic scattering on light nuclei. I. Energy dependence. *Phys. Rev. C*, 21(3):830–843, 1980.
- [150] E. Colombo, R. De Leo, J.L. Escudie, E. Fabrici, S. Micheletti, M. Pignanelli, and F. Resmini. Systematical ‘Anomalous‘ Features Of Proton Elastic Scattering Related To Shell Structure. page 543, Sep 1977. Int. Conf. on Nuclear Structure, Tokyo.
- [151] E. Khan, Y. Blumenfeld, Nguyen Van Giai, T. Suomijärvi, N. Alamanos, F. Auger, G. Colò, N. Frascaria, A. Gillibert, T. Glasmacher, M. Godwin, K.W. Kemper, V. Lapoux, I. Lhenry, F. Maréchal, D.J. Morrissey, A. Musumarra, N.A. Orr, S. Ottini-Hustache, P. Piattelli, E.C. Pollacco, P. Roussel-Chomaz, J.C. Roynette, D. Santonocito, J.E. Sauvestre, J.A. Scarpaci, and C. Volpe. Low-lying collective states in neutron-rich oxygen isotopes via proton scattering. *Physics Letters B*, 490(1):45 – 52, 2000.
- [152] S. N. Choudry, J. N. Orce, V. Varadarajan, S. Leshner, D. Bandyopadhyay, S. Mukhopadhyay, S. W. Yates, and M. T. McEllistrem. Symmetry and structure tests in ^{18}O and ^{18}Ne . volume 819, page 101, 2006. AIP Conference Proceedings.
- [153] J. L. Escudié, R. Lombard, M. Pignanelli, F. Resmini, and A. Tarrats. Macroscopic and microscopic model analysis of polarized protons scattering on ^{18}O . *Phys. Rev. C*, 10:1645–1662, Nov 1974.
- [154] J. F. Dicello, G. Igo, W. T. Leland, and F. G. Perey. Differential Elastic Cross Sections for Protons Between 10 and 22 MeV on ^{40}Ca . *Phys. Rev. C*, 4(4):1130–1138, 1971.
- [155] W. T. H. van Oers. Optical-Model Analysis of $p + ^{40}\text{Ca}$ Elastic Scattering from 10-180 MeV. *Phys. Rev. C*, 3:1550–1559, Apr 1971.

- [156] R. H. McCamis, T. N. Nasr, J. Birchall, N. E. Davison, W. T. H. van Oers, P. J. T. Verheijen, R. F. Carlson, A. J. Cox, B. C. Clark, E. D. Cooper, S. Hama, and R. L. Mercer. Elastic scattering of protons from $^{40,42,44,48}\text{Ca}$ from 20 to 50 MeV and nuclear matter radii. *Phys. Rev. C*, 33(5):1624–1633, 1986.
- [157] D. L. Watson, J. Lowe, J. C. Dore, R. M. Craig, and D. J. Baugh. Elastic scattering of 26.3 and 30 MeV protons. *Nucl. Phys.*, A92:193, 1967.
- [158] L. N. Blumberg, E. E. Gross Gross, A. van der Woude, A. Zucker, and R. H. Bassel. Polarizations and Differential Cross Sections for the Elastic Scattering of 40-MeV Protons from ^{12}C , ^{40}Ca , ^{58}Ni , ^{90}Zr , and ^{208}Pb . *Phys. Rev.*, 147(3):812–825, 1966.
- [159] C. B. Fulmer, J. B. Ball, A. Scott, and M. L. Whiten. Elastic Scattering of 61.4-MeV Protons. *Phys. Rev.*, 181(4):1565–1579, 1969.
- [160] T. Noro, H. Sakaguchi, M. Nakamura, K. Hatanaka, F. Ohtani, H. Sakamoto, and S. Kobayashi. Isospin dependence of the 65 MeV proton optical potential in f-p shell nuclei. *Nucl. Phys.*, A366:189, 1981.
- [161] A. Nadasen, P. Schwandt, P. P. Singh, W. W. Jacobs, A. D. Bacher, P. T. Debevec, M. D. Kaitchuck, and J. T. Meek. Elastic scattering of 80-180 MeV protons and the proton-nucleus optical potential. *Phys. Rev. C*, 23(3):1023–1043, 1981.
- [162] P. Schwandt, H. O. Meyer, W. W. Jacobs, A. D. Bacher, S. E. Vigdor, M. D. Kaitchuck, and T. R. Donoghue. Analyzing power of proton-nucleus elastic scattering between 80 and 180 MeV. *Phys. Rev. C*, 26(1):55–64, 1982.
- [163] H. Seifert. *Energy Dependence of the Effective Interaction for Nucleon-Nucleus Scattering*. PhD thesis, University of Maryland, 1990.
- [164] C. Rolland, B. Geoffrion, N. Marty, M. Morlet, B. Tatischeff, and A. Willis. Modele optique pour la diffusion elastique des protons de 75 MeV et 150 MeV. *Nucl. Phys.*, 80:625, 1966.
- [165] Philip G. Roos and N. S. Wall. Elastic Scattering of 160-MeV Protons from Be9 , Ca40 , Ni58 , Sn120 , and Pb208 . *Phys. Rev.*, 140(5B):B1237–B1244, 1965.
- [166] A. Johansson, U. Svanberg, and P. E. Hodgson. The Elastic-Scattering of 180 MeV Protons from Nuclei. *Arkiv för Fysik*, 19:541, 1961.
- [167] D. P. Murdock and C. J. Horowitz. Microscopic relativistic description of proton-nucleus scattering. *Phys. Rev. C*, 35(4):1442–1462, 1987.

BIBLIOGRAPHY

- [168] W. Tornow, E. Woye, G. Mack, C. E. Floyd, K. Murphy, P. P. Guss, S. A. Wender, R. C. Byrd, R. L. Walter, T. B. Clegg, and H. Leeb. Analyzing power and differential cross section at 9.9, 11.9 and 13.9 MeV for Ca(n, n)Ca. *Nucl. Phys.*, A385:373, 1982.
- [169] J. Rapaport, J. D. Carlson, D. Bainum, T. S. Cheema, and R. W. Finlay. Neutron elastic scattering on $T = 0$ nuclei. *Nucl. Phys.*, A286:232, 1977.
- [170] G. M. Honoré, W. Tornow, C. R. Howell, R. S. Pedroni, R. C. Byrd, R. L. Walter, and J. P. Delaroche. Coupled-channel analysis of nucleon scattering from ^{40}Ca up to 80 MeV. *Phys. Rev. C*, 33(4):1129–1140, 1986.
- [171] R. Alarcon, J. Rapaport, and R. W. Finlay. Nucleon elastic scattering from ^{40}Ca between 11 and 48 MeV. *Nucl. Phys.*, A462:413, 1987.
- [172] R. P. DeVito, Sam M. Austin, W. Sterrenburg, and U. E. P. Berg. Limit on Charge Symmetry Breaking in the Optical Model and the Coulomb-Energy Anomaly. *Phys. Rev. Lett.*, 47(9):628–631, 1981.
- [173] E. L. Hjort, F. P. Brady, J. L. Romero, J. R. Drummond, D. S. Sorenson, J. H. Osborne, B. McEachern, and L. F. Hansen. Measurements and analysis of neutron elastic scattering at 65 MeV. *Phys. Rev. C*, 50:275–281, Jul 1994.
- [174] J. H. Osborne, F. P. Brady, J. L. Romero, J. L. Ullmann, D. S. Sorenson, A. Ling, N. S. P. King, R. C. Haight, J. Rapaport, R. W. Finlay, E. Bauge, J. P. Delaroche, and A. J. Koning. Measurement of neutron elastic scattering cross sections for ^{12}C , ^{40}Ca , and ^{208}Pb at energies from 65 to 225 MeV. *Phys. Rev. C*, 70(5):054613, 2004.
- [175] J. C. Lombardi, R. N. Boyd, R. Arking, and A. B. Robbins. Nuclear sizes in $^{40,44,48}\text{Ca}$. *Nucl. Phys.*, 188:103, 1972.
- [176] E. T. Boschitz, R. W. Bercaw, and J. S. Vincent. Effects on nuclear structure on the scattering on polarized protons. *Phys. Lett.*, 13:322, 1964.
- [177] V. Hnizdo, O. Karban, J. Lowe, G. W. Greenlees, and W. Makofske. Elastic scattering of 30.3-MeV Polarized Protons from ^{40}Ca , ^{56}Fe , and ^{59}Co . *Phys. Rev. C*, 3(4):1560–1565, 1971.
- [178] R. M. Craig, J. C. Dore, J. Lowe, and D. L. Watson. Polarization in the elastic scattering of 49 MeV protons by Ca, ^{58}Ni , ^{60}Ni and ^{208}Pb . *Nucl. Phys.*, 86:113, 1966.
- [179] H. Sakaguchi, M. Nakamura, K. Hatanaka, A. Goto, T. Noro, F. Ohtani, H. Sakamoto, H. Ogawa, and S. Kobayashi. Elastic scattering of 65 MeV polarized protons. *Phys. Rev. C*, 26(3):944–960, 1982.

-
- [180] J. F. Dicello and G. Igo. Proton Total Reaction Cross Sections in the 10-20-MeV Range: Calcium-40 and Carbon-12. *Phys. Rev. C*, 2:488–499, Aug 1970.
- [181] J. F. Turner, B. W. Ridley, P. E. Cavanagh, G. A. Gard, and A. H. Hardacre. Optical model studies of proton scattering at 30 MeV: (II). Proton total reaction cross sections at 28.5 ± 1.5 MeV. *Nucl. Phys.*, 58:509, 1964.
- [182] C. I. Zanelli, P. P. Urone, J. L. Romero, F. P. Brady, M. L. Johnson, G. A. Needham, J. L. Ullmann, and D. L. Johnson. Total non-elastic cross sections of neutrons on C, O, Ca, and Fe at 40.3 and 50.4 MeV. *Phys. Rev. C*, 23(3):1015–1022, 1981.
- [183] H. S. Liers. Cross sections and polarizations for protons scattered from ^{48}Ca between 6.0 and 12.7 MeV. *Nucl. Phys.*, A170:616, 1971.
- [184] S. Hicks. *Neutron Scattering Studies of the Doubly Magic Calcium Nuclei, CALCIUM-40 and CALCIUM-48, in the Low Energy Resonance Region*. PhD thesis, University of Kentucky, 1988.
- [185] Sally F. Hicks, S. E. Hicks, G. R. Shen, and M. T. McEllistrem. Collective doorway configurations in ^{49}Ca through neutron scattering on ^{48}Ca . *Phys. Rev. C*, 41(6):2560–2570, 1990.
- [186] R. F. Carlson, A. J. Cox, N. E. Davison, T. Eliyakut-Roshko, R. H. McCamis, and W. T. H. van Oers. Proton total reaction cross sections for ^{42}Ca , ^{44}Ca , and ^{48}Ca between 21 and 48 MeV. *Phys. Rev. C*, 49(6):3090–3097, 1994.
- [187] A. N. Djumin, A. I. Egorov, V. M. Lebedev, G. N. Popova, and V. A. Smolin. All Union Conference on Neutron Physics. volume 2, Kiev, USSR, 1977.
- [188] L. L. Lee and J. P. Schiffer. Studies of Elastic Scattering of Protons, Deuterons, and Alpha Particles from Isotopes of Cu, Ni, and Fe. *Phys. Rev.*, 134(4B):B765–B772, 1964.
- [189] G. W. Greenlees, C. H. Poppe, J. A. Sievers, and D. L. Watson. Proton Elastic Scattering Measurements at 9.8 MeV with Optical-Model Analysis. *Phys. Rev. C*, 3(3):1231–1242, 1971.
- [190] J. Benveniste, A. C. Mitchell, B. Buck, and C. B. Fulmer. Proton Scattering by Isobars and Single Isotopes. *Phys. Rev.*, 133:B323–B329, Jan 1964.
- [191] W. Makofske, G. W. Greenlees, H. S. Liers, and G. J. Pyle. Proton Elastic Scattering Measurements at 16 MeV with Optical-Model Analysis. *Phys. Rev. C*, 5(3):780–791, 1972.

BIBLIOGRAPHY

- [192] R. L. Varner. *A Parametrization of the Nucleon-Nucleus Optical Model Potential*. PhD thesis, Duke University, Durham, 1986.
- [193] P. Kossanyi-Demay, R. de Swiniarski, and C. Glashausser. An optical-model analysis of 18.6 MeV proton elastic scattering. *Nucl. Phys.*, A94(3):513 – 527, 1967.
- [194] J. R. Tesmer and F. H. Schmidt. Substate Excitation of 2+ States Produced by Inelastic Scattering of Protons on *C*12, *Fe*54, and *Ni*58. *Phys. Rev. C*, 5(3):864–875, 1972.
- [195] Norton Baron, Regis F. Leonard, and David A. Lind. Elastic Scattering of 21-MeV Protons from Nitrogen-14, Oxygen-16, Argon-40, Nickel-58, and Tin-116. *Phys. Rev.*, 180(4):978–986, 1969.
- [196] L. W. Put, P. P. Urone, and A. M. J. Paans. Scattering of 30 MeV protons from ²⁸Si, ⁵⁸Ni and ¹²⁰Sn at large backward angles. *Phys. Lett. B*, 35(4):311 – 313, 1971.
- [197] B. W. Ridley and J. F. Turner. Optical model studies of proton scattering at 30 MeV: (I). Differential cross sections for elastic scattering of protons at 30.3 MeV. *Nucl. Phys.*, 58:497, 1964.
- [198] E. Fabrici, S. Micheletti, M. Pignanelli, F. G. Resmini, R. De Leo, G. D’Erasmus, and A. Pantaleo. Proton elastic scattering on light nuclei. II. Nuclear structure effects. *Phys. Rev. C*, 21(3):844–860, 1980.
- [199] H. S. Liers, R. N. Boyd, C. H. Poppe, J. A. Sievers, and D. L. Watson. Elastic Scattering of 39.6-MeV Protons by Even Isotopes of Ni and Zn. *Phys. Rev. C*, 2(4):1399–1411, 1970.
- [200] Morton K. Brussel and John H. Williams. Elastic Scattering of 40-MeV Protons from Isotopes of Fe, Ni, and Cu. *Phys. Rev.*, 114(2):525–533, 1959.
- [201] M. P. Fricke, E. E. Gross, and A. Zucker. Inelastic Scattering of 40-MeV Polarized Protons. *Phys. Rev.*, 163(4):1153–1169, 1967.
- [202] H. Sakaguchi, M. Nakamura, K. Hatanaka, T. Noro, F. Ohtani, H. Sakamoto, H. Ogawa, and S. Kobayashi. Shell effects in the spin-orbit part of the optical potential. *Physics Letters B*, 99(2):92 – 95, 1981.
- [203] K. Kwiatkowski and N. S. Wall. Elastic scattering of 100 MeV protons and systematic optical model analysis. *Nucl. Phys.*, A301(2):349 – 358, 1978.
- [204] A. Ingemarsson, T. Johansson, and G. Tibell. Elastic and inelastic scattering of 178 MeV protons from ⁵⁸Ni and ⁶⁰Ni. *Nucl. Phys.*, A365(3):426 – 456, 1981.

- [205] H. Sakaguchi, H. Takeda, S. Toyama, M. Itoh, A. Yamagoshi, A. Tamii, M. Yosoi, H. Akimune, I. Daito, T. Inomata, T. Noro, and Y. Hosono. Elastic scattering of polarized protons from ^{58}Ni at $E_p = 192, 295,$ and 400 MeV. *Phys. Rev. C*, 57(4):1749–1755, 1998.
- [206] A B Smith, P T Guenther, J F Whalen, and S Chiba. Fast-neutron total and scattering cross sections of ^{58}Ni and nuclear models. *J. Phys G Nucl. Part. Phys.*, 18(4):629–654, 1992.
- [207] P. P. Guss, R. C. Byrd, C. E. Floyd, C. R. Howell, K. Murphy, G. Tungate, R. S. Pedroni, R. L. Walter, J. P. Delaroche, and T. B. Clegg. Cross sections and analyzing powers for fast-neutron scattering to the ground and first excited states of ^{58}Ni and ^{60}Ni . *Nucl. Phys.*, A438(1):187 – 211, 1985.
- [208] R. S. Pedroni, C. R. Howell, G. M. Honoré, H. G. Pfutzner, R. C. Byrd, R. L. Walter, and J. P. Delaroche. Energy dependence of the deformed optical potential for neutron scattering from $^{54,56}\text{Fe}$ and $^{58,60}\text{Ni}$ up to 80 MeV. *Phys. Rev. C*, 38(5):2052–2062, 1988.
- [209] Y. Yamanouti, J. Rapaport, S. M. Grimes, V. Kulkarni, R. W. Finlay, D. Bainum, P. Grabmayr, and G. Randers-Pehrson. Elastic And Inelastic Scattering Of 24 Mev Neutrons From Even Isotopes Of Ni. Technical Report 51245, Brookhaven National Laboratory, 1980.
- [210] L. Rosen and L. Stewart. Isotopic, Isotonic, and Shell Closure Effects on the Large-Angle Scattering of Polarized Protons. *Phys. Rev. Lett.*, 10(6):246–247, 1963.
- [211] P. J. Van Hall, J. P. M. G. Melssen, S. D. Wassenaar, O. J. Poppema, S. S. Klein, and G. J. Nijgh. Scattering of polarized protons by iron and nickel isotopes. *Nucl. Phys.*, A291(1):63 – 84, 1977.
- [212] R. M. Craig, J. C. Dore, G. W. Greenlees, J. S. Lilley, J. Lowe, and P. C. Rowe. Optical model studies of proton scattering at 30 MeV: (III). Polarization in Elastic Scattering by Ca, Co 59 , Ni 58 , Ni 60 , Sn 120 and Pb 208 . *Nucl. Phys.*, 58:515, 1964.
- [213] D. C. Kocher, F. E. Bertrand, E. E. Gross, and E. Newman. $^{58}\text{Ni}(p \rightarrow , p')$ reaction at 60 MeV: Study of the analyzing power for inelastic excitation of the giant resonance region of the nuclear continuum and of low-lying bound states. *Phys. Rev. C*, 14(4):1392–1411, 1976.
- [214] F. Hofmann, C. Bäumer, A.M. van den Berg, D. Frekers, V.M. Hannen, M.N. Harakeh, M.A. de Huu, Y. Kalmykov, P. von Neumann-Cosel, V.Yu. Ponomarev, S. Rakers,

BIBLIOGRAPHY

- B. Reitz, A. Richter, A. Shevchenko, K. Schweda, J. Wambach, and H.J. Wörtche. Polarized proton scattering on ^{58}Ni at small momentum transfer: A test of the microscopic optical model and effective interactions. *Phys. Lett. B*, 612(3-4):165 – 172, 2005.
- [215] P.J. Bulman, G.W. Greenlees, and M.J. Sametband. Proton reaction cross sections at 8.8 MeV. *Nuclear Physics*, 69(3):536 – 544, 1965.
- [216] K. Bearpark, W. R. Graham, and G. Jones. Total proton and neutron reaction cross-sections in the energy range 8.5 to 11.5 MeV. *Nucl. Phys.*, 73:206, 1965.
- [217] J. F. Dicello, G. J. Igo, and M. L. Roush. Proton Total Reaction Cross Sections for 22 Isotopes of Ti, Fe, Ni, Cu, Zn, Zr, and Sn at 14.5 MeV. *Phys. Rev.*, 157(4):1001–1015, 1967.
- [218] T. Eliyakut-Roshko, R. H. McCamis, W. T. H. van Oers, R. F. Carlson, and A. J. Cox. Measurements of proton total reaction cross sections for ^{58}Ni and ^{60}Ni including nonrelativistic and relativistic data analyses. *Phys. Rev. C*, 51(3):1295–1302, 1995.
- [219] J. J. H. Menet, E. E. Gross, J. J. Malanify, and A. Zucker. Total-Reaction-Cross-Section Measurements for 30-60-MeV Protons and the Imaginary Optical Potential. *Phys. Rev. C*, 4(4):1114–1129, 1971.
- [220] C. M. Perey, F. G. Perey, J. K. Dickens, and R. J. Silva. 11-MeV Proton Optical-Model Analysis. *Phys. Rev.*, 175(4):1460–1475, 1968.
- [221] P. Beuzit, J. Delaunay, J.P. Fouan, and N. Cindro. Levels of ^{62}Ni and ^{64}Ni . *Nuclear Physics A*, 128(2):594 – 608, 1969.
- [222] S. D. Wassenaar, P. J. van Hall, S. S. Klein, G. J. Nijgh, J. H. Polane, and O. J. Poppema. Journal of Physics G: Nuclear and Particle Physics Scattering of polarised protons by Ni, Sr, Cd, In and Sn isotopes. I. Elastic scattering. *J. Phys. G: Nucl. Part. Phys.*, 15:181, 1989.
- [223] W. Makofske, W. Savin, H. Ogata, and T. H. Kruse. Elastic and inelastic proton scattering from even isotopes of cd, sn, and te. *Phys. Rev.*, 174:1429–1441, Oct 1968.
- [224] A.G. Hardacre, J.F. Turner, J.C. Kerr, G.A. Gard, P.E. Cavanagh, and C.F. Coleman. Proton differential elastic scattering cross sections for the even isotopes of tin at 30.4 MeV. *Nucl. Phys.*, A173(2):436 – 448, 1971.
- [225] R. F. Carlson, A. J. Cox, T. Eliyakut-Roshko, and W. T. H. van Oers. Measurements of proton total reaction cross sections for $^{112,114,116,118,120,122,124}\text{Sn}$ from 22 to 48 MeV. *Can. J. Phys.*, 73:512, 1995.

- [226] D. J. Abbott, T. B. Clegg, and J. P. Delaroche. Polarized proton scattering from 116,120,124Sn at 16 MeV. *Phys. Rev. C*, 35(6):2028–2032, 1987.
- [227] R. N. Boyd and G. W. Greenlees. Nuclear-Matter Sizes in the Tin Isotopic Sequence. *Phys. Rev.*, 176(4):1394–1401, 1968.
- [228] G. S. Mani, D. T. Jones, and D. Jacques. Elastic scattering of 50 MeV Protons by Nuclei in the range from 42Ca to 208Pb. *Nucl. Phys.*, A165:384, 1971.
- [229] J. Rapaport, Mohammed Mirzaa, H. Hadizadeh, D. E. Bainum, and R. W. Finlay. Neutron elastic scattering from 116,118,120,122,124Sn. *Nucl. Phys.*, A341(1):56 – 74, 1980.
- [230] W. T. H. van Oers, Huang Haw, N. E. Davison, A. Ingemarsson, B. Fagerström, and G. Tibell. Optical-model analysis of $p + {}^{208}\text{Pb}$ elastic scattering from 15 - 1000 MeV. *Phys. Rev. C*, 10(1):307–319, 1974.
- [231] G. W. Greenless, V. Hnizdo, O. Karban, J. Lowe, and W. Makofske. Elastic scattering of 30.3-mev polarized protons from $ni58$, $sn120$, and $pb208$. *Phys. Rev. C*, 2(3):1063–1070, 1970.
- [232] A. Willis, B. Geoffrion, N. Marty, M. Morlet, C. Rolland, and B. Tatischeff. Diffusion élastique et inélastique des protons de 155 MeV sur 24Mg, 28Si, 32S et 40Ca. *Nucl. Phys.*, A112(2):417 – 442, 1968.
- [233] L. Lee, T. E. Drake, S. S. M. Wong, D. Frekers, R. E. Azuma, L. Buchmann, A. Galindo-Uribarri, J. D. King, R. Schubank, R. Abegg, R. Helmer, K. P. Jackson, C. A. Miller, S. Yen, and H. V. Von Geramb. Intermediate energy proton scattering from 40Ca, 90Zr and 208Pb. *Phys. Lett. B*, 205(2-3):219 – 222, 1988.
- [234] J. R. M. Annand, R. W. Finlay, and P. S. Dietrich. A low-energy optical-model analysis of 208Pb and 209Bi. *Nucl. Phys.*, A443(2):249 – 282, 1985.
- [235] M. L. Roberts, P. D. Felsher, G. J. Weisel, Zemin Chen, C. R. Howell, W. Tornow, R. L. Walter, and D. J. Horen. Measurement of $Ay(\theta)$ for $n+208\text{Pb}$ from 6 to 10 MeV and the neutron-nucleus interaction over the energy range from bound states at -17 MeV up to scattering at 40 MeV. *Phys. Rev. C*, 44(5):2006–2024, 1991.
- [236] W. E. Kinney and F. G. Perey. Technical Report 4909, Oak Ridge National Lab., 1974.
- [237] J. Rapaport, T. S. Cheema, D. E. Bainum, R. W. Finlay, and J. D. Carlson. Neutron scattering from 208Pb. *Nucl. Phys.*, A296(1):95 – 108, 1978.

BIBLIOGRAPHY

- [238] J. P. Delaroche, C. E. Floyd, P. P. Guss, R. C. Byrd, K. Murphy, G. Tungate, and R. L. Walter. Complex spin-orbit potential for $Pb208(n, n)Pb208$ at 10 MeV. *Phys. Rev. C*, 28(3):1410–1413, 1983.
- [239] C. E. Floyd, P. P. Guss, K. Murphy, C. R. Howell, R. C. Byrd, G. Tungate, S. A. Wender, R. L. Walter, and T. B. Clegg. Analyzing powers for neutron elastic scattering at forward angles. *Phys. Rev. C*, 25(3):1682–1684, 1982.
- [240] C. E. Floyd. *Scattering of Polarized Fast Neutrons from $9Be$, $54Fe$, $65Cu$ and $208Pb$: the Determination of the Nucleon-Nucleus Spin-Orbit Interaction*. PhD thesis, Duke University, 1981.
- [241] L. F. Hansen, F. S. Dietrich, B. A. Pohl, C. H. Poppe, and C. Wong. Test of microscopic optical model potentials for neutron elastic scattering at 14.6 MeV over a wide mass range. *Phys. Rev. C*, 31(1):111–119, 1985.
- [242] R. W. Finlay, J. R. M. Annand, T. S. Cheema, J. Rapaport, and F. S. Dietrich. Energy dependence of neutron scattering from $Pb208$ in the energy range 7–50 MeV. *Phys. Rev. C*, 30(3):796–806, 1984.
- [243] R. P. Devito. *Determination of the Coulomb Correction and Isovector Term of the Nucleon-Nucleus Optical Model Potential From Neutron Elastic Scattering at 30.3 and 40 MeV*. PhD thesis, Michigan State University, East Lansing, MI, USA, 1980.
- [244] W. Kretschmer, H. Löh, K. Spitzer, and W. Stach. Volume integrals for low-energy $p+208Pb$ optical potentials. *Phys. Lett. B*, 87(4):343 – 345, 1979.
- [245] R.D. Rathmell and W. Haeberli. Elastic scattering of polarized protons from nuclei near $A = 200$ between 11 and 14 MeV. *Nucl. Phys.*, A178(2):458 – 468, 1972.
- [246] J. J. H. Menet, E. E. Gross, J. J. Malanify, and A. Zucker. Total Reaction Cross-Section Measurements With 60-MeV Protons. *Phys. Rev. Lett.*, 22(21):1128–1131, 1969.
- [247] Gregory M. Haas and Pablo L. Okhuysen. Nonelastic Cross Sections of $Pb206$ and $Pb208$ for 14-MeV Neutrons. *Phys. Rev.*, 132(3):1211–1212, 1963.

ISOTOPIC COMPOSITION OF ENRICHED SAMPLES

Tables A.1-A.6 give the isotopic distributions of the enriched samples used in neutron σ_{tot} and $\frac{d\sigma}{d\Omega}$ measurements. The distributions were determined by mass spectrometry or are from the manufacturer's certificate of analysis. To create the 4.9 g ^{112}Sn sample, 3.9 g of ^{112}Sn foil (on semi-permanent loan from the group of Lee Bernstein of Lawrence Livermore National Laboratory) and 1.0 g of ^{112}Sn powder were combined. The ^{112}Sn sample abundances given here are a mass-weighted average of the isotopic abundances of the foil and powder.

For all of our samples, impurities from other elements were $< 0.01\%$. The natural abundances listed are from [117] and are rounded to the nearest 0.01%. Physical dimensions and masses of each sample are given in Table 2.2.

Table A.1: D₂O sample isotopic distribution

Isotope	Natural [%]	Sample [%]
H	99.98-100.00	< 0.1
D	0.02-0.00	99.9

Table A.2: H₂¹⁸O sample isotopic distribution

Isotope	Natural [%]	Sample [%]
¹⁶ O	99.74-99.78	< 0.1
¹⁷ O	0.04	< 0.1
¹⁸ O	0.22-0.19	99.9

Table A.3: ⁵⁸Ni sample isotopic distribution

Isotope	Natural [%]	Sample [%]
⁵⁸ Ni	99.56	68.08
⁶⁰ Ni	0.31	26.22
⁶¹ Ni	0.01	1.14
⁶² Ni	0.05	3.63
⁶⁴ Ni	0.07	0.93

Table A.4: ⁶⁴Ni sample isotopic distribution

Isotope	Natural [%]	Sample [%]
⁵⁸ Ni	4.68	68.08
⁶⁰ Ni	2.30	26.22
⁶¹ Ni	0.14	1.14
⁶² Ni	0.72	3.63
⁶⁴ Ni	92.16	0.93

Table A.5: ¹¹²Sn sample isotopic distribution

Isotope	Natural [%]	Sample [%]
¹¹² Sn	0.97	99.89
¹¹⁴ Sn	0.66	0.08
¹¹⁵ Sn	0.34	0.01
¹¹⁶ Sn	14.54	< 0.01
¹¹⁷ Sn	7.68	< 0.01
¹¹⁸ Sn	24.22	< 0.01
¹¹⁹ Sn	8.59	< 0.01
¹²⁰ Sn	32.59	< 0.01
¹²² Sn	4.63	< 0.01
¹²⁴ Sn	5.79	< 0.01

Table A.6: ¹²⁴Sn sample isotopic distribution

Isotope	Natural [%]	Sample [%]
¹¹² Sn	0.97	< 0.01
¹¹⁴ Sn	0.66	< 0.01
¹¹⁵ Sn	0.34	< 0.01
¹¹⁶ Sn	14.54	< 0.01
¹¹⁷ Sn	7.68	< 0.01
¹¹⁸ Sn	24.22	< 0.01
¹¹⁹ Sn	8.59	< 0.01
¹²⁰ Sn	32.59	< 0.01
¹²² Sn	4.63	0.10
¹²⁴ Sn	5.79	99.90

EXPERIMENTAL DATA USED TO CONSTRAIN DOM POTENTIALS

In this work, each DOM fit incorporated up to nine types of experimental data. Sources for proton and neutron scattering data ($\frac{d\sigma}{d\Omega}$, analyzing powers, σ_{rxn} , σ_{tot}) are listed, starting with ^{16}O . For bound state data (binding energies, single-particle level energies, spectral function widths, charge density distributions, and RMS charge radii), we drew on compilations given in Table B.1. For ^{18}O and ^{112}Sn , the full Fourier-Bessel-parameterized charge density distributions were unavailable. In these cases, we scaled the charge density distributions of ^{16}O and ^{124}Sn , respectively, so that they would reproduce the experimentally-known RMS charge radii of ^{18}O and ^{112}Sn .

Data types are abbreviated as follows: AP (analyzing power), BE (binding energy), $\rho_{ch}(r)$ (charge density distribution), ΔSF (spectral function widths), and r_{rms} (root-mean-square charge radius). All energy ranges listed refer to the energy range of data used in the fit, not the energy range available in the reference, which in some cases is larger.

Table B.1: Sources for bound-state data on all nuclei

Type	Reference
$\rho_{ch}(r)$	[11]
r_{rms}	[11]
ΔSF	[9, 10]
SP levels	[43]
BE	[43]

B.1 ^{16}O Scattering Data

Table B.2: ^{16}O proton $\frac{d\sigma}{d\Omega}$ data

Energy [MeV]	Reference
7.13	[118]
8.04	[118]
9.42	[118]
10.2	[118]
11	[119]
12.9	[118]
13.9	[118]
15.4	[120]
16.6	[120]
17.5	[121]
19.8	[122]
20.4	[122]
21.4	[122]
23.4	[123]
24.5	[123]
27.3	[123]
30.1	[123]
34.1	[123]
39.7	[123]
46.1	[123]
49.48	[124]
61	[125]
65	[126]
135	[127]
142	[128]
179.9	[129]
200	[130]

Table B.3: ^{16}O neutron $\frac{d\sigma}{d\Omega}$ data

Energy [MeV]	Reference
4.92	[131]
6.01	[131]
7.03	[131]
8	[132]
9.708	[133]
10	[134]
11.147	[133]
12	[134]
13.61	[135]
14	[134]
15	[136]
17	[134]
18	[137]
20	[137]
22	[137]
23	[138]
24	[137]
26	[137]
94.8	[139]

APPENDIX B: EXPERIMENTAL DATA USED TO CONSTRAIN DOM POTENTIALS

Table B.4: ^{16}O proton AP data

Energy [MeV]	Reference
5.66	[140]
6	[140]
7.01	[140]
8.5	[140]
9.5	[140]
10.6	[141]
11.9	[140]
12.42	[141]
19.8	[122]
20.4	[122]
21.4	[122]
30.4	[142]
35	[143]
40.9	[144]
65	[126]
117	[145]
135	[127]
179.9	[129]
200	[130]

Table B.5: ^{16}O neutron AP data

Energy [MeV]	Reference
10	[134]
12	[134]
14	[134]
17	[134]
23	[138]

Table B.6: ^{16}O proton σ_{rxn} data

Energy [MeV]	Reference
18.8-47.7	[146]
20.9-43.2	[111]
65.5	[112]

Table B.7: ^{16}O neutron σ_{rxn} data

Energy [MeV]	Reference
14.1	[147]

Table B.8: ^{16}O neutron σ_{tot} data

Energy [MeV]	Reference
10-200	this work

B.2 ¹⁸O Scattering Data

Table B.9: ¹⁸O proton $\frac{d\sigma}{d\Omega}$ data

Energy [MeV]	Reference
7.89	[148]
8.77	[148]
9.24	[148]
9.66	[148]
10.61	[148]
10.71	[148]
11.16	[148]
12.37	[148]
13.04	[148]
13.29	[148]
14.7	[149]
16.28	[148]
17.7	[149]
19.1	[149]
20.6	[149]
22.3	[149]
24.5	[149]
26.2	[149]
28.2	[149]
30.5	[149]
32.7	[149]
35.2	[150]
37.3	[149]
39.5	[149]
41.4	[149]
43	[151]
44.1	[149]

Table B.10: ¹⁸O neutron $\frac{d\sigma}{d\Omega}$ data

Energy [MeV]	Reference
8.5	[152]
14.14	[147]
24	[105]

APPENDIX B: EXPERIMENTAL DATA USED TO CONSTRAIN DOM POTENTIALS

Table B.11: ^{18}O proton AP data

Energy [MeV]	Reference
24.5	[153]

No ^{18}O neutron AP data were used

No ^{18}O proton σ_{rxn} data were used

Table B.12: ^{18}O neutron σ_{rxn} data

Energy [MeV]	Reference
14.1	[147]

Table B.13: ^{18}O neutron σ_{tot} data

Energy [MeV]	Reference
10-200	this work

B.3 ⁴⁰Ca Scattering Data

Table B.14: ⁴⁰Ca proton $\frac{d\sigma}{d\Omega}$ data

Energy [MeV]	Reference
17.57	[154]
19.57	[155]
21	[156]
25	[156]
26.3	[157, 156]
30	[156]
35	[156]
40	[156, 158]
45	[156]
48	[156]
61.4	[159]
65	[160]
80.2	[161, 162]
100.6	[163]
135.1	[161]
152	[164]
160	[165]
160	[162]
179.5	[166]
181	[161, 162]
181.5	[166]
200	[167]

Table B.15: ⁴⁰Ca neutron $\frac{d\sigma}{d\Omega}$ data

Energy [MeV]	Reference
9.9	[168]
11	[169]
11.9	[168]
13.9	[170]
16.9	[170]
19	[171]
20	[169]
21.7	[171]
25.5	[171]
26	[169]
30	[172]
40	[172]
65	[173]
75	[174]
85	[174]
95	[174]
107.5	[174]
127.5	[174]
155	[174]
185	[174]

APPENDIX B: EXPERIMENTAL DATA USED TO CONSTRAIN DOM POTENTIALS

Table B.16: ^{40}Ca proton AP data

Energy [MeV]	Reference
14.08	[175]
15.65	[175]
16.25	[175]
21	[156, 176]
26.3	[157, 156]
30.3	[177]
49	[178]
65	[160]
65	[179]
100.6	[163]
152	[164]
160	[162, 161]
175	[145]
181	[162, 161]
200	[167]

Table B.17: ^{40}Ca neutron AP data

Energy [MeV]	Reference
9.9	[168]
11.9	[168]
13.9	[170]
16.9	[170]

Table B.18: ^{40}Ca proton σ_{rxn} data

Energy [MeV]	Reference
10.3-21.6	[180]
24.9-48.0	[110]
28.5	[181]
65.5	[112]
81-180	[113]

Table B.19: ^{40}Ca neutron σ_{rxn} data

Energy [MeV]	Reference
40.3-50.4	[182]

Table B.20: ^{40}Ca neutron σ_{tot} data

Energy [MeV]	Reference
10-200	[37]

B.4 ^{48}Ca Scattering Data

Table B.21: ^{48}Ca proton $\frac{d\sigma}{d\Omega}$ data

Energy [MeV]	Reference
8	[183]
10	[183]
12	[183]
14.03	[175]
15.05	[175]
15.65	[175]
21	[156]
25	[156]
30	[156]
35	[156]
40	[156]
45	[156]
48.4	[156]
65	[160]
200	[167]

Table B.22: ^{48}Ca neutron $\frac{d\sigma}{d\Omega}$ data

Energy [MeV]	Reference
6	[184]
7.97	[185]
11.9	[96]
16.8	[96]

APPENDIX B: EXPERIMENTAL DATA USED TO CONSTRAIN DOM POTENTIALS

Table B.23: ^{48}Ca proton AP data

Energy [MeV]	Reference
8	[183]
10	[183]
12	[183]
14.03	[175]
15.05	[175]
15.65	[175]
65	[160]
200	[167]

No ^{48}Ca neutron AP data were used

Table B.24: ^{48}Ca proton σ_{rxn} data

Energy [MeV]	Reference
23-48	[186]

No ^{48}Ca neutron σ_{rxn} data were used

Table B.25: ^{48}Ca neutron σ_{tot} data

Energy [MeV]	Reference
6.15-17.1	[185]
14.2	[187]
18.2-200	[37]

B.5 ⁵⁸Ni Scattering Data

Table B.26: ⁵⁸Ni proton $\frac{d\sigma}{d\Omega}$ data

Energy [MeV]	Reference
7	[188]
8	[188]
9	[188]
9.51	[189]
10	[189]
11	[189]
11.7	[190]
12	[188]
16	[191]
16	[192]
18.6	[193]
18.6	[194]
20	[194]
21	[195]
30	[196]
30.3	[197]
35.2	[198]
39.6	[199]
39.8	[200]
40	[158, 201]
61.4	[159]
65	[160]
65	[179]
65	[202]
100	[203]
178	[204]
192	[205]

Table B.27: ⁵⁸Ni neutron $\frac{d\sigma}{d\Omega}$ data

Energy [MeV]	Reference
4.5	[206]
5.5	[206]
6.5	[206]
7.5	[206]
8.399	[206]
9.99	[206]
11.952	[207]
14	[206]
16.934	[208]
21.5	[206]
24	[209]

APPENDIX B: EXPERIMENTAL DATA USED TO CONSTRAIN DOM POTENTIALS

Table B.28: ^{58}Ni proton AP data

Energy [MeV]	Reference
9.51	[189]
14	[210]
16	[192]
18.6	[193]
21	[195]
24.6	[211]
26.3	[157]
29	[212]
40	[158, 201]
49	[178]
60.2	[213]
65	[179]
172	[214]
178	[204]
192	[205]

Table B.29: ^{58}Ni neutron AP data

Energy [MeV]	Reference
9.92	[207]
13.91	[207]
16.934	[208]

Table B.30: ^{58}Ni proton σ_{rxn} data

Energy [MeV]	Reference
8.8	[215]
9.1	[216]
14.5	[217]
22.7-47.9	[218]
28.5	[181]
30-60.8	[219]
65.5	[112]
81	[113]

No ^{58}Ni neutron σ_{rxn} data were used

Table B.31: ^{58}Ni neutron σ_{tot} data

Energy [MeV]	Reference
10-200	this work

B.6 ^{64}Ni Scattering Data

Table B.32: ^{64}Ni proton $\frac{d\sigma}{d\Omega}$ data

Energy [MeV]	Reference
9.6	[190]
9.69	[189]
11	[220]
11.7	[190]
12	[221]
12	[188]
16	[191]
18.6	[193]
39.6	[199]
65	[160]

Table B.33: ^{64}Ni neutron $\frac{d\sigma}{d\Omega}$ data

Energy [MeV]	Reference
5	[108]
6	[108]
7	[108]

APPENDIX B: EXPERIMENTAL DATA USED TO CONSTRAIN DOM POTENTIALS

Table B.34: ^{64}Ni proton AP data

Energy [MeV]	Reference
9.69	[189]
18.6	[193]
20.4	[222]
39.6	[199]
65	[160]
65	[202]

No ^{64}Ni neutron AP data were used

Table B.35: ^{64}Ni proton σ_{rxn} data

Energy [MeV]	Reference
40-60.8	[219]

No ^{64}Ni neutron σ_{rxn} data were used

Table B.36: ^{64}Ni neutron σ_{tot} data

Energy [MeV]	Reference
10-200	this work

B.7 ^{112}Sn Scattering Data

Table B.37: ^{112}Sn proton $\frac{d\sigma}{d\Omega}$ data

Energy [MeV]	Reference
16	[223]
30.4	[224]

No ^{112}Sn proton AP data were used

Table B.39: ^{112}Sn proton σ_{rxn} data

Energy [MeV]	Reference
22.8-47.8	[225]
65.5	[112]

Table B.38: ^{112}Sn neutron $\frac{d\sigma}{d\Omega}$ data

Energy [MeV]	Reference
11	this work
17	this work

No ^{112}Sn neutron AP data were used

No ^{112}Sn neutron σ_{rxn} data were usedTable B.40: ^{112}Sn neutron σ_{tot} data

Energy [MeV]	Reference
10-200	this work

B.8 ^{124}Sn Scattering Data

Table B.41: ^{124}Sn proton $\frac{d\sigma}{d\Omega}$ data

Energy [MeV]	Reference
16	[223]
16	[226]
20.4	[222]
30.4	[224]
39.6	[227]
49.35	[228]

Table B.42: ^{124}Sn neutron $\frac{d\sigma}{d\Omega}$ data

Energy [MeV]	Reference
11	[229]
17	this work
24	[229]

Table B.43: ^{124}Sn proton AP data

Energy [MeV]	Reference
16	[226]
20.4	[222]
39.6	[227]

No ^{124}Sn neutron AP data were used

Table B.44: ^{124}Sn proton σ_{rxn} data

Energy [MeV]	Reference
22.9-47.9	[225]
65.5	[112]

No ^{124}Sn neutron σ_{rxn} data were used

Table B.45: ^{124}Sn neutron σ_{tot} data

Energy [MeV]	Reference
10-200	this work

B.9 ^{208}Pb Scattering Data

Table B.46: ^{208}Pb proton $\frac{d\sigma}{d\Omega}$ data

Energy [MeV]	Reference
16	[29, 192]
21	[230]
24.1	[230]
26.3	[230, 157]
30.3	[230, 231]
35	[230]
40	[158]
45	[230]
47.3	[230]
61	[159]
65	[179]
80	[161]
121	[161]
155	[232]
160	[161, 162]
182	[161, 162]
200	[233]

Table B.47: ^{208}Pb neutron $\frac{d\sigma}{d\Omega}$ data

Energy [MeV]	Reference
4	[234]
5	[234]
6	[234]
7	[234]
7.97	[235]
8.5	[236]
9	[237]
9.97	[238]
11	[237]
13.9	[239, 240]
14.6	[241]
16.9	[240]
20	[242]
22	[242]
24	[242]
26	[237]
30.3	[243]
40	[243]
65	[174]
75	[174]
85	[174]
95	[174]
96	[174]
107.5	[174]
127.5	[174]
155	[174]
185	[174]

APPENDIX B: EXPERIMENTAL DATA USED TO CONSTRAIN DOM POTENTIALS

Table B.48: ^{208}Pb proton AP data

Energy [MeV]	Reference
9	[244]
12.98	[245]
16	[192]
26.3	[230, 157]
29	[212]
30.3	[230, 231]
40	[158]
49	[178]
49.3	[228]
65	[179]
79.8	[162]
98	[162]
155	[232]
160	[161, 162]
182	[161, 162]
185	[230]
200	[233]

Table B.49: ^{208}Pb neutron AP data

Energy [MeV]	Reference
5.969	[235]
6.967	[235]
7.97	[235]
8.958	[235]
9.97	[238]
13.9	[240]

Table B.50: ^{208}Pb proton σ_{rxn} data

Energy [MeV]	Reference
21.1-48.0	[110]
28.5	[181]
30.0-60.8	[219]
60.0	[246]
65.5	[112]
81.0-180	[113]

Table B.51: ^{208}Pb neutron σ_{rxn} data

Energy [MeV]	Reference
14	[247]

Table B.52: ^{208}Pb neutron σ_{tot} data

Energy [MeV]	Reference
10-200	[20]

PARAMETER VALUES OF DOM POTENTIALS

Below are the parameter values from our best DOM fits for each nucleus in the present work. The parameter labels correspond to those in the equations of Chapter 6. For symmetric nuclei ^{16}O and ^{40}Ca , the asymmetry-dependent parameters were disabled during fitting. As mentioned in Chapter 7, for a few nuclei, one or more parameters were set to zero to prevent the fit from drifting into unphysical territory, most notably the negative imaginary surface and real wine-bottle parameters for $^{16,18}\text{O}$.

Table C.1: Real parameters (volume-like, symmetric)

Parameter	^{16}O	^{18}O	^{40}Ca	^{48}Ca	^{58}Ni	^{64}Ni	^{112}Sn	^{124}Sn	^{208}Pb
V_1	104.79	104.03	104.01	93.68	97.72	89.19	82.28	85.54	88.93
r_1	1.03	1.03	1.08	1.11	1.10	1.11	1.15	1.16	1.17
a_1	0.45	0.57	0.63	0.55	0.63	0.65	0.42	0.50	0.62
β_1	1.13	1.04	1.13	1.05	1.04	0.98	0.99	1.04	1.04
V_2	-	-	23.73	29.51	21.90	16.76	3.65	3.09	32.07
σ_2	-	-	0.36	0.48	0.57	0.49	1.71	1.94	0.33

Table C.2: Real parameters (volume-like, asymmetric)

Parameter	^{16}O	^{18}O	^{40}Ca	^{48}Ca	^{58}Ni	^{64}Ni	^{112}Sn	^{124}Sn	^{208}Pb
V_{asym}	-	49.87	-	37.80	24.86	59.41	44.56	33.62	38.63

APPENDIX C: PARAMETER VALUES OF DOM POTENTIALS

Table C.3: Imaginary parameters (volume-like, symmetric)

Parameter	^{16}O	^{18}O	^{40}Ca	^{48}Ca	^{58}Ni	^{64}Ni	^{112}Sn	^{124}Sn	^{208}Pb
r_4	1.17	1.22	1.21	1.11	1.16	1.15	1.21	1.18	1.22
a_4	0.59	0.60	0.64	0.61	0.66	0.61	0.58	0.64	0.63
β_4	0.96	0.98	0.82	0.94	1.10	1.07	0.89	0.93	0.85
A_5^+	27.58	33.87	39.89	24.84	24.14	32.68	24.50	21.17	31.96
B_5^+	117.15	117.51	139.91	143.69	78.43	77.72	65.72	54.20	59.07
A_5^-	14.20	10.27	10.16	10.70	15.69	25.66	19.06	16.80	19.99
B_5^-	25.57	28.83	31.82	24.40	19.56	46.12	33.97	28.95	34.15
E_6^+	47.88	114.69	103.51	60.55	140.06	118.54	48.86	130.90	67.07
E_6^-	88.28	127.10	102.20	97.89	60.83	94.07	75.60	72.62	76.26
α_6	0.17	0.16	0.12	0.15	0.14	0.18	0.13	0.13	0.14

Table C.4: Imaginary parameters (volume-like, asymmetric)

Parameter	^{16}O	^{18}O	^{40}Ca	^{48}Ca	^{58}Ni	^{64}Ni	^{112}Sn	^{124}Sn	^{208}Pb
$A_{vol,asym}^+$	-	-35.44	-	23.39	-95.19	31.65	43.20	-11.25	20.49
$A_{vol,asym}^-$	-	3.39	-	-19.96	-68.62	-20.66	-39.79	-22.09	-5.97

Table C.5: Imaginary parameters (surface-like, symmetric)

Parameter	^{16}O	^{18}O	^{40}Ca	^{48}Ca	^{58}Ni	^{64}Ni	^{112}Sn	^{124}Sn	^{208}Pb
A_7^+	16.81	23.42	13.19	40.36	17.00	27.02	43.45	28.54	28.68
B_7^+	23.88	19.22	18.64	25.90	12.51	23.27	23.45	24.05	15.07
$B_7'^+$	86.88	64.81	210.84	64.06	650.12	54.68	48.10	131.88	43.28
C_7^+	3.46	3.89	5.41	3.92	3.26	3.82	3.35	3.41	3.01
A_7^-	-	-	2.50	5.94	2.69	8.32	6.53	3.35	0.39
B_7^-	-	-	15.99	18.15	10.00	19.48	15.12	13.71	8.75
$B_7'^-$	-	-	30.71	37.99	20.75	35.88	28.00	22.40	18.21
C_7^-	-	-	5.10	8.50	10.81	13.92	7.00	5.66	8.45

APPENDIX C: PARAMETER VALUES OF DOM POTENTIALS

Table C.6: Imaginary parameters (surface-like, asymmetric)

Parameter	¹⁶ O	¹⁸ O	⁴⁰ Ca	⁴⁸ Ca	⁵⁸ Ni	⁶⁴ Ni	¹¹² Sn	¹²⁴ Sn	²⁰⁸ Pb
$A_{sur,asym}^+$	-	-39.33	-	-24.67	-17.56	1.09	17.14	37.59	36.83
$A_{sur,asym}^-$	-	-	-	15.76	25.14	-8.78	24.09	10.06	-

Table C.7: Spin-orbit parameters

Parameter	¹⁶ O	¹⁸ O	⁴⁰ Ca	⁴⁸ Ca	⁵⁸ Ni	⁶⁴ Ni	¹¹² Sn	¹²⁴ Sn	²⁰⁸ Pb
V_3	10.01	14.63	10.18	15.47	10.14	11.78	11.99	13.17	11.61
r_3	1.00	0.73	0.95	1.15	1.06	1.08	1.16	1.16	1.16
a_3	0.68	0.63	0.69	1.00	0.84	0.95	0.56	0.54	0.99
W_7	-0.15	-	-0.16	-0.28	-0.10	-0.23	-0.15	-0.21	-0.19
β_3	0.28	0.27	0.33	0.43	0.28	0.32	0.44	0.41	0.49

VISUALIZATION OF DOM FIT RESULTS

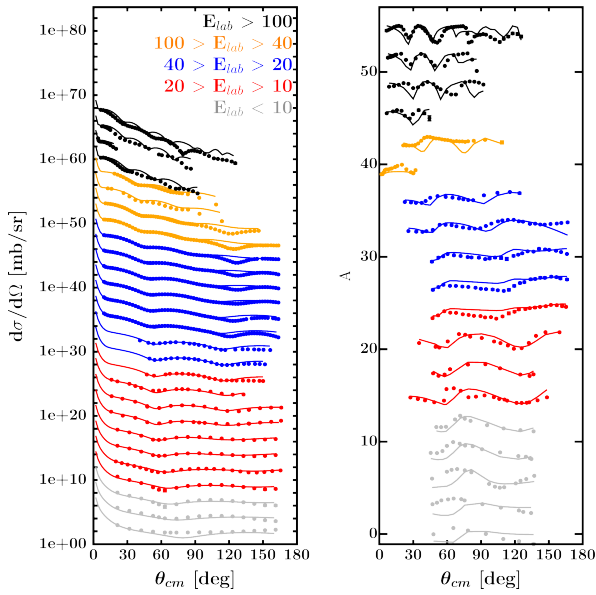
For each nucleus studied with the DOM in this treatment, this Appendix visualizes the quality of the DOM reproduction of experimental data and predictions of structural observables. Nucleon scattering data is presented first, followed by charge density and single-particle level information, followed by visualization of the optimized potentials, followed by structural predictions (spectral functions, momentum distributions, and matter distributions). Additional detail on the quantities plotted is included in Chapters 6 and 7.

In all figures below, experimental data (referenced in Appendix B) are shown as points with error bars and DOM calculations are shown as lines. In the elastic scattering figures, data sets at different energies are offset vertically for clarity; points and data in these figures have been colored according to the energy of the data set. We drew all charge density distributions from the compilation of [11], except for the distributions of ^{18}O and ^{112}Sn , which we generated by scaling the ^{16}O and ^{124}Sn distributions to reproduce the ^{18}O and ^{112}Sn RMS radii given in [11]. The charge density distributions in [11] are reported without errors; in the figures below, we display them with an arbitrary 1% uncertainty band, in blue. Experimental single-particle levels were assigned from proton and neutron separation energies in [43], for the valence levels, and roughly estimated from systematics in (e,e'p) and (p,2p) compilations, for the deeper levels. Thus the location of experimental deeply bound levels should only be taken as approximate.

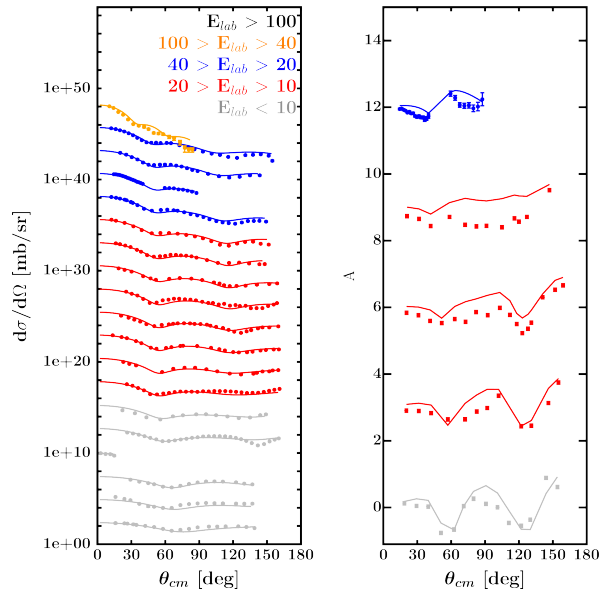
In spectral function figures, the vertical lines near the Fermi energy show the threshold used in the piecemeal approach for calculating particle occupations needed for certain LJs

(see Eq. 6.29 for discussion). In single-particle level figures for nuclei with open neutron shells, the upper and lower levels E_{\pm} , split by the pairing term Δ , are both shown (see Eq. 6.31 for discussion).

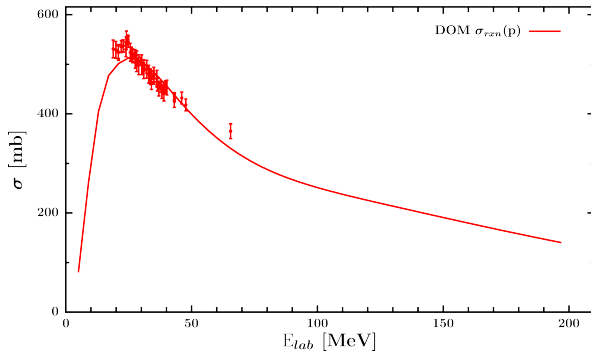
D.1 DOM fit of ^{16}O



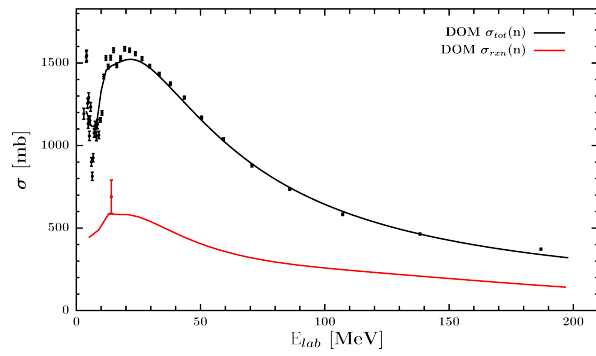
^{16}O proton elastic scattering



^{16}O neutron elastic scattering

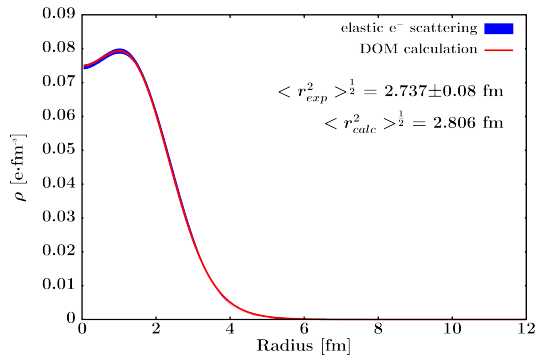


^{16}O proton σ_{rxn}

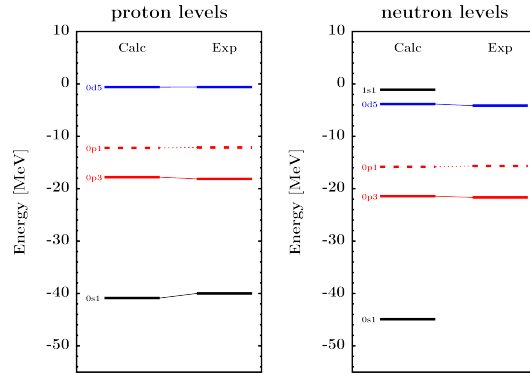


^{16}O neutron σ_{rxn} and σ_{tot}

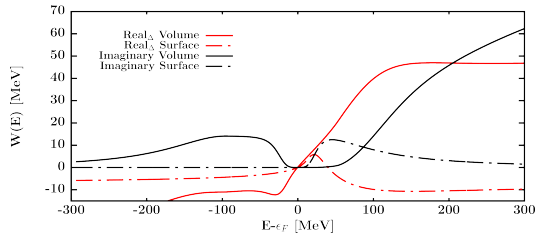
DOM FIT OF ^{16}O



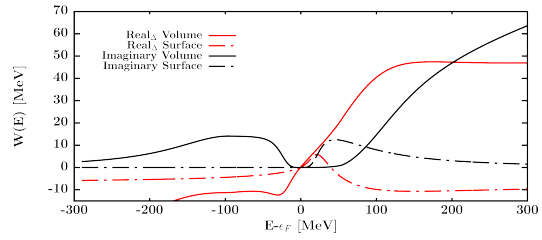
^{16}O charge density



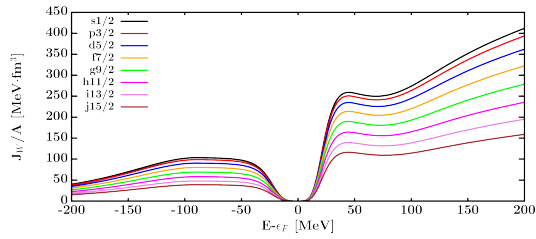
^{16}O single-particle levels



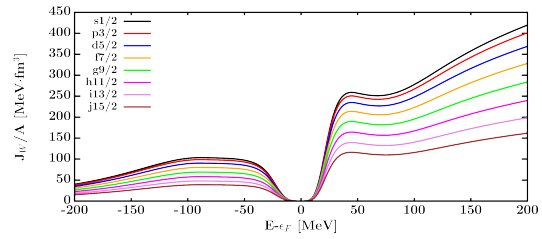
^{16}O proton potential energy dependence



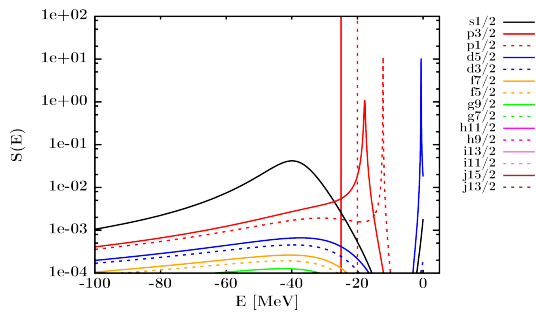
^{16}O neutron potential energy dependence



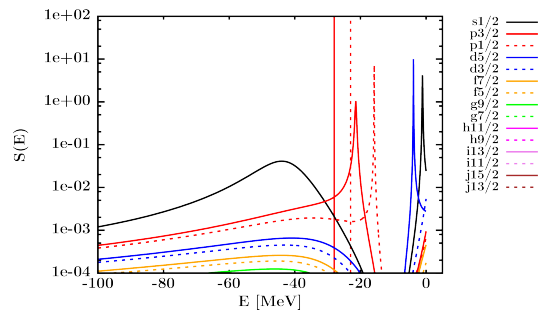
^{16}O proton volume integral



^{16}O neutron volume integral

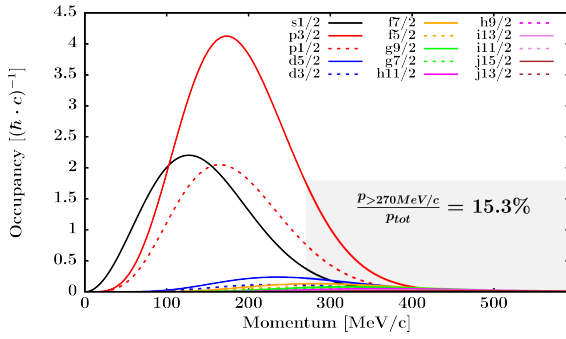


^{16}O proton spectral functions

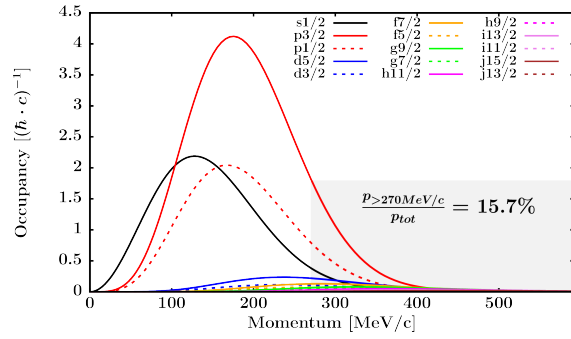


^{16}O neutron spectral functions

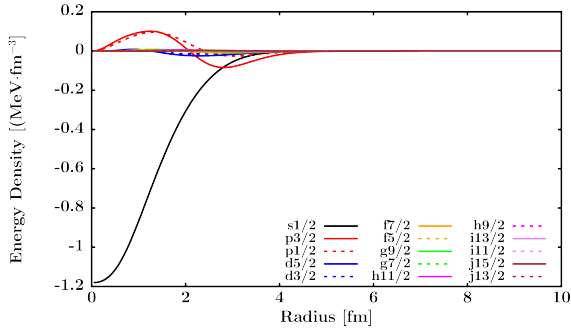
APPENDIX D: VISUALIZATION OF DOM FIT RESULTS



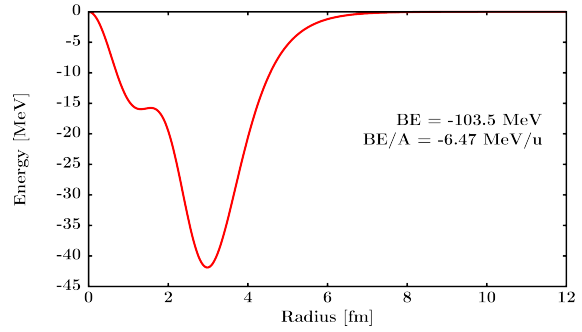
^{16}O proton momentum distribution



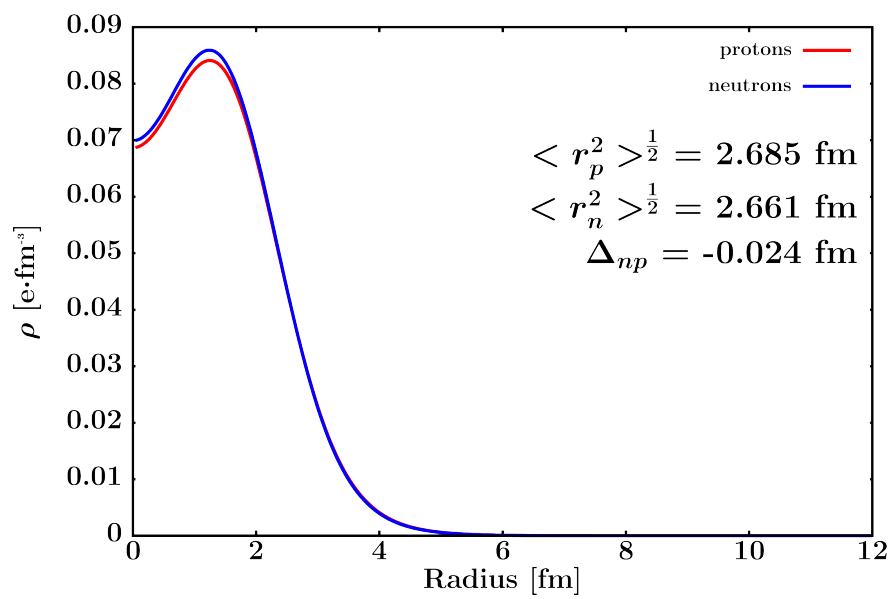
^{16}O neutron momentum distribution



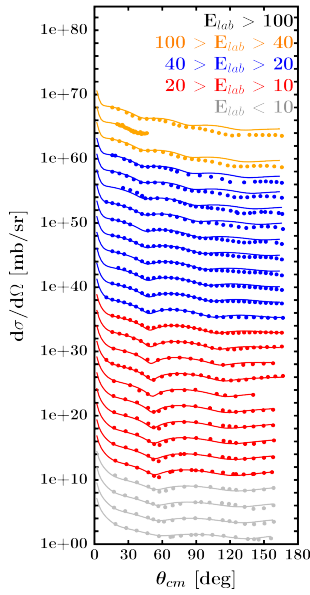
^{16}O energy distribution by LJ



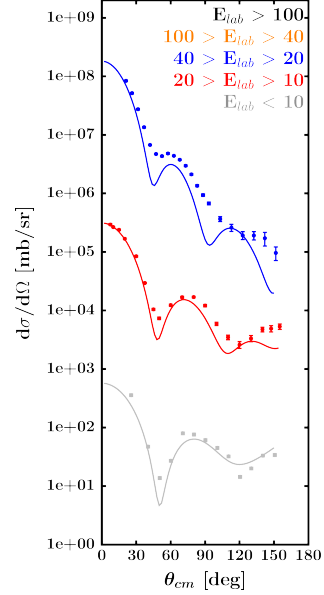
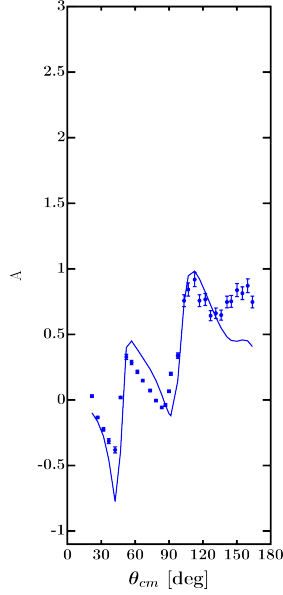
^{16}O energy distribution integral

 ^{16}O matter density distribution

D.2 DOM fit of ^{18}O

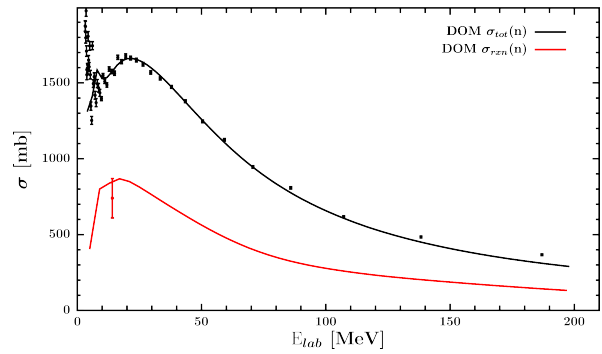


^{18}O proton elastic scattering



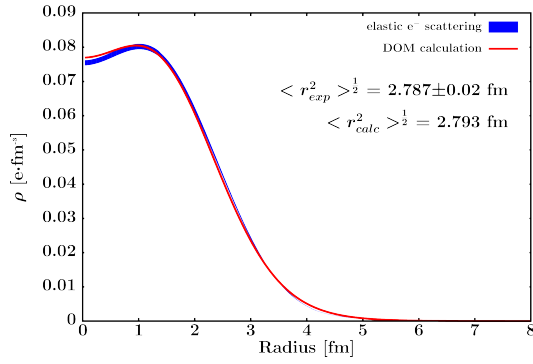
^{18}O neutron elastic scattering

No ^{18}O proton σ_{rxn} data were available

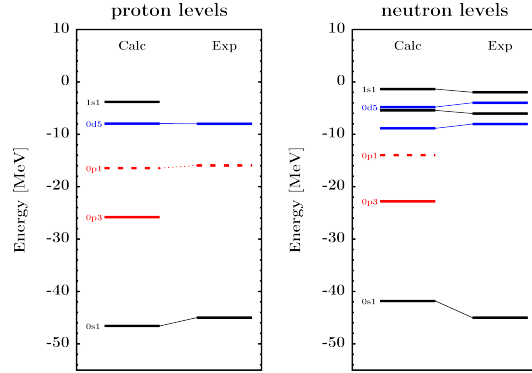


^{18}O neutron σ_{rxn} and σ_{tot}

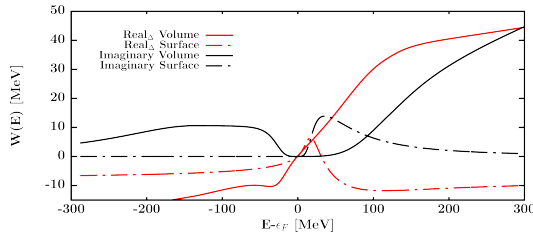
DOM FIT OF ^{18}O



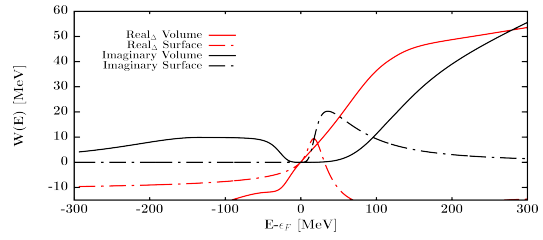
^{18}O charge density



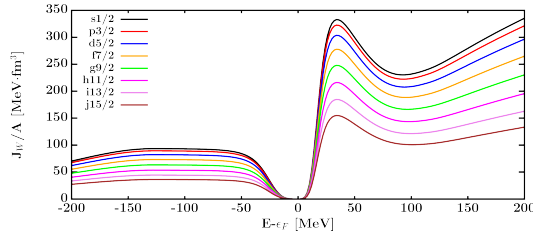
^{18}O single-particle levels



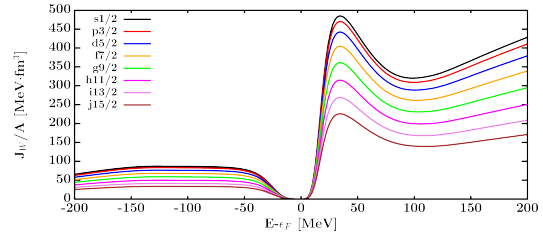
^{18}O proton potential energy dependence



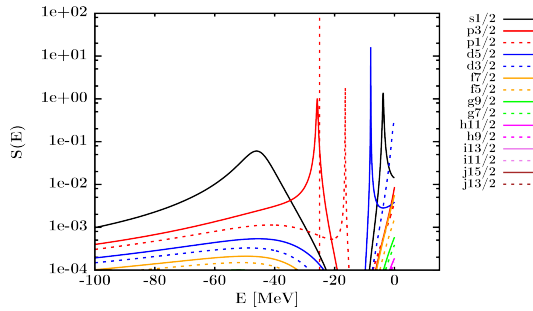
^{18}O neutron potential energy dependence



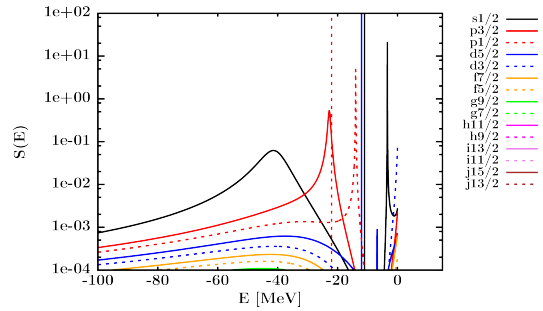
^{18}O proton volume integral



^{18}O neutron volume integral

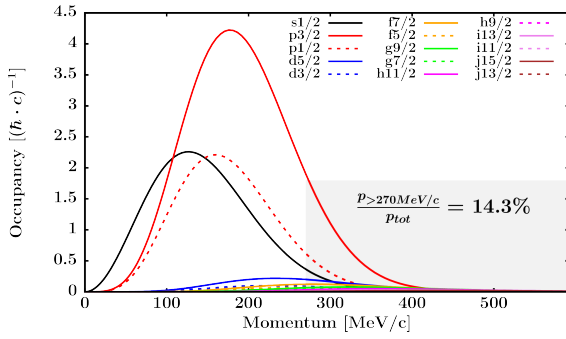


^{18}O proton spectral functions

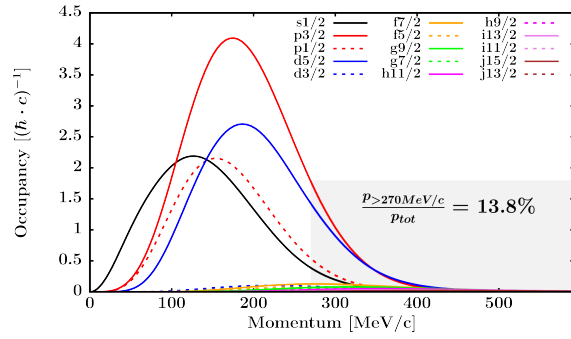


^{18}O neutron spectral functions

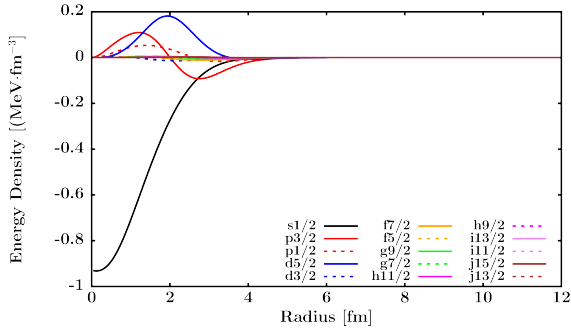
APPENDIX D: VISUALIZATION OF DOM FIT RESULTS



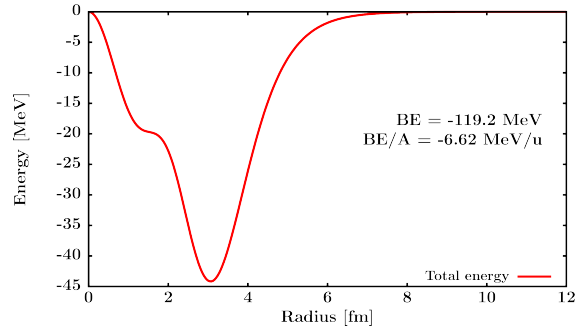
^{18}O proton momentum distribution



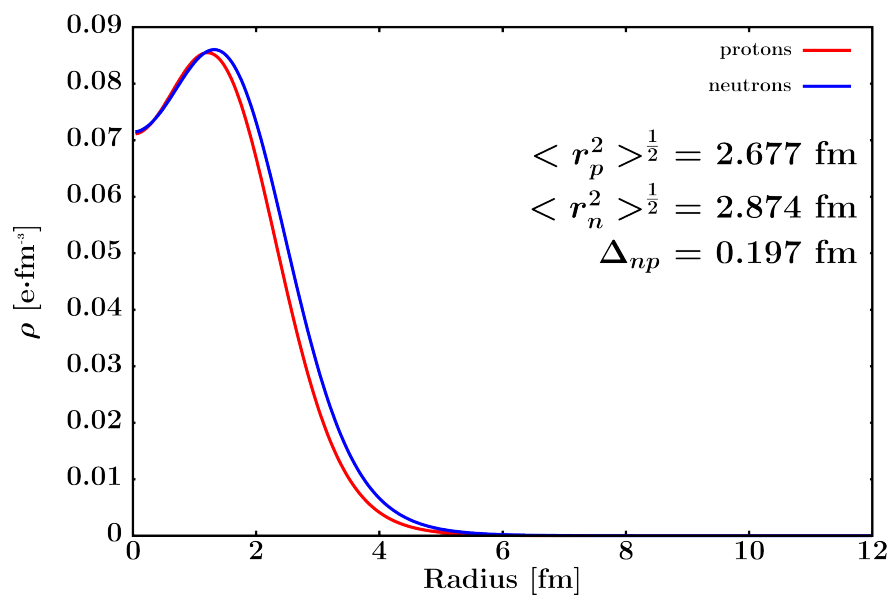
^{18}O neutron momentum distribution



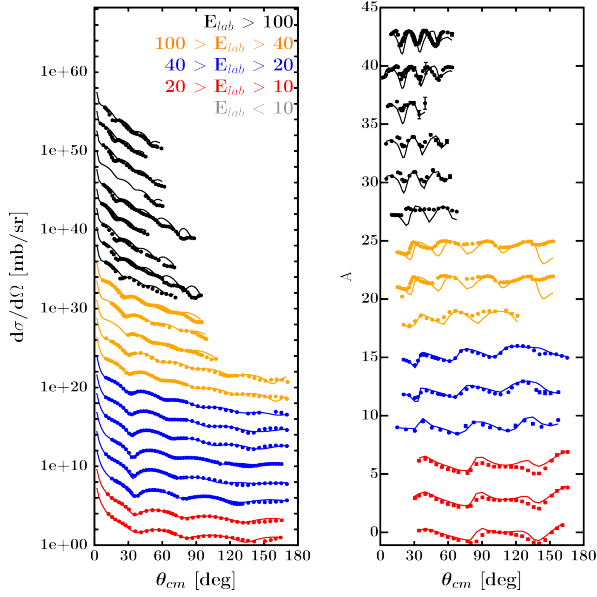
^{18}O energy distribution by LJ



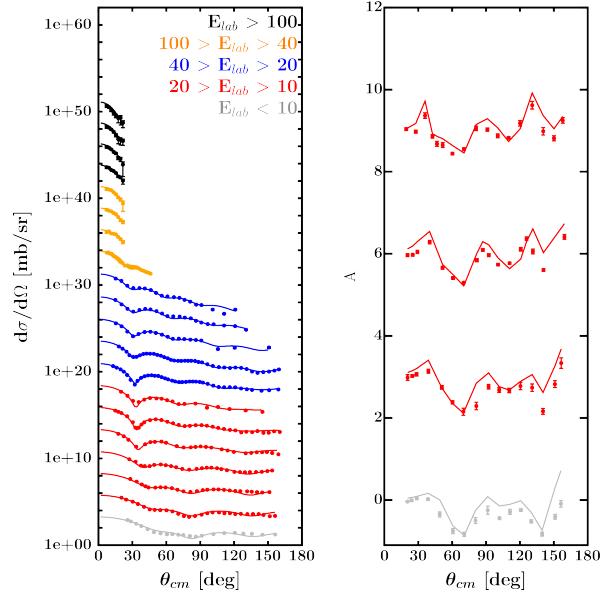
^{18}O energy distribution integral

 ^{18}O matter density distribution

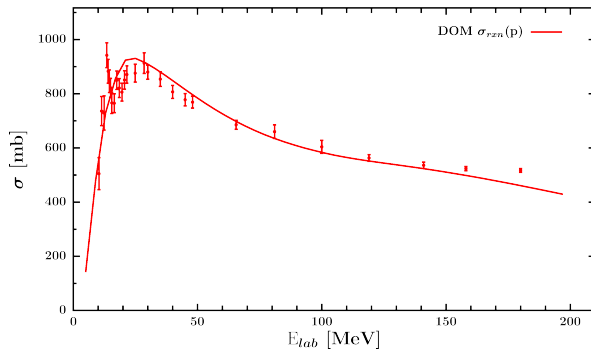
D.3 DOM fit of ^{40}Ca



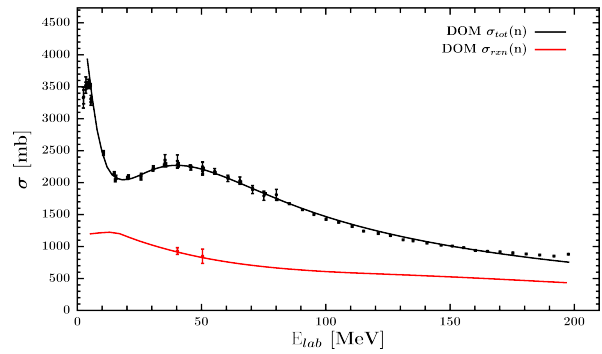
^{40}Ca proton elastic scattering



^{40}Ca neutron elastic scattering

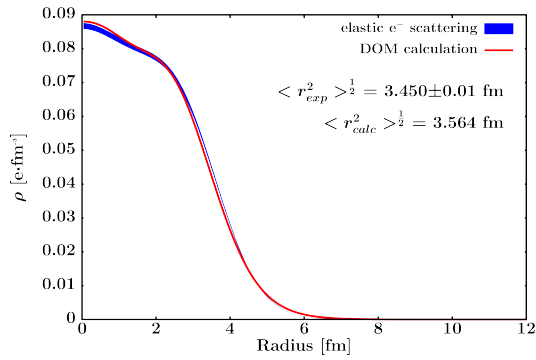


^{40}Ca proton σ_{rxn}

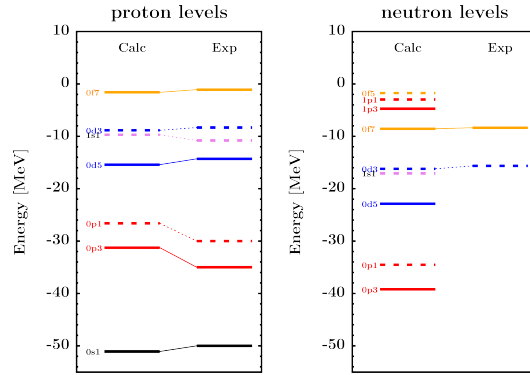


^{40}Ca neutron σ_{rxn} and σ_{tot}

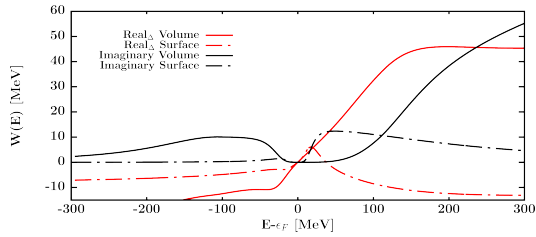
DOM FIT OF ^{40}Ca



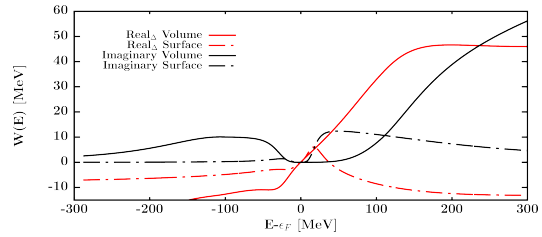
^{40}Ca charge density



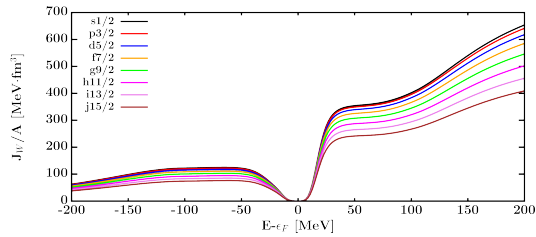
^{40}Ca single-particle levels



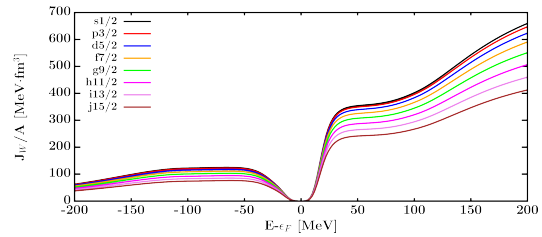
^{40}Ca proton potential energy dependence



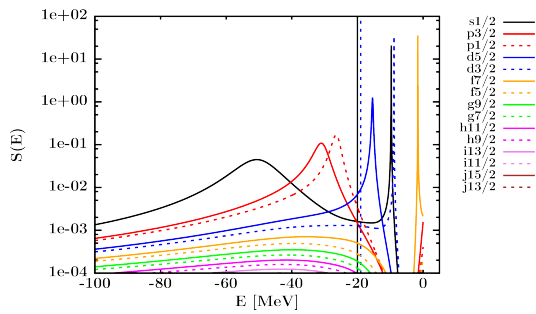
^{40}Ca neutron potential energy dependence



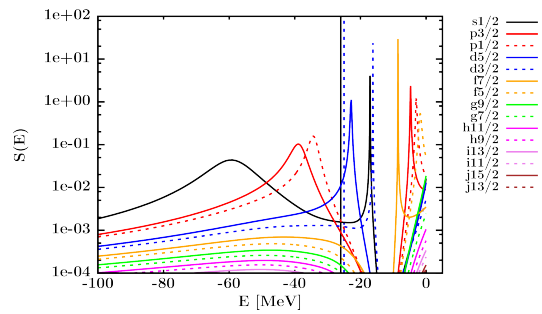
^{40}Ca proton volume integral



^{40}Ca neutron volume integral

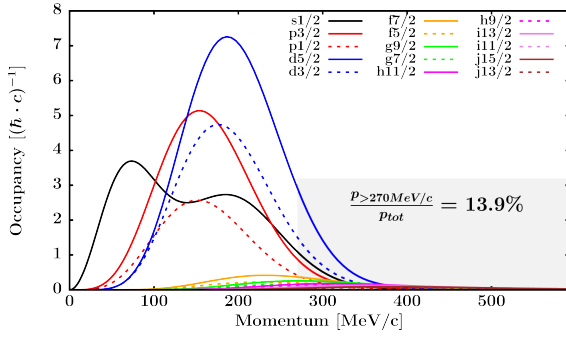


^{40}Ca proton spectral functions

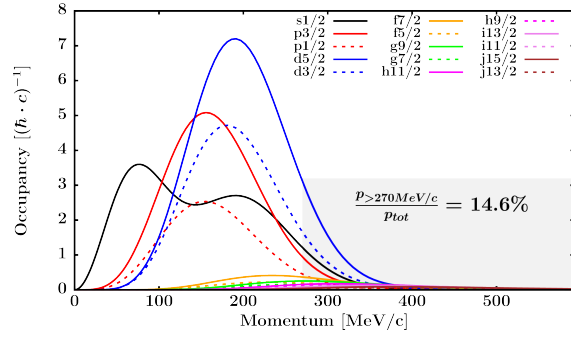


^{40}Ca neutron spectral functions

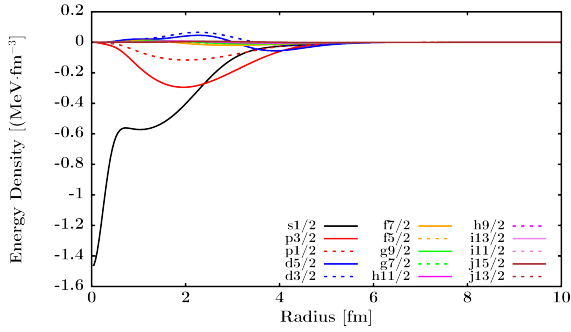
APPENDIX D: VISUALIZATION OF DOM FIT RESULTS



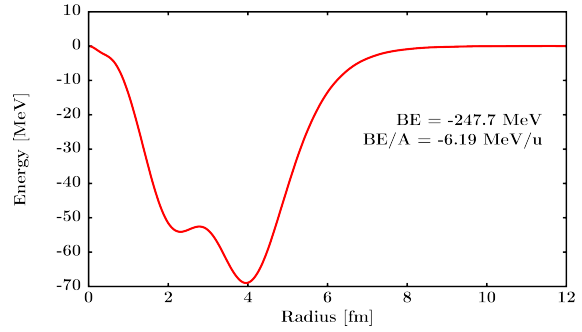
^{40}Ca proton momentum distribution



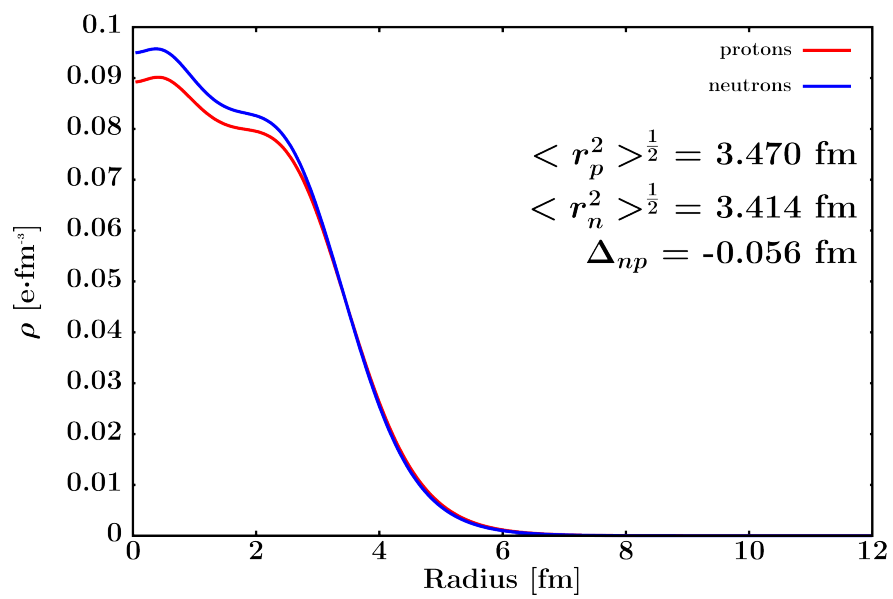
^{40}Ca neutron momentum distribution



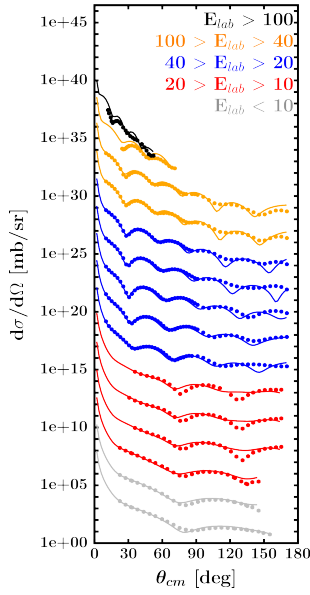
^{40}Ca energy distribution by LJ



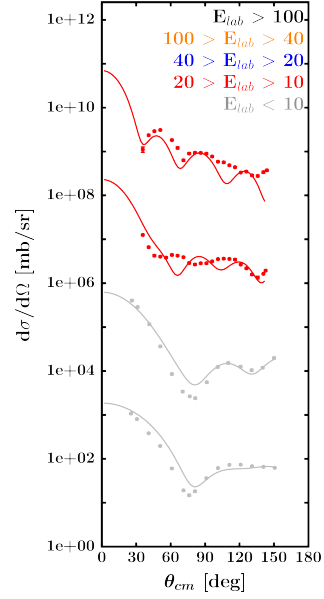
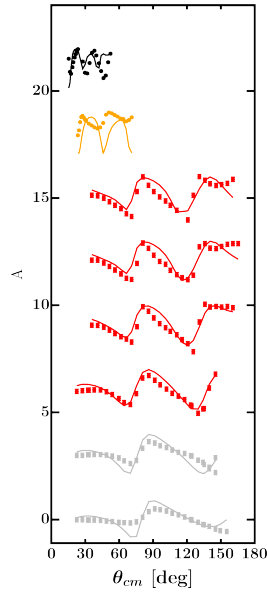
^{40}Ca energy distribution integral

 ^{40}Ca matter density distribution

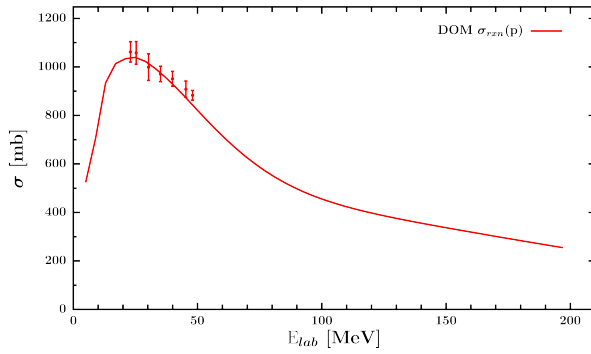
D.4 DOM fit of ^{48}Ca



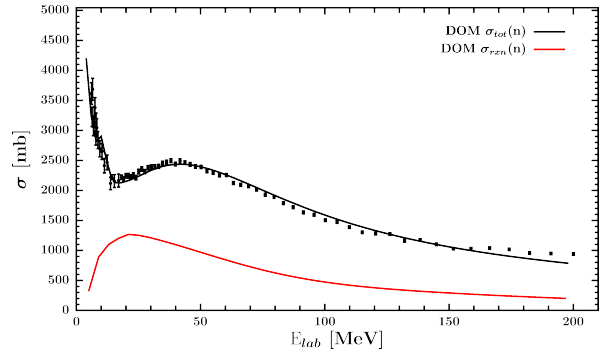
^{48}Ca proton elastic scattering



^{48}Ca neutron elastic scattering

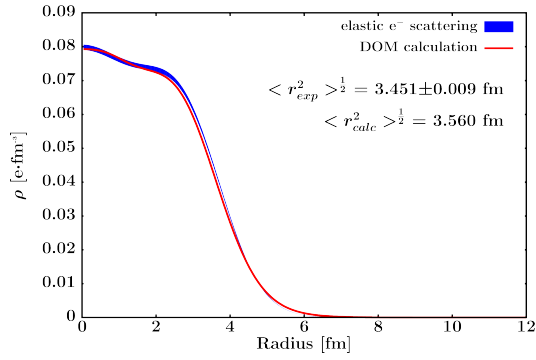


^{48}Ca proton σ_{rxn}

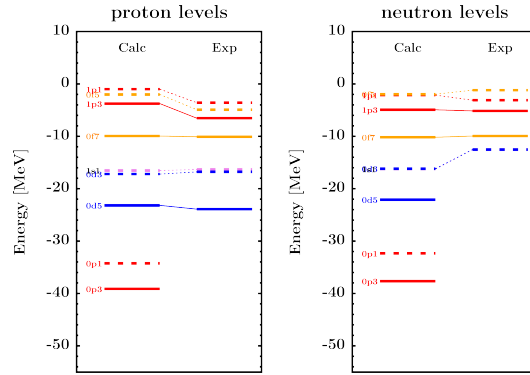


^{48}Ca neutron σ_{rxn} and σ_{tot}

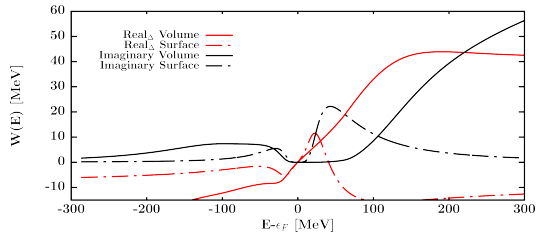
DOM FIT OF ^{48}Ca



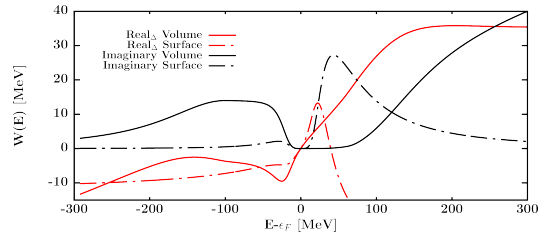
^{48}Ca charge density



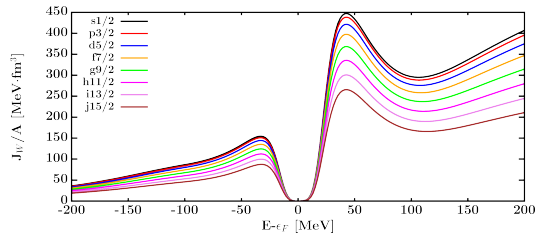
^{48}Ca single-particle levels



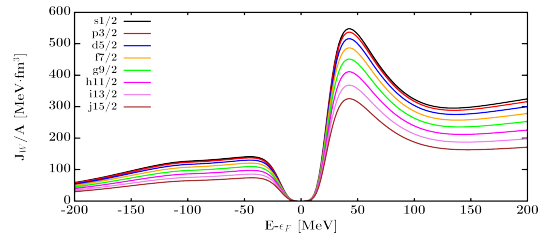
^{48}Ca proton potential energy dependence



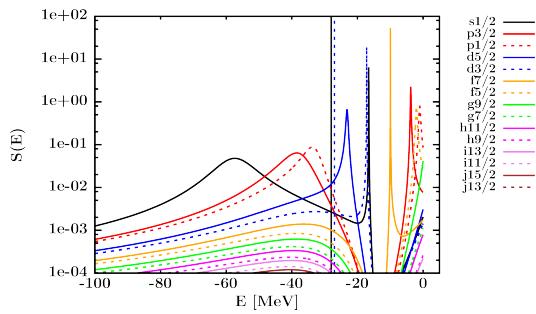
^{48}Ca neutron potential energy dependence



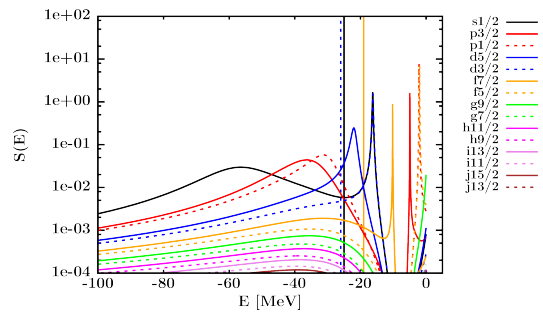
^{48}Ca proton volume integral



^{48}Ca neutron volume integral

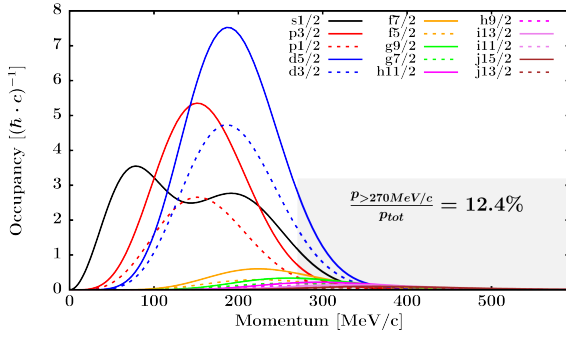


^{48}Ca proton spectral functions

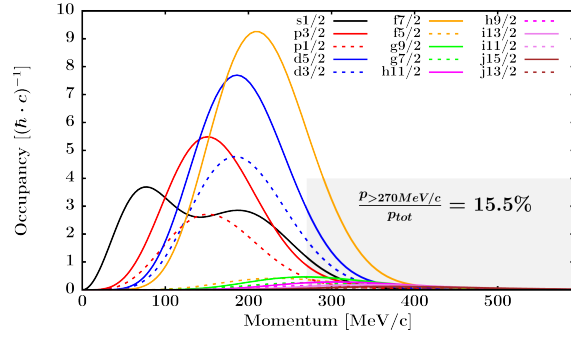


^{48}Ca neutron spectral functions

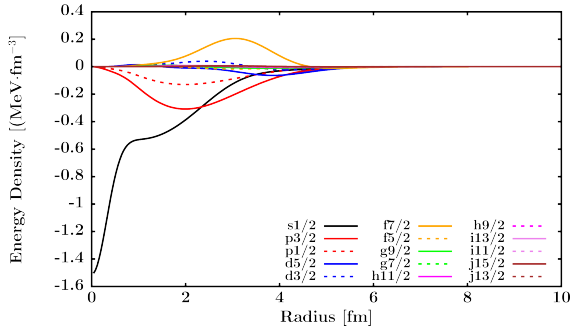
APPENDIX D: VISUALIZATION OF DOM FIT RESULTS



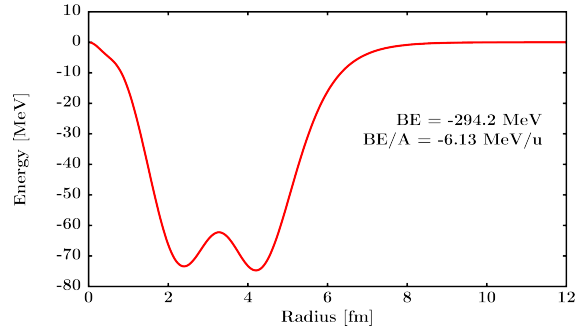
^{48}Ca proton momentum distribution



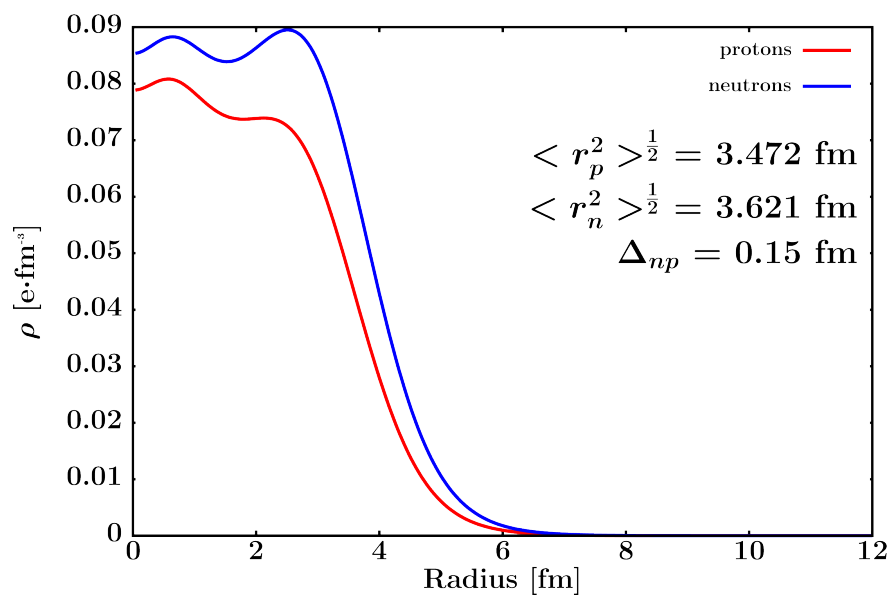
^{48}Ca neutron momentum distribution



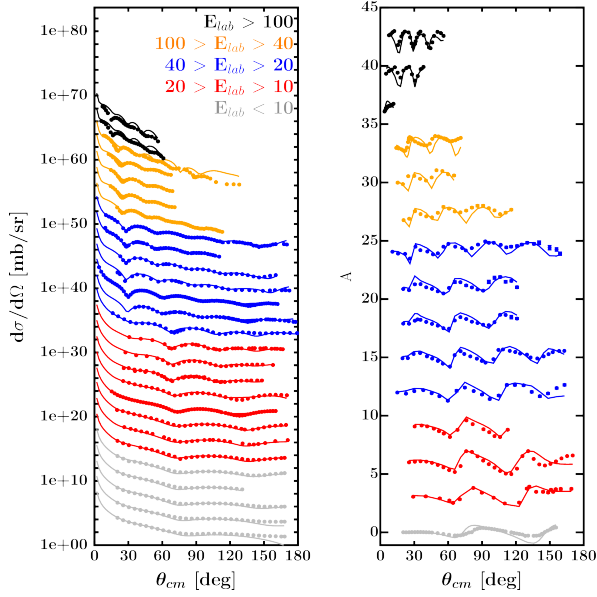
^{48}Ca energy distribution by LJ



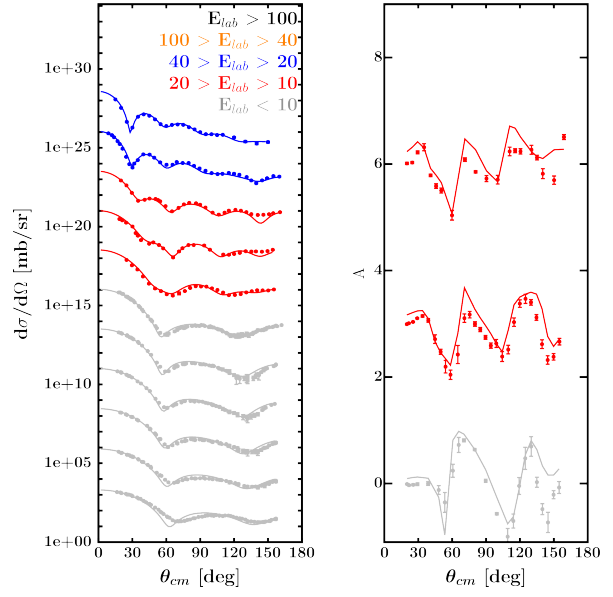
^{48}Ca energy distribution integral

 ^{48}Ca matter density distribution

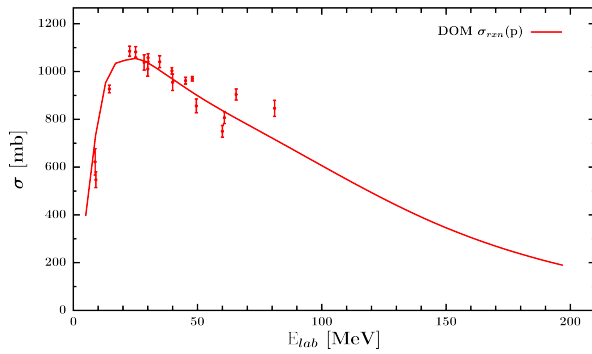
D.5 DOM fit of ^{58}Ni



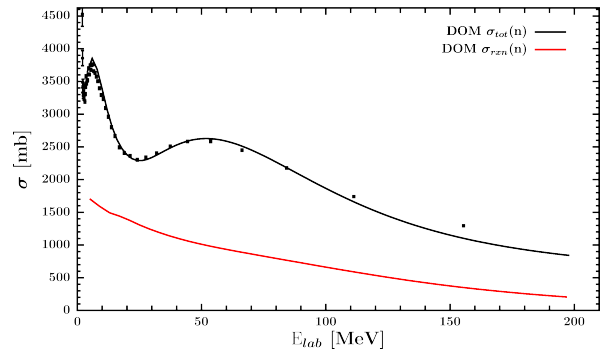
^{58}Ni proton elastic scattering



^{58}Ni neutron elastic scattering

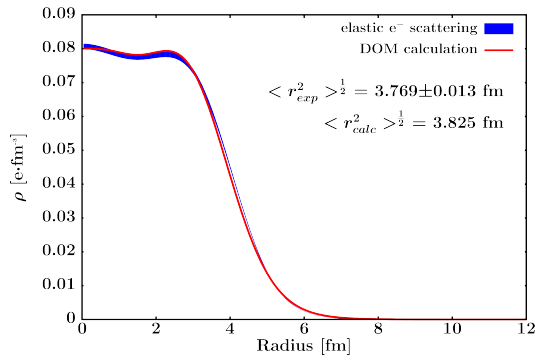


^{58}Ni proton σ_{rxn}

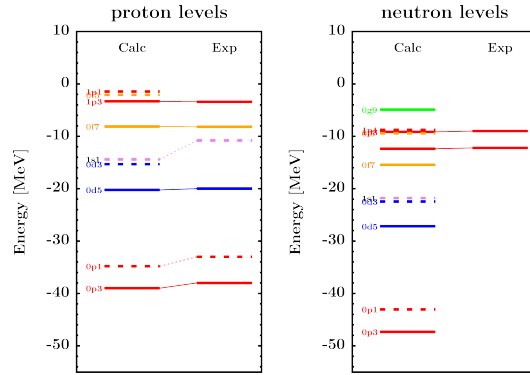


^{58}Ni neutron σ_{rxn} and σ_{tot}

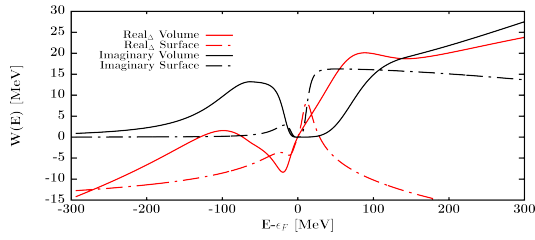
DOM FIT OF ^{58}Ni



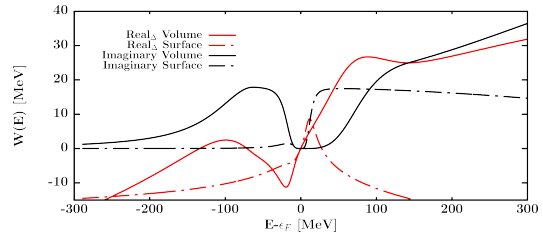
^{58}Ni charge density



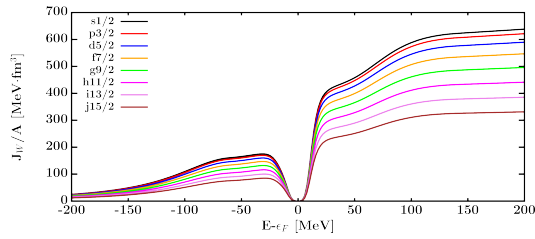
^{58}Ni single-particle levels



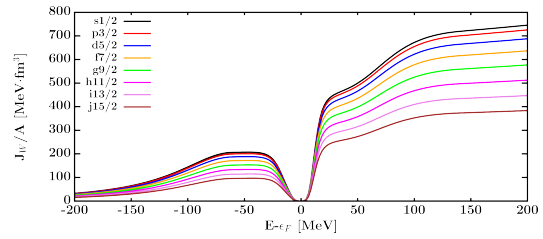
^{58}Ni proton potential energy dependence



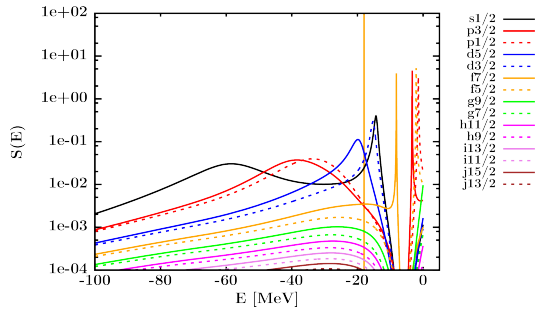
^{58}Ni neutron potential energy dependence



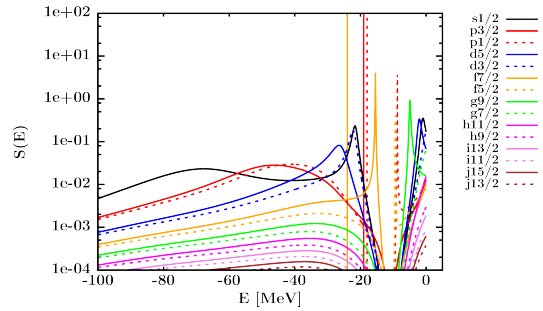
^{58}Ni proton volume integral



^{58}Ni neutron volume integral

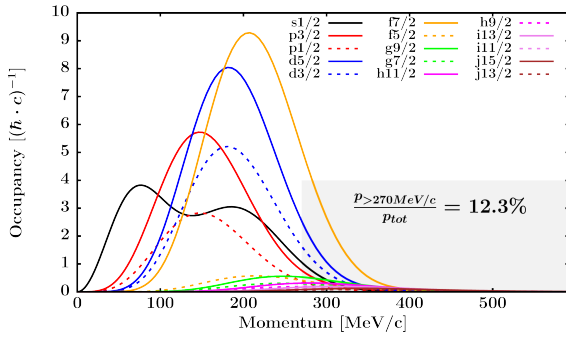


^{58}Ni proton spectral functions

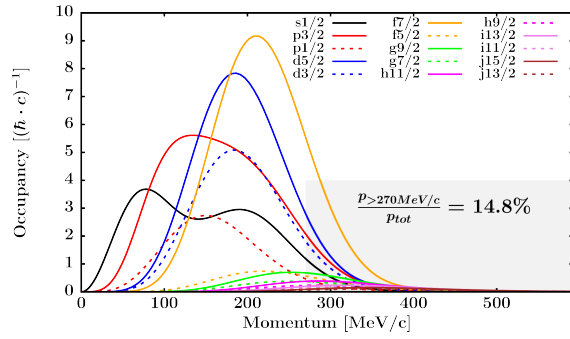


^{58}Ni neutron spectral functions

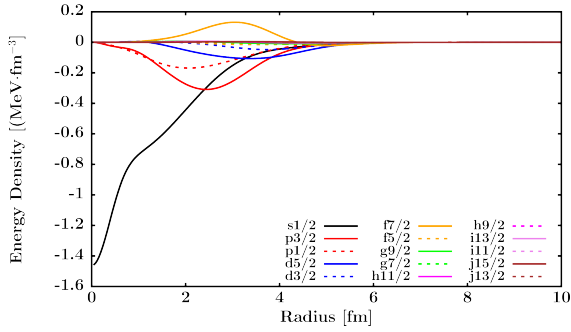
APPENDIX D: VISUALIZATION OF DOM FIT RESULTS



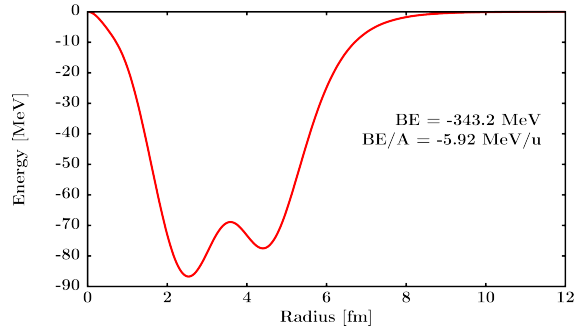
^{58}Ni proton momentum distribution



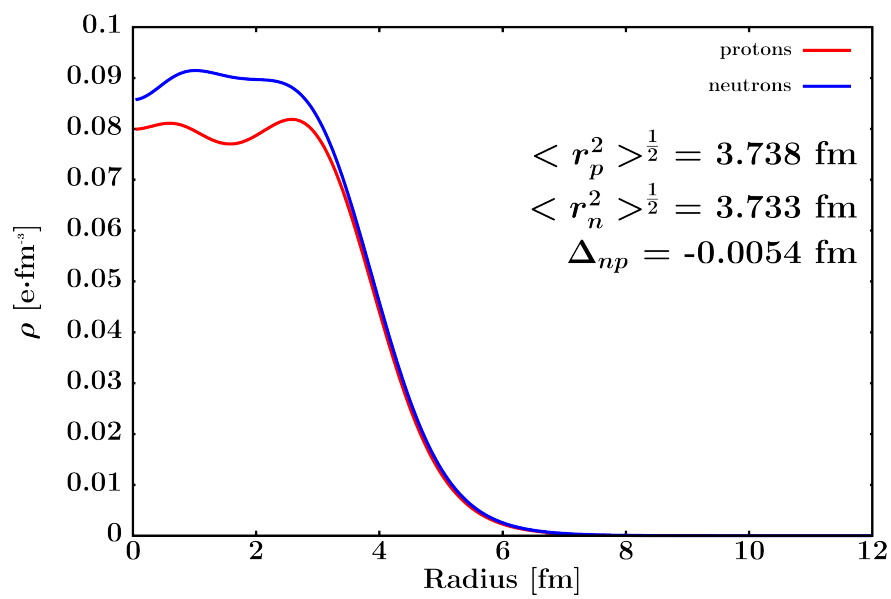
^{58}Ni neutron momentum distribution



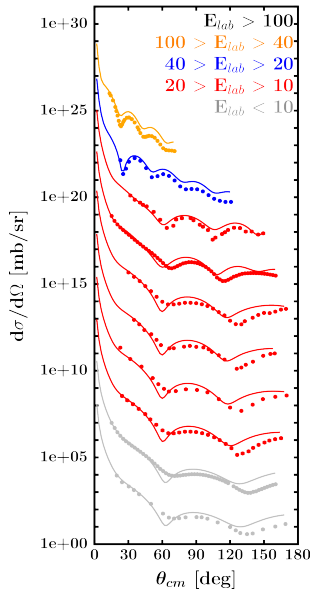
^{58}Ni energy distribution by LJ



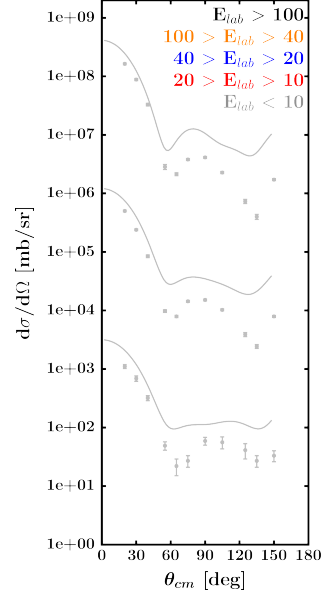
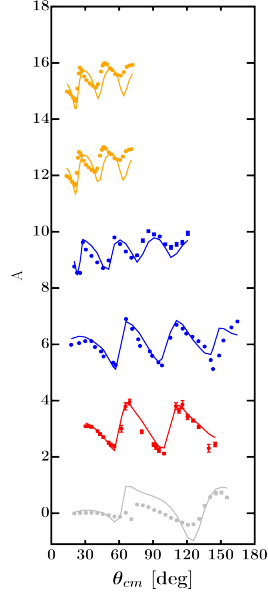
^{58}Ni energy distribution integral

 ^{58}Ni matter density distribution

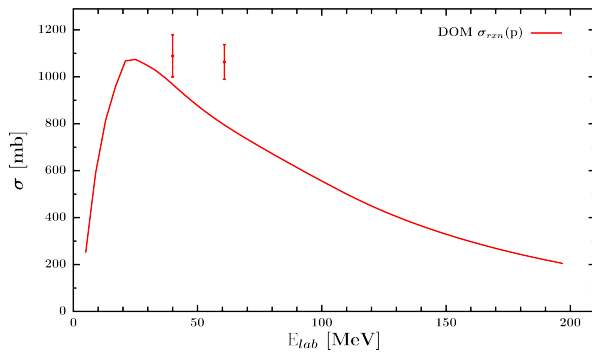
D.6 DOM fit of ^{64}Ni



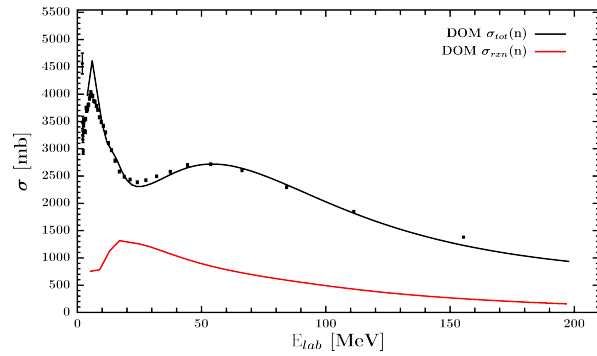
^{64}Ni proton elastic scattering



^{64}Ni neutron elastic scattering

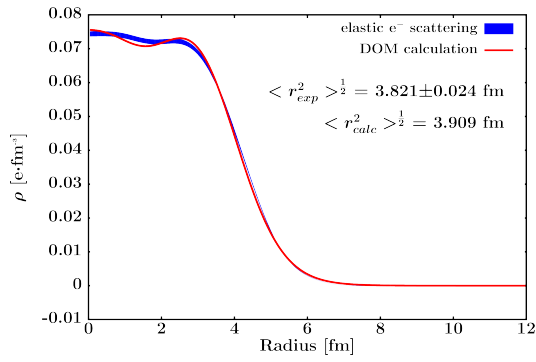


^{64}Ni proton σ_{rxn}

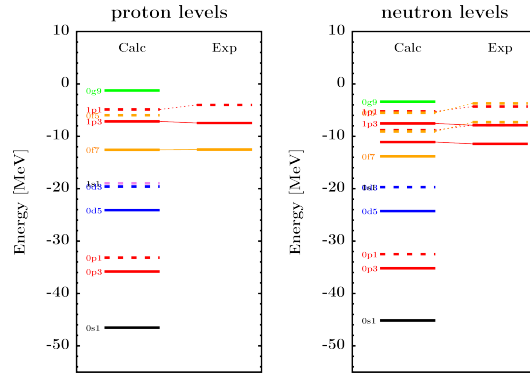


^{64}Ni neutron σ_{rxn} and σ_{tot}

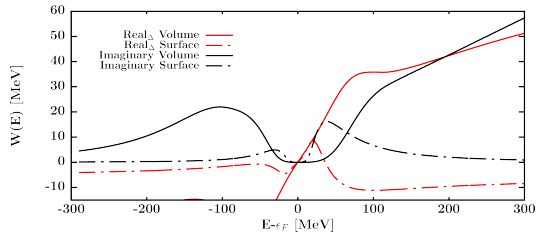
DOM FIT OF ^{64}Ni



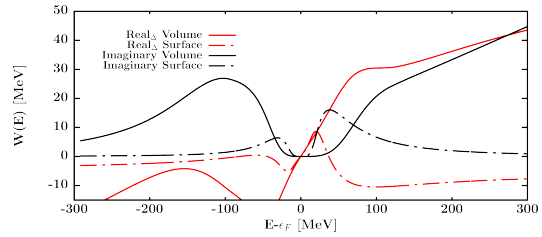
^{64}Ni charge density



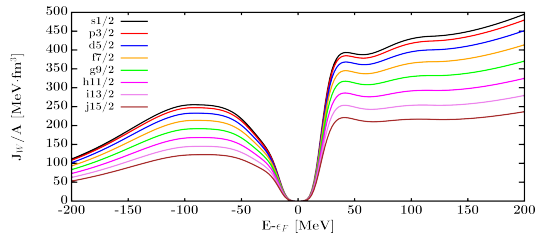
^{64}Ni single-particle levels



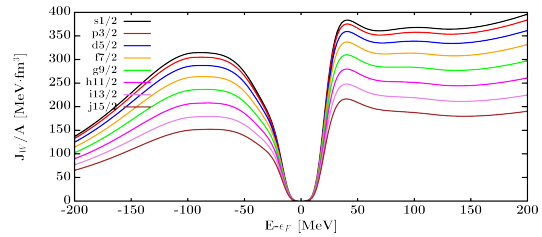
^{64}Ni proton potential energy dependence



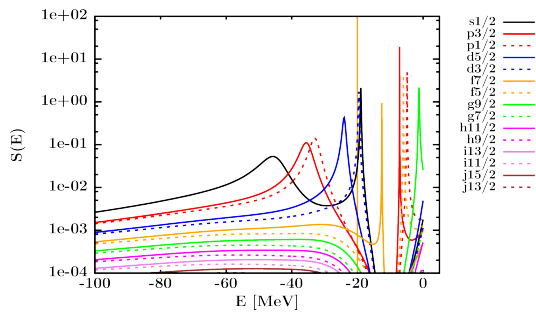
^{64}Ni neutron potential energy dependence



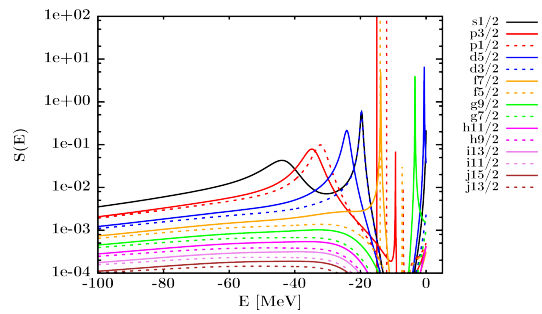
^{64}Ni proton volume integral



^{64}Ni neutron volume integral

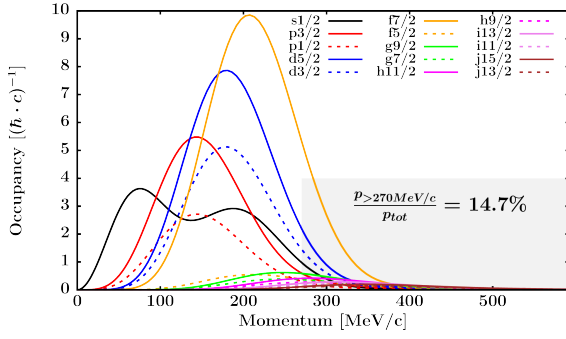


^{64}Ni proton spectral functions

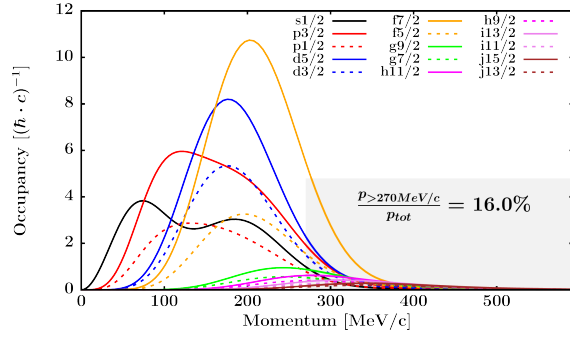


^{64}Ni neutron spectral functions

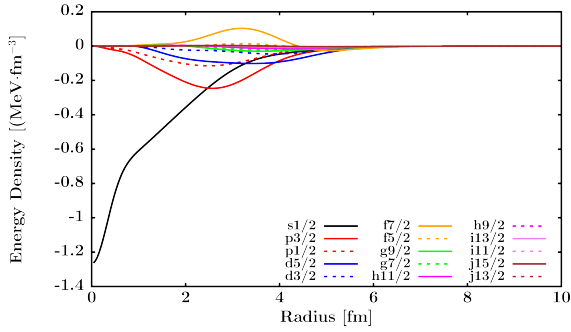
APPENDIX D: VISUALIZATION OF DOM FIT RESULTS



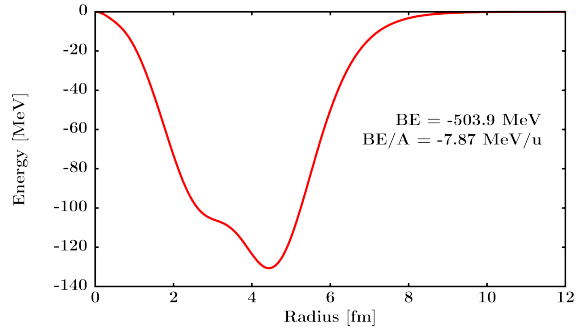
^{64}Ni proton momentum distribution



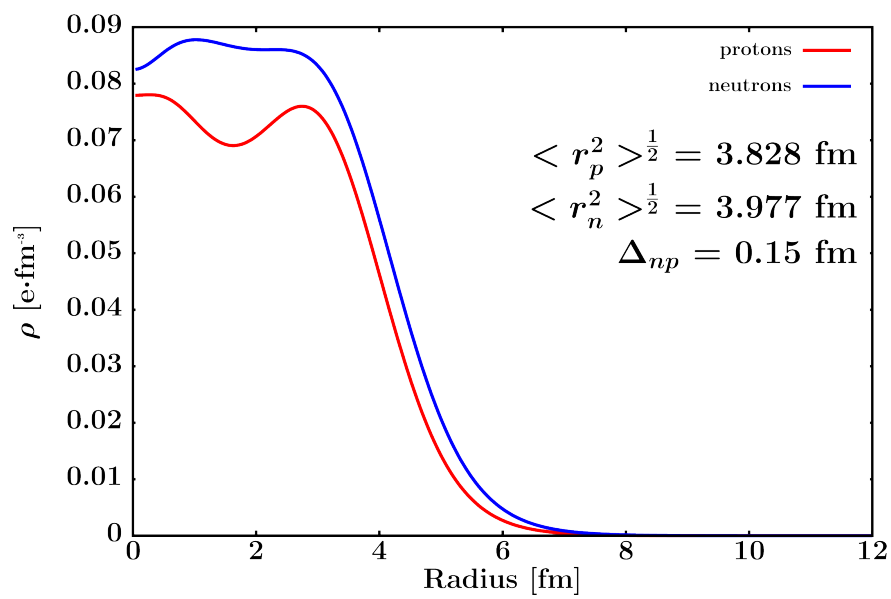
^{64}Ni neutron momentum distribution



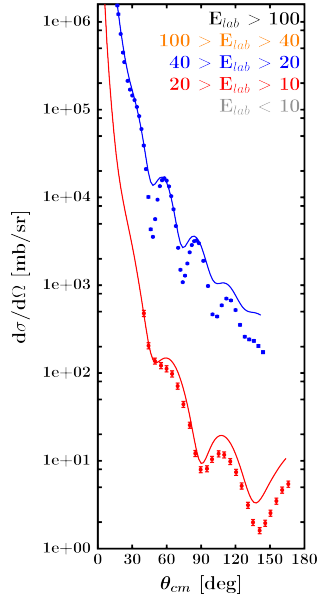
^{64}Ni energy distribution by LJ



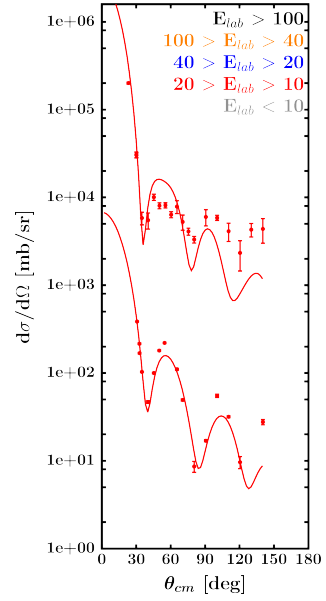
^{64}Ni energy distribution integral

 ^{64}Ni matter density distribution

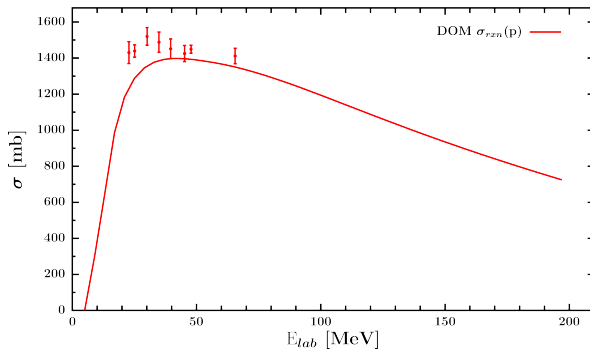
D.7 DOM fit of ^{112}Sn



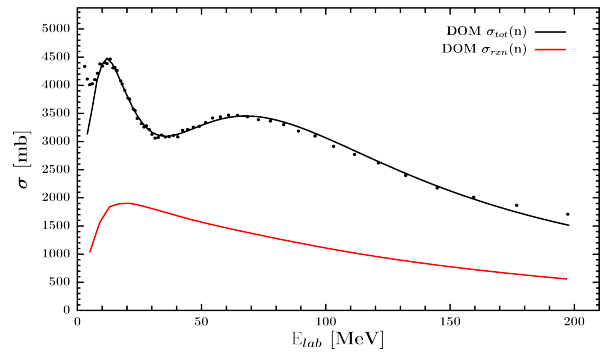
^{112}Sn proton elastic scattering



^{112}Sn neutron elastic scattering

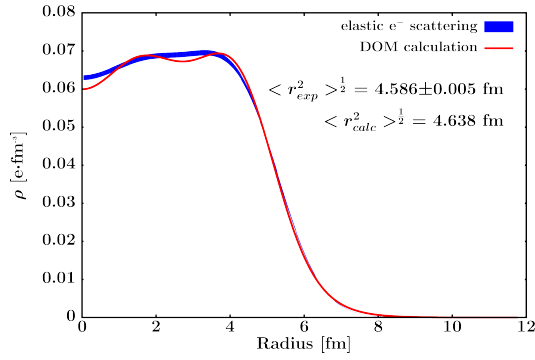


^{112}Sn proton σ_{rxn}

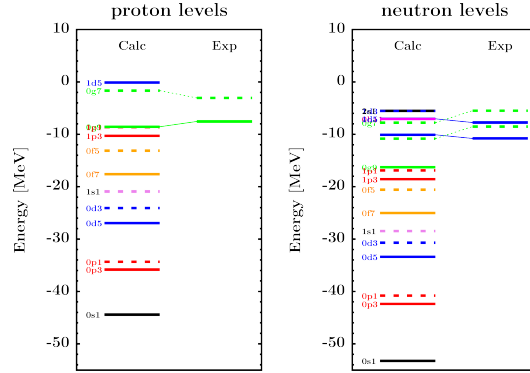


^{112}Sn neutron σ_{rxn} and σ_{tot}

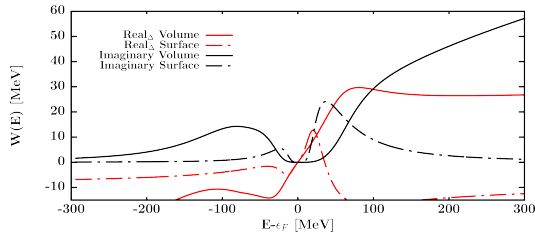
DOM FIT OF ^{112}Sn



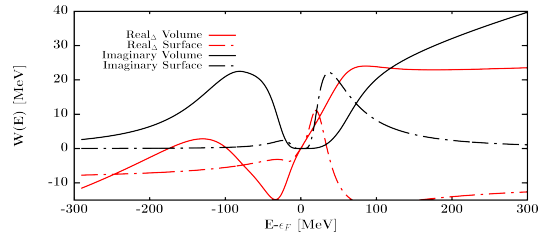
^{112}Sn charge density



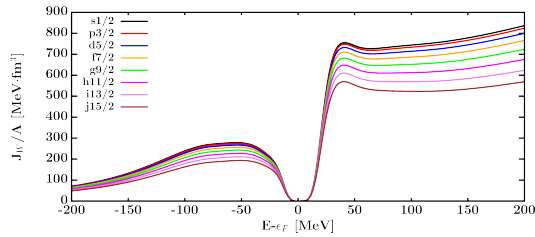
^{112}Sn single-particle levels



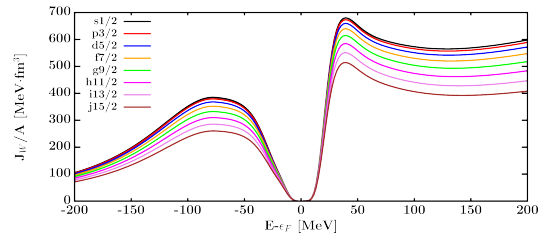
^{112}Sn proton potential energy dependence



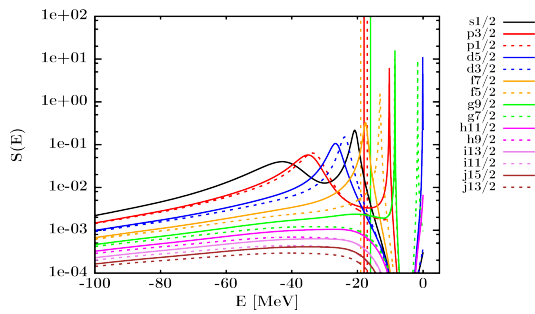
^{112}Sn neutron potential energy dependence



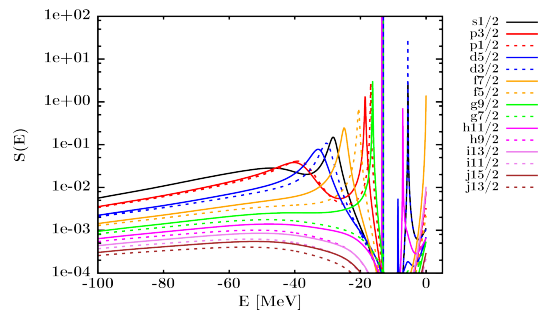
^{112}Sn proton volume integral



^{112}Sn neutron volume integral

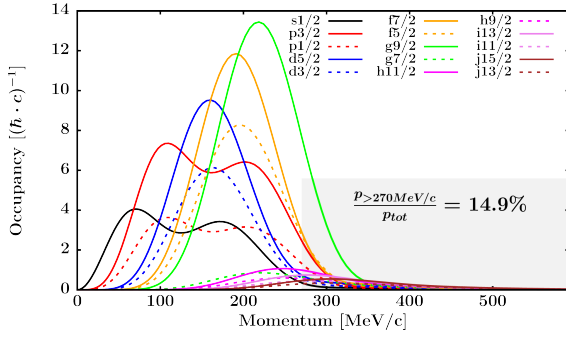


^{112}Sn proton spectral functions

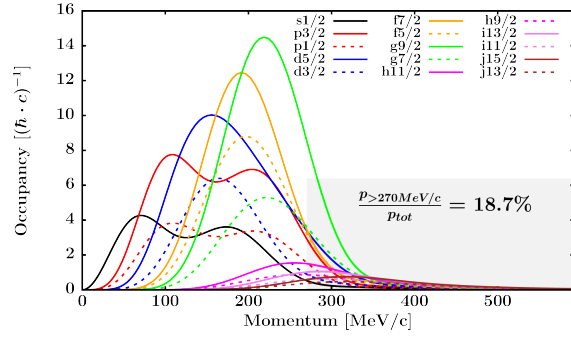


^{112}Sn neutron spectral functions

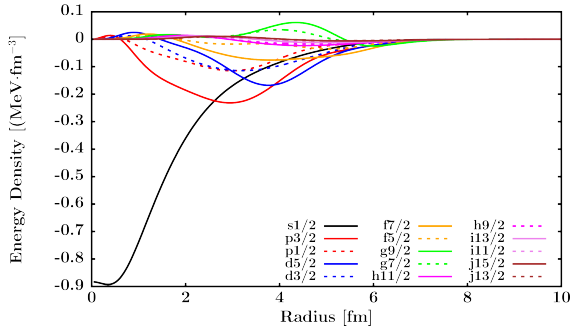
APPENDIX D: VISUALIZATION OF DOM FIT RESULTS



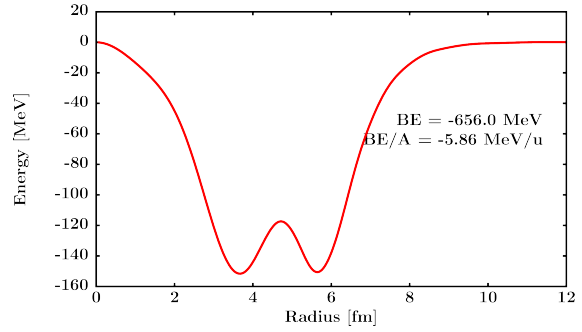
^{112}Sn proton momentum distribution



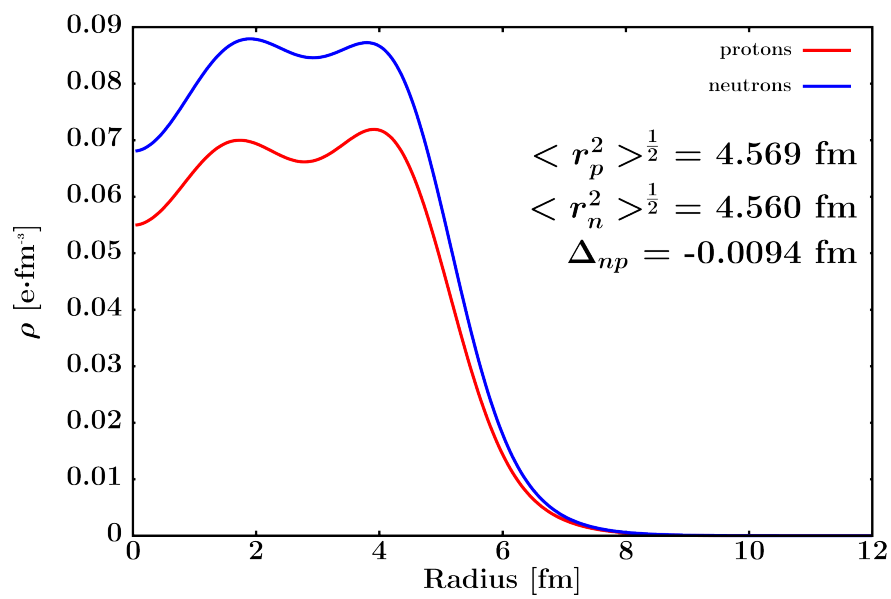
^{112}Sn neutron momentum distribution



^{112}Sn energy distribution by LJ

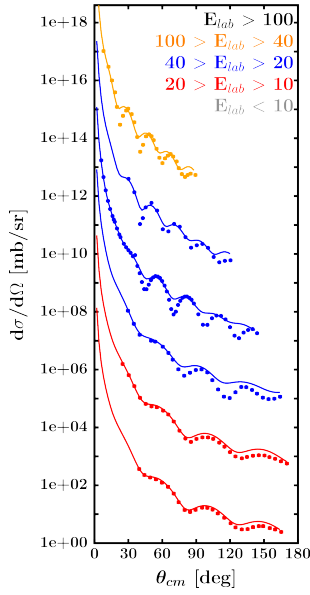


^{112}Sn energy distribution integral

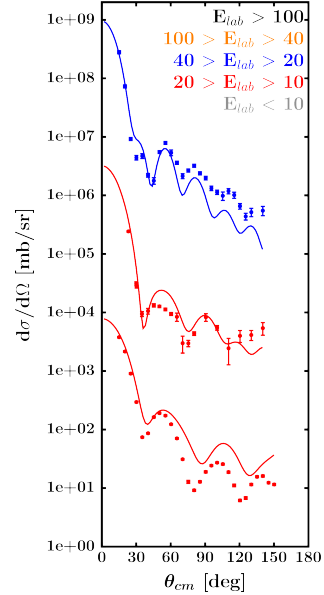
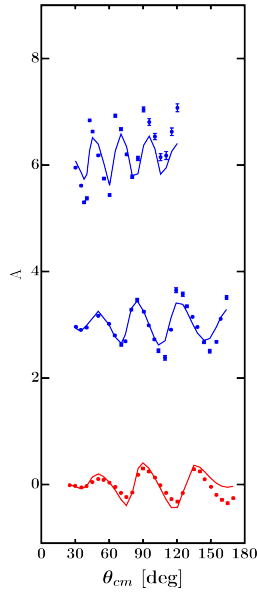


^{112}Sn matter density distribution

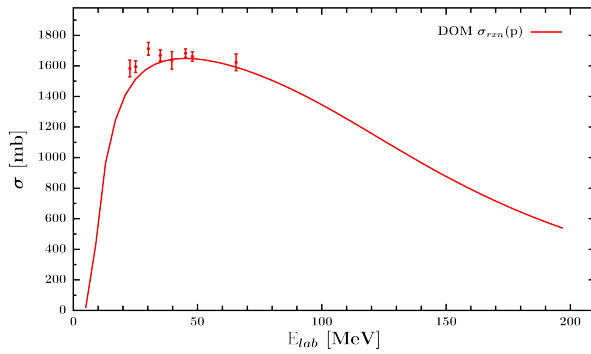
D.8 DOM fit of ^{124}Sn



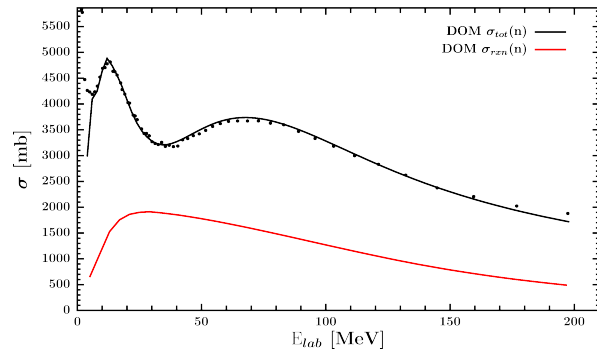
^{124}Sn proton elastic scattering



^{124}Sn neutron elastic scattering

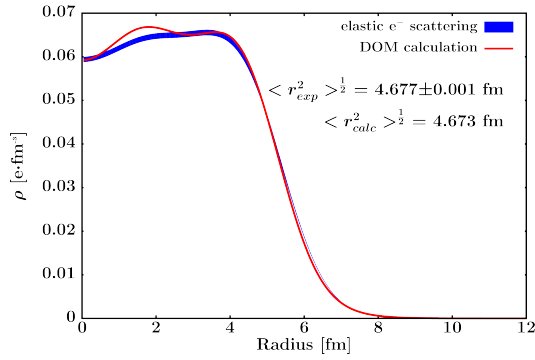


^{124}Sn proton σ_{rxn}

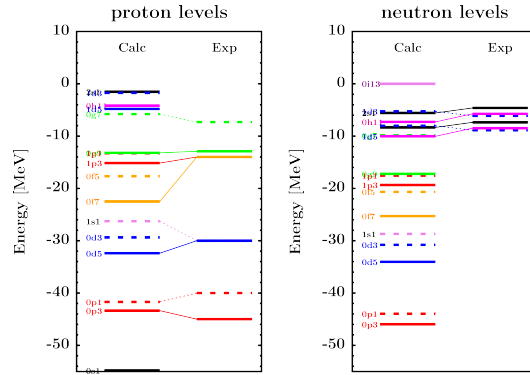


^{124}Sn neutron σ_{rxn} and σ_{tot}

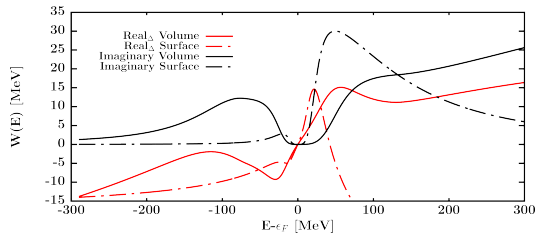
DOM FIT OF ^{124}Sn



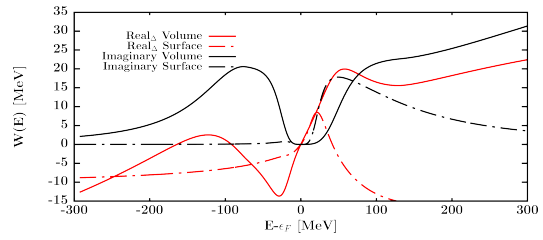
^{124}Sn charge density



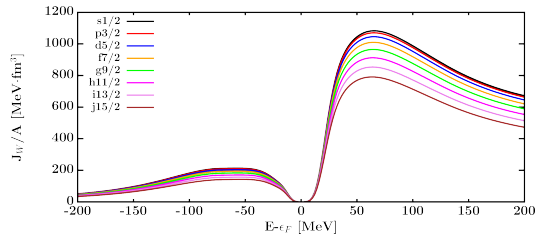
^{124}Sn single-particle levels



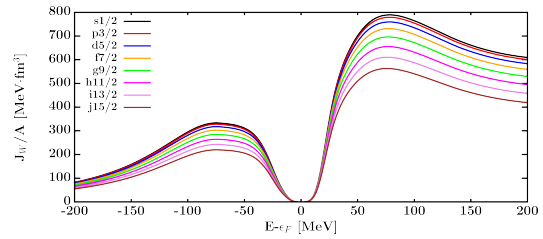
^{124}Sn proton potential energy dependence



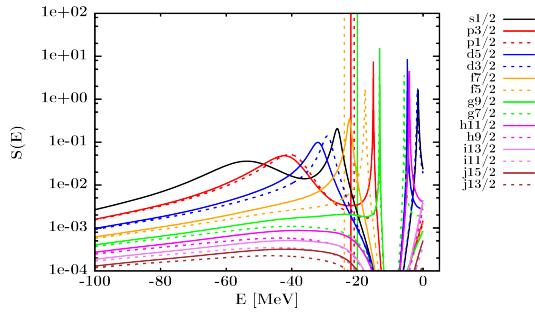
^{124}Sn neutron potential energy dependence



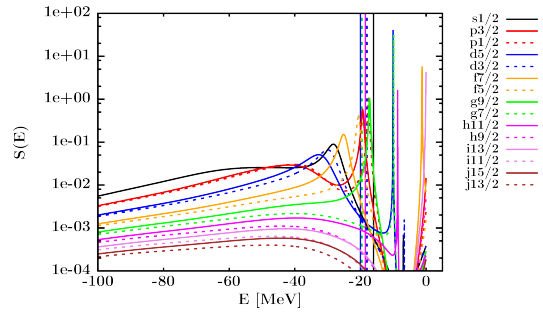
^{124}Sn proton volume integral



^{124}Sn neutron volume integral

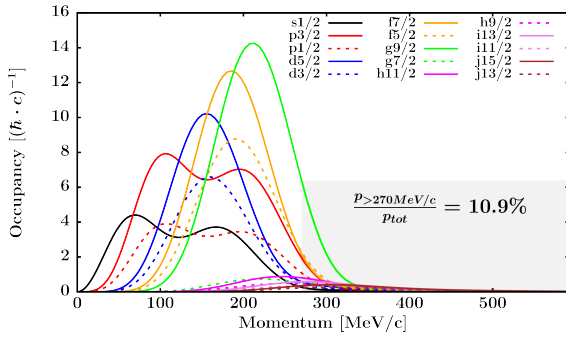


^{124}Sn proton spectral functions

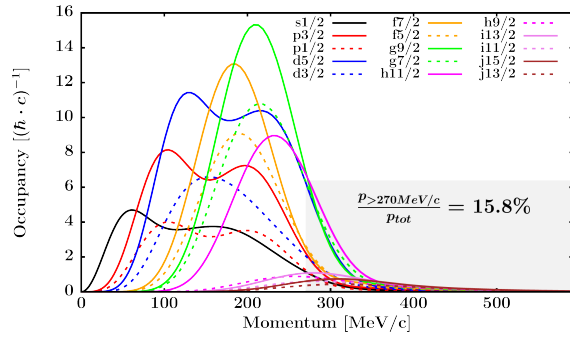


^{124}Sn neutron spectral functions

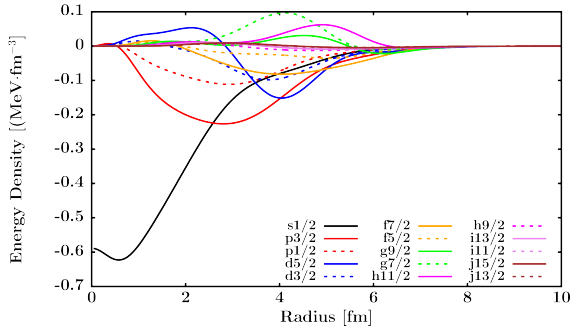
APPENDIX D: VISUALIZATION OF DOM FIT RESULTS



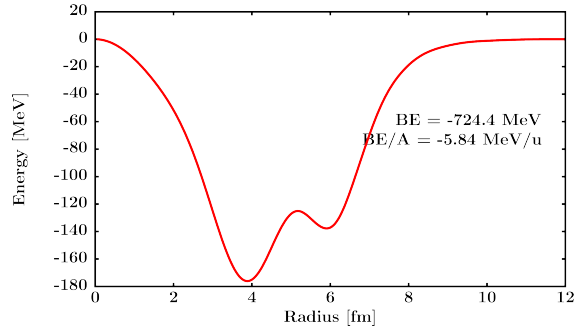
^{124}Sn proton momentum distribution



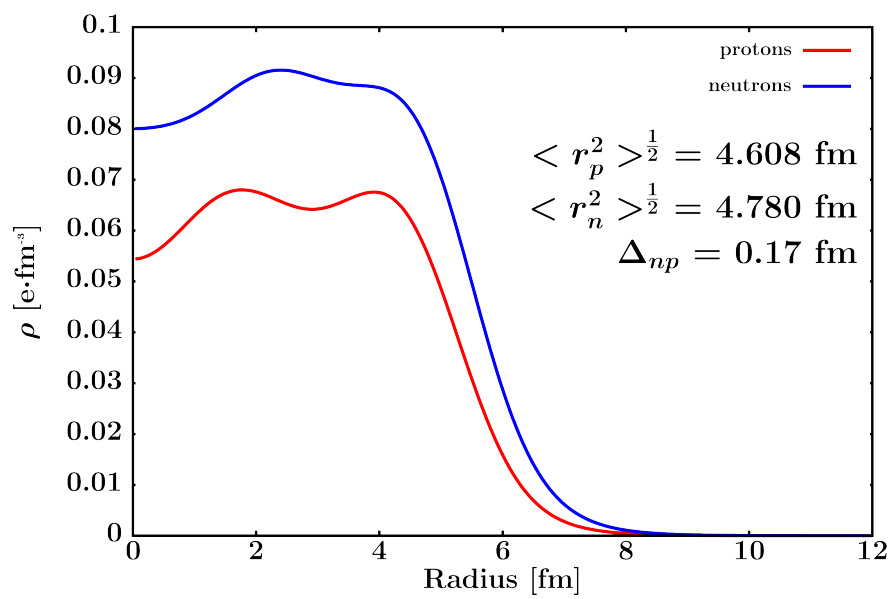
^{124}Sn neutron momentum distribution



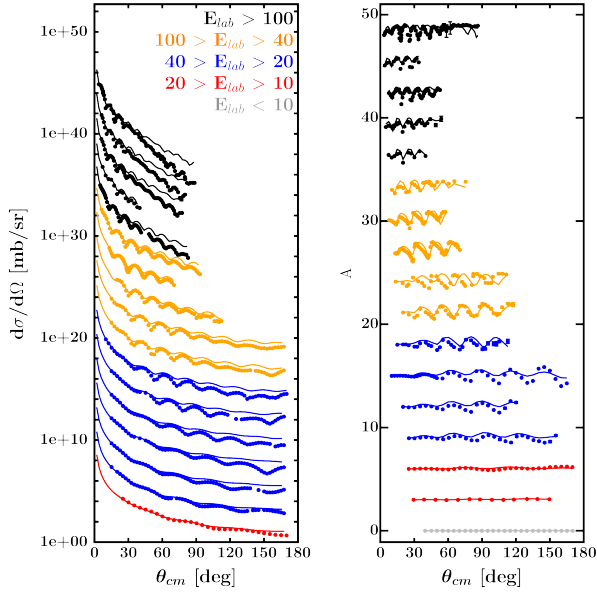
^{124}Sn energy distribution by LJ



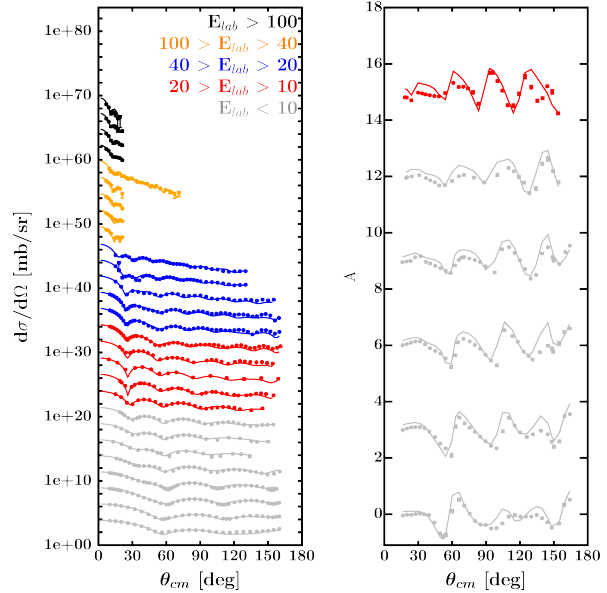
^{124}Sn energy distribution integral

 ^{124}Sn matter density distribution

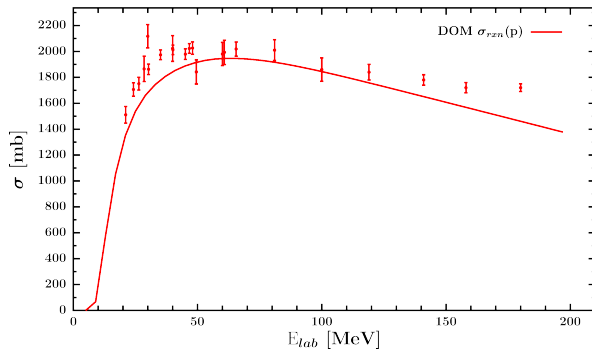
D.9 DOM fit of ^{208}Pb



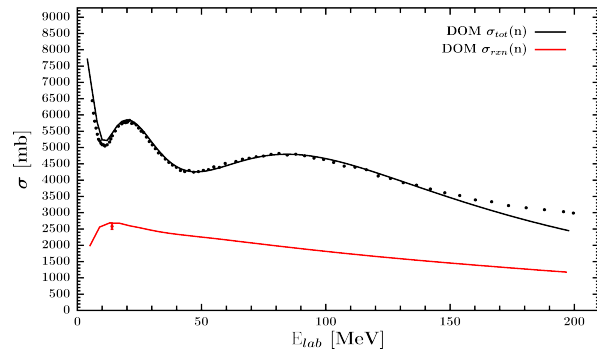
^{208}Pb proton elastic scattering



^{208}Pb neutron elastic scattering

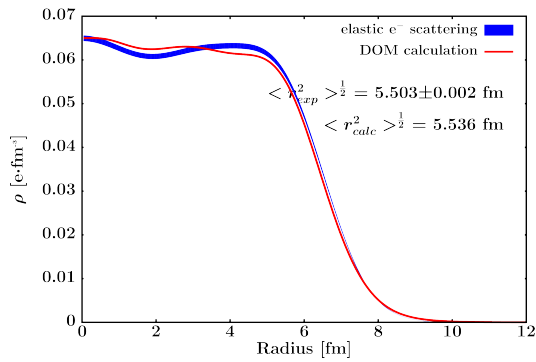


^{208}Pb proton σ_{rxn}

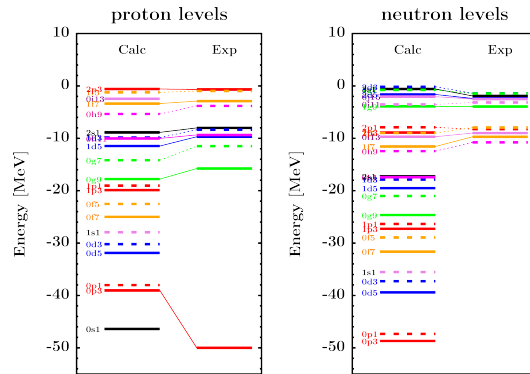


^{208}Pb neutron σ_{rxn} and σ_{tot}

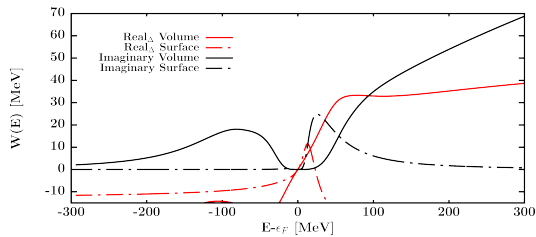
DOM FIT OF ^{208}Pb



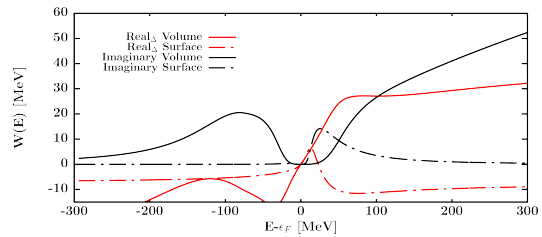
^{208}Pb charge density



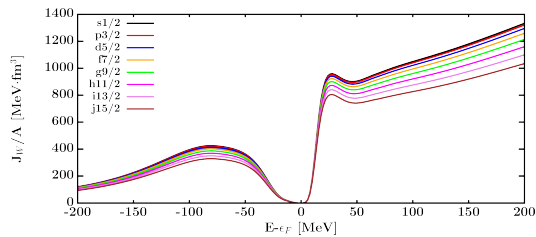
^{208}Pb single-particle levels



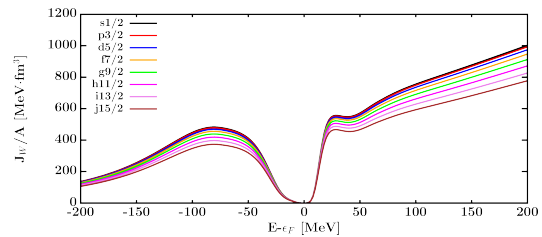
^{208}Pb proton potential energy dependence



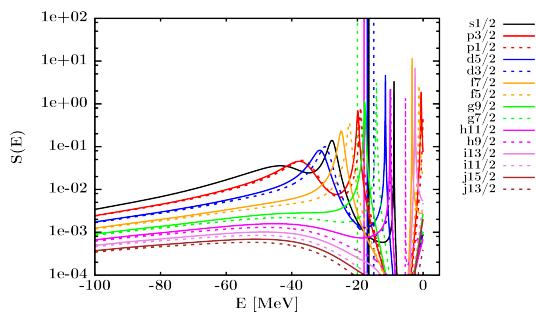
^{208}Pb neutron potential energy dependence



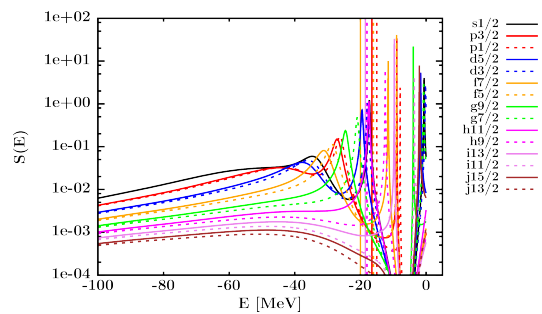
^{208}Pb proton volume integral



^{208}Pb neutron volume integral

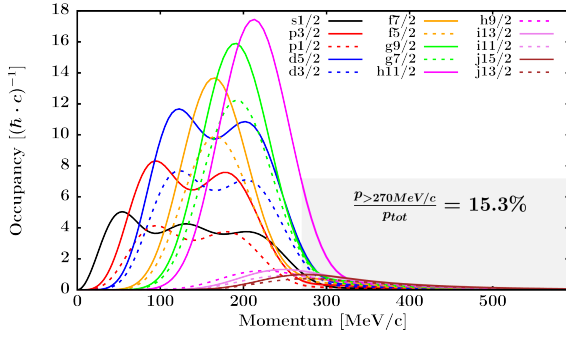


^{208}Pb proton spectral functions

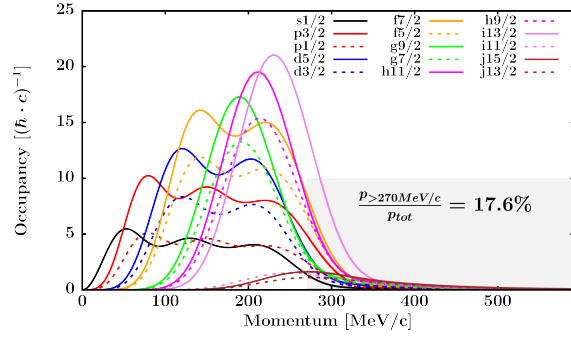


^{208}Pb neutron spectral functions

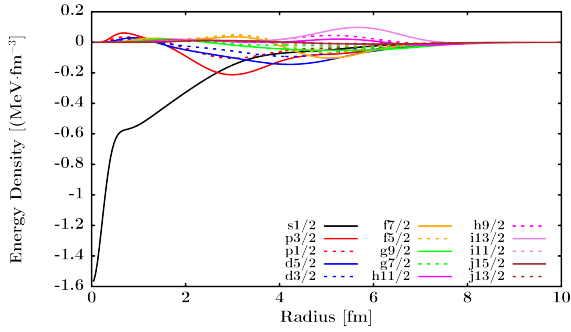
APPENDIX D: VISUALIZATION OF DOM FIT RESULTS



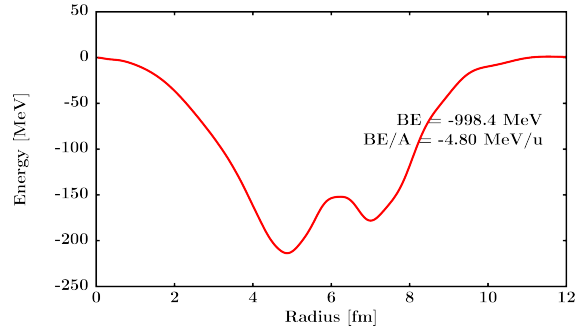
^{208}Pb proton momentum distribution



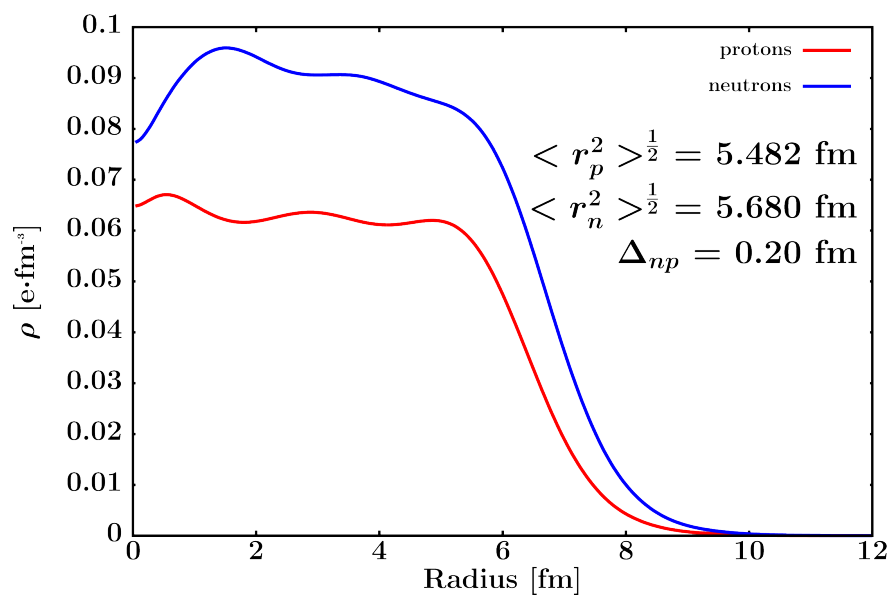
^{208}Pb neutron momentum distribution



^{208}Pb energy distribution by LJ



^{208}Pb energy distribution integral

 ^{208}Pb matter density distribution

PHYSICAL CONSTANTS

fermi (fm)	$1 \cdot 10^{-15}(\text{m})$
barn (b)	$100 (\text{fm}^2) = 10^{-24} (\text{cm}^2)$
eV	$1.6022 \cdot 10^{-19} (\text{Joules})$
Planck's Constant (\hbar)	$6.582 \cdot 10^{-22} (\text{MeV} \cdot \text{s})$
Speed of Light (c)	$2.99792458 \cdot 10^8 (\text{m/s}) \approx 29.98 (\text{cm/ns})$
$\hbar c$	$197.3 (\text{MeV} \cdot \text{fm})$
Elementary Charge (e)	$1.60217662 \cdot 10^{-19} (\text{Coulombs})$
Coulomb's Constant (k_e)	$1.44 (\text{MeV} \cdot \text{fm}/e^2)$
amu (u)	$931.494 (\text{MeV}/c^2)$
Neutron Mass (m_n)	$939.565 (\text{MeV}/c^2) = 1.0087u$
Proton Mass (m_p)	$938.272 (\text{MeV}/c^2) = 1.0073u$
Electron Mass (m_e)	$0.5110 (\text{MeV}/c^2) = 5.486 \cdot 10^{-4}u$

GLOSSARY

ADC Analog-to-digital converter, a device that digitally records the integral of an incident electrical signal over a window specified by the user. 95

CFD Constant-fraction discrimination, a technique for determining event timestamps independent of the pulse amplitude of the signal. 49, 52

DOM The Dispersive Optical Model, a phenomenological framework for extracting nuclear structure and reaction information from experimental data. 20, 113, 141

Dyson equation A self-consistent relationship between the dressed propagator G , the free propagator G_0 , and the irreducible nucleon self-energy, Σ^* (shown in Eq. 6.14). The equation can be expressed pictorially via Feynman diagrams (shown in Fig. 6.2). 121

finite-size correction Any of a series of corrections that account for the non-zero size of scattering targets used in cross section measurements, including flux attenuation, angular uncertainty in the scattering path, and multiple scattering. 106

inverse kinematics An experimental approach where the nucleus under study (e.g., ^{14}O) is bombarded onto a sample containing a typical scattering particle (e.g., protons or

α -particles). By reversing the usual kinematics of scattering, reactions can be studied on unstable nuclei that cannot be made into a fixed target. 25

LANSCE The Los Alamos Neutron Science Center, the site of our neutron σ_{tot} measurements on $^{16,18}\text{O}$, $^{58,64}\text{Ni}$, ^{103}Rh , and $^{112,124}\text{Sn}$. 26

LDM Liquid Drop Model. An early, physically-intuitive model that treats the nucleus as a charged drop of nuclear fluid. 2

LED Leading-edge discrimination, where event timestamps are assigned according to the time the leading edge of the signal crosses a fixed threshold. 49

nucleon self-energy A complex, non-local mathematical object that describes the interaction of a nucleon with another body (typically a nucleus) via an infinite sum of relevant Feynman diagrams. If the nucleon self-energy is known in a given system, a multitude of other important physics quantities (scattering amplitudes, the mean free path, the level density) can be extracted. The DOM links the optical potential and the nucleon self-energy, enabling a phenomenological approach for extracting information about the nuclear many-body problem. 121, 129

optical potential A complex potential used to approximate the microscopic nuclear many-body problem. Incident nucleons scatter off the potential in analogy to the refraction and absorption of light in optical media. In both cases, the real component of the potential determines elastic scattering, and the imaginary component determines inelastic scattering. 11, 13, 113, 121, 130

- PSD** Pulse-shape discrimination, a technique for differentiating between detector events caused by neutrons, heavy ions, and γ rays. 86, 87
- single-particle propagator** a mathematical object (specifically, a Green's function) that dictates the evolution of a single-particle state per the Schrödinger equation. 114
- TDC** Time-to-digital converter, a device that digitally records the timestamp of an incident electrical signal according to a threshold specified by the user. 95
- TOF** Time-of-flight. Measuring neutron TOF from a pulsed source is a common neutron energy determination technique. 28
- TUNL** The Triangle Universities Nuclear Laboratory, the site of our neutron $\frac{d\sigma}{d\Omega}$ measurements on ^{112}Sn and ^{124}Sn . 87
- WNR** Weapons Neutron Research facility at LANSCE, site of a spallation neutron source useful for σ_{tot} measurements. 26